GROWTH AND CHARACTERIZATION OF CHEMICAL SOLUTION BASED NANOSTRUCTURED COATED CONDUCTORS WITH CeO_2 CAP LAYERS

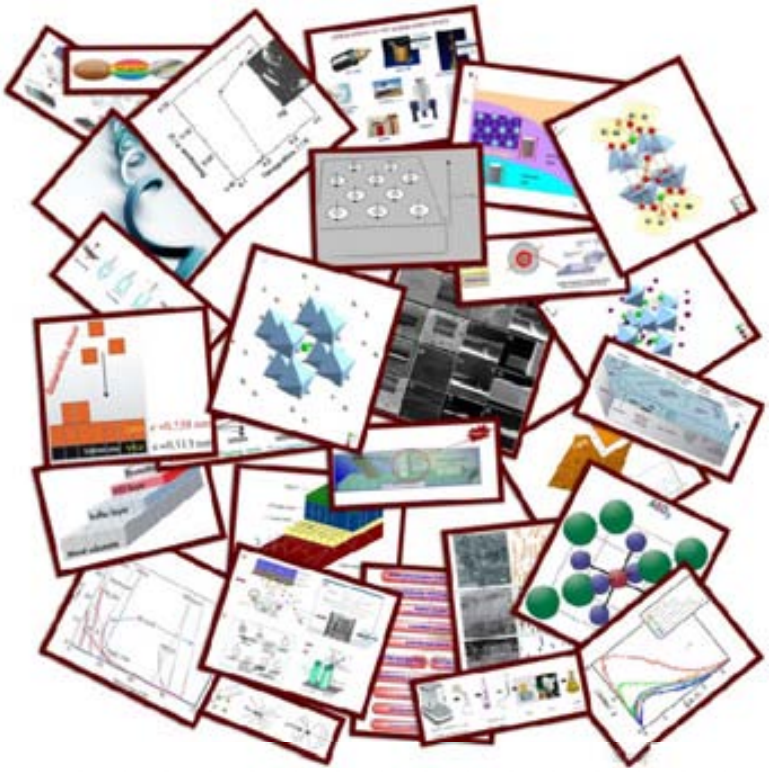

VALENTINA ROXANA VLAD

PROGRAMA DE DOCTORAT EN CIÈNCIA DE MATERIALS
Departament de Física de la Universitat Autònoma de Barcelona
Departament de Materials Superconductors i Nanoestructuració a Gran Escala, ICMAB-CSIC

Directors: Prof. Xavier Obradors i Dr. Alberto Pomar
Tutor: Prof. Francesc Pi

Mèmoria presentada per a l'obtenció del grau de doctor
Maig 2011

AKNOWLEDGEMENTS

No work of this magnitude is complete without support and a great number of people deserve my gratitude. First of all, I want to thank Prof. Xavier Obradors, my director of thesis, for accepting me in ICMAB to prepare this PhD, for the scientific support in every moment and also for the personal support and understanding when life was not so easy for me. Next, I need to thank Prof. Teresa Puig for her dedication, for the training in the NESPA experience and for being human in the personal fight that I had to give. Thanks to my second supervisor, Dr. Alberto Pomar, for giving me directions in the scientific research. I thank also Dr. Albert Calleja for the time spent sharing the same office and for the confidence deposited in me.

The stage that I realized in IFW Dresden helped me to interact with wonderful people who made my stay there very pleasant and fruitful. Special thanks to Dr. B. Holzapfel and Dr. R. HÜhne for their advice and valuable discussions in the field of superconductivity. To Silja Schumann for all the pleasant time spent together and for her "I know all will be good with you, Rox".

I would like to thank from my bottom of my soul to A. Chabra for his unconditional friendship, real one, for the moral support and for believing in me from the very beginning. The meaning of the friendship was underlined also in my life by Denny S. P. which brought joy and confidence from far away.

Special thanks to Ana Cioran for her responsible behaviour in a delicate moment of my life and bringing me hope and joy. Thanks from my part to the romanian community from ICMAB for all the time spent together.

I spent many gorgeous moments in good company, visiting new places which I discovered, between laughs and tranquillity together with my "travelling team": Silvia, Noe, Ana L., Aura, Maite, Jessy. Thank you for these memories which will always stay in a special corner of my soul.

I would like to express my appreciation to Neus for showing me how the things go on in the labs at the beginning of my spanish life in ICMAB. Thank you for the help on developing my experimental capabilities in the laboratory and also the personal one, very appreciated, for all the moments spent together, for your concern, care and your friendship.

I have also had the benefit of considerable discussion and interaction with all the technicians from ICMAB – Anna C, Maite, Noemi, Bernat, Ana Esther, Judith, Francisco, Joan, Xavi, Enrique, Edgar – who were an appreciable help for the measurements and results presented here.

To Anna P. I say thanks for the transport measurements presented in this thesis and also for the good moments spent together.

With your efficiency and also your smile and hugs, Patty A., life seems easier! Thank you for the time spent with me.

The lively and always cooperative atmosphere in our labs was certainly inspired and upheld by all the present and past PhD students and PostDocs. Many, many thanks to: Jone, Mariona de P, Gian, Mariona C, Jaume, Carlos M, Patricia Ab., Anna Ll., Marta G., Bianca, Mircea, Cornelia, MJey, Yenai, Josh, Albert Q., Cesar S., Victor Ro., Victor R., Marta V., Roberto, Cesar M., Fernando, Xavi P., Adrian , Roger, Berto, Simo, Xavi, Shuai for an excellent environment, help in practical matters and various discussions. With all of you, working in lab was really fun.

Particular thanks must be given to all those who provided indispensable assistance at ICMAB, the administration service (Pietat, Mariona, Trini, Montse C, Maria, Rebeca, Eva, Vicente), informatics department (Marc, Javier) and all the other scientific members of the Superconducting Materials and Large Scale Nanostructuration Department (Susagna, Jordi, Narcis, Xavier G., Felip).

Grateful thanks to my family for letting me go follow my wonderful spanish dream.

Finally, I would like to express my gratitude to the EU projects (HIPERCHEM, NESPA), to the Spanish Ministry projects (Consolider Nanoselect, Nanosuperenergy – All solution based nanostructured for energy applications), to CSIC and Generalitat de Catalunya (XaRMAE, Grup de recerca Consolidat – SGR_2009_0070070) for the financial support.

A tod@s vosotr@s, muchas gracias!

MOTIVATION AND OVERVIEW OF THE THESIS

100 years after Dutch physicist Heike Kamerlingh Onnes found that mercury has an electrical resistance of zero when cooled in liquid helium, superconductors are finally being rolled out for use in electricity grids. Superconductive wiring carries about ten times as much power as the same volume of conventional copper wiring. Although some of that power is lost (ac losses) and liquid nitrogen must be used to keep cool the superconducting cables or other devices, such power systems are still more efficient than those based on copper wiring, which losses 7-10% of the power it carries as heat. Because of this, several countries, such as USA, Japan, South Korea, China and Europe have established objectives for 'green' electricity networks reducing the greenhouse gas generation (CO_2) and build more efficient and robust 'smart grids' based on the superconductors.

The high temperature superconducting wires are made based on the ceramic compound yttrium barium copper oxide (YBCO), part of a family of 'high-temperature' superconducting ceramics that were first discovered in 1986. It remains in the superconducting state up to 93 kelvin (–180 ºC), meaning it can be cooled using liquid nitrogen. This is in contrast to low temperature superconductors, which are made of metal alloys and must be cooled to below about 20 kelvin (–253 ºC) with liquid helium. That makes them too expensive to be used in large-scale commercial applications. Superconductors also lose their remarkable properties when current above a critical value is passed through them, so the search for a commercially viable superconductor has focused on materials that operate at a high temperature relative to low temperature superconductors and can carry large currents. At the moment, $YBa_2Cu_3O_{7-x}$ (YBCO) is the most promising material available [1].

The attractive perspectives offered by coated conductors, known as the 2nd generation of high temperature superconductors (2G-HTS), have triggered broad and fruitful R&D efforts to make them ready for the market place [2]. Recently, LS Cable, a South Korean company based in Anyang-si near Seoul, has ordered three million meters of superconducting wire from the US firm American Superconductor in Devens, Massachusetts, which is the highest commercial order so far of HTS CC [1]. High Temperature Superconductors (HTS) have an enormous potential for significantly improving existing power systems, such as cables, motors, transformers, magnets and generators, because higher power densities and reduced losses can be achieved by replacing copper or low temperature superconductor wires [3]. Superconducting materials will also enable completely new technologies in the power sector,

such as fault current limiters or inherently stable magnetic levitation. As examples for innovative applications, advanced energy systems for "all-electrical" ships, off-shore windmills and transportation systems should be mentioned. Although research on the materials aspects of HTS has been highly successful in the past, the development of low cost - high performance HTS materials remains a key factor of success and, in order to bring these emerging materials onto the market in a reasonable time frame, requires significantly more basic and applied materials research. The development of HTS materials for power applications is a highly multidisciplinary task involving chemistry, physics, materials science and electrical engineering. This task is currently addressed along three quite differently oriented routes:

i. the construction and implementation of the first "real" industrial systems based on HTS materials,
ii. the development of HTS coated conductors (CC) that will result in economic conductor production and
iii. the controlled nano-engineering of superconducting materials (highly textured HTS bulk materials and thin films, polycrystalline MgB_2) to enhance flux pinning and thus to improve the material to the necessary performance in magnetic fields.

The anisotropic features of YBCO and its weak-link behaviour require the processing of almost single crystalline thin films into flat tapes of coated conductors by basically two different methods: RABiTS—rolling-assisted biaxially textured substrates; and IBAD—ion-beam assisted deposition. Reliable processing technologies are now at hand, and critical current carrying capacities can be raised to almost 10–20% of the theoretically possible limit by optimizing current transfer through grain boundaries as well as flux pinning through control and design of the microstructural landscapes. The optimization of the in-field properties of the 2G-HTS wires, as well as the manufacturing of coated conductors with low ac losses and of assembled conductors for high current application remain active development areas. Cost reduction and more economic processing are still an issue. However, coated conductors are now beginning to penetrate the market, particularly for power and electrical applications, where savings in energy are essential and where the unique features of high temperature superconducting materials can be utilized [2].

The main objective of this thesis is to develop new simplified nanostructured Coated Conductors architectures based on Chemical Solution Deposition (CSD). For that, the growth and characterization of these Coated Conductors was investigated first on YSZ single

crystals where CeO_2-derived cap layer can be easily grown. The knowledge generated can be useful for two types of metallic substrates:

1.- ^{MOD}LZO buffered Ni5%W RABiTS substrates;

2.- ^{ABAD}YSZ buffered Stainless Steel (SS) polycrystalline substrates.

Taking into account the quality of the existing metallic substrates, this thesis has concentrated on ^{ABAD}YSZ/SS substrates, provided by Bruker HTS, Germany.

The first step for achieving simplified architectures was the investigation of Gd,Zr doped CeO_2 which better adapts to the mentioned substrates. The second step consisted in growing $YBa_2Cu_3O_{7-x}$ superconducting films using the trifluoracetates route.

This work is structured in seven chapters. The first chapter entitled “Introduction” gives a brief description of the superconductivity, followed by a short introduction about the superconductive compound YBCO and ending with the principal methods for obtaining high quality textured YBCO films. Next chapter briefly describes the experimental techniques used in this thesis for the characterization of the buffer layers and YBCO films like Atomic Force Microscopy (AFM), X-ray Diffraction (XRD), Scanning Electron Microscopy (SEM), Transmission Electron Microscopy (TEM), Reflection High-Energy Electron Diffraction (RHEED), Pulsed Laser Deposition (PLD), SQUID, X-ray reflectivity (XRR) and electrical transport measurements. A complete characterization of the samples with all these techniques is necessary in order to understand the complex mechanism of each superconductor and the interactions between different layers. The third chapter is dedicated to various doped cerium oxide thin films used as cap layer which were prepared by spin coating and characterized by mean of various techniques: AFM, XRD, RHEED and XRR. Chapter 4 details the efforts to produce a highly textured superconducting YBCO film on the architectures with different buffer layers described in Chapter 3 which have in common that the cap layer is CeO_2. The technical requirements for high quality Coated Conductors are very diverse. To achieve a high quality epitaxy and high J_c, it is necessary to perform a detailed morphological and structural characterization by means of SEM and XRD. This microstructure of the YBCO layer needs to be closely correlated with that of the cap layer. In order to study the superconducting properties in more detail, inductive and transport measurements have been performed to examine current flow in YBCO films deposited on different substrates. Chapter 5 reports the results obtained with CeO_2-derived cap layers grown on Alternating Beam Assisted Deposition (ABAD) substrates. Next chapter, the sixth one, is dedicated to the development of $BaZrO_3$-$YBa_2Cu_3O_{7-x}$ and $BaCeO_3$-$YBa_2Cu_3O_{7-x}$ nanocomposites thin films by MOD using the in-situ approach. Barium zirconate is the most

attractive material to induce artificial pinning centers both in YBCO thin films, in order to increase the critical current density. Detailed characterization by SEM, XRD and TEM of $BaZrO_3$ (BZO) nanocomposite grown by MOD will be presented. The last chapter gives the general conclusions of this thesis.

References

[1] Joseph Milton, "Superconductors come of age," Nature (2010).
[2] C. Freyhardt Herbert and et al., "Coated conductors and their applications," Superconductor Science and Technology **23** (1), 010201 (2010).
[3] "Nespa - NanoEngineered Superconductors for Power Applications," http://www.ifw-dresden.de/nespa.

TABLE OF CONTENTS

LIST OF SYMBOLS AND ABBREVIATION

$\Delta\Phi$	FWHM of the in-plane texture
$\Delta\omega$	FWHM of the out-of-plane texture
ε	lattice mismatch
θ	wetting angle
θ	misorientation angle or tilt angle
τ	shear stress
γ	shear rate
η	viscosity
c	molar concentration
γ_i	surface energies
λ	wavelength of radiation
a, b, c	unit cell parameters
a.u	arbitrary units
H^*	irreversibility field
H_c	critical magnetic field
H_{c1}	lower critical magnetic field
H_{c2}	upper critical magnetic field
H	external magnetic field
I_c	critical current
J_c	critical current density
p O_2	oxygen partial pressure
rms	root-mean-square-roughness
T	temperature
T_c	superconducting critical temperature
t	time
ABAD	Alternating Beam Assisted Deposition
AFM	Atomic force microscopy
BZO	$BaZrO_3$
BCO	$BaCeO_3$
CC	Coated conductor
CSD	Chemical Solution Deposition
EDX	X-ray energy dispersive spectroscopy
EELS	Electron energy loss spectroscopy

FIB	Focused Ion Beam
FWHM	Full Width Half Maximum
GB	grain boundary
2D	two dimensional
HR	High resolution
HRDRX	High resolution X-ray diffraction
HTS	High temperature superconductors
IBAD	Ion Beam Assisted Deposition
LAO	$LaAlO_3$
MOD	Metal organic decomposition
NC(s)	Nanocomposite(s)
Np(s)	Nanoparticle(s)
NESPA	NanoEngineered Superconductors for Power Applications
PLD	Pulsed Laser Deposition
RE	Rare earth
RABiTS	Rolling-Assisted Biaxially Textured Substrate
RHEED	Reflection High Energy Electron Diffraction
SEM	Scanning Electron Microscopy
SQUID	Superconducting Quantum Interference Device
SPUT	Sputtering
SS	Stainless Steel
STO	$SrTiO_3$
TEM	Transmission Electron Microscopy
TFA	trifluoracetate
WH	Williamson Hall
XPS	X-ray Photoelectron Spectroscopy
XRD	X-ray Diffraction
XRR	X-ray Reflectivity
YSZ	Yttria-stabilized zirconia
YBCO	Yttrium barium copper oxide ($YBa_2Cu_3O_{7-\delta}$)

CHAPTER 1 INTRODUCTION

1.1. Brief history

Progress in science in general, and in physics in particular, is characterized by many great discoveries both in theory and experiment [1]. The phenomenon of superconductivity, in which the electrical resistance of certain materials completely vanishes at low temperature is one of the most interesting and sophisticated in condensed matter physics. It was first discovered by the Dutch physicist Heike Kamerlingh Onnes, who was the first to liquefy helium (which boils at 4.2 Kelvin at standard pressure). In 1911 Kamerlingh Onnes and one of his assistants discovered the phenomenon of superconductivity while studying the resistance of metals at low temperatures. They studied mercury because very pure samples could easily be prepared by distillation.

The historic measurement of superconductivity in mercury is shown in Figure 1.1–1. As in any other metals, the electrical resistance of mercury decreased steadily upon cooling, but dropped suddenly at 4.2 K, and became undetectably small. Soon after this discovery, many other elemental metals were found to exhibit zero resistance when their temperatures were lowered below a certain characteristic temperature of the material, called the critical temperature, T_c.[2]

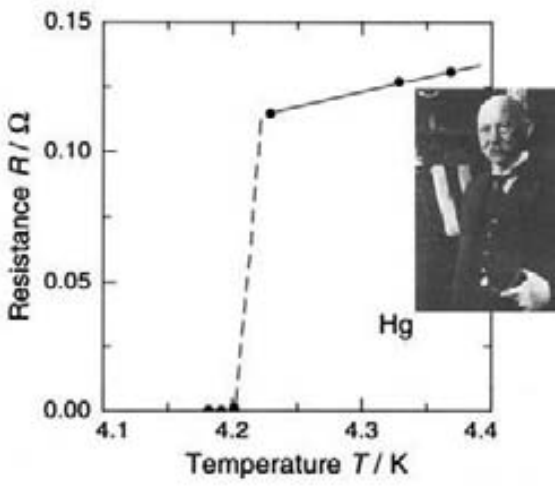

Figure 1.1–1 The resistance of mercury measured by Onnes.

A breakthrough came in 1933 when Meissner and Ochsenfeld [3] showed that in magnetic fields below a certain threshold value the flux inside the superconductor was expelled, and that this defined a new thermodynamic state and was not a consequence of

infinite conductivity. The phenomenon became known as the Meissner effect, and laid the foundation for a thermodynamic treatment of superconductivity, later to be expanded when Abrikosov [4] was finally permitted to report his theory of the magnetic properties of superconductors at a meeting in Moscow in 1957.

1957 was also the year when the quantum theory, known as the BCS theory, was published by Bardeen, Cooper and Schrieffer [5], finally giving microscopic explanation of fascinating properties of superconductors from first principles. A few years later Josephson's[6] astonishing predictions regarding the physical properties of inhomogeneous superconductors in the field of electronics were announced. 25 years later, the superconductivity made an important transition with the discovery of a new class of superconductors, known as high-T_c cuprates by Bednorz and Müller [7] at the IBM laboratory in Rüschlikon near Zürich in 1986. In 1987, Paul Chu produced a new ceramic material by replacing lanthanum by yttrium, and found that it had a critical temperature of 90 K. This great jump in the critical temperature made it possible to use liquid nitrogen as a coolant, and with the promise of commercial viability for the new materials, a scramble ensued to find new high-temperature superconductors and to explain why they superconduct at such high temperatures.

In recent years, no materials with significantly higher critical temperatures have been found, but other discoveries of equal importance have been made. These include the discovery that, against conventional wisdom, several materials exhibit the coexistence of ferromagnetism and superconductivity. We have also seen the discovery of the first high-temperature superconductors that do not contain copper. Startling discoveries like these are demanding that scientists continually re-examine long-standing theories on superconductivity and consider novel combinations of elements.

Unfortunately, no superconductors have yet been found with critical temperatures above room temperature, so cryogenic cooling is still a vital part of any superconducting application. Difficulties with fabricating ceramic materials into conducting wires or tapes have also slowed down the development of new applications of high-temperature superconductors. However, despite these drawbacks, the commercial use of superconductors continues to rise [8].

1.2. High Temperature Superconductors (HTS)

The HTSs are variations of the crystal type known as perovskites [9]. Perovskites are minerals whose chemical formula is ABO_3 [10] (Figure 1.2–1).They can have several crystal structures, including a simple cubic structure. However, the new superconductors do not have the simple formula ABO_3. Instead, they usually have more than one kind of A-atom. It is conducive to understanding these structures to examine models (or at least pictures) of the various crystals [11].

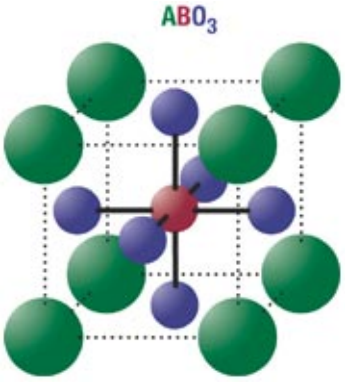

Figure 1.2–1 The cubic ABO_3 structure [10].

There are several ceramics, based on copper oxide, which remain superconducting near 100 K. For example, the compound yttrium barium copper oxide (YBCO) has been found to be superconducting up to 92 K. This may not seem like a "high" temperature to most people, but to the engineers figuring the cost of refrigerants, it is high enough: liquid nitrogen is sufficient to cool YBCO into its superconducting range. Additional important ceramic superconductors include BSCCO (bismuth strontium calcium copper oxide) and TBCCO (thallium barium calcium copper oxide); and HBCCO (mercury barium calcium copper oxide). The latter has the highest critical temperature of superconductivity, T_c = 133 K. Table 1.2-1 presents the chemical formulas and T_c values for each of these compounds [12].

Name	Formula	Transition Temperature
Yttrium barium copper oxide	$Y_1Ba_2Cu_3O_7$	92 K
Bismuth strontium calcium copper oxide (2223 phase)	$(Bi,Pb)_2Sr_2Ca_2Cu_3O_x$	105
Thallium barium calcium copper oxide (1223 phase)	$Tl_1Ba_2Ca_2Cu_3O_y$	115
Mercury barium calcium copper oxide (1223 phase)	$Hg_1Ba_2Ca_2Cu_3O_y$	135

Table 1.2-1 The critical temperatures, T_cs, of different HTSC materials.

1.3. $YBa_2Cu_3O_{7-x}$ - structure and properties

The first superconductor found with $T_c > 77$ K and subsequently the most widely studied HTSC, is yttrium barium copper oxide,$YBa_2Cu_3O_{7-x}$ (YBCO), commonly termed "1-2-3"[12]. Its structure appears in Figure 1.3–1.

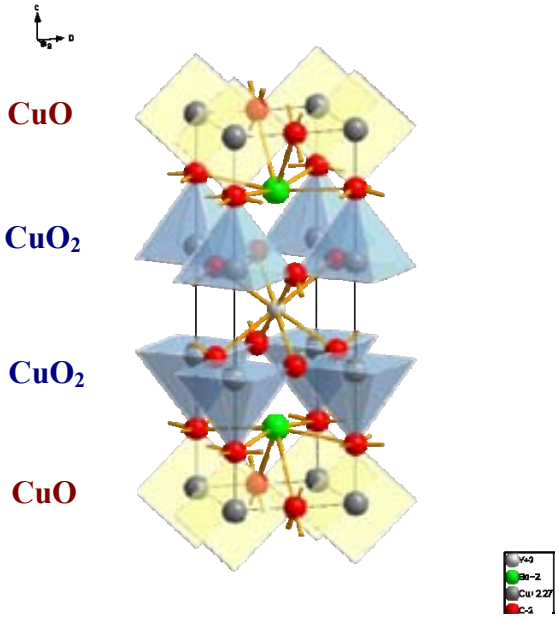

Figure 1.3–1 YBCO orthorhombic unit cell. YBCO is a complex, layered perovskite centred on a yttrium layer, around which are stacked the CuO_2 superconducting planes and a double layer of BaO and CuO.

YBCO is a ceramic material with the following unit cell parameters: a = 3.8185 Å, b = 3.8856 Å and c = 11.6804 Å. It is related to the perovskite structure as follows: by tripling the (ABO_3) unit cell and substituting one yttrium atom for every third barium atom, the formula $Y_1Ba_2Cu_3O_9$ results. However, a little more than two oxygen vacancies are required for superconductivity. The formula can be thought of as

$Y_1Ba_2Cu_3O_{9-2-x}$.The unit cell is orthorhombic—almost but not quite three cubes stacked upon one another.

A key feature of this unit cell is the presence of two layers or planes of CuO_2. There is widespread agreement that the superconductivity takes place in the CuO_2 planes. One particularly noticeable feature in Figure 1.3-1 is that the two copper oxide planes are separated by a single yttrium atom; the yttrium plane contains no oxygens. Basically, this is because Y has a valence of +3, as contrasted with the +2 of Ba. Because of the bond sum rule for charge balancing, each Y coordinates with eight oxygens (valence = – 2), located in

the layers above and below the Y atom. With no oxygens in the yttrium layer, the formula is $Y_1Ba_2Cu_3O_7$ instead of $Y_1Ba_2Cu_3O_9$.

The role of yttrium is very minor: it just pries the two layers apart. When yttrium is replaced by many of the lanthanide series of rare-earth elements, there is no appreciable change in superconducting properties. Thus, the yttrium (or other choice) serves only as a spacer—a "shim" between CuO_2 layers.

Outside this sandwich (but still within the unit cell) is a BaO plane. Referring to Figure 1.3–1, this means one barium atom surrounded by four oxygens along the edges of the unit cell. Finally, at the top (or bottom) of each unit cell is a copper oxide region that has certain oxygens missing. Since this does not qualify any longer as a plane, it is known as a copper oxide chain. Figure 1.3–1 shows the single Y atom and the two Ba atoms; the copper oxide planes near the middle each contribute one net copper atom (their four copper ions are shared with four unit cells), and the top and bottom chains each contribute 1/2 copper ions (four copper atoms shared with eight unit cells). Hence, the name "1-2-3".

The missing oxygens are very important in $Y_1Ba_2Cu_3O_{7-x}$[12]. Depending on temperature and oxygen content, y = 7 - x, [13] are possible two polymorphous changes: tetragonal for $y \leq 6.5$ and orthorhombic for the range $6.5 \leq y \leq 7$. The orthorhombic phase is superconductor. The orthorhombic deformation decreases direct proportional with oxygen content; for $y \sim 6.5$ the phase is tetragonal. Optimal doping (corresponding to the highest T_c) of YBCO therefore is achieved in $Y_1Ba_2Cu_3O_{7-x}$ with $x \approx 0.07$ [1].

Increasing the oxygen content up to y = 6.6, the compound undergoes a phase transition from tetragonal to orthorhombic being only superconducting in the latter. Finally, raising y to 6.94, T_c approaches its maximum value (91K). Above y = 6.94 the compound is overdoped and T_c drops (Figure 1.3–2).

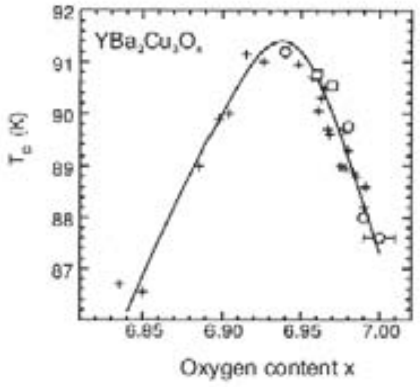

Figure 1.3–2 Dependence of T_c on y in $YBa_2Cu_3O_y$ (y = 7-x)

1.4. Vortex pinning and the irreversibility line in YBCO thin films

Superconductors are special materials capable of carrying electrical current without resistance. Beside zero resistance, another interesting property is that they expel applied magnetic field from its interior by generating electrical currents on the surface (Meissner effect – 1933) [14]. Superconductors are classified in two types according to their behaviour in an applied magnetic field (Figure 1.4–1):

- ✓ Type I superconductors, which include most pure metal superconductors, exclude magnetic flux until a maximum field (H_c) is exceeded at which point the material loses its superconductivity. In general, type I superconductors are not technologically important because H_c is very low—100 to 1,000 gauss (0.01 to 0.1 tesla). By comparison, the field of a typical magnet used in an MRI system is around 15,000 gauss. None of the type I superconductors remains superconducting in such a high field. Virtually all superconductors of technological importance are type II, including the new HTS materials.

- ✓ Type II superconductors have two critical fields, H_{c1} and H_{c2}. They behave like type I materials at low magnetic fields, below H_{c1}. At fields above H_{c2}, the superconductor is driven into its normal state. For fields between H_{c1} and H_{c2}, the magnetic field penetrates the superconductor, forming a lattice of vortices or supercurrent 'whirlpools' (Figure 1.4–2). These vortices repel one another, and arrange themselves in a regular array so as to be as far from one another as possible. As the magnetic field increases toward H_{c2}, more vortices are formed; the lattice spacing is decreased, until at H_{c2}, the superconductivity disappears.

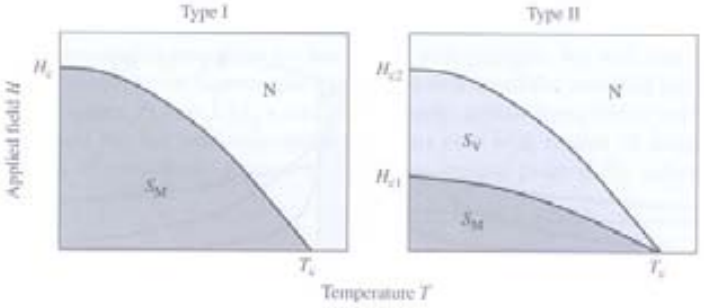

Figure 1.4–1 Phase diagram of type I (left) and type II (right).
S = superconducting, M = Meissner phase, V = vortex phase, N = normal phase [1].

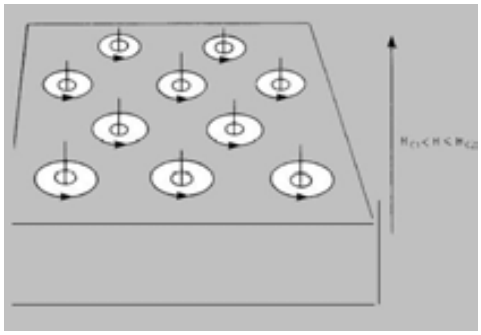

Figure 1.4–2 Schematic Representation of Flux Vortices in a Type II Superconductor [14].

High temperature superconductors are type II superconductors, so the zone between the H_{c1} and H_{c2} permits that an external magnetic field enters in the material in form of vortices without destroying the superconductivity (Figure 1.4–3).

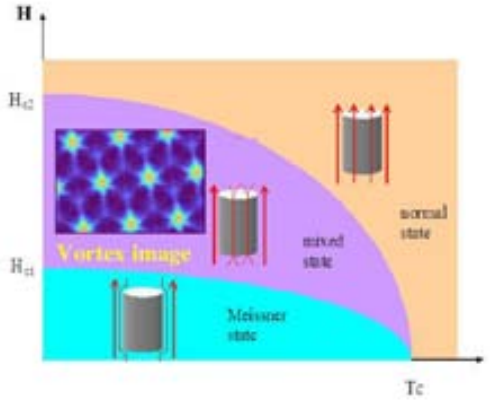

Figure 1.4–3 Magnetic phase diagram of type II superconductors.

The vortex penetrates from the surface and goes inside the material until reaches a position in which all the energy of the system is reduced to minimum. This energy depends on the temperature and the magnetic field in which is the material. Usually, the vortex finds microstructural defects where it is trapped. At high magnetic fields and temperatures, even below $H_{c2}(T)$, the vortex can become unpinned and it can move. This is the as called vortex liquid state. In these conditions, the critical current is zero. The irreversibility line $H^*(T)$ divide the two domains, one where the vortex is trapped and the J_c is not zero and the other where the vortex moves and the $J_c = 0$. This $H^*(T)$ line actually depends on the microstructure of the material, i.e. on the pinning efficiency of the existing defects. In Figure 1.4–4 is presented the irreversibility curve of several HTS and LTS where it's seen that YBCO has the highest values.

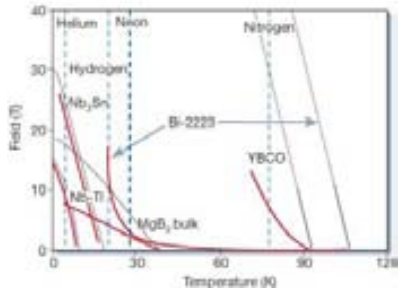

Figure 1.4–4 Irreversibility lines of cuprates (HTSC) at high T_cs. At 77K (liquid nitrogen), YBCO has the highest irreversibility line. The upper critical field H_{c2} at which bulk superconductivity is destroyed is indicated in black, while the irreversibility field H^* at which the bulk critical current density goes to zero is indicated in red [15].

Superconductors can carry bulk current density only if there is a macroscopic vortex density gradient [16], defined by the Maxwell equation $\nabla \times \mathbf{B} = \mu_0 \mathbf{J}$. This gradient can be sustained only by pinning the vortices (flux pinning) at microstructural defects. Increasing T and H weakens the potential wells at which vortices are pinned, thus lessening $J_c(T,H)$. Flux pinning is determined by spatial perturbations of the free energy of the vortex lines due to local interactions of their normal cores and screening currents with these microstructural imperfections [16]. In addition, the vortex structure is subjected to the Lorentz force $\mathbf{F_L} = \mathbf{J} \times \mathbf{B}$ of the macroscopic current. The critical current density $J_c(T,H)$ is then defined by the balance of the pinning and Lorentz forces, $F_p = F_L$, where F_p is the volume summation over all microstructural pinning defects in the strongly interacting network of flux lines. Ideally, a type II superconductor can carry any non-dissipative current density J smaller than J_c. When J exceeds J_c, a superconductor switches into a dissipative, vortex-flow state driven by the Lorentz force.

This description of flux pinning phenomena immediately suggests that tailoring the defect structure of the superconductor is necessary to maximize J_c. The physics of vortex dynamics and pinning is enormously interesting [16,17], but equally important in practical terms is the fact that the actual cross-section over which transport currents flow in HTS conductors is much less than the whole [18].

1.5. Coated Conductors and their applications

Two types of HTS conductors are currently available or coming to the worldwide market for use to make different HTS devices. They are known as first generation 1G HTS (usually Bi-2223 systems made with "powder-in-tube" methods) and second generation 2G HTS (coated conductors, usually made on the base of YBCO superconductor) [19].

2G HTS, based on the deposition of $YBa_2Cu_3O_{7-x}$ (YBCO) epitaxial thin films on metallic substrates, present an excellent potential for their use in power applications (electrical energy, superconducting coils) because they can transport great electrical traffic densities and this way generate intense magnetic fields. The same problem, the grain boundaries, is encountered both in the YBCO compound and in the 1G superconductors. Because of this, the grains are difficult to align.

YBCO is a perovskite ceramic and for its use in power applications it has to be put in form of Coated Conductor (CC). A Coated Conductor has a metallic substrate, one or more buffer layers and a superconducting film (Figure 1.5–1). There are several properties that the substrate must possess in order to be suitable for 2G YBCO-coated conductors. Some of these properties are: (a) the substrate must provide a suitable textured surface which will yield low-angle grain misalignment, (b) the substrate must have lattice parameters that are compatible with those of the deposited buffer layers (must have good lattice matching), (c) the substrate must be mechanically strong, (d) the substrate must be flexible, and (e) the substrate must have a thermal expansion coefficient which is similar to that of the deposited buffer layers. The buffer layers of 2G-YBCO coated conductors have several purposes; (a) they prevent the destructive reaction between the metal alloy substrate and the YBCO film, (b) they prevent the oxidation of the metallic substrate, and (c) they transfer the substrate texture to the YBCO film which allows for high critical current density. The buffer layers must also possess properties such as, (a) they should have good lattice matching with the substrate, the other buffer layers and the YBCO film, (b) buffer layers should have thermal expansion similar to that of the substrate and of the YBCO film, and (c) they should have an appropriate oxygen diffusion coefficient to prevent the oxidation of the substrate.

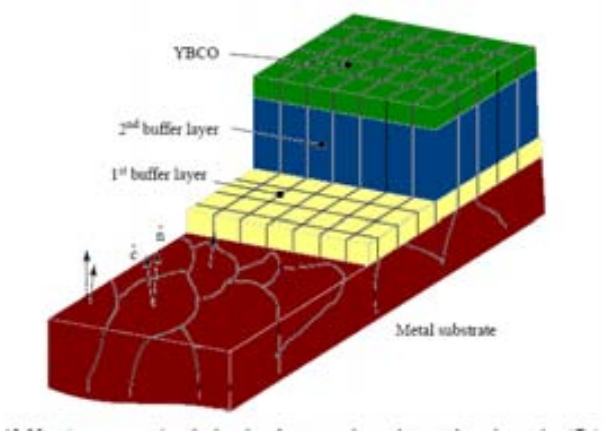

Figure 1.5–1 A cross-sectional sketch of a coated conductor. A biaxially textured metal substrate is coated with buffer layers of various oxides to serve as a diffusion barrier to substrate atoms and to replicate the template, on which YBCO is deposited with biaxial texture.

Because of the anisotropic superconducting properties of YBCO, misorientation angle between adjacent grains affects obviously the transport properties of YBCO superconductors (shown in Figure 1.5–3)[20]. The orientation of YBCO grains is the first question which must be solved. The key is to prepare a substrate, or template material that provide in-plane and out-of-plane crystallographic texture, i.e. biaxially textured (Figure 1.5–2 b)).

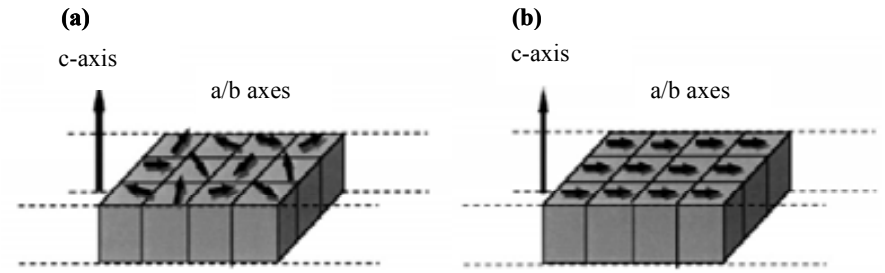

Figure 1.5–2 Schematic diagrams for crystalline alignment structures (a) uniaxially aligned (b) biaxially aligned [21].

Then, it is required that the orientation of underlying template or substrate could be transferred to YBCO film and thus, YBCO film grow in near single-crystal orientation (epitaxial growth). A c-axial orientation of YBCO grains is achieved in the melt-textured processes, but at high annealing temperature.

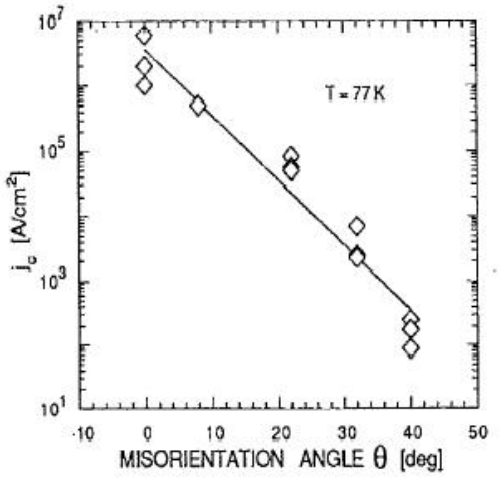

Figure 1.5–3 Effect of misorientation angle between the grains on the J_c value.

Thus, in order to transport large current, the orientation of YBCO grains must be biaxially textured, that is c axes and a axes of YBCO grains are parallel to each other respectively. In other words, not only c axes of YBCO grains are oriented, but also in-plane a or b axes of YBCO grains must be arranged with specific orientations.

Today, there are three principal approaches for achieving long lengths of biaxially-textured coated conductor tape [1]. In the technique known as RABiTS (Rolling Assisted Biaxially Textured Substrates), [22] the substrate metal tape (alloys of nickel or copper) is textured by special thermo-mechanical processing procedures, providing an oriented template for the subsequent epitaxial deposition of buffer layer and YBCO coatings. Another approach uses Ion Beam Assisted Deposition (IBAD), [23] where an energetic ion beam irradiates the substrate at a particular angle during the deposition of an oxide buffer layer onto a polycrystalline metal tape (stainless steel or similar alloys). While the mechanism of the IBAD process is not completely understood, the buffer layer grows preferentially oriented with respect the ion beam and excellent biaxial texture can be achieved. A different method utilizing alternation of the molecular beam and ion beam, i.e. Alternating Ion Beam Assisted Deposition (ABAD)[24] , was recently suggested in order to improve the quality of the texture [25]. The third technique is surprisingly simple. By appropriately inclining the substrate with respect to the incident plume of deposited buffer layer, biaxial texture is achieved by a preferential shadowing of slowly growing crystallites in favour of those that grow rapidly along a particular crystal axis. This Inclined Substrate Deposition (ISD) [26] approach for biaxial texture is still under development at the laboratory level, while both the RABiTS and IBAD approaches are currently being developed for commercialization by several industries worldwide (Figure 1.5–4).

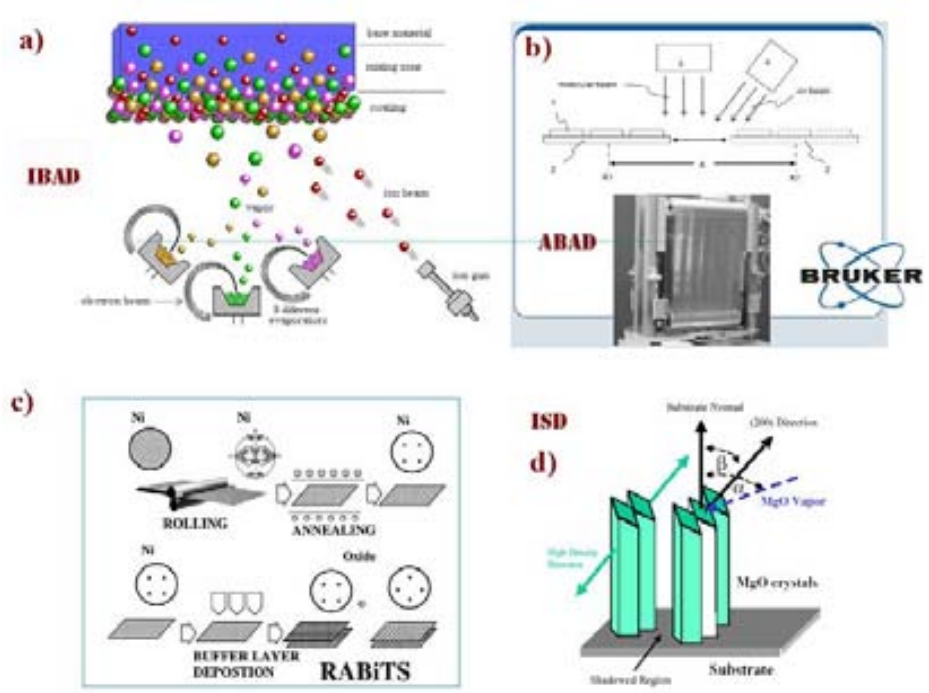

Figure 1.5–4 Methods for the fabrication of high quality Coated Conductors (CC): a) For Ion Beam Assisted Deposition (IBAD) an evaporation beam (common from an electron beam evaporator) and an ion beam from an ion source are directed simultaneously to a substrate; b) In Alternating Beam Assisted Deposition (ABAD), the film is periodically exposed to deposition pulses and to etching pulses; c) In the Rolling Assisted Biaxially Textured Substrates (RABiTS) process, an untextured metal alloy is rolled to produce a particular desired rolling texture which upon annealing results in a sharp cube texture; d) Inclined Substrate Deposition (ISD) produces biaxial texture on a substrate inclined at a angle relative to the vapour source.

For the production of Coated Conductors (CC) there are many important parameters that need to be controled . Some of them are indicated in the Table 1.5-1.

SUBSTRATE		BUFFER		SUPERCONDUCTOR	
Materials	**Parameters**	**Materials**	**Parameters**	**Materials**	**Parameters**
Compatibility	Rolling characteristics	Compatibility	Smoothness	Compatibility	Film surface quality
Mechanical properties	Texture/orientation	Availability	Biaxially alignment	Precursor availability	Large-area coverage
Availability	Annealing	Thermal expansion	Growth rate	Chemical stability	Growth rate
Cost	Surface roughness	Chemical stability	Coating thickness	AC losses	Coating thickness
Thermal expansion	Weak links and grain boundary characteristics	Buffer doping	Insulating or Metallica behaviour	Processing cost	Film stoichiometry

SUBSTRATE		BUFFER		SUPERCONDUCTOR	
Materials	**Parameters**	**Materials**	**Parameters**	**Materials**	**Parameters**
Magnetic properties	AC losses	Texturing and lattice mismatch	Grain size and grain boundaries	Thermal expansion	Texture/orientation
		Need for multiple layers.		Texturing and lattice mismatch	Improved pinning for high J_c.
		Processing cost		Cation and oxygen diffusion barrier	In-field performance
		Cation and oxygen diffusion barrier		Structure of nanocomposites	Percolating current through grain boundaries

Table 1.5-1 A selection of chemical and materials-related parameters relevant for processing and commercialization of HTSC coated conductors [27].

Thin HTS coatings on single crystals and metallic tapes are suitable for a large variety of technical applications (Figure 1.5–5). The major commercial applications of superconductivity at present is in the medical diagnostic (MRI and NMR spectroscopy), scientific equipment and industrial processing fields. They involve mainly LTS materials to generate relatively high magnetic fields. Indeed, without superconducting technology most of these applications would not be viable. Several smaller scale applications utilizing LTS materials have also been commercialized, e.g. research magnets and Magneto-Encephalography (MEG). The latter is based on Superconducting Quantum Interference Device (SQUID) technology which detects and measures very weak magnetic fields generated by the brain. The only substantive commercial products incorporating HTS materials are electronic filters used in wireless base stations. About 10,000 units have been installed in wireless networks worldwide to date.

Figure 1.5–5 Applications of the superconductivity

Superconductor-based products are extremely environmentally friendly compared to their conventional counterparts. They generate no greenhouse gases and are cooled by non-flammable liquid nitrogen (nitrogen comprises 80% of our atmosphere) as opposed to conventional oil coolants that are both flammable and toxic. They are also typically at least 50% smaller and lighter than equivalent conventional units which translate into economic incentives. These benefits have given rise to the ongoing development of many new applications in the following sectors:

Electric Power: Superconductors enable a variety of applications to aid our aging and heavily burdened electric power infrastructure - for example, in generators, transformers, underground cables, synchronous condensers and fault current limiters. The high power density and electrical efficiency of superconductor wire results in highly compact, powerful devices and systems that are more reliable, efficient, and environmentally benign.

Transportation: The rapid and efficient movement of people and goods, by land and by sea, poses important logistical, environmental, land use and other challenges. Superconductors are enabling a new generation of transport technologies including ship propulsion systems, magnetically levitated trains, and railway traction transformers.

BioMedicine: Advances in HTS promise more compact and less costly Magnetic Resonance Imaging (MRI) and NMR systems with superior imaging capabilities. In addition, Magneto-Encephalography (MEG), Magnetic Source Imaging (MSI) and Magneto-Cardiology (MCG) enable non-invasive diagnosis of brain and heart functionality.

Industry: Large motors rated at 1000 HP and above consume 25% of all electricity generated in the United States. They offer a prime target for the use of HTS in substantially

reducing electrical losses. Powerful magnets for water remediation, materials purification, and industrial processing are also in the demonstration stages.

Electronics and communications: Over the past decade, HTS filters have come into widespread use in cellular communications systems. They enhance signal-to-noise ratios, enabling reliable service with fewer, more widely-spaced cell towers. As the world moves from analog to all digital communications, LTS chips offer dramatic performance improvements in many commercial and military applications.

Scientific Research: Using superconducting materials, today's leading-edge scientific research facilities are pushing the frontiers of human knowledge - and pursuing breakthroughs that could lead to new techniques ranging from the clean, abundant energy from nuclear fusion to computing at speeds much faster than the theoretical limit of silicon technology [28].

In summary, there are a number of components and systems in the different fields of electric power, industrial processing, transportation, medical applications as well as information and communication, in which superconductors offer unique functions (Table 1.5-2)[29] .

a)

Application	Major Technical Features
Power Cables	higher current densities, smaller conductor diameters, lower transmission losses, (side effect: oil-free)
Current Limiters	highly non-linear super-normal-conductor transition, self-controlled current limitation
Transformers	higher current densities, smaller size, lower weight, lower losses, (side effect: oil-free)
Motors / Generators	higher current densities, higher magnetic fields, smaller size, lower weight, lower losses
Magnets for RTD, Magnetic Energy Storage, Magnetic Separation, .. NMR Spectroscopy, MRI, .. Magnetic Levitation Systems	higher current densities, higher & ultra-high magnetic fields, higher magnetic field gradients, smaller size, lower weight, lower losses persistent currents, ultra-high temporal field stabilities stronger levitation forces, larger air gaps
Cavities for Accelerators (based on LTS sheets or coatings)	lower surface resistances, higher quality factors, higher microwave-power handling capability
Magnetic Bearings (based on HTS bulk material)	higher current densities, lower losses, stronger levitation forces, self-controlled autostable levitation

b)

Application	Major Technical Features
High-Frequency Sensor Coils for NMR	lower resistive losses, higher quality factors, smaller size
Microwave Filters for Wireless Communication	lower surface resistances, smaller size, lower transmission losses, higher quality factors
Resonators for Oscillators & Other Passive Microwave Devices	lower surface resistances, higher quality factors, lower transmission losses, smaller size
Far-Infrared Bolometers	highly non-linear super-normal-conductor transition, higher irradiation-mediated temperature sensitivities
Microwave Detectors	highly non-linear junction characteristics, higher conversion efficiencies for frequency-mixing
X-Ray Detectors	lower particle excitation energies, higher photon energy resolutions
SQUID Sensors for RTD, Medical Diagnosis & Non-Destructive Testing SQUID-based Amplifiers	persistent currents, quantum interference effects, ultra-high magnetic field sensitivities low-noise low-signal amplification
Voltage Standards for Metrology & Industry	voltage steps in microwave-irradiated junction arrays, quantum-precision output voltages
Digital Circuits & Microprocessors	persistent currents, single flux quantum signal levels, ultra-fast ultra-low power data transfer & processing

Table 1.5-2: a) Large Scale Applications of Superconductivity; b) Electronics Applications of Superconductivity [29].

1.6. Sol–Gel route

1.6.1. Chemical Solution Deposition (CSD)

The achievement of low cost deposition techniques for high critical current $YBa_2Cu_3O_7$ coated conductors is one of the major objectives to achieve a widespread use of superconductivity in power applications. Several deposition methods are being used to prepare the buffer and the YBCO layers of 2G-YBCO wires. Generally, these methods can be classified as physical deposition techniques and chemical deposition techniques. Examples of physical deposition techniques are pulsed laser deposition (PLD), sputtering, thermal and e-beam evaporation. Examples of chemical deposition techniques are chemical vapor deposition (CVD) and chemical solution deposition (CSD). In all these techniques, the choice of the buffer materials is important and several parameters for the buffer layers must be taken into account such as the lattice matching, structural and chemical compatibility and similar thermal expansion coefficients [27]. Chemical solution deposition techniques are appearing as a very promising methodology to achieve epitaxial oxide thin films at a low cost, so an intense effort is being carried out to develop routes for all chemical coated conductor tapes [30].

CSD is widely considered the most promising route to the low-cost commercial production of HTS wires due to its advantages, including inexpensive non-vacuum equipment, precise control of metal–oxide precursor stoechiometry, ease of compositional modification on a molecular level, high deposition rates on large areas, and potentially near 100% utilization of the precursor material [31].

The chemical solution deposition method for the preparation of thin layers can be subdivided into three main stages (Figure 1.6–1):

1) The precursor solution synthesis from educts according to the designated layer composition and the chemical process to be used;
2) The coating procedure to obtain homogeneous precursor layers of controlled thickness;
3) The thermal treatment of the precursor layer converting the as-deposited layer into a crystallized final oxide layer via an amorphous or nanocrystalline state [31].

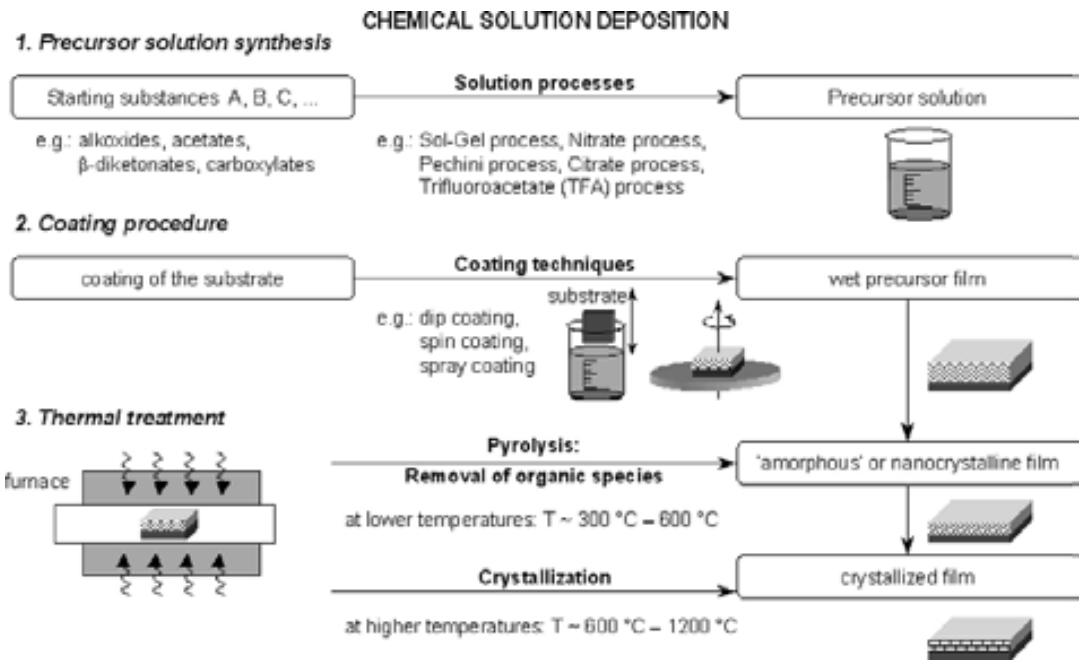

Figure 1.6–1 Overview of the Chemical Solution Deposition (CSD) process [31].

There are three principal categories in which the chemical routes utilized for obtaining electronic oxides can be grouped depending on the procedures utilized during coating solution preparation, the gelation behaviour of the deposited film, and the reactions that take place during thermal annealing [32]:

a) *sol–gel processes* that use alkoxide precursors that undergo primarily hydrolysis and polycondensation in which metal–oxygen–metal (M–O–M) bonds are formed:

Hydrolysis: $M(OR)_x + H_2O \rightarrow M(OR)_{x-1}(OH) + ROH$ **Eq. 1.6-1**

a. Condensation (alcohol elimination): $2M(OR)_{x-1}OH \rightarrow M_2O(OR)_{2x-3}(OH) + ROH$ **Eq. 1.6-2**

b. Condensation (water elimination): $2M(OR)_{x-1}(OH) \rightarrow M_2O(OR)_{2x-2} + H_2O$ **Eq. 1.6-3**

b) *Metal Organic Decomposition (MOD)* routes that utilize carboxylate precursors that do not undergo significant condensation reactions during either solution preparation or film deposition;

The method consists of dissolving the metal–organic compounds in a common solvent, usually xylene, and combining the solutions to yield the desired stoichiometry. Since the starting compounds are water insensitive, they do not display the oligomerization behaviour as in sol–gel chemistry, and the precursor species that exist in solution retain a strong resemblance to the starting molecules. This aspect of the process, together with the use of non-interacting solvents, allows for the characterization of the solution as a simple mixture of the starting compounds. There are also some limitations in this fabrication method:

- cracking of the film because of the large organic ligands;

- the minimal reactivity of the starting reagents;
- restriction of the process flexibility because the incapacity of tailoring the properties of the low reactivity starting salts;
- limitations in control the structural evolution because of the variations in solvent, film deposition, solution concentration and annealing [32].

c) *hybrid routes* that exhibit condensation reactions at several process stages; frequently, this route is used when multicomponent oxide films, e.g., perovskite materials, are prepared from multiple precursor types or when chelating ligands are added to solutions with multiple precursor types [33].

1.6.2. Techniques for precursor solution deposition

There are different coating techniques for depositing thin precursor layers: spin coating, dip coating, spray coating, ink jet printing (Figure 1.6–2). For all coating methods, the precursor layer thickness is governed by solution properties like molarity and viscosity and furthermore as well as by the deposition speed and coating time [31].

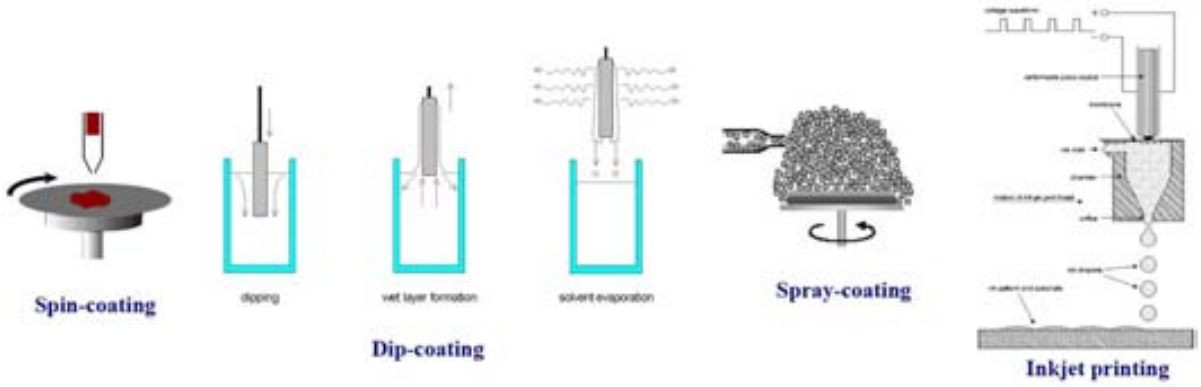

Figure 1.6–2 The most common used coating techniques.

a) Spin-coating

Spin coating is a technique used at the laboratory scale for several decades for the application of thin films. This process consists in depositing a small puddle of a precursor solution onto the center of a substrate and then spinning the substrate at high speed (between 1500 rpm and 6000 rpm). A thin film from the solution which was spread on the substrate with a certain centripetal acceleration is formed. There are lots of parameters which will influence the thickness and other properties of the final film: viscosity, drying rate, percent

solids, surface tension, etc. The properties of the coated films are defined depending of the acceleration, the final rotational speed and fume exhaust.

Repeatability is one of the most important factors in spin coating. Subtle variations in the parameters that define the spin process can result in drastic variations in the coated film. One of the most important parameters in the spin coating is the *spin speed*. The degree of radial (centrifugal) force applied to the liquid as well as the velocity and characteristic turbulence of the air immediately above it is affected by the speed of the substrate (rpm). In particular, the high speed spin step generally defines the final film thickness. *The acceleration* of the substrate is the second very important parameter which can also affect the coated film properties. Since the solution begins to dry during the first part of the spin cycle, it is important to accurately control acceleration. In some processes, 50% of the solvents in the precursor solution will be lost to evaporation in the first few seconds of the process [34].

The effect of spin speed and time on film thickness it is shown in the Figure 1.6–3. Thinner films are obtaining with higher speed and longer spin time. However, the film thickness becomes constant at very high spin speed and long spin time [32].

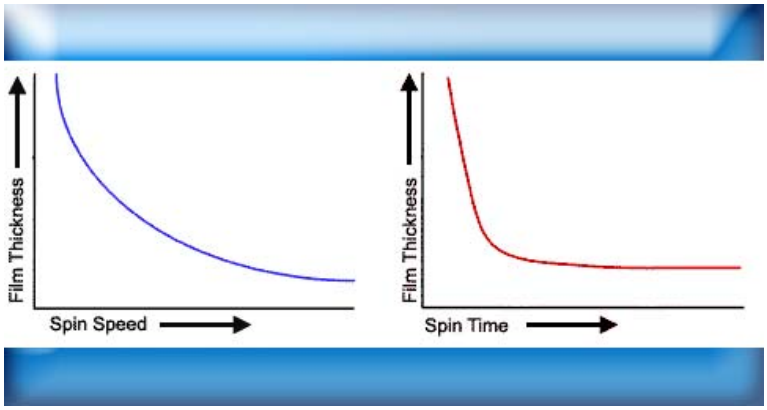

Figure 1.6–3 Influence of spin speed and time on film thickness [32].

One of the main advantages of this method is that using spin-coating the result is a homogenous film but the main disadvantage is the impossibility to scale the samples to production and using them for the industry of Coated Conductors (CC).

b) Dip-coating

Dip-coating consists in the formation of a film through a liquid entrainment process that may be either batch or continuous in nature. The steps of this process include immersion of the substrate into the dip-coating solution, start-up, where withdrawal of the substrate from the solution begins, film deposition, solvent evaporation, and continued drainage as the substrate is completely removed from the liquid bath [32]. The balance of forces at the

stagnation point on the liquid surface determines the thickness. There are various parameters which affect the thickness: fluid viscosity, fluid density, and surface tension [35].

Dip-coating is a technique which permits industrial scalability with deposition on the two sides of the substrates. One main disadvantage is the storage of the solution in an open tray which leads to solvent loss due to the destabilization of the solution by evaporation and also produces changes in concentration and rheological properties (thickness control).

Dip-coating is excellent for producing high-quality and uniform coatings but requires precise control and a clean environment because the applied coating may remain wet for several minutes until the solvent evaporates. The process can be accelerated by heated drying. In addition, the coating may be cured by a variety of means including conventional thermal, UV, or IR techniques depending on the coating solution formulation. Once a layer is cured, another layer may be applied on top of it with another dip-coating / curing process and in this way obtaining a multilayer [35].

c) Spray-coating

Conformal film deposition on non-planar structures (e.g., steps, stacks or trenches) on semiconductor chips can be obtained by spray-coating technique. In this technique, the coating solution is transformed into an aerosol by means of an ultrasonic nebulizer or appropriate pressure-driven, nozzle-based atomizer. An important point is that, in this technique, the solution viscosity must be reduced for facilitating the nebulising process and the formation of sufficiently small droplets. The misted solution is transferred into the deposition chamber by a carrier gas where the droplets settle onto the wafer surface by gravitation, or more efficiently, by an electrostatic field.

d) Inkjet printing

Inkjet printing is one of the most promising techniques for the fabrication and commercialization of low cost electronic biosensor platforms, which are more and more demanded on the market. The principle is based on the operation of the highly controlled ejection of low volumes of ink from a printhead employing single nozzle or a series of nozzles. It permits the deposition of tiny droplets ($\geq$ 1pl) onto a substrate (glass, plastic, metal, etc.) with high precision and reproducibility.

There are four techniques to bring about ejection of droplets from a printhead: thermal, piezoelectric, electrostatic and acoustic. The most common inkjet printers are based on either drop-on-demand *thermal* and *piezoelectric printheads*. *Thermal printheads* possess a resistor element inside each nozzle and when this resistor is heated, ink in proximity to it reaches the

threshold temperature, Tt, and it is formed a vapour bubble. Usually, bubble formation occurs in just 2 ms, at a temperature of approx. 300 ºC. Because of the pressure which increases when the bubble grows, a droplet of ink is ejected through the orifice, almost simultaneously with the collapse of the bubble. The pressure then decreases within the system and the nozzle becomes refilled with ink. The potential for very small drop sizes and high nozzle density which leads to compact devices and lower printhead and product costs is one of the advantages of thermal inkjet. Disadvantages are primarly related to limitations of the fluids that can be used [36]. The second type of printhead uses a piezoelectric crystalline material confined within the nozzle. As the piezoelectric inkjet technology doesn't require the high temperatures used for thermal printing (200–300ºC) is favoured over thermal printing in many applications, when it contains materials such as organics or biological materials [37]. The highest level of ink development freedom of any ink technology and long head life are two of the advantages of this technique, meanwhile the higher cost for printheads represents a disadvantage [36].

Inkjet printing is a method compatible with the industrial scalability in which the deposition in only one side of the substrate leads to low material consumption. Also, this way, there is the possibility to deposit according to patterns that optimize the current distribution in the superconducting layers. The solution is stored in a closed tray with controlled atmosphere and independent of the substrate used, the thickness of the layer can be controlled.

1.6.3. Crystallization and growth

The process of the transformation of the as-deposited precursor layer into the desired crystalline phase can be divided in four steps: pyrolysis, nucleation, crystal growth and oxygenation (Figure 1.6–4).

Figure 1.6–4 Thermal treatment - The formation of crystallized textured layers

At lower temperatures, typically between 300 °C and 600 °C, the as-deposited precursor layer is pyrolyzed, leading to a removal of the organic species associated with a high volume shrinkage of the layer. Depending on the chemical process, microcracks and stress can

appear (Figure 1.6–5). Depending on the chemical route used an amorphous or nanocrystalline metastable and porous layer is formed as a intermediate state. Its transformation to the final oxide is controlled by the chemical composition of this oxide, as different cations have different tendencies to form stable intermediate compounds such as carbonates [31].

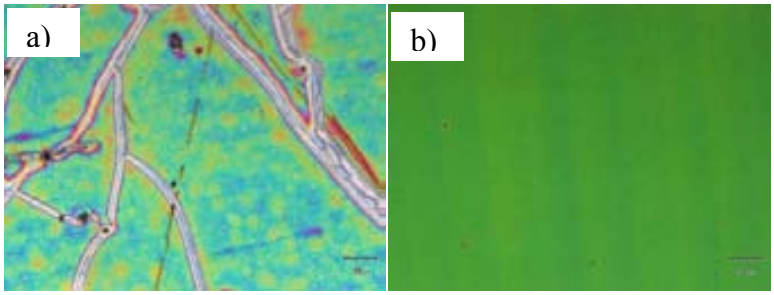

Figure 1.6–5 Optical micrographs of decomposed trifluoroacetates precursor films showing a) the formation of cracks because of the excessive stress during the thermal decomposition and b) a defect-free film.

The pyrolysis is carried out in a humid, oxidizing atmosphere at temperatures below 400 ºC. Water vapour is added to the process atmosphere to suppress sublimation of the $Cu(O_2CCF_3)_2$ from the film, water molecules seem to stabilize $Cu(TFA)_2$ although this phenomenon has not been clearly described up to now.

The next two steps, *the nucleation and the growth*, are done at high temperature in the range of 600-1100ºC. High-temperature annealing is used for densification and crystallization of the amorphous intermediate layer into the desired oxide phase. This crystallization is based on the thermodynamic principles valid for nucleation and growth processes. After pyrolysis, a heterogeneous nucleation produces the epitaxial growth at the interface between the amorphous layer and the substrate. This growth mechanism is called solid phase epitaxy (SPE). These two steps can be merged to one step at high temperatures, but the general procedure results are the same. Bond reorganization, structural relaxation processes and complex structural reorganization are a few of the changes that occur during the conversion of the as-deposited film into the crystalline ceramic state. These rearrangement processes result in the removal of the organic species and the elimination of structural free volume within the film. There are some parameters evolved in the result which implies the crystalline phase: the precursor chemistry employed the material chemistry, the heating rate and the heating temperature. Crystal structures similar to the substrate and compressive stresses within the deposited layer also lead to successful epitaxial growth. Different transformations (solid-state reactions) from the amorphous state into the

crystallized textured oxide control the quality of the epitaxial growth and the microstructural evolution [27].

1.7. References

[1] Kristian Fossheim and Asle Sudbø, *Superconductivity. Physics and Applications*. (John Wiley & Sons, Ltd, 2004).

[2] Joe Khachan and Stephen Bosi, "Superconductivity," http://blogs.usyd.edu.au/ptf/year_12/ideas_to_implementation/superconductivity/superconductivity_downloads/ (2009).

[3] W. Meissner and R. Ochsenfeld, "Short initial announcements," Naturwissenschaften **21**, 787-788 (1933).

[4] A. A. Abrikosov, "On the magnetic properties of superconductors of the second group," Soviet Physics Jetp-Ussr **5** (6), 1174-1183 (1957).

[5] Cooper LN Bardeen J, Schrieffer JR "Theory of Superconductivity," Physical Review **108** (5), 1175-1204 (1957).

[6] B. D. Josephson, "Possible new effects in superconductive tunnelling," Physics Letters **1** (7), 251-253 (1962).

[7] J. G. Bednorz and K. A. Muller, "Possible High-Tc Superconductivity in the Ba-La-Cu-O system," Zeitschrift Fur Physik B-Condensed Matter **64** (2), 189-193 (1986).

[8] Superconductivity, (http://openlearn.open.ac.uk/mod/resource/view.php?id=192974).

[9] Lilian Bouyssiéres, René Schifferli, Loreto Urbina et al., "Study of peroskites obtained by the sol-gel method," Journal of the Chilean Chemical Society **50**, 407-412 (2005).

[10] James N. Eckstein, "Oxide interfaces: Watch out for the lack of oxygen," Nat Mater **6** (7), 473-474 (2007).

[11] I. K. Schuller and J. D. Jorgensen, MRS Bulletin, 27-30 (January 1989).

[12] Thomas P. Sheahen, *Introduction to High- Temperature Superconductivity*. (Kluwer Academic Publishers (New York, Boston, Dordrecht, London, Moscow), 2002).

[13] M. Kimura, M. Matsuo, M. Murakami et al., "Characterization of oxide superconductor by means of X-ray diffractometry and X-ray absorbtion near edge structure," Isij International **29** (3), 213-222 (1989).

[14] U.S. Congress Office of Technology Assessment, "High Temperature Superconductivity in perspective," OTA-E-440 (Washington, DC: U.S. Government Printing Office) (April 1990).

[15] David Larbalestier, Alex Gurevich, D. Matthew Feldmann et al., "High-Tc superconducting materials for electric power applications," Nature **414** (6861), 368-377 (2001).

[16] A. M. Campbell and J. E. Evetts, "Flux vortices and transport currents in Type II Superconductors," Advances in Physics **21** (90), 199-& (1972).

[17] G. Blatter, M. V. Feigelman, V. B. Geshkenbein et al., "Vortices in High-Temperature Superconductors," Reviews of Modern Physics **66** (4), 1125-1388 (1994).

[18] A. A. et al. Polyanskii, "Examination of current limiting mechanisms in monocore Ag/BSCCO tape with high critical current density," IEEE Trans. Appl. Supercond. **11**, 3269-3270 (2001).

[19] V. E. Sytnikov, V. S. Vysotsky, I. P. Radchenko et al., "1G versus 2G-comparison from the practical standpoint for HTS power cables use," 8th European Conference on Applied Superconductivity **97** (2008).

[20] Redwing R D Heinig N F, Nordman J E, Larbalestier D C, "Strong to weak coupling transition in low misorientation angle thin film $YBa_2Cu_3O_{7-x}$ bicrystals," Physical review B **60** (2), 1409-1417 (1999).

[21] Y. Iijima and K. Matsumoto, "High-temperature-superconductor coated conductors: technical progress in Japan," Superconductor Science & Technology **13** (1), 68-81 (2000).

[22] A. Goyal, R. Feenstra, F. List et al., "Using RABiTS to fabricate high-temperature superconducting wire," JOM Journal of the Minerals, Metals and Materials Society **51** (7), 19-23 (1999).
[23] James R. Groves, Paul N. Arendt, Stephen R. Foltyn et al., "Recent progress in continuously processed IBAD MgO template meters for HTS applications," Physica C: Superconductivity **382** (1), 43-47 (2002).
[24] A. Usoskin, L. Kirchhoff, J. Knoke et al., "Processing of long-length YBCO coated conductors based on stainless steel tapes," Ieee Transactions on Applied Superconductivity **17** (2), 3235-3238 (2007).
[25] A. Usoskin and L. Kirchhoff, "In-Plane Texturing of Buffer Layers by Alternating Beam Assisted Deposition: Large Area and Small Area Applications," Mater. Res. Soc. Symp. Proc. **1150**, 117-122 (2009).
[26] B. Ma, M. Li, B. L. Fisher et al., "Inclined-substrate deposition of biaxially aligned template films for YBCO-coated conductors," Physica C: Superconductivity **382** (1), 38-42 (2002).
[27] Borhan A. Albiss and Ihab M. Obaidat, "Applications of YBCO-coated conductors: a focus on the chemical solution deposition method " J. Mater. Chem. **20**, 1836-1845 (2010).
[28] Coalition for the Commercial Application of Superconductors (CCAS) & Council on Superconductivity (CSC), "Superconductivity - Present and future applications," (2009).
[29] http://www.conectus.org/superconductivity.html.
[30] X. Obradors, T. Puig, A. Pomar et al., "Chemical solution deposition: a path towards low cost coated conductors," Superconductor Science & Technology **17** (8), 1055-1064 (2004).
[31] K. Knoth, S. Engel, C. Apetrii et al., "Chemical solution deposition of YBa2Cu(3)O(7-x)coated conductors," Current Opinion in Solid State & Materials Science **10**, 205-216 (2006).
[32] M. S. Bhuiyan, M. Paranthaman, and K. Salama, "Solution-derived textured oxide thin films - a review," Superconductor Science & Technology **19** (2), R1-R21 (2006).
[33] R. W. Schwartz, T. Schneller, and R. Waser, "Chemical solution deposition of electronic oxide films," Comptes Rendus Chimie **7** (5), 433-461 (2004).
[34] Spin Coater Theory http://www.brewerscience.com/research/processing-theory/spin-coater-theory/.
[35] YTC America INC. http://www.ytca.com/dip_coating.
[36] Magdassi Shlomo, *The Chemistry of Inkjet Inks*, 2010 ed. (World Scientific Publishing Co. Pte.Ltd., 2010).
[37] L. Gonzalez-Macia, A. Morrin, M. R. Smyth et al., "Advanced printing and deposition methodologies for the fabrication of biosensors and biodevices," Analyst **135** (5), 845-867 (2010).

CHAPTER 2 EXPERIMENTAL TECHNIQUES

In this chapter, we will briefly describe the experimental techniques used in this thesis for the growth and characterization of the buffer layers and YBCO films like Atomic Force Microscopy, X-ray Diffraction, Scanning Electron Microscopy, Transmission Electron Microscopy, Reflection High-Energy Electron Diffraction, Pulsed Laser Deposition, SQUID, X-ray reflectivity and electrical transport measurements. A complete characterization of the samples with all these techniques is necessary in order to understand the complex growth mechanisms of the superconductor and the interactions between different layers.

2.1. Atomic Force Microscopy

Atomic Force Microscopy (AFM) is a simple technique which provides high-resolution and three-dimensional information at atomic level, with little sample preparation. In AFM, as shown in Figure 2.1–1 a), a sharp tip at the free end of a cantilever (the "probe") is brought into contact with the sample surface. The tip interacts with the surface, causing the cantilever to bend. A laser spot is reflected from the cantilever onto a position-sensitive photodiode detector. As the cantilever bends, the position of the laser spot changes. The resulting signal from the detector is the Deflection, in volts. The difference between the Deflection value and the user-specified Set Point is called the "error signal." There are three modes of function (Figure 2.1–1 b)): contact mode, intermittent or tapping mode and non-contact mode. Figure 2.1–1 c) shows the force interaction as the tip approaches the sample. At the right side of the curve the tip and sample are separated by large distance. As they approach, tip and sample atoms first weakly attract each other. This zone of interaction is known as the "non-contact" regime. Closer still, in the "intermittent contact" regime, the repulsive van der Waals force predominates. When the distance between tip and sample is just a few angstroms, the forces balance, and the net force drops to zero. When the total force becomes positive (repulsive), the atoms are in the "contact" regime. There are also other complications of the tip-sample interaction because of additional forces, including strong capillary and adhesive forces that attract the tip and sample [1].

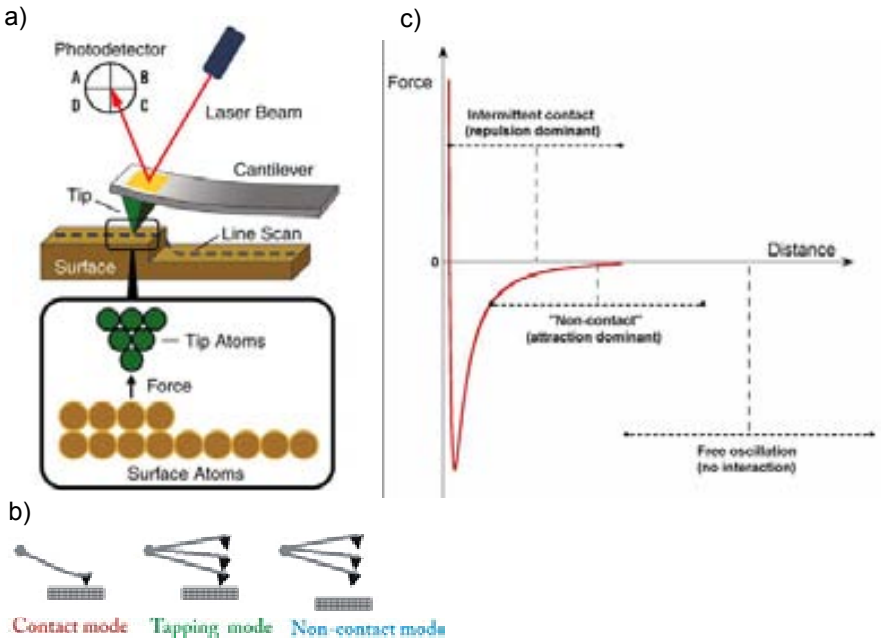

Figure 2.1–1 a) AFM's principie; b) AFM's operation modes; c) Interactions between tip and sample.

The samples characterized in this thesis were analyzed with two different AFM devices, Agilent 5100 and Agilent 5500 LS, which are encountered in ICMAB. Silicone tips were used and tapping mode was engaged. This mode is used for scanning the surface of the fragile samples. In this working mode, the tip vibrates to a frequency close to her resonance frequency (200-400 kHz) and the contact between tip and surface alternates. During intermittent contact, the tip is brought close to the sample so that it lightly contacts the surface at the bottom of its travel, causing the oscillation amplitude to drop. In this way, the friction forces are avoided. A force of some piconewtons is employed in the scan.

The commercial MountainsMap SPM-Image 5.0 was used for treating the images obtain from the AFM device. The roughness mean values were extracted with this program and also a quantification of the area fraction occupied by the flat terraces was done following the methodology developed previously in the group [2]. This method consists in, first defining a threshold height value above which surface can not longer be considered as flat. In the present case we have taken 1.5 nm, i.e., deviations from flat surface lower than one and a half fluorite unit cell height. Then, this threshold is applied to the whole image as a binary mask. The final result is a two-colour image as that shown in Figure 2.1–2 (right) where bright (blue) regions correspond to flat area (i.e., measured heights below the threshold value) whereas dark regions are the rougher areas (typically, holes and dots). Now, a value for flat area fraction of 90% was easily quantified by just counting bright pixels in the image.

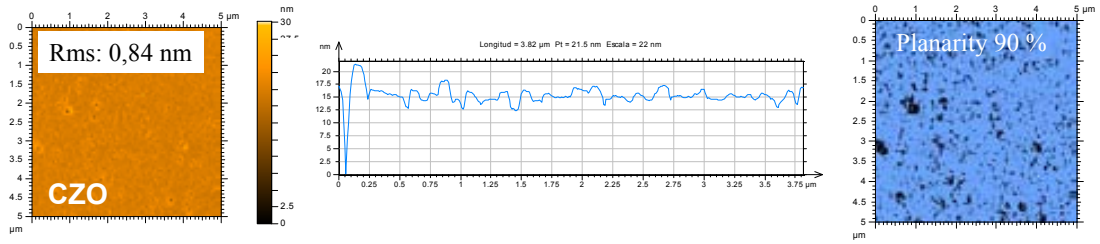

Figure 2.1–2 AFM image of a chemical solution deposited $(Ce,Zr)O_2$ buffer layer grown on YSZ single crystal (rms = 0,84 nm) together with the line profile and two-colour image obtained after applying a threshold mask of 1.5 nm. Bright (blue) area corresponds to the flat terraces whereas dark (black) area is considered as rough surface.

2.2. X-Ray Diffraction

X-rays are electromagnetic radiations with a wavelength in the range of 0,01-100 Å [3]. X-ray diffraction (XRD) is a universal technique used to measure the atomic arrangement of materials and to identify the nature and structure of the crystallized products. This allows doing various types of analysis: a) fast θ-2θ fast scan; b) quantification of epitaxial/random fraction (GADDS); c) q-plots; d) x-ray reflectivity (XRR); e) pole figures. When a monochromatic X-ray beam hits a sample, in addition to absorption and other phenomena, we observe X-ray scattering with the same wavelength as the incident beam, called coherent X-ray scattering. The coherent scattering of X-ray from a sample is not evenly distributed in space but is a function of the electron distribution in the sample.

There are many theories and equations about the relationship between the diffraction pattern and the material structure. Bragg's law is a simple way to describe the diffraction of X-rays by a crystal. In Figure 2.2–1 a), the incident X-rays hit the crystal planes in an angle θ, and the reflection angle is also θ. The diffraction pattern is a delta function when the Bragg condition is satisfied:

$$\lambda = 2d\sin\theta \qquad \textbf{Eq. 2.2-1}$$

where λ is the wavelength, d is the distance between each adjacent crystal plane (d spacing), and θ is the Bragg angle at which one observes a diffraction peak. For real materials, the diffraction patterns vary from theoretical delta functions with discrete relationships between points to continuous distributions with spherical symmetry. Figure 2.2–1 b) and c) shows the diffraction from a single crystal and from a polycrystalline sample. In the case of a single crystal, the diffracted beams point to discrete directions each corresponding to a family of diffraction planes for a polycrystalline (powder) sample forms a series of diffraction cones if

a large number of crystals oriented randomly in the space are covered by the incident X-ray beam. Each diffraction cone corresponds to the diffraction from the same family of crystalline planes in all the participating grains. The theory also applies to any system with a two-dimensional detector. Polycrystalline materials consist of many crystalline domains, numbering from two to more than a million in the incident beam. In single-phase polycrystalline materials, all these domains have the same crystal structure with multiple orientations. Polycrystalline materials could also be multiphase materials with more than one kind of crystal blended together. Polycrystalline materials can also be bonded to different materials such as semiconductor thin films on single-crystal substrates. The crystalline domains could be embedded in an amorphous matrix or stressed from a forming operation. Usually, the sample undergoing X-ray analysis has a combination of these effects. The myriad properties that can be measured with X-rays are related to material purity, strength, durability, electrical conductivity, coefficient of expansion, and so forth [4].

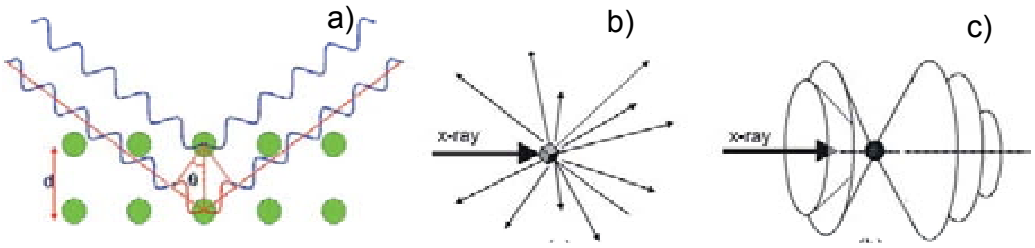

Figure 2.2–1 a) Schematic representation of x-ray scattering from a crystalline material; b) a single crystal XRD pattern; c) the pattern of diffracted X-rays for a polycrystalline sample.

The samples from this thesis were characterized in ICMAB using a Siemens D5000, a Rigaku Rotaflex RU-200BV diffractometers with Cu-K_α, λ=1.5418 Å, and a General Area Detection Diffraction System (GADDS). Bruker-AXS General Area Detection Diffraction System (GADDS) is a two-dimensional detector and permits the rapid viewing of a large volume of reciprocal space within a single collection frame. This added collection dimension capability becomes very significant for the accurate phase identification and quantitative analysis of textured, weakly scattering or large grained samples in which diffracted intensities differ greatly from expected values or are totally unregistered by 1D-type detectors. Texture analysis of quasi-single crystal textured thin films used as epitaxial buffer layers in making high temperature superconductor tape is also dramatically improved by the analysis of partial Debye rings captured by the 2D detector [5].

2.3. Reflection High-Energy Electron Diffraction

Reflection High Energy Electron Diffraction (RHEED) is a powerful technique for obtaining structural information of different materials. The need for this type of crystallographic information is strongly driven by the nature of complex oxide materials—complex in structure and composition—where epitaxially driven changes in atomic coordination and small changes in bond lengths can have dramatic effects on their properties [6].

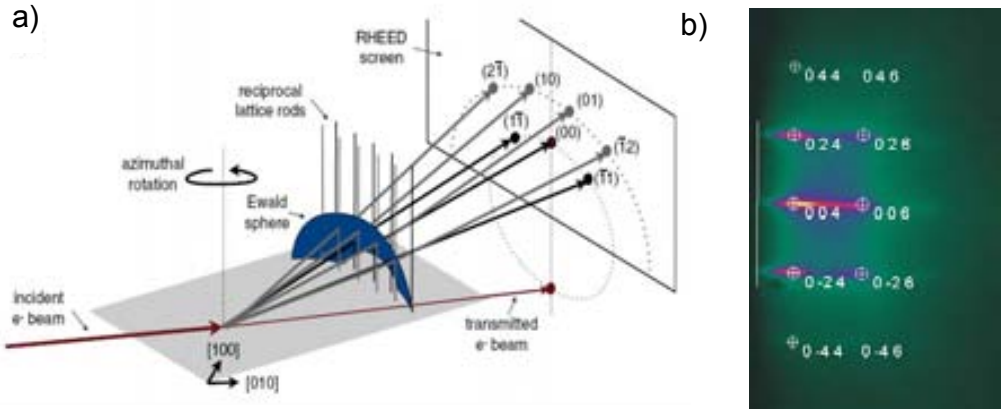

Figure 2.3–1 a) The Basic geometrical setup of RHEED with Ewald sphere construction highlighted; b) an example of RHEED pattern for CZO with elongated spots indicating big and flat grains.

RHEED measures elastic electrons scattered from a surface. The electron gun generates a beam of electrons which strikes the sample at a very small angle (1º-3º) relative to the sample surface. Incident electrons diffract from atoms at the surface of the sample, and a small fraction of the diffracted electrons interfere constructively at specific angles and form regular patterns on the detector, typically a flat phosphor screen. For an ideal flat surface, the RHEED diffraction pattern is a projection of the intersection of the crystal truncation rods and the Ewald sphere resulting in a series of high intensity points on a dark background. In addition to the Bragg diffraction which is the primary information in RHEED images, there can also be strong patterns generated by the subsequent diffraction of inelastically scattered electrons. These patterns, called Kikuchi patterns, can be quite sharp and contain significant intensity in the case of crystals with very high bulk and surface order [6].

The RHEED measurements used for the investigation of the structure of CZO buffer layers and presented in this thesis were performed at IFW Dresden during my NESPA stage there. This technique is usually an in-situ one and permits the texture analysis of a thin

superficial layer (~ 2 nm). In this thesis, it was used as a ex-situ technique. The samples were previously cleaned with isopropanol and glued with silver paste on a support which was introduced in the RHEED after.

2.4. X-Ray Reflectivity

A highly accurate method for thickness determination is X-ray reflectivity (XRR). In this technique, the reflectance of the sample is measured as a function of the grazing incidence angle of X-rays. Due to interference effects of radiation reflected on the layer surface and radiation reflected on the layer/substrate interface, oscillations occur in the reflectance curve which can be fitted according to the Fresnel equations [7].

A monochromatic x-ray beam of wavelength λ irradiates a sample at a grazing angle ω and the reflected intensity at an angle 2θ is recorded by a detector (Figure 2.4–1). The detector D rotates at twice the speed of the sample P. The beam makes an incident angle ω with the surface of the sample P. The reflected intensity at angle of 2θ is measured. Above the critical angle θ_c the reflection from the different interfaces interfere and give rise to interference fringes [8]. The period of the interference fringes and the fall in the intensity are related to the thickness and the roughness of the layer (layers in case of multilayers). The simplified formula for calculating the thickness is:

$$d = \frac{\lambda}{\Delta(2\theta^{o})} \qquad \textbf{Eq. 2.4-1}$$

where d = film thickness, λ is the x-ray wavelength and Δ(2θº) is the distance between two consecutive minimum or maximum of the interference fringes [9].

The thickness of the films was determined by XRR measurements using Rigaku Rotaflex RU-200BV diffractometers with Cu-K_α, λ=1.5418 Å. Scans at low angles, between 0,5º and 3º with a stepsize of 0,002 were performed for calculating the thickness of the CZO buffer layers. The number of fringes is different depending on the growth atmosphere. This technique gives also information about of the roughness of the cap layer.

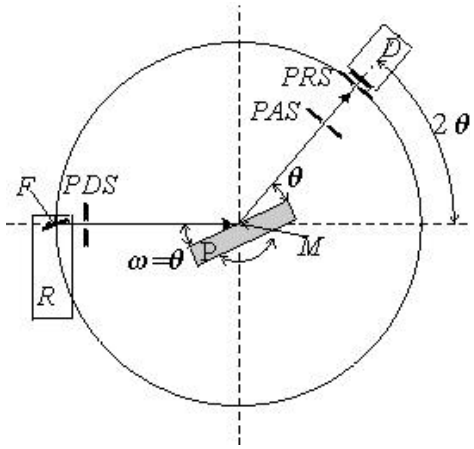

Figure 2.4–1 Principle of θ-2θ scan in reflectometry.

2.5. Reciprocal Space Mapping

In thin-film analysis we are mainly interested in the investigation of the surface regions of the sample that are most advantageously investigated by reflection measurements [10]. The latter are restricted to the range between the minimum $\omega_{min} = 0$ and the $\omega_{max} = 2\theta$ condition above which the scattered beam cannot exit the surface. We can visualize the different scanning techniques in the plane of momentum transfer by the in-plane component *Qx* and the out-of-plane component *Qz* of the scattering vector (Figure 2.5–1).

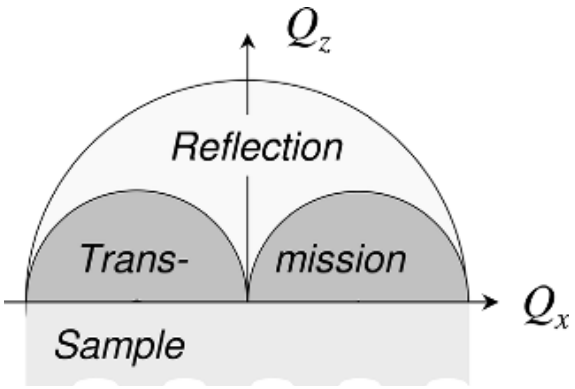

Figure 2.5–1 Plane of momentum transfer (*Qx*, *Qz*) in coplanar diffraction geometry.

The Q representation is more directly translatable than the diffraction space angular coordinates for analysis or for comparison with other measurement methods. The usefulness of the *Q* representation is fully realized when this plot is combined with a reciprocal space map of the sample. Such a combined plot is shown in Figure 2.5–2 for a silicon wafer of (001) orientation. The [110] direction has been aligned along the sample *x* axis.

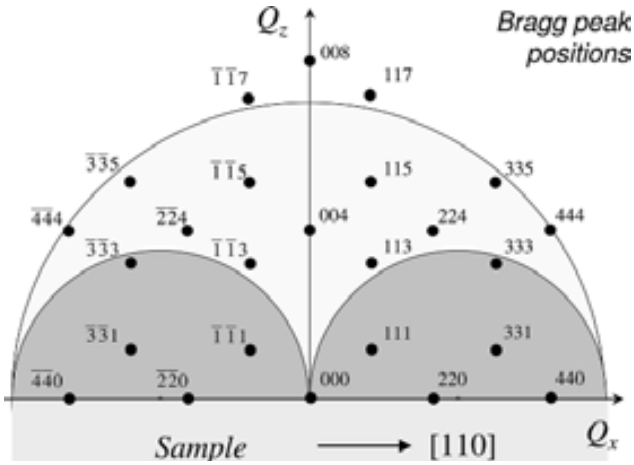

Figure 2.5–2 Combined plot of (*Qx*, *Qz*) plane and net of position of Bragg peaks for an epitaxial film on a Si substrate of (001) orientation. Use of Cu K_α radiation is assumed.

Reciprocal space mapping is performed such that the Bragg ref lection under investigation is fully mapped in a confined area in *Q* space. This means that the reflection is not only monitored by one rocking curve crossing it, but the whole area in the vicinity of the ref lection is included in the measurement. Reciprocal space maps may be obtained by joining together successive one-dimensional scans in *Q* space for which different procedures are possible. One way of mapping consists in performing various rocking curves with increasing scattering angle 2θ. This is shown schematically in the *Q* space representation in Figure 2.5–3 (a). Another technique makes use of successive radial scans (Figure 2.5–3 (b)). In both cases an intensity map of the *Q* area around the Bragg ref lection is obtained. A further approach is to use the relationships given in Eqs. 2.5.1,2 and map directly in reciprocal space.

$$Q_x = K\left[\cos(\theta-\omega)-\cos(\theta+\omega)\right] \qquad \textbf{Eq. 2.5-1}$$

$$Q_z = K\left[\sin(\theta-\omega)+\sin(\theta+\omega)\right] \qquad \textbf{Eq. 2.5-2}$$

where $K = 2\pi/\lambda$.

These maps might deliver further structural information of epilayers to that obtained by rocking curve scans alone.

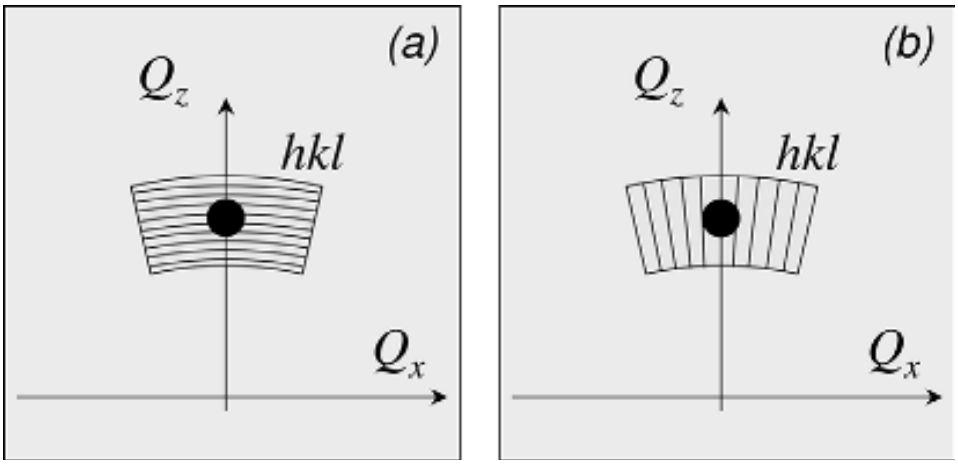

Figure 2.5–3 Two different ways by which reciprocal space maps may be recorded either by (a) subsequent rocking curve measurements or (b) subsequent radial scans.

2.6. Scanning Electron Microscopy

The SEM is a microscope that uses electrons instead of light to form an image and have developed new areas of study in the medical and physical science communities. With the SEM, the examination of big variety of materials is possible being a non-destructive technique. The scanning electron microscope has many advantages comparing with traditional microscopes: large depth of field, which allows more of a specimen to be in focus at one time, much higher resolution, so closely spaced specimens can be magnified at much higher levels. Because the SEM uses electromagnets rather than lenses, the researcher has much more control in the degree of magnification. All of these advantages, as well as the actual strikingly clear images, make the scanning electron microscope one of the most useful instruments in research today. The principle of function is presented in Figure 2.6–1 a). A beam of electrons is produced at the top of the microscope by an electron gun. The electron beam follows a vertical path through the microscope, which is held within a vacuum. The beam travels through electromagnetic fields and lenses, which focus the beam down toward the sample. Once the beam hits the sample, electrons and X-rays are ejected from the sample. Detectors collect these X-rays, backscattered electrons, and secondary electrons and convert them into a signal that is sent to a screen similar to a television screen and the final image is produced [11].

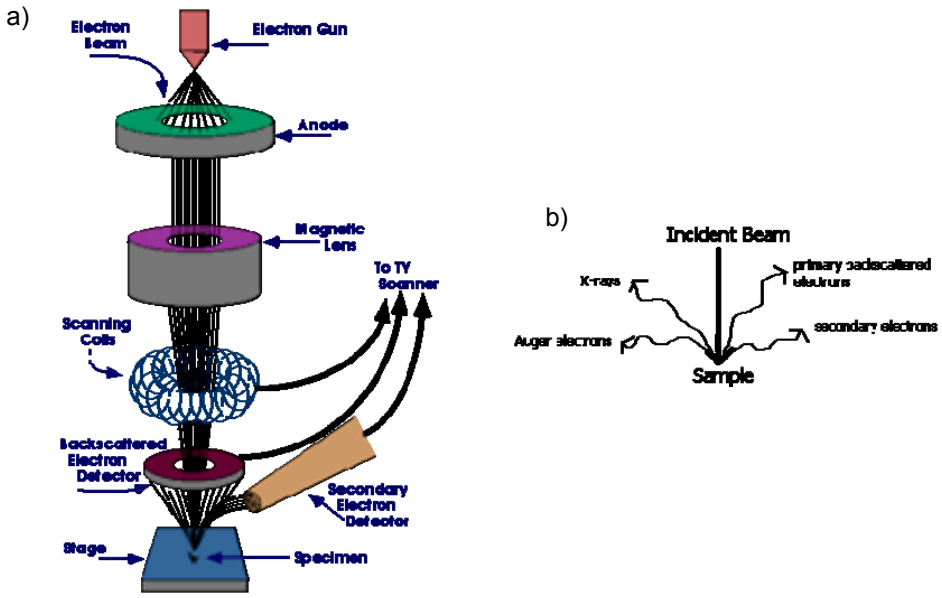

Figure 2.6–1 a) Schematic presentation of a SEM; b) Interaction between the beam and the sample when electrons and x-rays are ejected [11].

SEM images presented in this thesis were made part using a JEOL JSM-6300 SEM in the 'Servei de Microscopia Electrònica' at UAB and the other part using a FEI Quanta 200 FEG in ICMAB. The beam was focused to a final probe distance around 10 nm. We have worked in five magnifications - 50×, 2000×, 6000×, 10000×, 30000× for obtaining information about YBCO surface, porosity and a/b nucleation.

2.7. Transmission Electron Microscopy

Transmission Electron Microscopy (TEM) is a well known technique for imaging solid materials at atomic resolution. Structural information can be acquired both by (high resolution) imaging as well as by electron diffraction. Additional detectors allow for elemental and chemical analysis down to this sub-nanometer scale. The design of a transmission electron microscope (TEM) is analogous to that of an optical microscope. In a TEM high-energy (>100 kV) electrons are used instead of photons and electromagnetic lenses instead of glass lenses [12]. The TEM is presented schematically in Figure 2.7–1. A "light source" at the top of the microscope emits the electrons that travel through vacuum in the column of the microscope. Instead of glass lenses focusing the light in the light microscope, the TEM uses electromagnetic lenses to focus the electrons into a very thin beam. The electron beam then travels through the specimen you want to study. Depending on the density of the material present, some of the electrons are scattered and disappear from

the beam. At the bottom of the microscope the unscattered electrons hit a fluorescent screen, which gives rise to a "shadow image" of the specimen with its different parts displayed in varied darkness according to their density. The image can be studied directly by the operator or photographed with a CCD camera [13].

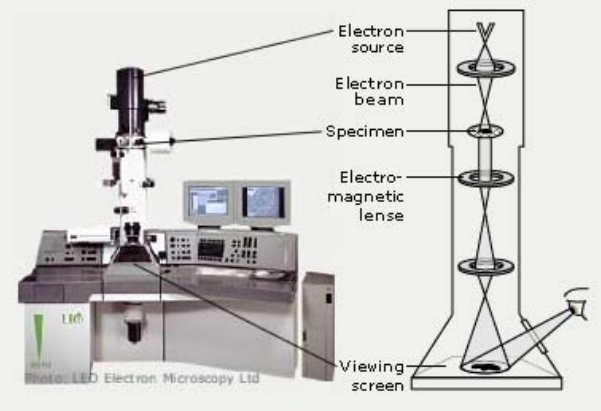

Figure 2.7–1 Schematic view of a general Transmission Electron microscope [13]**.**

In this thesis, high resolution TEM investigations were carried out with a 200 kV Jeol JEM-2010F field emission gun microscope equipped with an electron energy loss spectrometer (EELS) with a nominal energy resolution of 0.8 eV. High resolution STEM images were acquired by using the aberration-corrected JEOL 2100F STEM microscope at UC Davis., USA.

2.8. Inductive measurements

The superconducting properties of the films were determined with magnetisation measurements which were made with a Quantum Design Magnetic Property Measurement System MPMS-XL. This system contains superconducting coils able to generate magnetic fields up to 7T. The sample space is filled with helium at low pressure at temperatures ranging from 2 to 400 Kelvin. The sensitivity of the system is 10^{-8} emu or 10^{-11} Joule per Tesla. The magnetic field was always applied along the c-axis and perpendicular to the film surface.

The Superconducting Quantum Interference Device (SQUID) is a superconducting ring with one or two weak links (i.e. regions with very low critical current density). The device measures the flux Φ_i created by an external field inside this ring. The construction of the device leads to an output voltage, which depends periodically on this flux, with the period Φ_0

= h/(2e), where h is Planck's constant, and e the electric charge of an electron. In order to utilize this periodic curve over a useful range, a feedback mechanism keeps the working point of the device always at the same value of Φ_i, with accuracy far better than $10^{-5}\ \Phi_0$. The actually measured output signal is created by this feedback current. As a first consequence of this mechanism, the SQUID can only detect changes in Φ_i. The SQUID ring itself is usually not accessible. Flux (or current) is coupled into the ring by a superconducting input coil. This input coil Li is - in most currently available instruments - part of a flux transformer, which in the simplest case consists of an external superconducting coil L_e. The flux changes in L_e are directly mirrored in L_i and, hence, detected by the SQUID [14].

From the measurement of the M(H) curves at different temperatures and the M(T) curves at self-field was determined the inductive critical current density, J_c. The J_c was calculated using Bean model:

$$J_c(B) = \frac{m(B)}{V}\frac{12a}{b(3a-b)} \qquad \textbf{Eq. 2.8-1}$$

where *a, b* are the lateral sample dimension, V the volume and m the magnetization. In our case, because on the edges the deposition is not homogeneous, we consider the sample a sphere in which 0,25 mm were substracted from the radius for the calculation of J_c.

2.9. Electrical transport measurements

Electric transport measurements have been done using a Physical Properties Measurements System (PPMS) from Quantum Design, equipped with a 9 T superconducting magnet and a helium cryostat for the temperature control (1.8 K and 400 K). The sample is mounted in a single-axis rotor with a total angular range of 370º and a 0.1º of precision. Currents down to 1 μA and up to 2 A are provided from the dc/ac current source. Samples for transport measurements were prepared by a method previously developed in the group [15]. Using a thermal evaporation system with a vacuum pressure chamber (~ 10^{-6} mbar), silver contact pads are deposit on the YBCO films (Figure 2.9–1 a)). After, the contacts are annealed under a flowing oxygen (0.12 l/min) atmosphere in a tubular oven at a temperature of 400ºC during 60 minutes, followed by a cool down to room temperature. On the surface of the sample was put previously a brass shadow mask, which is processed using standard photolithography and etched using a 1:10 H_3PO_4:H_2O mixture. The image of the sample after etching is presented in Figure 2.9–1 b).

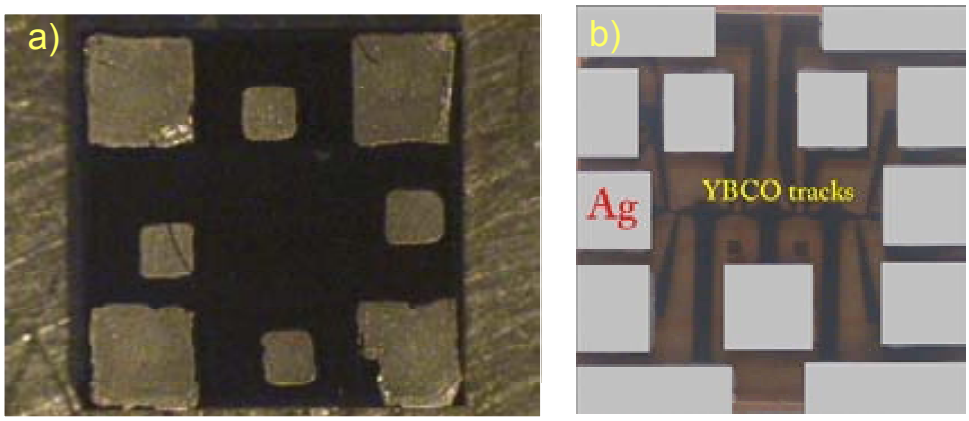

Figure 2.9–1 a) A YBCO sample with contact pads after thermal annealing; b) YBCO tracks after photolithography and etching. Different masks were used in the two images.

What is important in a superconducting sample is to determine the maximum critical current (I_c) which can be carried without dissipation; when the injected current exceeds I_c a voltage drop develops across the superconductor and the resistance becomes non zero. This is the ideal case, because, in reality, different dissipation like flux creep and flux flow, each one with a different *I-V* signature, occurs in the HTS. The way to determine this is by mean of the study of the *I-V* shapes of the material, or more generally the *J-E* curves. 256 voltage readings for each non-linear *I-V* curve are performed after that the dc-current is ramped up to a maximum desired value IM. Above the I_c, the V rise very fast at low fields and temperatures and *I-V* rounding is observed due to flux creep is less present. The power and the voltage drop are controlled during all the measurement with security values in the range of $VM \approx 3\ \mu V - 10\ \mu V$ and $PM = VMIM$. The criteria used in this thesis to define I_c (J_c) is the current needed to develop an electrical field inside the superconductor of 1 μVcm^{-1}[15,16].

2.10. Pulsed Laser Deposition

Laser deposition has become in the last few years a powerful tool in thin-film deposition of high-temperature superconductors (HTSC), especially in the field of device fabrication [17]. With Pulsed Laser Deposition (PLD), the ablation of one or more targets illuminated by a focused pulsed-laser beam is used for the preparation of thin films [18]. Figure 2.10–1 shows a typical set-up for PLD. Elementary or alloy targets are struck at an angle of 45º by a pulsed and focused laser beam in an ultrahigh vacuum (UHV) chamber. The atoms and ions ablated from the target(s) are deposited on substrates, which are attached, mostly, with the surface parallel to the target surface at a target-to-substrate distance of typically 2-10 cm.

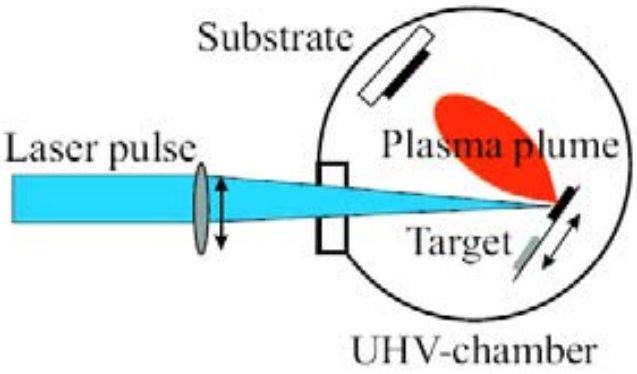

Figure 2.10–1 Schematic diagram of a typical laser deposition set-up.

During the deposition process, a pulsed laser beam (typically 30ns pulses with energy in the range of 0.1-1 J and a frequency of 1-20 Hz) is focused onto the target in a vacuum chamber. ArF, KrF excimer lasers and Nd:YAG, are the most commonly used lasers [19]. It was shown that the shorter the wavelength, the more effective the ablation [20]. When the laser energy density (energy per unit area at the target surface) is above a threshold value, the target (bulk ceramic of crystal) is evaporated, forming a plasma plume, which is normal to the target surface and collected on a suitably positioned and heated substrate. For achieving high quality epitaxial films, the deposition parameters such as substrate temperature, laser energy density and frequency, target-to-substrate distance, base pressure, deposition gas pressure should be optimized. During oxide deposition, oxygen must be introduced into the chamber in order to assisting the formation of the desired phase and film composition [19]. More details will be presented in Chapter 3 (Section 3.5.1).

2.11. References

[1] Agilent Technologies, "Agilent Technologies 5500 Scanning Probe Microscope," User's guide (2009).

[2] M. Coll, A. Pomar, T. Puig et al., "Atomically Flat Surface: The Key Issue for Solution-Derived Epitaxial Multilayers," Applied Physics Express **1** (12) (2008).

[3] B.B. He, "Two-Dimensional X-Ray Diffraction," John Wiley & Sons, Inc. (2009).

[4] Bruker AXS Inc., "General Area Detector Diffraction System (GADDS)," User's manual, Version 4.0 (1998, 1999).

[5] M. B. Dickerson, K. Pathak, K. H. Sandhage et al., "Applications of 2D Detectors in X-ray Analysis," JCPDS-International Centre for Diffraction Data 2002, Advances in X-ray Analysis **45** (2002).

[6] N. J. C. Ingle and et al., "The structural analysis possibilities of reflection high energy electron diffraction," Journal of Physics D: Applied Physics **43** (13), 133001.

[7] "X-ray Reflectometry," http://www.ptb.de/mls/aufgaben/xray-refl.html.

[8] "X-ray-reflectometry (XRR)," http://ia.physik.rwth-aachen.de/methods/xray/www-xray-eng.pdf?menu_id=80&language=german.

[9] A. Cavallaro, "Optimization of CSD buffer layers for $YBa_2Cu_3O_7$ coated conductor development," PhD Thesis, UAB, Bellaterra (2005).

[10] Mario Birkholz, "Thin Film Analysis by X-Ray Scattering," WILEY-VCH Verlag GmbH & Co. KGaA, Weinheim (2006).

[11] "Scanning Electron Microscope," http://www.purdue.edu/rem/rs/sem.htm.

[12] Koninklijke Philips Electronics N.V., "Transmisson Electron Microscopy (TEM)," http://www.research.philips.com/technologies/projects/matanalysis/downloads/7-temtn.pdf (2008).

[13] "The Transmission Electron Microscope," http://nobelprize.org/educational/physics/microscopes/tem/index.html.

[14] "2nd NESPA Training Lab Course"Basic Superconductor Measuring Techniques"," Atominstitut, Vienna University of Technology (2009).

[15] J. G. Royo, "Vortex pinning and critical currents in $YBa_2Cu_3O_{7-x}$ MOD-TFA thin films and Coated Conductors," PhD Thesis, UAB, Bellaterra (2008).

[16] V. R.Gómez, "Ancoratge de vortex en capes fines de $YBa_2Cu_3O_{7-x}$ nanocomposades crescudes pel metode de deposicio de solucions quimiques," UAB, Bellaterra (2010).

[17] B. Holzapfel, B. Roas, L. Schultz et al., "Off-axis laser deposition of $YBa_2Cu_3O_{7-delta}$ thin-films," Applied Physics Letters **61** (26), 3178-3180 (1992).

[18] H. U. Krebs, M. Weisheit, J. Faupel et al., "Pulsed laser deposition (PLD) - A versatile thin film technique," Advances in Solid State Physics 43 **43**, 505-517 (2003).

[19] Junling Wang, "Introduction to Pulsed Laser Deposition," Nanyang Technological University, Singapore **http://www3.ntu.edu.sg/home/JLWang/PLD-introduction.pdf**.

[20] T. J. Jackson and S. B. Palmer, "Oxide superconductor and magnetic metal thin-film deposition by Pulsed-Laser Ablation - A Review," J. Phys. D-Appl. Phys. **27** (8), 1581-1594 (1994).

CHAPTER 3 GROWTH OF DOPED CeO_2 BUFFER LAYERS

Cerium oxide as well as mixed cerium oxide is widely used in various fields of science and engineering for the manufacture of solid-state oxide cells, gas sensors or coated conductors. Systems with high content of zirconium dioxide are used in production of ceramic materials and ionic conductors, and systems with predominance of cerium dioxide form a basis of various catalysts [1]. In this chapter, various doped cerium oxide thin films were prepared by chemical methods and characterized by mean of various techniques: AFM, XRD, RHEED and XRR.

3.1. Requirements for a buffer layer

$YBa_2Cu_3O_{7-x}$ (YBCO) coated conductors (CCs) have received increased attention from researchers worldwide, due to their lower ac losses, better in-field performance, and lower processing costs compared with first-generation high-temperature superconductor wires [2]. In the recent years $YBa_2Cu_3O_{7-x}$ (YBCO) thin films on flexible metallic substrates, such as Ni and Ni alloys have attracted broad attention for the realization of large scale applications of coated conductors. Because of the chemical reaction between YBCO and the metallic substrates, the superconducting properties are poor and therefore, a buffer layer has to be engaged to solve this problem [3]. A superconducting HTS layer is deposited onto buffer layers, which coat a base metallic substrate that provides strength and flexibility. A typical architecture of a coated conductor is shown in Figure 3.1–1.

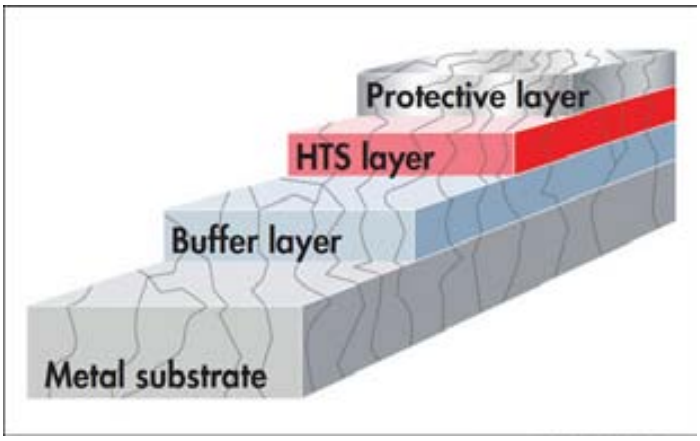

Figure 3.1–1 Coated Conductor architecture showing the ceramic oxide buffer and the superconducting layer.

Grain alignment of the HTS is achieved by growing it *epitaxially* on a polycrystalline template of some suitable oxide, which itself must be bi-axially textured.

For epitaxy, its structure and in-plane crystal lattice constants should closely match the nearly square *a-b* plane dimensions of the HTS. Ideally, other main properties of buffer layer(s) are: chemically stable and non-reactive with the HTS, nonporous and strongly bonding [4].

Recently, a huge effort has been made to scale up the production of coated conductors of RE-BCO to commercial length. The three principal approaches used for the fabrication of textured-template include: (a) the Ion Beam Assisted Deposition (IBAD); (b) the Rolling Assisted Biaxially textured substrates (RABiTS), and (c) the Inclined Substrate Deposition process. For any one of these techniques, at least one buffer layer is needed to grow high quality RE-BCO film on the metal substrates. Functionally, buffer layers are a barrier between the YBCO and the substrate and also a texture base. The nature of the optimal buffer layer architecture will depend on whether the route is the RABiTS or the IBAD. In all cases, however, with several oxide layers, are used complex architectures to satisfy all the diverging requirements. In the RABiTS route, the texture is formed on a metallic substrate, hence the buffer layers need to act first as a barrier: preventing diffusion of metal atoms up into the superconductor, as well as prevent oxygen diffusing down through to the substrate and cause oxidation of the metal. It's essential, therefore, for the buffer to be free of cracks, which may appear either because of the stress induced through differential thermal contractions or as a mechanism to relax the stress induced by the lattice misfit. In the first case, it is essential to have a closely matched thermal expansion coefficient with the substrate and the superconductor and in the second case to select the correct thickness to avoid the formation of cracks. An additional requirement of a buffer layer is to be biaxially textured with suitable lattice parameters and non-reactive with a HTS layer and also to have a (00l) crystallographic orientation, mainly in the case of the cap layer to be in contact with RE-BCO. In the IBAD approach, the key function of the first buffer layer (seed layer) is to generate a texture on a randomly oriented polycrystalline metallic substrate. The buffer layer should be also a good diffusion barrier, and be defect free as well. An additional property, which may be desirable for some applications, is to have a high electrical conductivity, so that currents may be transferred through it into the metallic substrate [5]. Tailoring a suitable lattice parameter of the buffer layer to adapt it to that of the HTS film can be achieved in principle by utilizing mixed rare-earth oxides, since the ionic radius of the rare-earth elements (from La to Lu) decreases monotonically with increasing atomic number. This

requires precise determination of the value of a mixing parameter x which gives the exact lattice parameter needed for complete matching [6]. This approach, however, introduces additional modifications of the processing or may also generate modifications of the SC properties.

Several materials, like YSZ, CeO_2, Y_2O_3, MgO, $BaZrO_3$ and $SrTiO_3$, or combinations of them, have been considered as potential buffer layers in order to reach high critical current densities [7]. The most important properties of some of these materials used for substrates and also for buffer layers are presented in Table 3.1-1.

Materials	Crystal structure	Lattice constant (nm)	Plane Space d (nm)	Misfit to YBCO (%)	α (10^{-6}/°C)	m.p. (°C)
$YBa_2Cu_4O_{8.18}$	Orthorhombic	a=0.3817 b=0.3883 c=1.1633	(a+b)/2 =0.385	0	7.9 (11) 16 (33)	1150
$Zr_{0.8}Y_{0.2}O_{1.9}$	Cubic	0.5147	0.3640	-5.45	10.3	2680
$Zr_{0.85}Y_{0.15}O_{1.93}$	Cubic	0.5139	0.3656	-5.56		2730
CeO_2	Cubic (CaF_2)	0.5411	0.3826	-0.62	9.9-13.2	2600
$SrTiO_3$	c.p.	0.3905	0.3905	+1.43	10.4	2080
$LaAlO_3$	r.p.	0.3792	0.3792	-1.31	9.2	2100
LSAT	c.p.	0.3868	0.3868	+0.47	10	1840
$LaMnO_3$	c.p.	0.3880	0.3880	+0.78		
$La_2Zr_2O_7$	c.p.	1.0786	0.3813	-0.96		
$BaZrO_3$	c.p.	0.4193	0.4193	+8.91		
$BaCeO_3$	c.p.	0.4377	0.4377	+13.7		
Y_2O_3	Cubic (Mn_2O_3)	1.055	0.3723	-3.30	8.5	2410
MgO	Cubic (Al_2MgO_4)	0.4216	0.4216	+9.35	8.0-12.8	2852
$NdGaO_3$	o.p.	a=0.543 b=0.550 c=0.770	0.384 0.389	-0.26 +1.04	7.8	1600
NiO	cFR (NaCl)	0.4177	0.4177	+8.49		1990
Si	CFR (C)	0.543	0.384	0.27	3.12	1410
SiO_2 (Quartz)		a=0.515 c=1.388			0.59	1720
Al_2O_3 (Sapphire)	Hexagonal	a=0.4758 c=1.299			8.31-9.03	2040

Keys: values at room temperature unless otherwise stated;
α: coefficient of thermal expansion
m.p.: melting point;
o.p.: orthorhombic perovskite;
c.p.: cubic perovskite;
r.p.: rhombohedral perovskite;
f.c.c.: face-centred cubic

Table 3.1-1 Properties of the most commonly used materials for substrates and buffer layers [5].

For YBCO CC production, CeO_2 has been considered as one of the best cap layer because the misfit is low and it is often a chemically stable material for growth of RE-BCO superconductor. To obtain the buffer layer architectures, vacuum deposition methods (PLD and sputtering), or chemical methods (CSD), including sol-gel and MOD, may be used. The investment cost is higher in the case of vacuum deposition methods, while no complex equipments are required in the CSD method and hence it a very appealing to scale-up. This is the approach that will be investigated in this chapter. The capability of the doped CeO_2 was investigated before in the group and showed that high J_c superconductors (4 MA/cm^2) can be obtained using this cap layer [8].

3.2. Preparation of the $Zr^{4+}(Gd^{3+})$ doped CeO_2 precursor solution

The protocol for the preparation of the Zr-doped CeO_2 solution is a simple one and is presented in Figure 3.2–1. For 10% Zr^{4+} dopant, an amount of 0,025 g zirconium pentadionate $Zr(CH_3COCHCOCH_3)_4$ (Sigma-Aldrich, 99,9%) and 0,1968 g cerium (III) acetylacetonate hydrate $Ce(CH_3COCHCOCH_3)_3 \cdot xH_2O$ (Alfa Aesar, 99,9%) was mixed with 1mL of propionic acid (Sigma-Aldrich), CH_3CH_2COOH, and 1 mL of anhydrous isopropanol (2-propanol) (Sigma-Aldrich), $(CH_3)_2CHOH$. For accelerating the solubility of the salts the mixture was heated at 50ºC for 20 minutes stirring in the same time. After this time, the mixture was filtered using a 0,2 μm filter. The final yellow solution has a total metal concentration of 0,25 M. In the case of doping with Gd^{3+}, the preparation protocol is the same with the difference in the amount of the $Gd(CH_3COCHCOCH_3)_3\ xH_2O$ dopant salt weighted (Gd^{3+} - 0,023g).

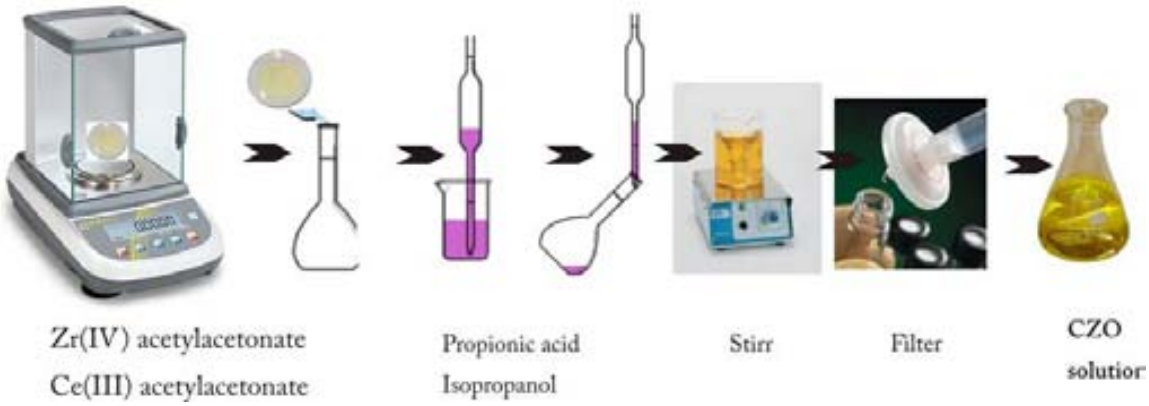

Figure 3.2–1 The preparation protocol for the Zr^{4+}, Gd^{3+} doped CeO_2 precursor solution starting from acetylacetonates salts.

3.3. Characterization of the solution

3.3.1. Viscosity

Rheology, as the science of the deformation and flow of matter, investigates the response of materials to an applied stress or strain. There are two types of rheological behaviour: elastic behaviour, where the material restores its original shape when the external force is removed, and viscous or plastic behaviour (such as in ideal Newtonian liquids), where the deformation ceases and the material doesn't regain the original shape when the external force is removed [9]. When attempting a material to flow, "viscosity" is the word most often used to convey an impression of the ease or degree of difficulty. The shear flow is the easiest

type of flow. A force applied to the top surface of a cube of material produces a deformation in that surface. This force, F, per unit area, A, is termed the shear stress (τ) and has been shown to create a deformation characterised by the angle γ known as shear. If this shear stress would be maintained with time on the surface of the fluid then the angle γ would change with time, however the rate of change of γ would be constant and this is called shear rate ($\dot{\gamma}$).

The viscosity (η) of the material is defined as the ratio of the applied force per unit area to the shear rate:

$$\eta = \frac{\tau}{\dot{\gamma}} \qquad \textbf{Eq. 3.3-1}$$

The unit of shear stress is Nm^{-2} and that of shear rate is s^{-1}, so [η] = Pa s [10].

The viscosity of the precursor solution is a measure of its stability. Changes within the solution due to incomplete reactions or evaporation of the solvents during coating or storage will alter the viscosity. Moreover, the viscosity directly influences the thickness of the coated films, when spin coating or dip coating techniques are used: higher viscosities result in enhanced film thicknesses. Higher viscosities can be reached by either increasing the concentration of the precursor solution or by using other solvents and solution-modifying additives. Increasing the concentration is the preferred method for raising the buffer film thickness, as it is desirable to keep the chemistry of the precursor solution as simple as possible. Even slight modifications of the solution can have a strong effect on the layer formation and resulting layer properties [11]. The viscosity of the $Ce_{0,9}Zr_{0,1}O_2$ buffer precursor solution was measured at a constant temperature of 22ºC using a Rheometer HAAKE RheoStress RS600 from Thermo Electron Corporation.

The viscosities of the CZO precursor solutions having solution concentrations of c = 0,25 M and c = 0,15 M were determined to be η = 2,4 mPa s and η = 2,2 mPa s, respectively. As expected, the viscosity decreases with decreasing the concentration of the solution. The graph of the viscosity as a function of time for the solution with the 0,25 M concentration is shown in Figure 3.3–1.

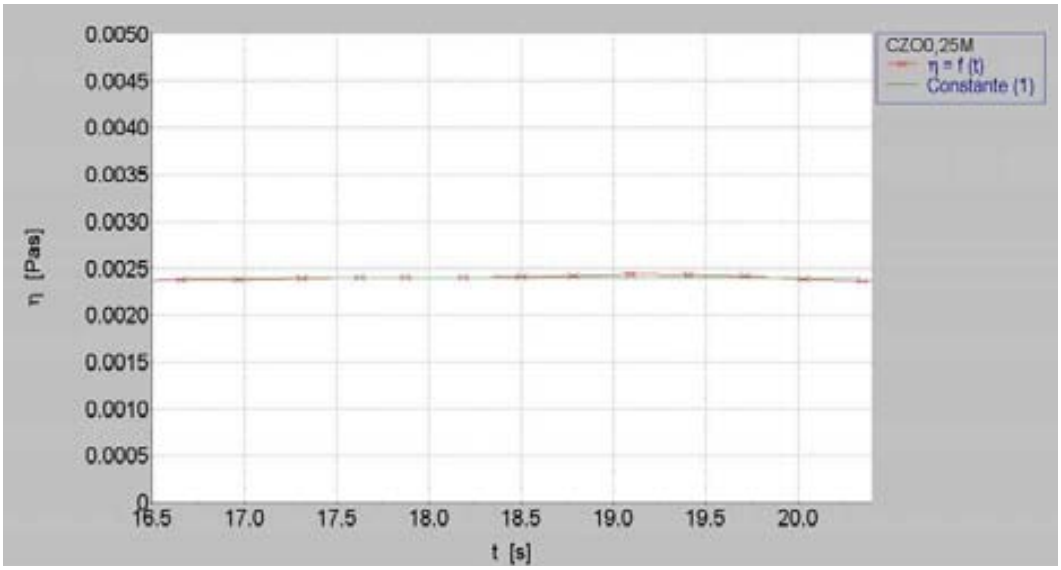

Figure 3.3–1 The dependence of the viscosity η as a function of time for a 0,25 M CZO solution.

3.3.2. Wetting

The behaviour of a solution on a solid surface is given by the contact angle ,θ ,which is a quantitative measure of the wetting of a solid by a liquid. It is defined geometrically as the angle formed by a liquid at the three phase boundary where a liquid, gas and solid intersect as shown below:

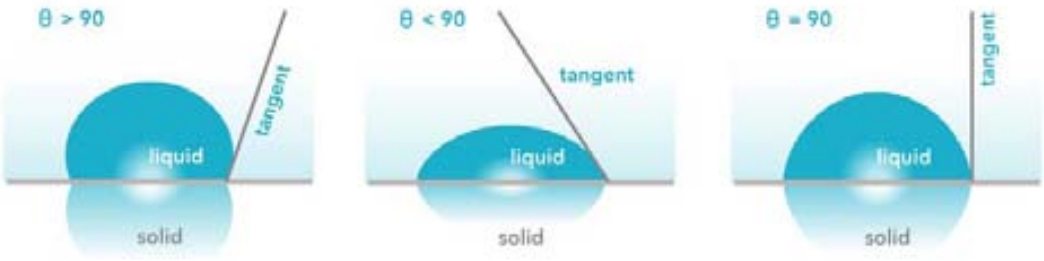

Figure 3.3–2 The contact angle, θ, formed by a liquid and a solid surface.

It can be seen from Figure 3.3–2 that a low value of contact angle (θ) indicates that the liquid spreads, or wets well, while a high contact angle indicates poor wetting. If the angle θ is less than 90 degrees the liquid is said to wet the solid. If it is greater than 90 degrees it is said to be non-wetting meanwhile a zero contact angle represents complete wetting [12]. The contact angle is actually determined for the equilibrium established at the interface between the three coexisting phases: solid–liquid γ_{SL}, liquid–vapor γ_{LV} and solid–vapor γ_{SV}, where γ_i are the corresponding surface energies. For incomplete wetting, the contact angle is given by Young's equation [11]:

$$\gamma_{SV} = \gamma_{SL} + \gamma_{LV} \cos\theta \qquad \text{Eq. 3.3-2}$$

In order to obtain a complete homogenous covering of the YSZ substrates leading to homogenous layer properties, a very small wetting angle is required. The wetting behaviour of two precursor CZO solution with 0,25 M and 0,15 M concentrations was investigated using the sessile drop method with a Contact Angle Measuring System DSA 100 from KRÜSS device. The experimental setup is presented in Figure 3.3–3, as well as the image of the contact angle for the solution with 0,25 M concentration.

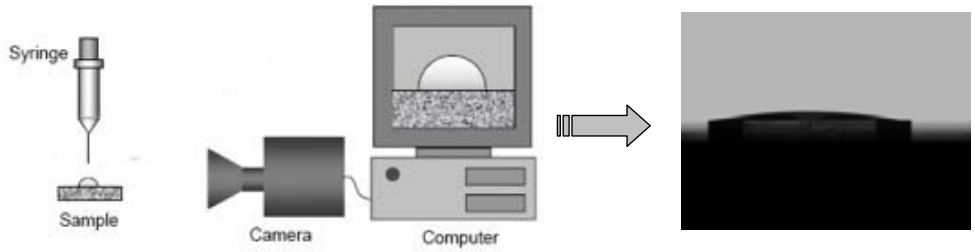

Figure 3.3–3 A schematic view of the experimental setup for contact angle measurements as well as the contact angle photo obtained for a 0,25 M CZO buffer solution on YSZ substrate.

For a volume of 2 µl precursor solution, values of 9,9º (0,25 M CZO) and 9,69º (0,15 M CZO) were registered on YSZ single crystal, showing an excellent wetting behaviour.

3.3.3. Surface Tension

Measurements of surface tension yield data which directly reflect thermodynamic characteristics of the liquid tested. Measurement of contact angles yield data which reflect the thermodynamics of a liquid/solid interaction. For characterizing the wetting behaviour of a particular liquid/solid pair it is need just to report the contact angle. It is possible to characterize the wettability of the solid in a more general way. Various methods are used but the same basic principle applies for each. The solid is tested against a series of liquids and contact angles are measured. Calculations based on these measurements produce a parameter (critical surface tension, surface free energy, etc) which quantifies a characteristic of the solid which mediates wetting. Using a series of homologous liquids of different surface tensions, a graph of cos θ versus γ is produced. It will be found that the data form a line which approaches cos θ = 1 at a given value of γ. This is the maximal surface tension of a liquid which may completely wet the solid. This value, called the critical surface tension, can be used to characterize the solid surface [12].

The surface tension of the CZO precursor solution with 0,25 M and 0,15 M concentrations was measured at room temperature. Before doing this, the density of these solutions, ρ, were determined with an analytical balance and found to be 1,0462 g/ml (c = 0,25 M) and 0,8916 g/ml (c = 0,15 M). The values obtained for the surface tension are presented in Table 3.3-1. In the case of the solution more diluted the values are close to the surface tension of propionic acid in air at room temperature (26,69 mN/m).

Concentration	Surface tension (mN/m)	Surface tension mean value (mN/m)
0,25 M CZO	24,91	25,33
	25,48	
	25,59	
0,15 M CZO	26,10	26,48
	26,75	
	26,76	
	26,23	
	26,58	

Table 3.3-1 The surface tension values for two CZO solutions with different concentrations: 0,25 M and 0,15 M.

3.4. Growth of $Ce_{0.9}Zr_{0.1}O_{2-x}$ and $Ce_{0.9}Gd_{0.1}O_{2-x}$ thin films

3.4.1. Optimization of the growth temperature in different atmospheres (Ar/H_2, O_2) on YSZ single crystals

The growth temperature is a very important parameter for obtaining well textured CZO buffer layers. Several samples were obtained by spin coating using 6000 rpm and an acceleration of 3000 rpm*s^{-1}. The gel films were treated at different temperatures to study the morphological and structural differences which the temperature can induce. The annealing time was maintain constant – 8 hours. (00l) YSZ single crystals were used as substrates. Morphological changes in the buffer surface grown at different temperatures were investigated with AFM (Figure 3.4–1). The surface of the buffer annealed at 800ºC (a) presents spike-shaped outgrowths of about 3-6 nm, meanwhile the morphology obtained at 900ºC (b) is homogeneous with big terraced grains. Small roughness (below rms~1 nm) is observed in that case. Increasing the temperature to 1000ºC (c) decreases the roughness but it maintains some outgrows on the surface.

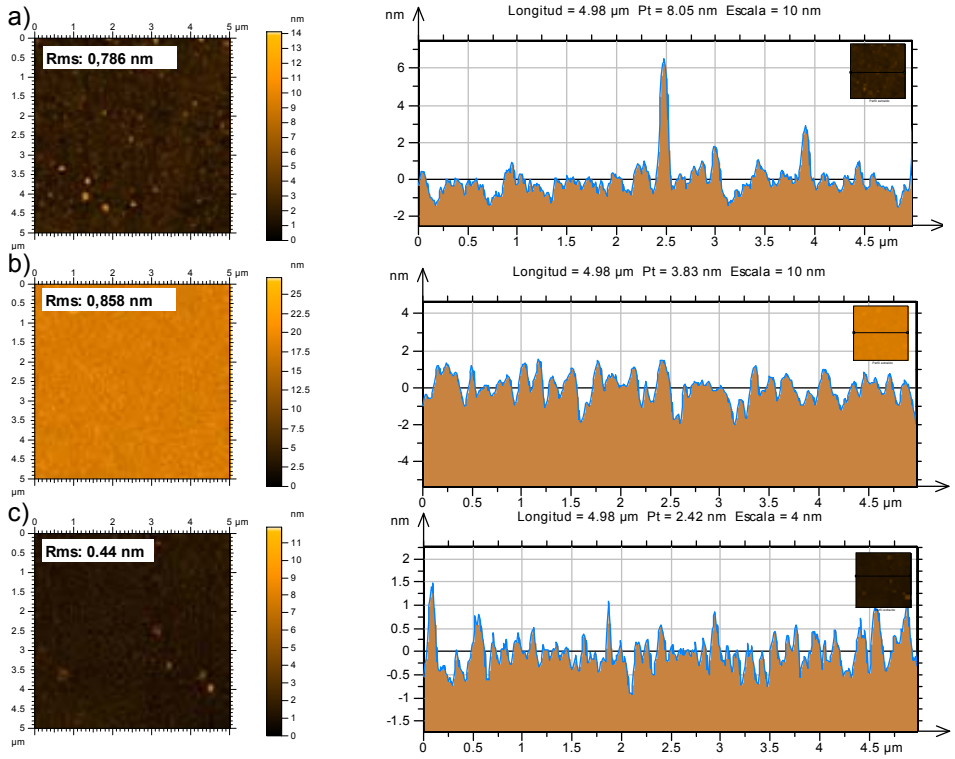

Figure 3.4–1 Morphological characterization using AFM for 3 CZO/YSZ films grown at different temperatures: a) 800ºC; b) 900ºC; c) 1000ºC.

The epitaxial nature of CZO films annealed at different temperatures was investigated using XRD, indicating that all the films had a good epitaxy with a cube –on-cube orientation on the YSZ substrate. Figure 3.4–2 shows the (002) peaks of the CZO together with those of YSZ. Differences in intensities for the (002) reflection of the CZO buffer layer at 900ºC, 1000ºC and 800ºC respectively are shown in Figure 3.4–2 d) (higher temperature, higher intensity). The intensities of the peaks at 900ºC and 1000ºC are higher than at 800ºC indicating a better crystallization of both cap layers [8].

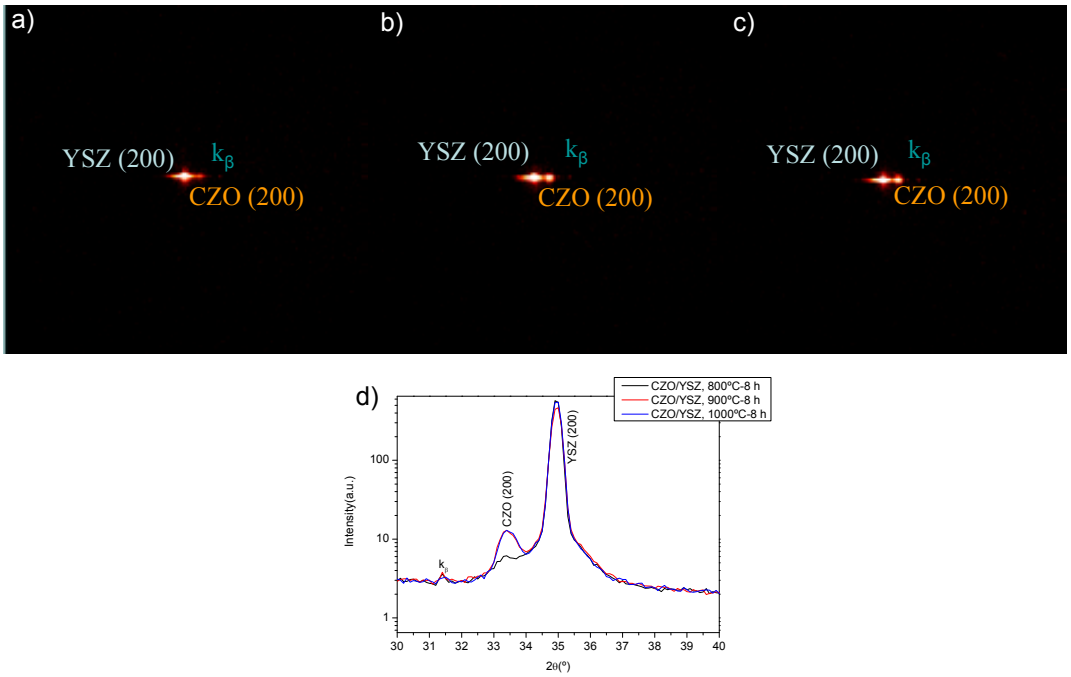

Figure 3.4–2 2 D XRD patterns of the CZO buffer layers grown on YSZ at different temperatures: a) 800ºC; b) 900ºC; c) 1000ºC. d) integration in chi of the previous XRD frames.

Another key parameter is the atmosphere in which the growth is done. Depending of the gas used, different surface morphologies can be observed. As reveled by AFM images, the surface of the CZO/YSZ sample grown in reducing atmosphere (Ar/H_2), shown in Figure 3.4–3 a), presents small globular grains, with a rms roughness of 2,3 nm. Instead, the film annealed under oxidizing atmosphere (O_2), Figure 3.4–3 b), shows a homogeneous terraced surface, with flat and large grains. This film displays an average roughness of 1,1 nm. This result is better understood if we carefully inspect a representative line profile selected for each image, encountered at the right of the corresponding topographic image.

From these profile scans it is easily seen that annealing in O_2 atmosphere lead to atomically flat terraced-like surface morphology, (001)-faceted, whereas Ar/H_2 -reducing treatment gives granular rough surface [8].

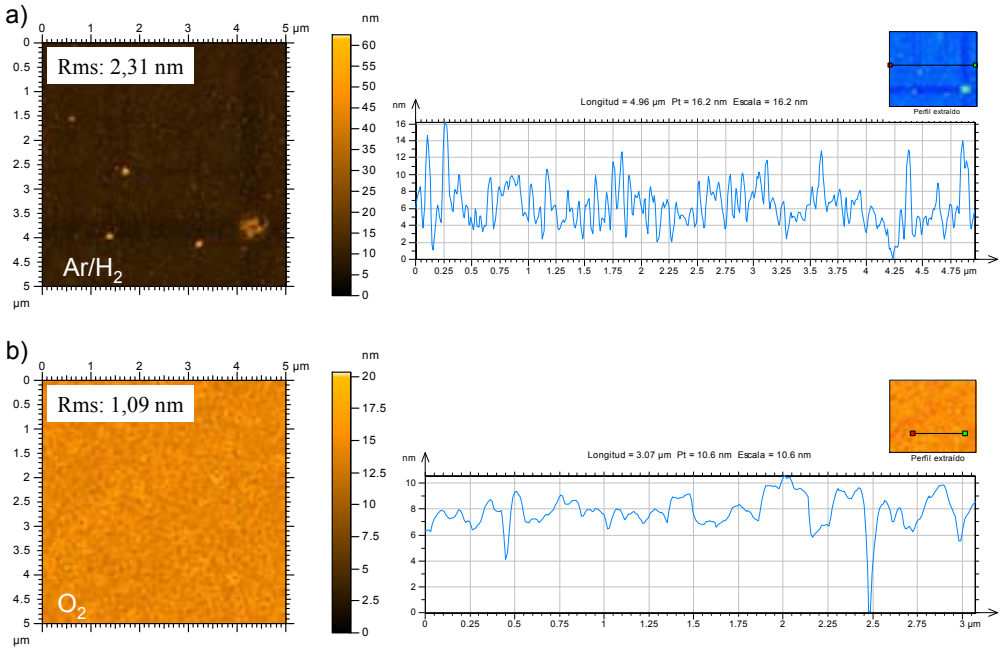

Figure 3.4–3 AFM images and height profile of CZO/YSZ samples: a) processed in Ar/H_2 with a rms of 2,31 nm; b) processed in O_2, rms = 1,09 nm.

Taking into account the AFM and XRD results, the optimum temperature for growing flat epitaxial CZO buffer layers was found to be 900ºC.

3.4.2. Determination of the film thickness using X-ray reflectivity

We use for finding the thickness of CZO on YSZ, X-ray reflectivity (XRR) as an alternative technique. In XRR, for incident angles θ below a critical angle θ_c, total external reflection occurs. Above θ_c, the reflections give rise to interference fringes, which are related to the thickness and the roughness of the layer. The simplified formula for calculating the thickness is

$$d = \frac{\lambda}{\Delta(2\theta^{o})} \qquad \textbf{Eq. 3.4-1}$$

where d = film thickness, λ is the x-ray wavelength and Δ(2θº) is the distance between two consecutive minimum or maximum of the interference fringes [13].

θ-2θ scans at low angles (0,5º-3º) with a stepsize of 0,002 were recorded with a Rigaku Rotaflex RU-200BV Diffractometer. Two different samples grown in Ar/H_2 and also in O_2 were analyzed and the results are presented in Figure 3.4–4. A thickness of 26,7 nm was obtained according to this graph for the CZO (0,25 M) grown in O_2.

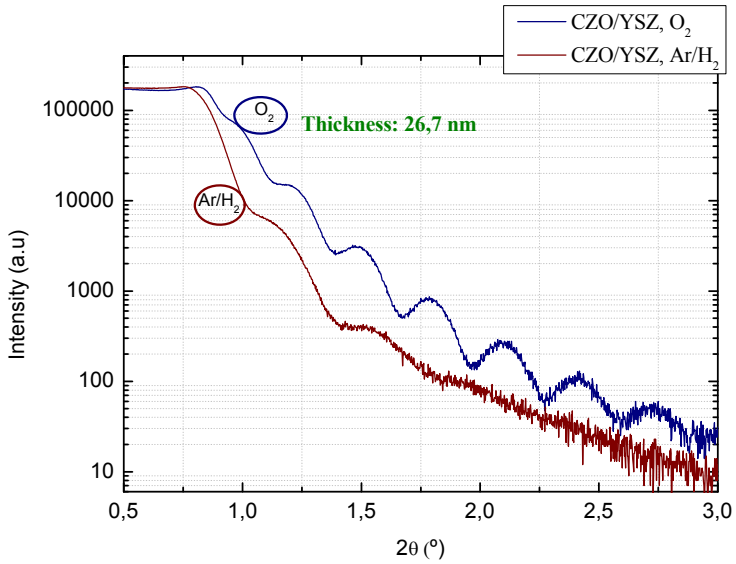

Figure 3.4–4 XRR fringes from where the thickness of the CZO film grown in Ar/H_2 and also in O_2 can be calculated.

3.4.3. Structural characterization of the buffer layers

3.4.3.1. X-Ray Diffraction

Cerium dioxide, CeO_2, has been widely used as a cap layer and also a seed layer for high superconductor [14]. As a promising candidate of buffer material for YBCO CCs, CeO_2 film development has been attempted by many groups due to its excellent chemical compatibility with Ni-based alloy substrates as well as good lattice match with YBCO or ReBCO (Re = Rare earth element). Unfortunately, due to the existence of a critical thickness of 50 nm, beyond which cracks are known to form and micro-cracks propagate, CeO_2 has seldom been successfully used as a single buffer layer. Alternatively, the use of Zr-doped CeO_2 allows for a very thick and crack-free $Ce_xZr_{1-x}O_2$ (CZO) layer, making it possible to combine the previously stated functions into one single layer and replace the tri-layer of CeO_2/ YSZ/CeO_2 [2].

From structural point of view, CeO_2 is a face-centered cubic material with a fluorite structure and the lattice parameter a = 0,541 nm. When doping with zirconium, this parameter decreases till reaching the value a = 0, 538 nm (Figure 3.4–5 b)). Since the epitaxial orientation relation in CZO/YSZ system is (001) CZO // (001)YSZ, the lattice mismatch between CZO and YSZ is "$\varepsilon = (a_{CZO}-a_{YSZ})/a_{CZO} = -4,6\%$" ($a_{YSZ}$ = 0,513 nm). Under epitaxial growth conditions, CZO films are under compressive stress due to the larger parameter of the buffer compared to the substrate (Figure 3.4–5 b)).

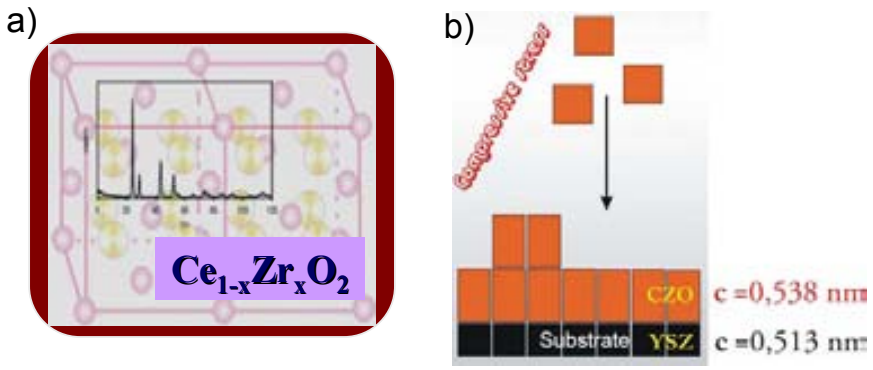

Figure 3.4–5 a) the crystal structure of $Ce_{1-x}Zr_xO_2$; b) the CZO/YSZ system under compressive stress.

Films of $Ce_{0,9}Zr_{0,1}O_2$ were prepared on YSZ substrates by MOD using two different buffer solution concentrations: 0,25 M and 0,4 M. The buffers were heated 8 hours at 900ºC. Typical XRD θ-2θ scans of the two films are presented in Figure 3.4–6 a) and b). In the case of 0,25 M CZO, sharp spots revealed by the 2D frame suggest that the buffer layer grows epitaxial on the substrate and no secondary phases are observed. If we increase the concentration of the CZO to 0,4 M, a deterioration of the crystalline quality of the buffer is noted and the (111) and (220) polycrystalline reflections are visible in Figure 3.4–6 b). A comparison between the two concentrations, 0,25 M and 0,4 M, after integratation in chi the previous frames is shown in Figure 3.4–6 c).

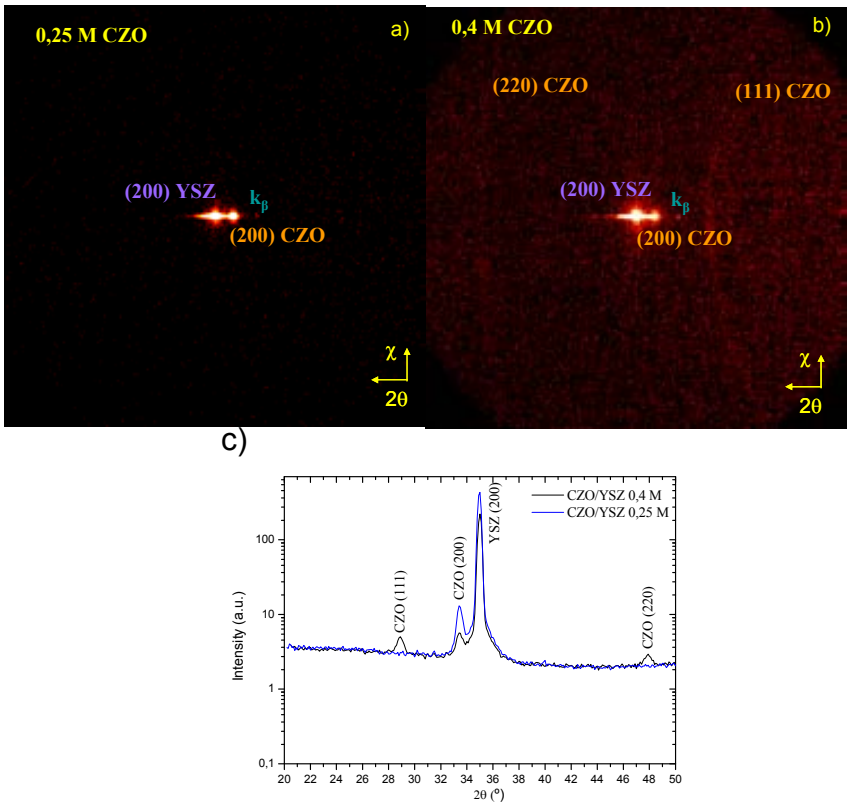

Figure 3.4–6 a) Epitaxial growth of CZO revealed by XRD for 0,25 M CZO; the measurements were done with a 2D detector diffractometer where the sharp spots correspond to epitaxial reflections; b) increasing the concentration of the buffer precursor solution to 0,4 M leads to the appearance of the polycrystalline reflections (111) and (220) of the CZO; c) integration in chi of the 2D XRD patterns for the two samples of different concentrations: 0,25 M and 0,4 M CZO where the reflections (111) and (220) are clearly observed .

The lattice parameter, a, was calculated from (200) and (400) peaks of CZO and compared with the one found for the bulk CeO_2. The results are presented in

Table **3.4-1**. For the calculation was used Bragg law (Eq. 3.4-2)

$$2d\sin\theta = n\lambda \qquad \textbf{Eq. 3.4-2}$$

where d was deduced for a cubic lattice (Eq. 3.4-3):

$$d_{hkl} = \frac{a}{\sqrt{h^2 + k^2 + l^2}} \qquad \textbf{Eq. 3.4-3}$$

In this equation, d is the distance between planes, θ is the Bragg angle, n is the order of the reflection and λ = 1,54178 Å is the wavelength of CuK_α. The lattice parameter a of the doped CeO_2 (a_{CZO} = 5,347 Å) is 0,063 Å lower than the one of the bulk CeO_2 (a_{CeO_2} = 5,41 Å). Higher diffraction angle goes to lower lattice parameter. The reason of this difference could be the difference in structural defects which were created in the growth process with the variation of oxygen content because of the mobility at high temperature and long time annealing.

Reflection CZO 0,25 M	2θ (º)	θ (º)	sinθ	a_{pp} (Å)	Mean a_{pp} (Å)	a (Å) bulk CeO_2
(200)	33,45	16,725	0,2878	**5,350 ± 0,003**	**5,347 ± 0,005**	5,41
(400)	70,37	35,185	0,5762	**5,345 ± 0,007**		

Table 3.4-1 Calculation of the a lattice parameter for CZO ($a_{CZO\ bulk}$ = 5,385 **Å**). The difference between this one and parameter for the bulk CeO_2 is because of the defects introduced in the structure with the addition of Zr.

3.4.3.2. Reflection High Energy Electron Diffraction

For obtaining good textured buffer layers and YBCO superconducting films, a high quality surface texture is essential. Therefore, RHEED is a necessary and useful tool to investigate the texture quality of buffer films up to the surface for the purpose to developing buffer layer architectures for YBCO coated conductors [15].

Reflection High Energy Electron Diffraction (RHEED) measurements were carried out on CZO/YSZ with 0,25 M and 0,4 M to investigate the surface texture. The two samples were fixed one by one on a metallic support with silver paste and heated at ~105ºC inside the low pressure chamber. Electron energies of 30 keV were used under a grazing incidence angle of 0,5-1,5º to the substrate surface in order to examine the texture of the upper 5 nm of the layer. The results of the measurements are presented in

Figure 3.4–7. CZO 0,25 M layers (

Figure 3.4–7 a) and b)) show a well textured surface with elongated spots indicating large and flat epitaxial grains. Two different views are presented: along <100> and along <110> axis. A RHEED pattern with rings suggesting misorientation of the grains can be seen when increasing the concentration of the buffer to 0,4 M. In this case, the spots are sharp and rounded indicating a rougher surface morphology. The appearance of these rings is a sign of structural disorder and is in concordance with XRD pattern presented in Section 3.4.3.1 where (111) and (220) polycrystalline reflections can be seen.

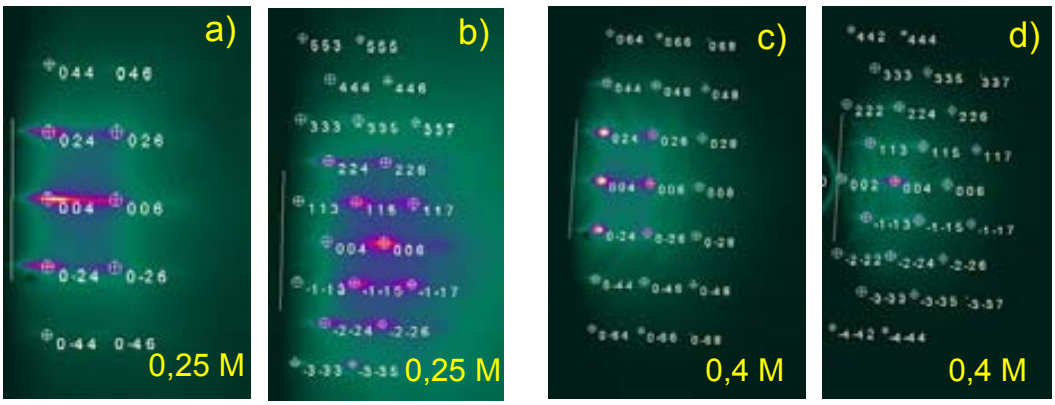

Figure 3.4–7 RHEED diffraction pattern for CZO buffer layer with different concentrations – 0,25 M and 0,4 M. a) experimental pattern of CZO 0,25 M with the electron beam directed along <100>; experimental pattern of CZO 0,25 M with the electron beam directed along <110>; c) RHEED pattern of CZO 0,4 M with the electron beam directed along <100> where rings corresponding to a disorder of the texture are observed; >; d) RHEED pattern of CZO 0,4 M with the electron beam directed along <110>.

3.4.3.3. Reciprocal Space Mapping (RSM) - Q-Plot

The structural properties of thin epitaxial films such as composition, layer tilt, lattice relaxation and structural quality can be studied using Reciprocal Space Mapping (RSM) [16]. Bragg's Law is a scalar description of the diffraction process. Since we live in a 3-D world, something a little more vectorial is needed. The reciprocal space in which the Ewald sphere has an important role is directly connected to real space. For doing a reciprocal space map, 2-dimensional scans representing ω-2θ versus ω are necessary (Figure 3.4–8).

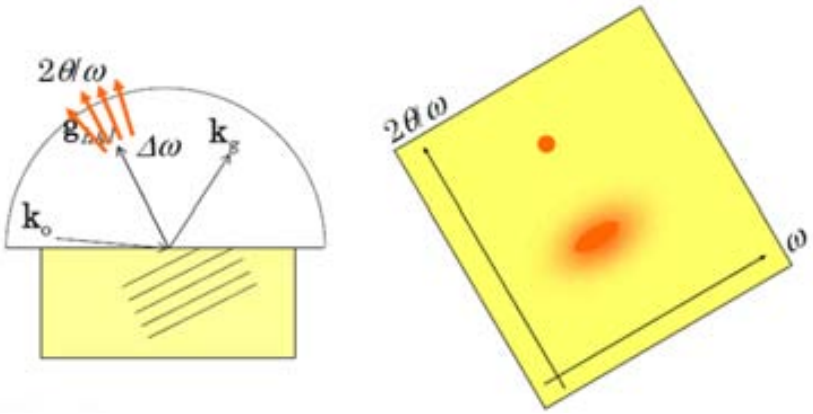

Figure 3.4–8 Reciprocal space mapping requires 2-dimensional scans: ω-2θ versus ω for obtaining more information about the state of crystal structure, such as defects and relaxation.

The X-ray measurements were performed with a 2D GADDS at ICMAB and two samples of CZO/YSZ grown in different atmospheres, O_2 and Ar/H_2, were studied (Figure 3.4–9).The thicknesses of the two samples are different depending on the atmosphere (O_2-26,7 nm and Ar/H_2-18,8 nm). The measurements were done with a 0,3 mm collimator and without a Ni filter. First the detector was centered at half distance between YSZ-CZO (2θ = 91º). Then ω was set to 7,5º, φ = 45º, step 0,05º, time/step = 20 s. With the detector fixed, the

ω (sample) was moved 6,5º in 130 frames. The reflections around the (004) and (224) Bragg points for both buffer and substrate were taken for recording RSMs. The positions of the maxima of the diffuse intensity distribution of the CZO buffer are corrected with the substrate. In the RSM analysis procedure the conversion of the experimental data from real space units (ω, 2θ, intensity) into reciprocal space units (q_x, q_y, intensity) is necessary. The equations used for this are:

$$q_x = \sin\theta \sin(\theta - \omega) \text{ and } q_y = \sin\theta \cos(\theta - \omega) \qquad \textbf{Eq. 3.4-4}$$

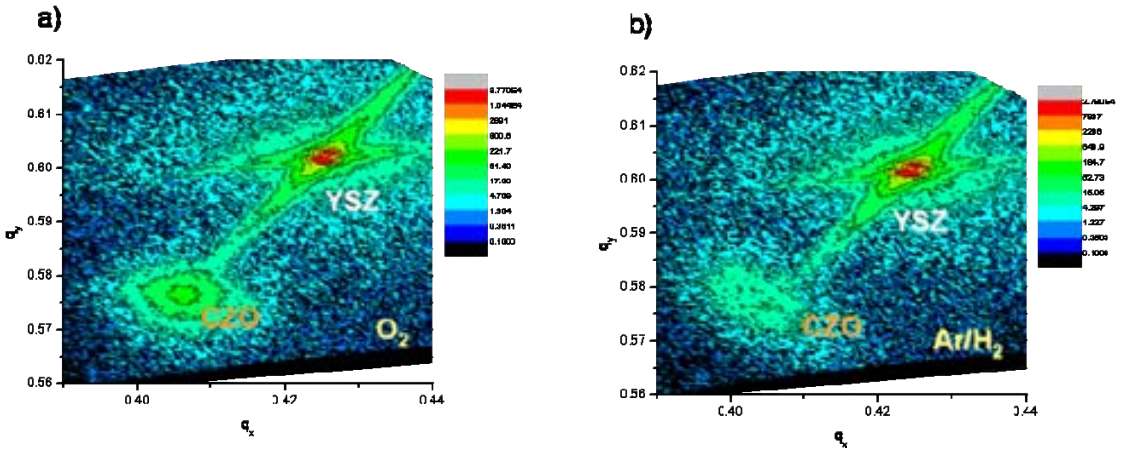

Figure 3.4–9 Comparison of the RSMs for two CZO buffer layers grown at 900ºC on YSZ during 8 hours in different atmospheres: a) O_2 and b) Ar/H_2. (004) reflections were used for the calculation of the out-of-plane lattice constant (a_{pp}) and (224) for the in-plane lattice parameter ($a_{//}$).

Bulk ceria has a cubic structure; however the lattice mismatch and difference in the thermal expansion coefficient between the film and substrate introduce tetragonal distortion which is detected as a difference between the lattice parameters in the directions parallel to $a_{//}$ and normal to a_{pp} the substrate face. As a result of the film-substrate interaction, the film can be either coherently strained (mesomorphic) or relaxed. In a mesomorphic film the lateral lattice constant is equal to that of the substrate, while in a relaxed or partially relaxed film it evolutes toward that of the bulk value [17].

We derived both in-plane and out-of-plane lattice constants from the reflections (224) and (004) assuming a tetragonal distortion of the cubic lattice. Figure 3.4–9 reveals that there is a displacement between the in-plane component q_x of CZO and the one of the YSZ substrate indicating that the buffer is partially relaxed. This relaxation was also observed by Solovyov [17] in ceria buffers deposited by PLD. The growth in O_2 atmosphere goes to compressive strains both in-plane as out-of-plane, much less than the misfit value 5-10 % ($a_{CZO\ bulk}$ = 5,38 Å [18]). The normal direction lattice constant a_{pp} is close to the bulk value, 5,38 Å, as it can be seen in Table 3.4-2. Both in-plane and out-of-plane lattice parameters

(O_2, Ar/H_2) were found to be bigger than the YSZ substrate parameter (a_{YSZ} = 5,16 Å). In an epitaxial CZO layer which has a perfect cubic fluorite structure (Figure 3.4–10 a)) [19], $a_{//} < a_{pp}$. If we look to the Table 3.4-2 to the values obtained for these two parameters, we see that, in our case, $a_{//} > a_{pp}$. So, it is not possible that the epitaxy determines these values. A possible explanation is that the oxygen vacancies are differently distributed in the zones parallel to the substrate compared with the zones perpendicular to the substrate. From $a_{//} > a_{pp}$ results that the oxygen vacancies are distributed more in the plane than out of the plane. Talking about the oxygen vacancies δ ($Ce_{0.9}Zr_{0.1}O_{2-\delta}$), XPS investigations done in the group showed that the percentage of oxygen vacancies is higher in Ar/H_2 than in O_2 (Table 3.4-2). For more information about the microstructure, TEM analysis should be carried out.

Atmosphere	$a_{//}$ (Å)	a_{pp} (Å)	Ce^{3+}	δ(%)
O_2	5.369 ± 0.021	5.348 ± 0.012	0.027	1.35
Ar/H_2	5.393 ± 0.04	5.340 ± 0.025	0.135	6.7

Table 3.4-2 In-plane and out-of-plane lattice parameters for CZO derived from reciprocal space maps. The content of Ce^{3+} and the percentage of oxygen vacancies were calculated by XPS.

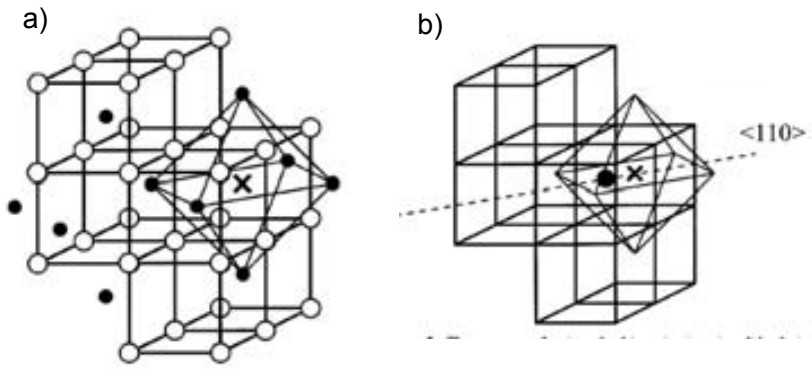

Figure 3.4–10 a)The perfect flourite structure of cubic ceria-zirconia. Cations (small filled circles) occupy each second interstitial site of the cubes of oxygen ions (open circles); b) Oxygen defects in fluorite structure. Some oxygen ions (filled circle) occupy the interstitial octahedral sites, leaving vacancies in the tetrahedral sites (not shown). The interstitial oxygen ions are displaced from the centers of the interstitial octahedral sites in the á110ñ directions. In the general case, the concentration of vacancies may exceed that of interstitial ions, resulting in oxygen nonstoichiometry [19].

3.4.4. Morphological characterization: AFM images

The roughness and the planarity of the cap layers are two critical key parameters for obtaining good epitaxial superconducting films, because the nucleation and growth of the

YBCO grains depends of the flatness of the buffer. A correlation between dopant, atmosphere and percentage of flat area of CeO_2 cap layers will be presented here.

When CeO_2 is reduced to CeO_{2-x} defects are formed in the form of Ce^{3+}, which in the Kröger–Vink-notation are written as Ce'_{Ce}, as the Ce^{3+} has one negative charge compared to the normal lattice. Different discussions exist about if these substitutional negative defects were balanced by some of the Ce^{3+} going on interstitial sites as $Ce_i^{\bullet\bullet\bullet}$ or by oxide ion vacancies, $V_O^{\bullet\bullet}$. Later, it was consistently adopted the oxygen vacancy model. Now it is generally agreed that the main compensating defects in CeO_{2-x} are oxygen vacancies. The process of ceria reduction may be written as [20]:

$$O_O + 2Ce_{Ce} = \frac{1}{2}O_2(gas) + V_O^{\bullet\bullet} + 2Ce'_{Ce} \qquad \textbf{Eq. 3.4-5}$$

But, let's take a look to what is happening when a dopant with lower valence is introduced in the lattice of cerium oxide. It was shown that the most well characterised, and perhaps best understood of all the fast oxygen ion conductors, are those based on the doped fluorite oxides; however, these materials became fast oxygen ion conductors when they are doped with aliovalent cations. As mentioned above, the introduction of aliovalent cations into the host lattice introduces oxygen vacancies, as for example the addition of gadolinia to ceria, process which can be illustrated by the following defect equation in Kröger–Vink notation [21]:

$$Gd_2O_3 \Rightarrow 2Gd'_{Ce} + 3O_O^x + V_O^{\bullet\bullet} \qquad \textbf{Eq. 3.4-6}$$

Referring to the activation enthalpy for a series of ceria solid solutions, Faber et al.[22] showed that there is a minimum found in this activation enthalpy which is poorly correlated with the maximum in conductivity. However, the origin of this minimum is still not very well understood (Figure 3.4–11). Explanations for the existence of this minimum were proposed in term of electrostatic effect of the charged dopant ions or an indication that defect association (at some level) is taking place, followed by the limitation of the conductivity of an acceptor doped material.

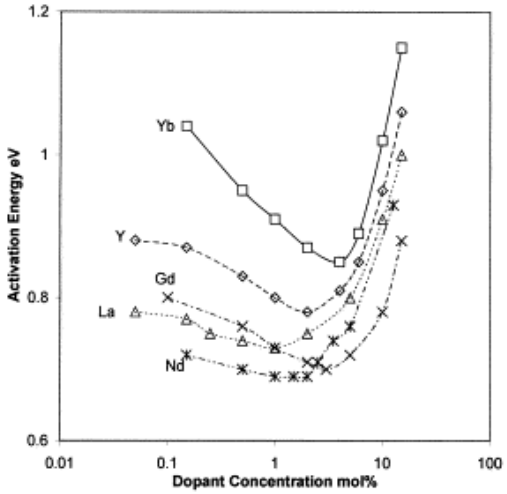

Figure 3.4–11 Concentration dependence of the activation energy for oxygen ion conduction in ceria solid solutions [22].

To investigate the roughness and the planarity of doped cerium oxide films, AFM analysis were performed on different samples: CeO_2, $Ce_{0.9}Gd_{0.1}O_2$(CGO) and $Ce_{0.9}Zr_{0.1}O_2$(CZO). It was demonstrated previously in the group that Gd^{3+}- and Zr^{4+}-doped CeO_2 samples are recognized as a reference formula for its high oxygen mobility because of the oxygen vacancies introduced for charge compensation [23] and also for reducing the carbon impurities when the films show a higher degree of epitaxy and a higher percentage of atomically flat area. If in the case of CGO, oxygen vacancies are formed by charge compensation, in the case of CZO, the key parameter for the mobility seems to be the small ionic radius of Zr^{4+}.

The topographic image was used to quantify the percentage of flat area, named planarity, and compared with the one of the undoped cerium oxide. A quantification of the flat area fraction is needed knowing that if the nucleation occurs on flat terraces, a highly epitaxial superconducting film will be achieved [24]. The methodology for the calculation of the planarity was developed in the group by M. Coll [8,24] and consists in defining a threshold value – in this case 1,5 nm – above which the surface cannot be considered flat. When applying this criterion to the image after binarization, the result is a blue-black surface in which blue means flat and black rougher areas than 1,5 nm [24]. In order to eliminate the slope of the surface and the errors from the AFM instrument, a Levelling Operator followed by Line by Line and Column by Column Operators from the software package MountainsMap SPM-Image 5.0 were used. We have evaluated the rms roughness surface in 5 x 5 μm area scan from these films measuring the surface topography as a surface profile

z(x), where the rms roughness is defined as the root mean square of the deviations of the surface profile z(x) from the mean line.

Figure 3.4–12 shows the surface morphologies of different buffer layers grown 8 hours at 900ºC in O_2: a) undoped CeO_2; b) Gd-doped CeO_2 ; c) Zr-doped CeO_2. Undoped CeO_2 has a smooth surface with roughness of 2,23 nm, but the fraction of flat area is small, just 58,3 %. When doping with Gd, the surface evolutes to more compact but some outgrows are seen on it. The roughness decreases to 1,9 nm and an augmentation of the flat area to 76 % is noted. When tetravalent Zr^{4+} cation is incorporated, a very smooth surface with roughness below 1 nm and high percentage of flat area (90 %) is obtained.

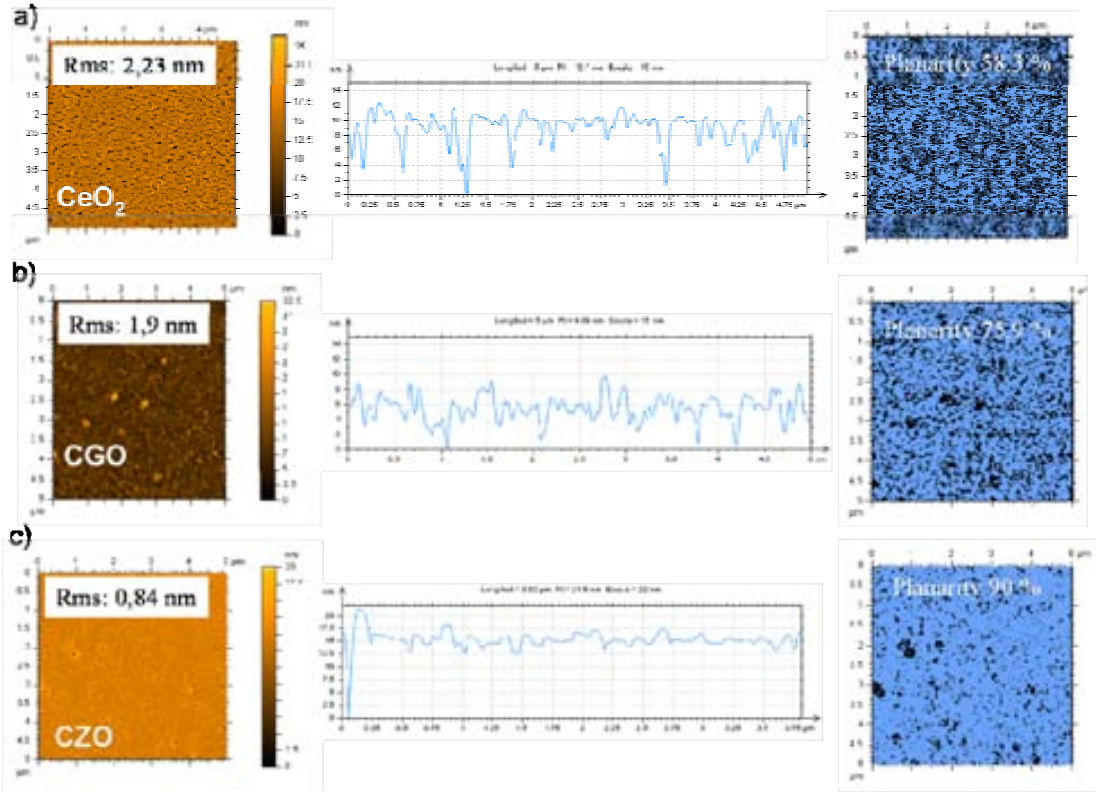

Figure 3.4–12 AFM topographic images, line profiles and planarities for different buffer layers grown in O_2: a) undoped CeO2; b) CGO; c) CZO.

The morphology of the buffer surface changes with the atmosphere. As reveled by AFM image (Figure 3.4–13), the surface of CZO sample grown under reducing atmosphere (Ar/H_2), presents a heterogeneous, hill-like surface with small globular grains, rms roughness of 3,12 nm and small planarity (53 %). The difference can be appreciated better from Figure 3.4–14. The surface of the sample annealed in O_2 presents big and flat terraced grains very different of the rounded ones found in reducing atmosphere.

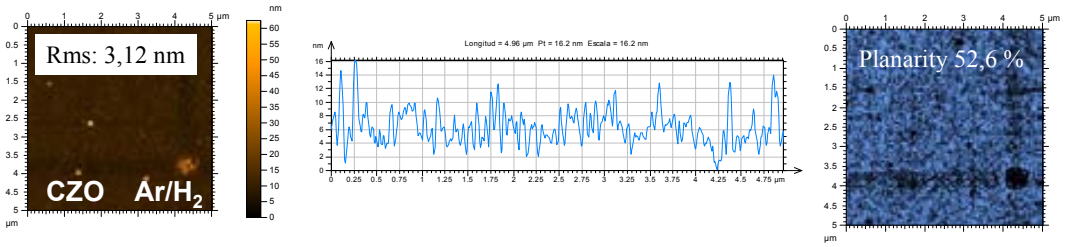

Figure 3.4–13 A CZO buffer layer processed in Ar/H_2, together with the line profile and the planarity.

This result is better understood if we carefully inspect the representative line profile selected for each image from the right of the corresponding topographic image. From the profile analysis, we studied the shape-rounded or flat-of the grains, the mean grain size and also its height using a 1 x 1 µm scan topographic image (Figure 3.4–14). The results are presented in Table 3.4-3. The mobility of the grain boundaries (low angle) depends of the oxygen partial pressure. It is found that under oxygen atmosphere the grain size increases faster than with Ar/H_2. This is probably not due to the carbon impurities in GB as it was shown before [25], it is probably because of the disordered structure of GB which results in a lower mobility in the case of Ar/H_2 annealing. In particular, we know that the oxygen vacancy concentration is much higher ($y = 0.3$). The reason for the different dimensions of the grains in the two of the atmospheres is that the nucleation density is bigger in Ar/H_2 than in O_2. In Volmer-Weber mode (Figure 3.4–14 c)) films initially grow by the nucleation of discrete islands of different crystallographic orientations (or no crystallinity at all, in the case of amorphous solids). Upon additional thermal annealing, the existing islands enlarge, and they coalesce, until a continuous percolating network is achieved. The film continues to grow until the substrate is covered, followed by additional film thickening and GB healing. Sheldon et al. proposed a model that describes this zipping process for low mobility materials that grow with a faceted morphology, as shown in the scheme of Figure 3.4–14 c). In this model, when step edges in adjacent grains get close together (i.e., near to forming a grain boundary), a short range attractive interaction between the steps becomes significant and leads to the development of tensile stress [26]. In oxygen, the mobility is higher and this is evident if we look to the dimensions of the grains which evolutes in time to bigger values, faster than in Ar/H_2.

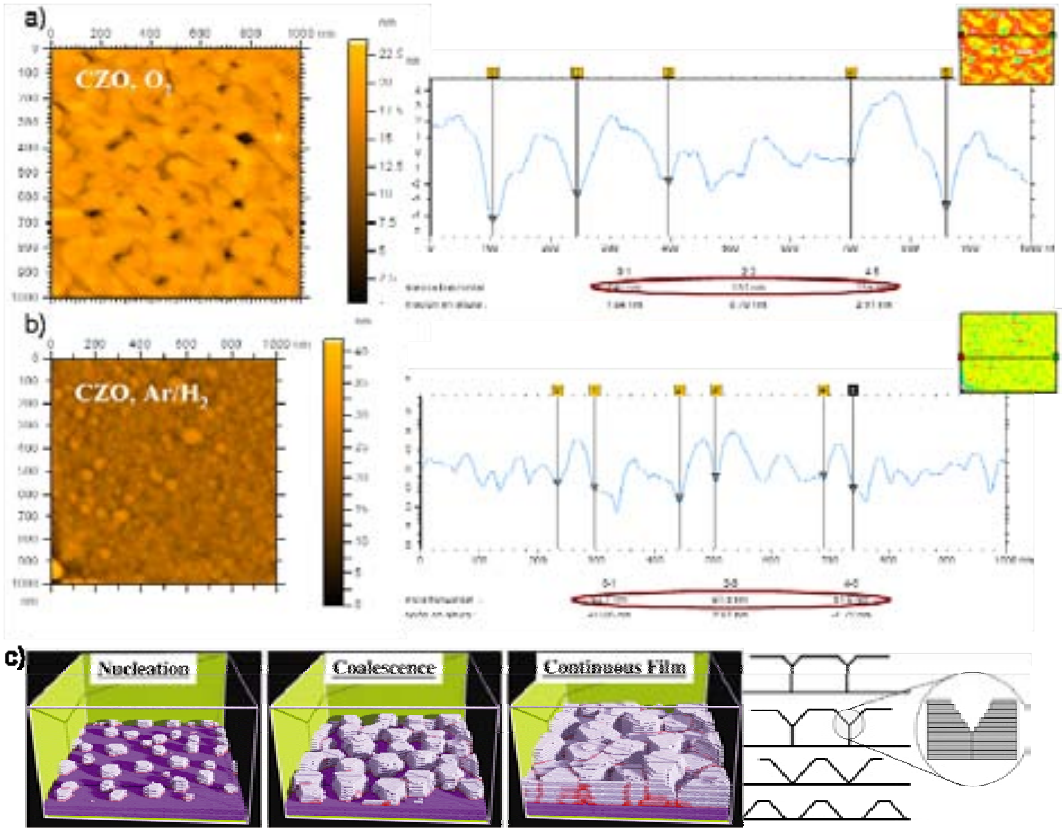

Figure 3.4–14 AFM images of a CZO film surface showing flat terraced grains in oxygen a) and rounded grains in Ar/H_2 b). The horizontal mean size of some grains can be calculated from the line profile found to the right of the topographic image; microstructural evolution during Volmer-Weber film growth together with the coalescence and GB formation in faceted islands [26].

Atmosphere	Mean grain height (nm)	Mean grain horizontal size (nm)
O_2 1h	2-3	80-85
O_2 8h	5-8	140-160
Ar/H_2 8h	5,5-7	50-65

Table 3.4-3 Dimensions of the CZO buffer grains processed in different atmosphere: O_2 and Ar/H_2.

3.4.5. Study of the Ag addition in the buffer precursor solution

The idea for studying the effect of the silver in the buffer layer solution started from the group previous experience of adding Ag in the YBCO precursor solution, which produces a better compactation of the ceramic and an augmentation of the planarity in the final superconducting layer [27]. Better quality of the buffer leads to a better orientation of the nanocrystals of the superconducting layer and so, a higher critical current density can be achieved.

At the beginning of our investigation, we had problems with the solution life time when a small quantity of silver solution was added in it. Usually, our CZO precursor solution can be used without problems for the deposition during 3-4 weeks. Typically, this solution contains $Ce(C_5H_7O_2)_3$, $Zr(C_5H_7O_2)_4$ as precursor salts and a mixture of isopropanol ($CH_3CHOHCH_3$) and propionic acid (CH_3CH_2COOH) as solvent. When small concentrations of Ag solution (0,3 M CF_3COOAg in MeOH) inferior to 5 % were added in the CZO solution, silver precipitates and the solution cannot be used. After many tests, we stabilized the solution using just propionic acid as solvent.

To analyze the effect of the silver in the buffer matrix, we prepared various samples of undoped CeO_2 and CZO 0,25M with and without Ag. From Figure 3.4–15 a) it can be seen that the roughness increases from 2,23 nm to 3,31 nm in the case of the sample with Ag and also the planarity decreases, which is quite contrary from what we expected. In the CZO samples, with and without Ag, the result is opposite to the one obtained for undoped CeO_2. The roughnesses are smaller in this case and the planarity increases with the addition of Ag and more terraces are formed (Figure 3.4–15 b)). It was already known that Zr in the crystalline structure by substituting 10% of Ce atoms leads to a better atomical mobility and a better crystallization. These results confirm this fact. By decreasing the growth time from 8 hours to 1 hour, although the grains are not so terraced and big, planarities of 74% and small roughness were achieved (rms = 1,47 nm).

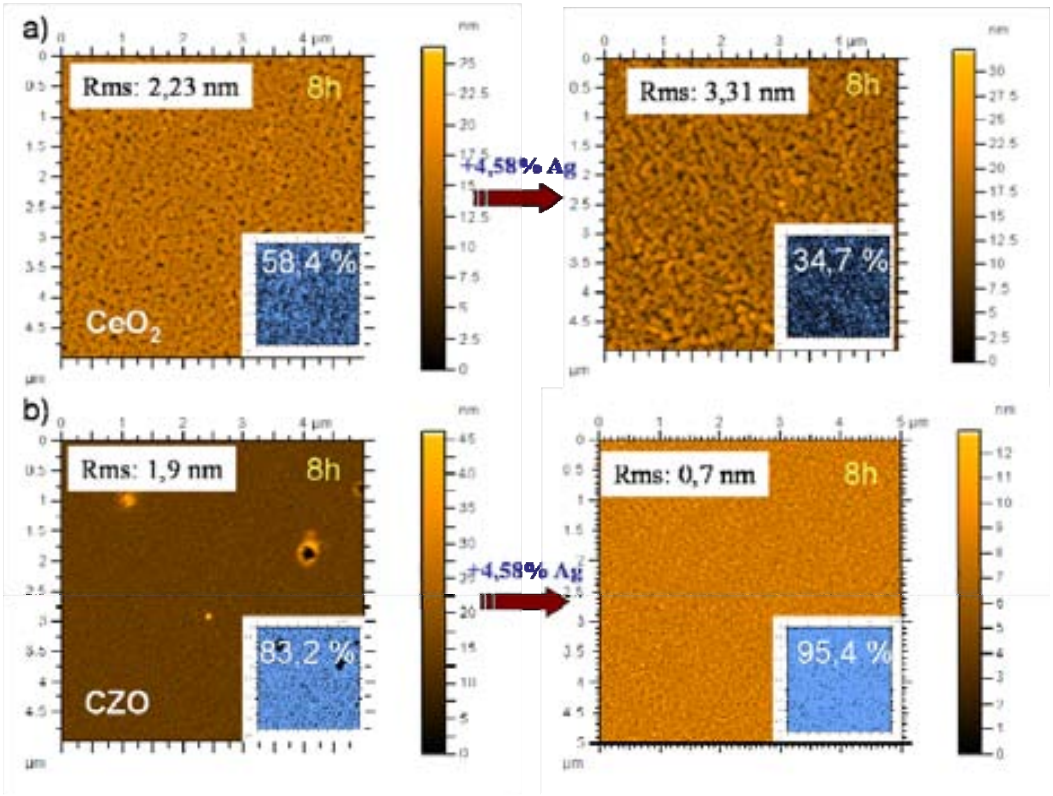

Figure 3.4–15 Illustration of the morphological changes produced by the addition of 4,58% silver in the buffer precursor solution for: a) undoped CeO_2, b) CZO. The films were grown 8 hours at 900ºC in O_2.

In order to see if Ag forms part of the crystalline structure of the buffer, x-ray diffraction patterns were obtained. In principle, the role of silver is not as substituting or interstitial atoms; it is an oxygen transporter who favourite the crystallization due to the high volatility of silver oxide. There is no shifting of the peaks or any secondary phase in the case of the sample doped with Ag, which it means that this element does not form part of the crystalline lattice (Figure 3.4–16).

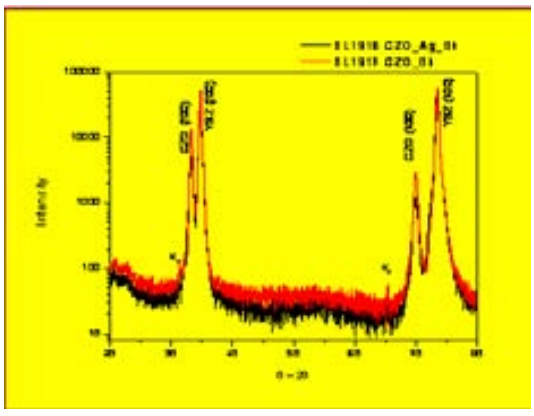

Figure 3.4–16 XRD patterns of two CZO samples, with and without Ag. No shifting of the peaks is observed in the case of silver.

Studies about how the silver affects the CZO polycrystalline structure with 0,4 M for increasing the thickness of the buffer were also done. With bigger thickness, more stress and strains are introduced in the layer. This stress and strains increase until the energy for compensation is high enough to relax the structure by creating dislocations and other defects. Figure 3.4–17 shows the surface morphologies of the 0,4 M CZO samples. When adding Ag, the surface is less rough and the terraces are more defined, although the planarity is poor in both cases (37,2 % for CZO and 49,3 % for CZO+Ag). The intent to calculate the thickness by reflectivity was not successful.

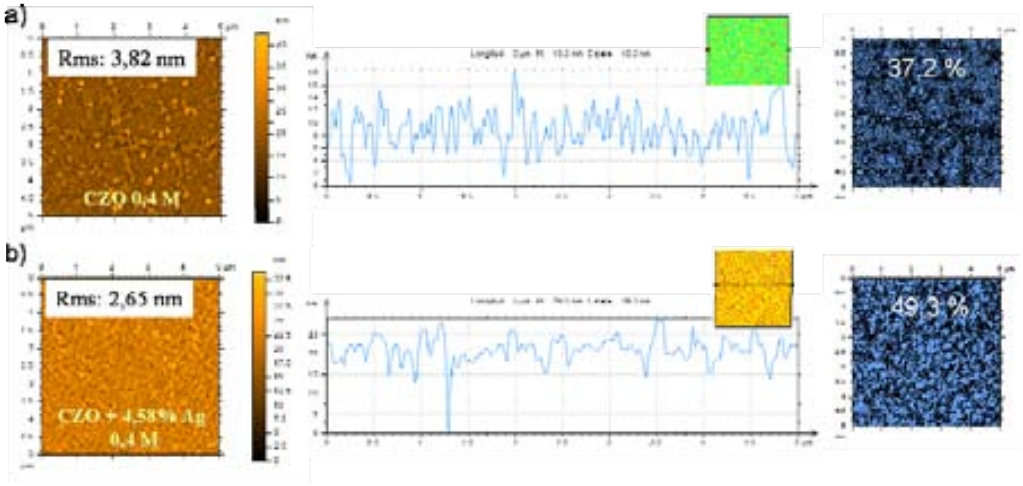

Figure 3.4–17 AFM images of the CZO samples when increasing the concentration from 0,25 mM to 0,4 M; a) CZO/YSZ b) CZO + 4,58 % Ag/YSZ. The planarities are drastically decreased in both cases.

The best point of the addition of Ag in the concentrated CZO buffer precursor solution has been seen when structural characterization by X-ray diffraction and RHEED was done. From the XRD pattern (Figure 3.4–18 a)), misoriented CZO buffer grains are seen by the appearance of (111) and (220) reflections. These reflections disappear when a small quantity of silver is added in the solution. This result is also underlined by the RHEED patterns. Rounded and sharp spots are presented in the sample without Ag, suggesting a rough surface with misoriented grains given by the visible Kikuchi lines (Figure 3.4–18 b)). Elongated spots indicating a flatter surface and elimination of Kikuchi lines are obtained instead in the case of Ag doped CZO (Figure 3.4–18 c)) which indicates that the silver decreases the grain boundaries.

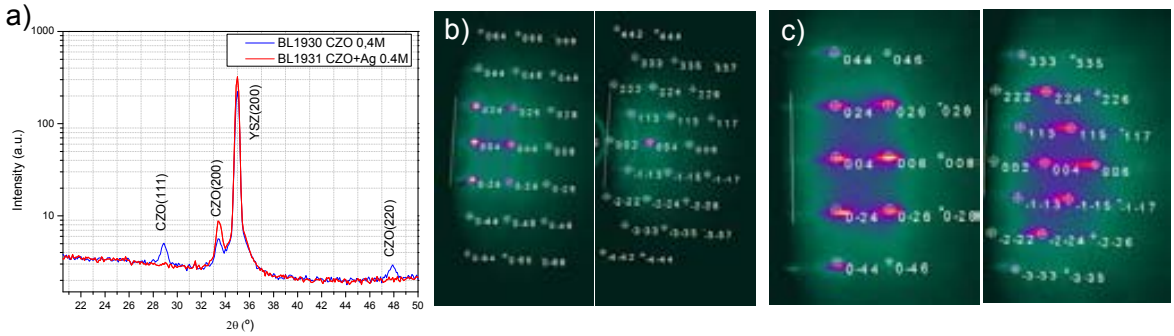

Figure 3.4–18 a) Comparison between the XRD patterns for two 0,4 M CZO/YSZ samples with (red) and without (blue) addition of Ag b) RHEED patterns of CZO 0,4 M with the electron beam directed along <100> and along <110> where rings corresponding to a disorder of the texture are observed; c)RHEED diffraction patterns for CZO+4,58 % Ag buffer layer with 0,4 M concentration.

3.5. Characterization of other architectures with CZO as cap layer

3.5.1. ^{MOD}CZO on ^{PLD}LZO/LAO

For YBCO-coated conductors on cube-textured Ni-based substrates there are many potential buffer layer materials identified, including CeO_2, Y-stabilized ZrO_2 (YSZ), Y_2O_3, $Gd_2Zr_2O_7$ (GZO) and $La_2Zr_2O_7$ (LZO), the latter being the most promising to date [11]. This was the motivation for obtaining YBCO superconducting films on PLD-LZO buffer layers used as model system for the conductor architecture YBCO/CGO/LZO/NiW RABiT. With this purpose, in my NESPA secondment to IFW Dresden, several epitaxial $La_2Zr_2O_7$ (LZO) layers have been grown on 10 x 10 mm LAO substrates. The buffer layers were prepared using Pulse Laser Deposition (PLD) (Figure 3.5–1 b)). Initial deposition of LZO was performed at 755ºC in O_2 using a pressure of 2,4 x 10^{-3} mbar. These conditions leads to a deposition rate roughly of 0,05 nm per pulse and 2000 pulses were used.

LZO has a cubic pyrochlore structure with a lattice parameter a = 10.79 Å (Figure 3.5–1 a)). The matching distance (one-quarter of the face diagonal of face-centered cubic (fcc) lattice cell) is 3.81 Å providing a very small lattice mismatch of 0.5% or 1.8% with the YBCO a- or b-axis (a = 3.83 Å and b = 3.88 Å). However, the lattice mismatch to Ni–5 at.%W (cubic, a = 3.54 Å) is 7.6%, which, although much higher, still allows good epitaxial growth [11].

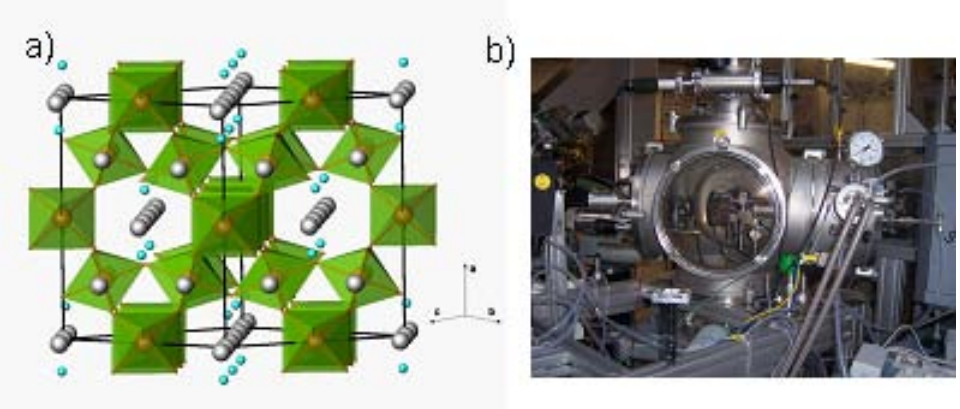

Figure 3.5–1 a) $La_2Zr_2O_7$ structure; b) PLD equipment used for the deposition of LZO buffer layers.

Figure 3.5–2 shows the structure and the texture of a LZO grown film. The four peaks of the pole figure (b) reveal that LZO grows epitaxial on the LAO substrate with a value of $\Delta\Phi$ = 0,97º (b) and $\Delta\omega$ =1,71º (c). A homogeneous and crack free surface structure is observed by means of AFM (Figure 3.5–2 d)).

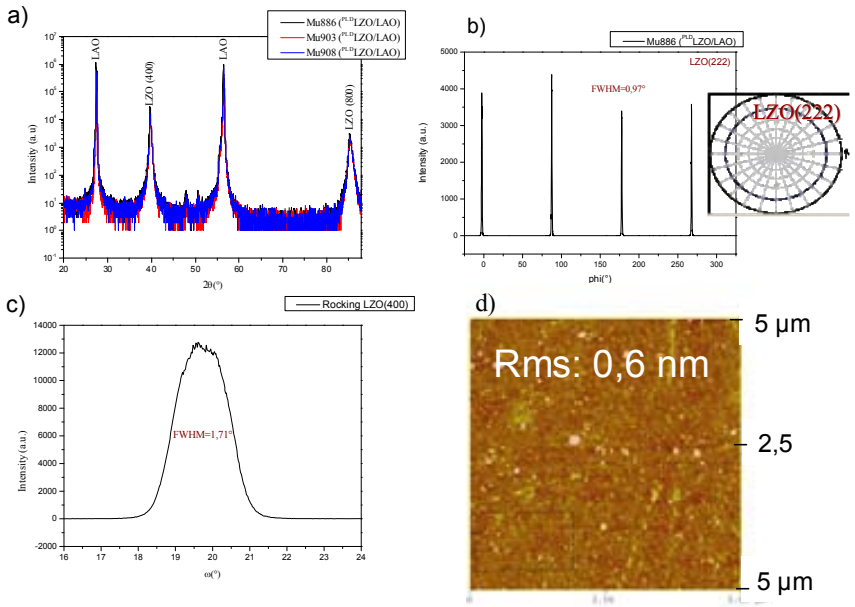

Figure 3.5–2 a) X-ray θ-2θ diffraction pattern for aprox. 100 nm LZO; b) phi-scan and pole figure for LZO(222); c)rocking curve of LZO(400) which shows the misorientation of the grains out of plane; d) AFM image showing the typical surface morphology of LZO buffer layer with small values of roughness (rms = 0,6 nm).

From our experiments, YBCO cannot be grown directly on LZO due to chemical interactions between LZO and YBCO and an additional $Ce_{0,9}Zr_{0,1}O_{2-x}$ (CZO) buffer layer, known for its high chemical and structural compatibility with YBCO, is required [28]. Films of Ce-Zr mixed oxide with thickness about 20-25 nm were deposited starting from a precursor solution having acetyl acetonates salts as starting salts. AFM micrograph of the flat

surface (planarity 81%) with a dense morphology and small roughness (rms = 1,2 nm) is shown in Figure 3.5–3 a) and b). No secondary phases are registered from the XRD pattern and the MOD-CZO epitaxial growth is observed in Figure 3.5–3 c). Therefore, this conductor architecture appears to be promising for TFA-YBCO. The analysis will be reported in Chapter 4, Section 4.2.4.

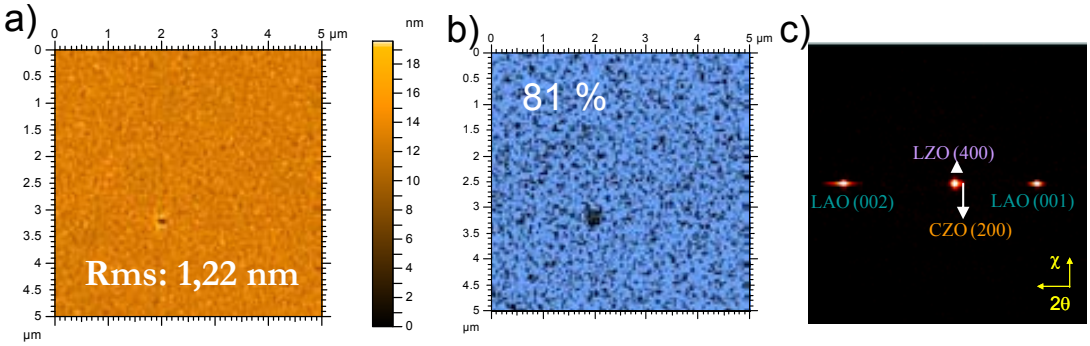

Figure 3.5–3 a) Morphology of MOD-CZO buffer layer grown on PLD-LZO with small roughness (rms =1,2 nm) and homogeneous surface; b) the percentage of flat area of MOD-CZO on PLD-LZO/LAO obtain after binarization of the topographic image; c) 2D pattern measured by GADDS which shows the epitaxial growth of CZO on top of LZO.

3.5.2. ^{MOD}CZO on ^{SPUT}YSZ/Al_2O_3

Between the superconducting film and the substrate there are interactions when annealing is produced at high temperature, resulting in the formation of an interfacial zone where new compounds are formed with structures different from both or a zone with a composition gradient where diffusion or inter-diffusion has taken place without forming new structures (Figure 3.5–4). From the substrates that have been used, the best from point of view of reactivity was YSZ, followed by BaF_2, $SrTiO_3$, MgO, and Al_2O_3 with the highest reactivity [29]. However, sapphire (Al_2O_3) has three main disadvantages: 1) lower thermal expansion coefficient than YBCO (sapphire: $5–7\times10^{-6}$/K; YBCO: ~12- 13×10^{-6}/K); 2) reactivity with YBCO, forming a secondary phase identified as $BaAl_2O_4$; and 3) large lattice mismatch with YBCO. For solving the chemical reaction problem and provide good lattice matching, various materials such as yttrium-stabilized ZrO_2 (YSZ), $SrTiO_3$, and CeO_2 have been employed as buffer layers for YBCO on sapphire. CeO_2 is the most attractive choice because it has good lattice matching with YBCO (-0,5%) [30]. This architecture is new and interesting for the epitaxial deposition of YBCO on R-plane faceted sapphire fibers [31],[32].

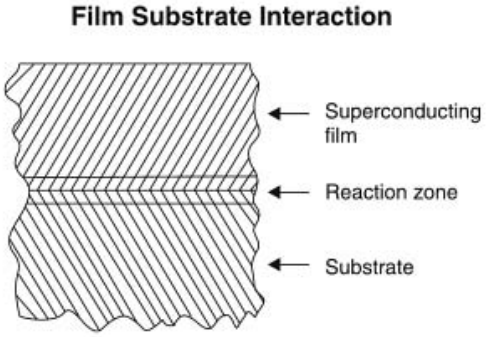

Figure 3.5–4 Schematic of the interaction between $YBa_2Cu_3O_7$ film and the substrate after annealing at 900ºC [29].

Various 10 x 10 mm YSZ on Al_2O_3 substrates were received from Tel-Aviv University, Israel. The buffer was deposited using magnetron sputtering at temperature about 700ºC. Figure 3.5–5 a) shows the surface morphology of as grown ^{SPUT}YSZ. Very flat surface with low roughness (rms = 0,57 nm) and high planarity (98,5 %) was obtained. Spikes of about 5-6 nm characteristic to vacuum deposition process are also observed. The XRD pattern revels sharp spot for the (200) reflection of YSZ which means that this buffer has grown epitaxially on the sapphire substrate (Figure 3.5–5 b)).

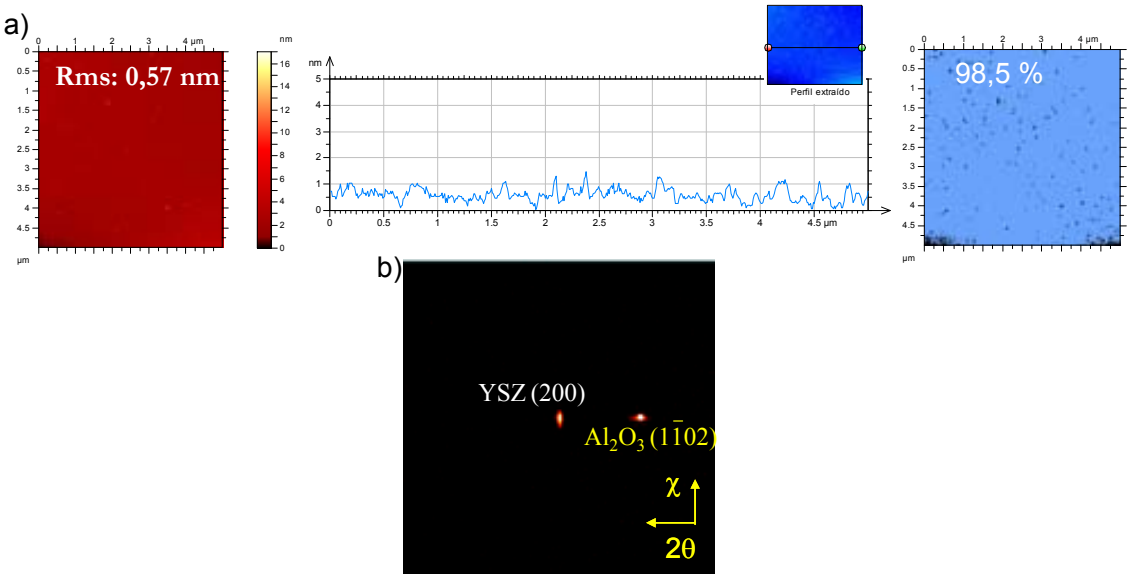

Figure 3.5–5 AFM showing the surface morphology, line profile suggesting a homogeneous growth, and very good planarity of the ^{SPUT}YSZ; B) epitaxial growth of ^{SPUT}YSZ on Al_2O_3 revealed by the 2D XRD pattern.

In order to obtain high J_c's, a decrease of the lattice mismatch between YSZ and YBCO (-5,7 %) was done by the deposition on 5 x 5 mm ^{SPUT}YSZ/Al_2O_3 of a second buffer layer, CZO, using spin coating. The topographic AFM image of the CZO on ^{SPUT}YSZ/Al_2O_3 is presented in Figure 3.5–6 a). The root-mean-square roughness (rms) was measured to be

2,13 nm. Figure 3.5–6 b) shows the XRD scan of the sample. Just (00l) reflections of the both buffers are registered without any other secondary phases.

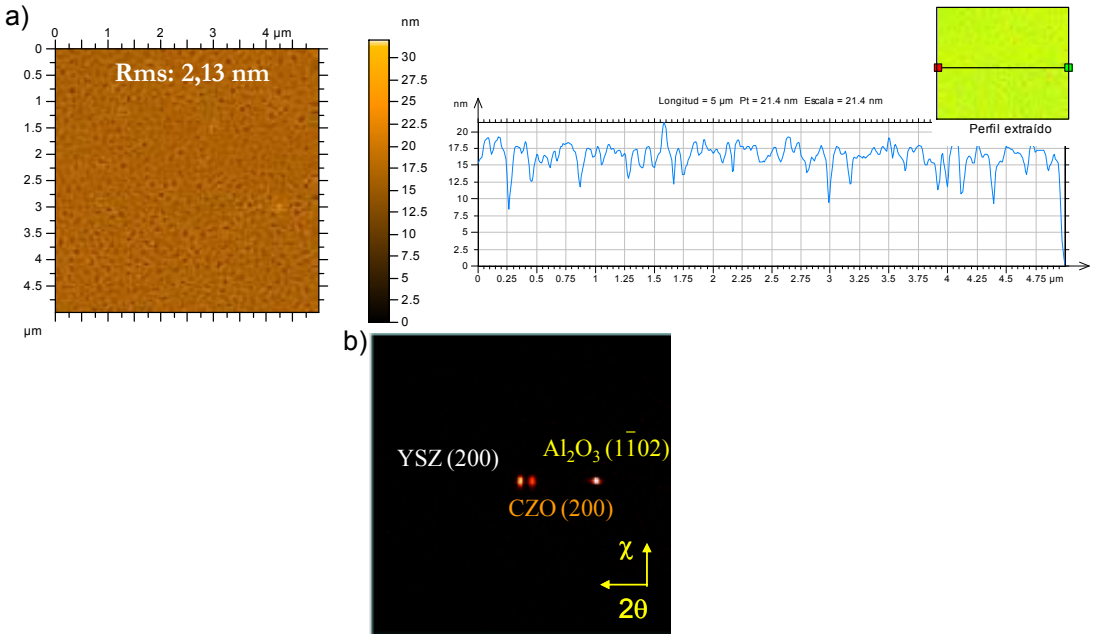

Figure 3.5–6 Topographic AFM image of ^{MOD}CZO/ ^{SPUT}YSZ on Al_2O_3; a line profile is presented to the right of the image; b) 2D XRD pattern of the ^{MOD}CZO/ ^{SPUT}YSZ on Al_2O_3.

3.6. Conclusions

The results presented in this chapter demonstrate that doped CeO_2 grown by chemical solution deposition is a promising buffer layer for the industry of coated conductors. Starting from acetylacetonates salts, a high stability doped CeO_2 precursor solution with time and good wettability (9º) was obtained and deposited onto different substrates (YSZ, ^{PLD}LZO/LAO, ^{SPUT}YSZ/Al_2O_3). Because CeO_2 is hard to attack for thickness measurements, reflectometry at small incident grazing angle was used for this. We have also observed that time, p_{O2}, Ag content and growth temperature conditions could also influence the mobility in 10% Zr-doped CeO_2 films. An open issue is still the influence of the oxygen partial pressure on the GB mobility. Talking about atmosphere, Ar/H_2 usually leads to high mobility of islands [33]. However, GB in Wolmer Weber films needs to be "zipped" and stress or defects there need to be healed. It is suggested that when the percentage of oxygen vacancies is too high (Ar/H_2), the mobility is reduced. Therefore, TEM studies could be welcome! The best combination of temperature-time with high percentage of planarity was found to be 900ºC-8 hours.

By investigating the influence of increasing the precursor solution concentration from 0,25 M to 0,4 M, we have found by XRD and RHEED analysis that films contain random orientations also (111 and 220) not just epitaxial ones. In this case, the addition of small concentration of a Ag solution in the buffer precursor seems to be helpful for obtaining just epitaxial reflection (00l). The values of the relaxation parameters, R~1, calculated from the reciprocal space maps indicates that the buffer CZO is fully relaxed in-plane for Ar/H_2 and out-of-plane for O_2 atmosphere and partially relaxed in the other cases. The lattice parameter a of the Zr doped CeO_2 (a_{CZO} = 5,347 Å) was found to be 0,063 Å lower than the one of the bulk CeO_2 (a_{CeO_2} = 5,41 Å). Higher diffraction angle goes to lower lattice parameter. The reason of this difference could be the difference in structural defects which were created in the growth process with the variation of oxygen content because of the mobility at high temperature and long time annealing.

By AFM, the results confirmed the previous work in the group in which doped CeO_2 film grown under reducing atmosphere is inherently granular with poor planarity (52,6 %) as a result of grain growth inhibition induced by grain-boundary contamination with C impurities. The mobility increases with dopants, Gd^{3+} and Zr^{4+}, although the mechanism is different in the two cases. High flat (90% planarity) surface and small roughness (0,84 nm) were obtained for the CZO when annealing in O_2.

3.7. References

[1] N. Gavrilova, O. Zhilina, and V. Nazarov, "Synthesis of mixed cerium-zirconium oxides by the sol-gel method," Russian Journal of Applied Chemistry **80** (9), 1468-1471 (2007).

[2] J. Xiong, W. Qin, M. Yu et al., "Single cerium zirconate buffer layer on biaxially textured metal substrates for high performance coated conductors," J Mater Sci (2010).

[3] YingXiao Zhang, HongLi Suo, Yue Zhao et al., "Epitaxial Growth of CeO_2 Buffer Layers on Both YSZ Single Crystal and Textured Ni5W Substrates by MOD Method," Materials Science Forum Vols. **546-549**, pp. 2011-2014 (2007).

[4] Kristian Fossheim and Asle Sudbø, *Superconductivity. Physics and Applications*. (John Wiley & Sons, Ltd, 2004).

[5] X. Yongli and S. Donglu, "A review of Coated Conductors Development."

[6] L. Arda and Z.K. Heiba, "Rare-earth mixed oxide thin films as 100% lattice match buffer layers for $YBa_2Cu_3O_{7-x}$ coated conductors," Thin Solid Films **518**, 3345-3350 (2010).

[7] K. Knoth, R. Huhne, S. Oswald et al., "Growth of thick chemical solution derived pyrochlore $La_2Zr_2O_7$ buffer layers for $YBa_2Cu_3O_{7-x}$ coated conductors," Thin Solid Films **516** (8), 2099-2108 (2008).

[8] M. Coll Bau, "Chemical Solution Deposition of Oxide Buffer and Superconducting Layers for $YBa_2Cu_3O_7$ Coated Conductors," PhD Thesis, UAB, Bellaterra (2006).

[9] E. A. El-hefian and A. H. Yahaya, "Rheological study of chitosan and its blends: An overview," Maejo International Journal of Science and Technology **4** (02), 210-220 (2010).

[10] A. R. Marrion, "The Chemistry and Physics of Coatings " The Royal Society of Chemistry (2004).

[11] K. Knoth, R. Hühne, S. Oswald et al., "Detailed investigations on La2Zr2O7 buffer layers for YBCO-coated conductors prepared by chemical solution deposition," Acta Materialia **55** (2), 517-529 (2007).

[12] http://www.attension.com/?id=1092&cid=.

[13] A. Cavallaro, "Optimization of CSD buffer layers for $YBa_2Cu_3O_7$ coated conductor development," PhD Thesis, UAB, Bellaterra (2005).

[14] J. Xiong, B. Tao, W. Qin et al., "Reel-to reel Continuous Deposition of $Ce_xZr_{1-x}O_2$ Single Buffer Layer for YBCO coated conductors," Journal of Physics **Conference Series** (153), 012036 (2009).

[15] Kerstin Knoth, Brigitte Schlobach, Ruben Hühne et al., "$La_2Zr_2O_7$ and Ce-Gd-O buffer layers for YBCO coated conductors using chemical solution deposition," Physica C: Superconductivity **426-431** (Part 2), 979-984 (2005).

[16] J.F. Woitok and A. Kharchenko, "Towards fast reciprocal space mapping," International Centre for Diffraction Data 2005, Advances in X-ray Analysis **48** (2005).

[17] V. F. Solovyov, K. Develos-Bagarinao, and D. Nykypanchuk, "Nanoscale abnormal grain growth in (001) epitaxial ceria," Physical review B **80** (10), 12 (2009).

[18] D. G. Lamas, R. O. Fuentes, I. O. Fabregas et al., "Synchrotron X-ray diffraction study of the tetragonal-cubic phase boundary of nanocrystalline ZrO_2-CeO_2 synthesized by a gel-combustion process," Journal of Applied Crystallography **38** (6), 867-873 (2005).

[19] E. Mamontov, T. Egami, R. Brezny et al., "Lattice Defects and Oxygen Storage Capacity of Nanocrystalline Ceria and Ceria-Zirconia," The Journal of Physical Chemistry B **104** (47), 11110-11116 (2000).

[20] Mogens Mogensen, Nigel M. Sammes, and Geoff A. Tompsett, "Physical, chemical and electrochemical properties of pure and doped ceria," Solid State Ionics **129** (1-4), 63-94 (2000).

[21] J. A. Kilner, "Fast oxygen transport in acceptor doped oxides," Solid State Ionics **129** (1-4), 13-23 (2000).

[22] J. Faber, C. Geoffroy, A. Roux et al., "A Systematic investigation of the dc electrical conductivity of rare-earth doped ceria," Applied Physics A: Materials Science & Processing **49** (3), 225-232 (1989).

[23] M. Coll, J. Gazquez, R. Huhne et al., "All chemical $YBa_2Cu_3O_7$ superconducting multilayers: Critical role of CeO_2 cap layer flatness," Journal of Materials Research **24** (4), 1446-1455 (2009).

[24] M. Coll, A. Pomar, T. Puig et al., "Atomically Flat Surface: The Key Issue for Solution-Derived Epitaxial Multilayers," Applied Physics Express **1** (12) (2008).

[25] M. Coll, J. Gazquez, F. Sandiumenge et al., "Nanostructural control in solution-derived epitaxial Ce1-xGdxO2-y films," Nanotechnology **19** (39) (2008).

[26] J. A. Floro, E. Chason, R. C. Cammarata et al., "Physical origins of intrinsic stresses in Volmer-Weber thin films," MRS Bulletin **27** (1), 19-25 (2002).

[27] F. Martinez, "Uso de sales inorgánicas y nanopartículas en el crecimiento de capas delgadas superconductoras crecidas por CSD," PhD Thesis, UAB, Bellaterra (2011).

[28] J. Gutierrez, A. Llordes, J. Gazquez et al., "Strong isotropic flux pinning in solution-derived $YBa_2Cu_3O_{7-x}$ nanocomposite superconductor films," Nature Materials **6** (5), 367 (2007).

[29] A. K. Saxena, "High-Temperature Superconductors," Springer Series in Materials Science 125 (2010).

[30] K. Develos-Bagarinao and H. Yamasaki, "$YBa_2Cu_3O_{7-delta}$ thin films with enhanced film properties grown on sapphire using Y_2O_3/CeO_2 bi-layer buffer," Thin Solid Films **517** (24), 6539-6545 (2009).

[31] B. Almog, "Superconducting wires and films for application," Barcelona, private communication (2010).

[32] A. Goyal and P. Paranthaman, "Strategic Substrate Development for Coated Conductors," Peer Review 2010, Alexandria, USA (2010).

[33] M. Gibert, P. Abellan, A. Benedetti et al., "Self-Organized $Ce_{1-x}Gd_xO_{2-y}$ Nanowire Networks with Very Fast Coarsening Driven by Attractive Elastic Interactions," Small **6** (23), 2716-2724 (2010).

CHAPTER 4 PREPARATION AND CHARACTERIZATION OF MOD-YBCO MULTILAYERS WITH DOPED CeO_2 AS CAP LAYER

This chapter details the efforts to produce a well textured superconducting YBCO film on the architectures with different buffer layers described in Chapter 3 which have in common that the cap layer is CeO_2. From the technical requirements for Coated Conductors until obtaining good epitaxiallity and high J_c, there is a long way controlled by a detailed morphological and structural characterization by mean of SEM and XRD. This microstructure needs to be closely correlated with that of the cap layer. This will be one of the main objectives of our investigation. In order to study the superconducting properties in more detail, inductive and transport measurements have been carried out to examine current flow in YBCO films deposited on different substrates.

4.1. Technical requirements for $YBa_2Cu_3O_{7-x}$ Coated Conductors

In the recent years, coated conductors (CC) have been developed as a second generation (2G) conductors with a high potentiality for power energy applications [1].

YBCO CCs have some technical requirements that have to be fulfilled to enable their implementation in power applications. One of the most challenging problems is the production of long YBCO CCs, which means the scaling of the production from a short to a longer sample fabrication by a continuous preparation process. This requires significant modification of the equipment and the necessary incorporation of reel-to-reel handling, for all the processing steps: substrate preparation, buffer layers and YBCO film deposition. The achievement of long CCs is a technical problem due to the necessity of a homogeneous heating, gas handling and oxygenation of the long substrate during YBCO deposition to obtain a YBCO CC with constant T_c and J_c values along the tape. In addition to the length problem, there are other tasks in the optimisation of the YBCO CCs that have to be solved: the substrate, which plays a crucial role, has to be flexible, non-magnetic and thin with the necessary mechanical strength to allow the production of cables or coils and, on the other hand, the YBCO film has to be thick enough to improve the current capability of the YBCO CC, i.e. the engineering critical current density which considers the whole thickness of the conductor architecture.

Thermal and electrical stability of coated conductors (CCs) is becoming another important issue and for that reason metallic coatings are also included in the CC architectures. CCs perform well under high magnetic field, mainly since nanostructuration approaches are used [2]. It is also expected to reach a reasonable cost in terms of the metric €/kA-m [3].

Due to the significant anisotropic properties of YBCO superconducting materials, three-dimensional grain alignment of the YBCO layer is required to obtain high performance. The grain boundaries represent a problem which need to be solved in order to have high J_cs. The ability to deposit biaxially textured YBCO films on a substrate is the key ingredient in the development of 2G-YBCO wires. In the early developments, YBCO films were deposited on single crystal dielectric substrates using physical deposition techniques such as laser ablation, sputtering and evaporation. The resulting films were found to be not suitable for some applications such as electric power wires and coils. Research was then shifted towards the depositing of the biaxially textured YBCO films on flexible metallic substrates. The reduction of the number of misaligned grains with high angles which are known to suppress the critical current density in the YBCO is done by using the biaxially textured YBCO films. The initial texture for the epitaxial growth of the 2G-YBCO wires can be formed within the metallic substrate or in one of the initial buffer layers above the metallic substrate. There are three main steps which compose the process of developing 2G-YBCO-coated conductors: (a) the preparation of a suitable substrate, (b) deposition of the buffer layers, and (c) deposition of the YBCO film [4]. Finally, the J_c is anisotropic, a future which introduces many difficulties in the design of the devices and so it needs to be minimized. Although using YBCO prepared by vacuum techniques on MOD-CeO_2 there is lot of work, this chapter concentrates on the YBCO prepared by chemical method on doped MOD-CeO_2 which is less known.

4.1.1. Synthesis of the precursor solution

Trifluoroacetic anhydride (TFAA) has been widely used in organic chemistry as a derivatization agent due to its high reactivity and low boiling point. This route replaces the trifluoroacetic acid with trifluoroacetic anhydride (TFAA) in order to eliminate the water that can be formed in the process.

The preparation process is simple and is presented in Figure 4.1–1. First, the YBCO powder (yttrium barium copper oxide, Solvay) is dissolved in an excess of TFAA (Aldrich 99%) and distilled acetone (Panreac PA) as solvent and a small quantity (10 vol%) of TFAH (Aldrich 99%) is added as catalyst. All the process is done in an inert atmosphere. After this,

the mixture is stirred and heated at 50ºC for 48-72 h. The resulting solution is filtered and evaporated under vacuum. The mixture of TFA salts ($Ba(TFA)_2$, $Cu(TFA)_2$ and $Y(TFA)_3$) is then dissolved in sufficient anhydrous methyl alcohol (Aldrich 99.8%) until reaching a total metal ion concentration of 1.5 M. This solution is kept in sealed vials, in an inert atmosphere. The final solution with viscosity between 2 and 5 mPa*s, is kept for several month in sealed vials. The chemical reaction which occurs is given by Eq. 4.1-1 [5] :

$$YBa_2Cu_3O_7 + 6{,}5\ TFAA \rightarrow Y(TFA)_3 + 2Ba(TFA)_2 + 3Cu(TFA)_2 \qquad \textbf{Eq. 4.1-1}$$

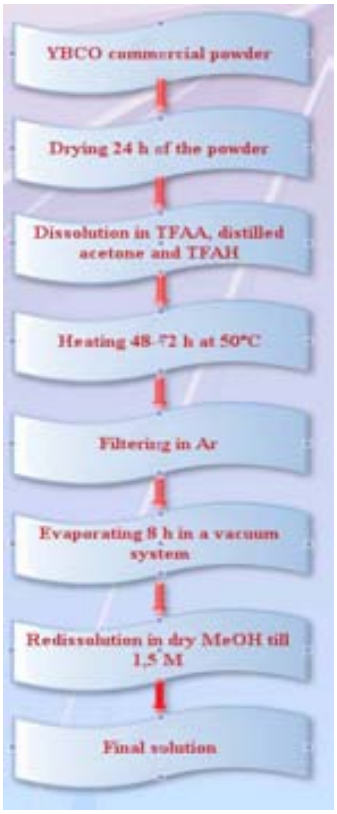

Figure 4.1–1 Synthesis of the $YBa_2Cu_3O_{7-x}$ solution.

4.1.2. Preparation of the substrates

For obtaining high-quality HTS thin films, the choice of the substrate material is of primary importance. The basic requirements for the substrates can be summarized as follows:

- ✓ crystallographic lattice match between HTS film and substrate;
- ✓ similar thermal expansivities of HTS and substrate;
- ✓ no chemical interaction at the interface between HTS and substrate;
- ✓ suitably polished surface, stable and reasonably robust.

Specific requirements are imposed on the substrate depending on the application of the films. For a number of applications twinning of the substrates should be avoided, while the

available size of the substrate or its cost are also of importance. For example, for microwave applications the dielectric properties, surface quality and available size of the substrate are relevant factors. Generally we can distinguish between two classes of substrates: (a) 'compatible' substrates onto which HTS material can be deposited without a buffer layer and (b) 'noncompatible' substrate materials, which have to be covered with an epitaxial buffer layer prior to the deposition of the HTS film owing to large lattice mismatch and/or chemical interaction between substrate and HTS material or owing to missing in-plane orientation (e.g. for deposition of biaxially oriented YBCO on polycrystalline substrates). Deposition onto compatible substrates such as $LaAlO_3$, $SrTiO_3$ and MgO is generally easier [6].

From applications point of view, substrates can be divided in two categories: dielectric and metallic. Some properties of the most used metallic substrates are presented in Table 4.1-1. Mechanical properties, surface quality of substrates such as cleanliness, roughness or grain boundary grooving are very important to achieve highly textured buffer and YBCO growth [7].

Materials	Crystal structure	Lattice constant (nm)	d (nm)	Misfit to YBCO (%)	Curie T (K)	α (10^{-6}/°C)	σ_y (MPa)	m.p. (°C)
$YBa_2Cu_3O_{6.88}$	Orthorhombic.	a=0.3817 b=0.3883 c=1.1633	(a+b)/2 =0.385	0		7.9(11) 16(33)		1150
Ag	cF4	0.4086	0.4086	+6.13	0	18.9-25		961
Cu	cF4	0.3615	0.3615	-6.10	0	17	75	1083
Ni	cF4	0.3524	0.3524	-8.57	627	13-17.4	59*	1455
Ni-7 at.%Cr	cF4				250		64	~1430
Ni-9 at.%Cr	cF4				124		87	~1430
Ni-11 at.%Cr	cF4				20		102	~1430
Ni-13 at.%Cr	cF4				0		157*	~1430
Ni-V	cF4	0.3520	0.3520	-8.57		11		~1425
Ni-Fe	cF4	0.3590	0.3590	-6.75		~12		~1450
Ni-5%W	cF4				334		254*	
Ni-2%Fe-3%W	cF4					12.9	183*	
Inconel 601	cF4						337	1384
Hastelloy	cF4						360	1370

Keys: values at room temperature unless otherwise stated;
*: denotes values at 76 K

Table 4.1-1 Properties of some of the commonly used metallic substrates [7].

In this thesis, a large variety of substrates was used. Starting from single crystals, such as YSZ, LAO, Al_2O_3 up to polycrystalline metallic substrates such as Stainless Steel. Before deposition, the substrate was cleaned in an ultrasonic bath using first acetone and later methanol, starting from the less polar solvent and ending with the more polar one for the elimination of a-polar and ionic substances from the sample surface.

4.1.3. TFA-YBCO processing (pyrolisis, growth and oxygenation)

The deposition of YBCO precursor solution on 5x5 mm^2 substrates was carried out by spin coating using a spinning rate of 6000 r.p.m and an acceleration of 6000 $r.p.m.s^{-1}$.

There are two known approaches for the complete transformation of the as-deposited film into the crystalline ceramic: the *two-step* and the *one-step* processes. In the *two-step* method, used here, the as-deposited film is subjected to separate decomposition of the organic species through pyrolysis prior to crystallization at high temperatures [8].

The pyrolysis is a calcination process at low temperature (320ºC) which allows to entirely eliminate harmful carbon content and so to generate a homogeneous nanocrystalline film (CuO, $(Y,Ba)F_2$,Y_2O_3). The decomposition reaction can be schematized as follows [9],[10]:

$$Cu(TFA)_2 + Ba(TFA)_2 + Y(TFA)_3 \rightarrow CuO + BaF_2 + Y_2O_3 + (CF_3CO)_2 + CO_2 + CO + H_2O \quad \textbf{Eq. 4.1-2}$$

The pyrolysis step was carried out under a wet oxygen atmosphere, in order to avoid any sublimation of $Cu(TFA)_2$ from the film. The pyrolysis is presented schematically in Figure 4.1–2 a). Previous works in the group have allowed to use fast heating ramps while avoiding the formation of any morphological or compositional inhomogeneity in the film which suffers a very strong shrinkage process during this calcination step. The homogeneity of the films after the pyrolysis was verified by polarized optical microscopy, which allows us easily to identify any macroscopic scale degradation of the films [1].

The next step in obtaining superconductor films is the high temperature heat treatment (770ºC-810ºC) used for crystallization of the amorphous intermediate layer into the desired oxide phase which also densifies the films. This crystallization is based on the thermodynamic principles describing the nucleation and growth process and the nucleation must be heterogeneous, i.e. it must ocurr at the interface with the substrate to achieve an epitaxial structure [4,11]. The heat treatment for the YBCO grown on doped cerium oxide (Figure 4.1–2 b)) consist of heating to the annealing temperature at a ramp rate of 25ºC/min, from room temperature up to 810ºC; the process is done in two steps: first nucleation at lower temperature (770ºC) and then the growth itself at high temperature (810ºC). Through oxygenation, $YBa_2Cu_3O_{6.5}$ tetragonal phase is transformed into YBCO orthorhombic superconducting phase. The humid gas flow is initiated at the furnace temperature of 110ºC to avoid water condensation on the film, and water vapour is introduced into the furnace by

bubbling the incoming gas through an attached reservoir of de-ionized water like in the pyrolysis process. The reaction of the growth process is:

$$1-xYF_3 + BaF_2 + Ba_{1-y}Y_xF_{2+x} + 3-yCuO + y/2Cu_2O \xrightarrow{H_2O+O_2} YBa_2Cu_3O_{7-x} + 4HF$$

Eq. 4.1-3

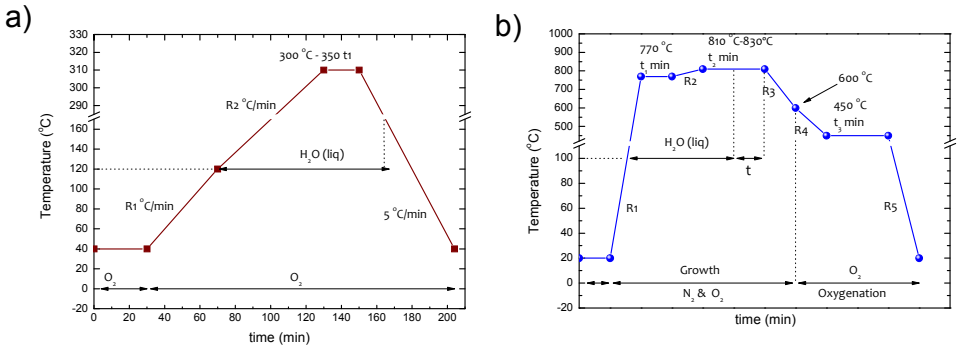

Figure 4.1–2 a) Pyrolysis process when the organic material is burned; b) a typical double step growth process used for obtaining YBCO superconducting films on doped cerium oxide buffer layer.

4.2. Results of the TFA-YBCO deposition on single crystals

4.2.1. ^{TFA}YBCO/^{MOD}CZO/YSZ

High J_c YBCO films were grown on the ^{MOD}CZO buffer annealed in O_2 presented in Figure 3.4-3. This system was used as a model system for IBAD coated conductors on metallic substrates (SS) and YSZ biaxially textured layers. Typical θ-2θ pattern of 275 nm thin ^{TFA}YBCO films on ^{MOD}CZO is shown in Figure 4.2–1 a) and indicates the presence of a c-axis aligned film. Two peaks at 2θ = 28,8º and 2θ = 41,2º, indexed as belonging to $BaCeO_3$ indicates that there is some interaction between the CZO and YBCO due to the high temperature processing. Detailed pole figure analysis indicated the presence of a diagonal-on-cube texture for YBCO and YSZ (Figure 4.2–1 c)). Both of the XRD measurements indicate the presence of a strong c-axis (00l) aligned YBCO films.

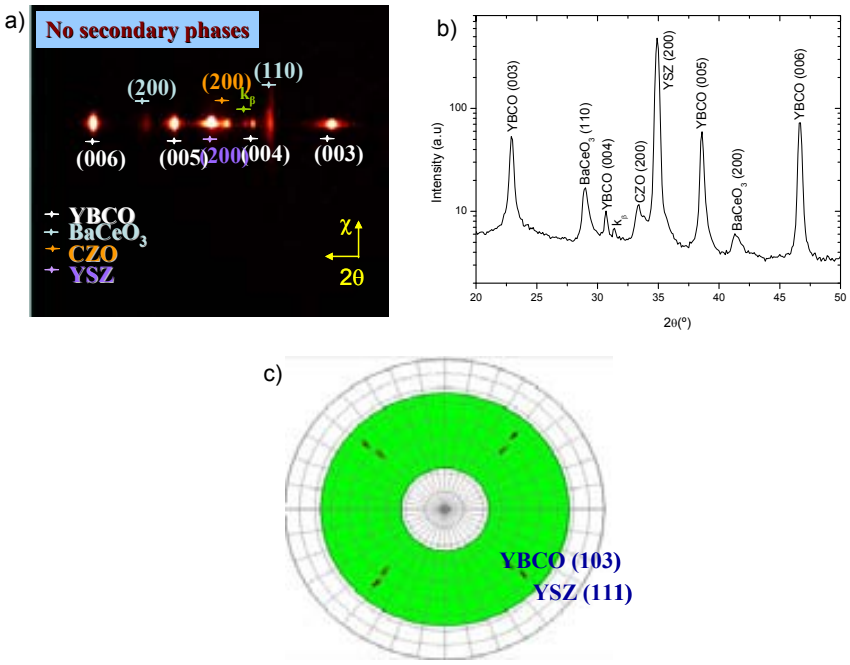

Figure 4.2–1 a) θ-2θ scan for a ^{TFA}YBCO/^{MOD}CZO/YSZ sample; b) integration in χ of the previous frame; c) X-ray pole figure of YBCO(103). High epitaxiallity and good texture is observed.

The rocking curve permits to determine the misorientation of the grains out-of-plane. For a given position of 2θ and a fixed χ, we measured the diffracted intensity as a function of ω. The angle ω between the x-ray source and the sample varies and the movements of the detector permits to observe the texture of the sample out-of-plane. Figure 4.2–2 (right) represents the ω scan distribution for a sample ^{TFA}YBCO/^{MOD}CZO/YSZ compared with the one of an ideal film (left). The value of the misorientation out-of-plane calculated from the full with at half maximum (FWHM) is found to be 0,63º. The out-of-plane misorientation of YBCO/LAO system was found to be 0,4º [1].

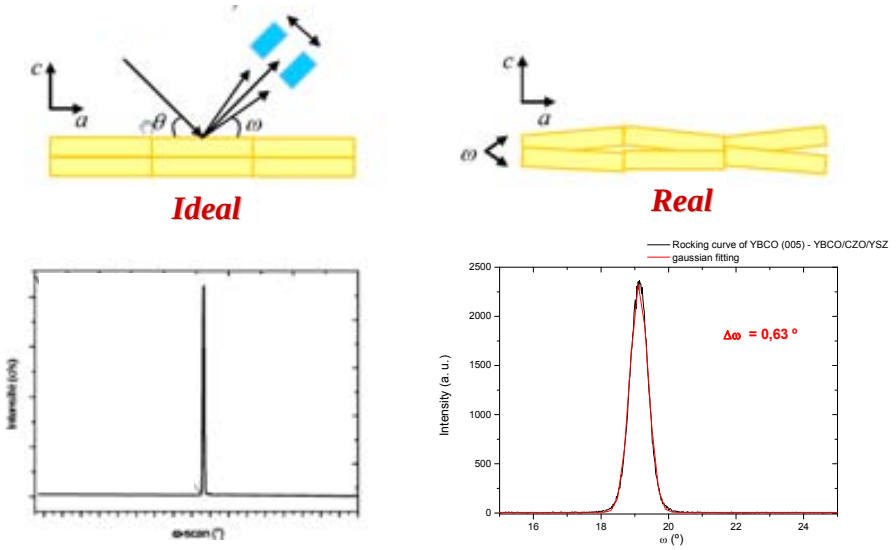

Figure 4.2–2 Rocking curve of the (005) reflection of YBCO (Δω = 0,63º) showing the misorientation out-of-plane (right); the representation of the rocking peak in the case of an ideal sample is presented for comparing (left).

Figure 4.2–3 shows the SEM planar morphology for ^{TFA}YBCO on ^{MOD}CZO/YSZ. The surface morphology is relatively smooth, but pores and precipitates are visible. No a/b grains are observed.

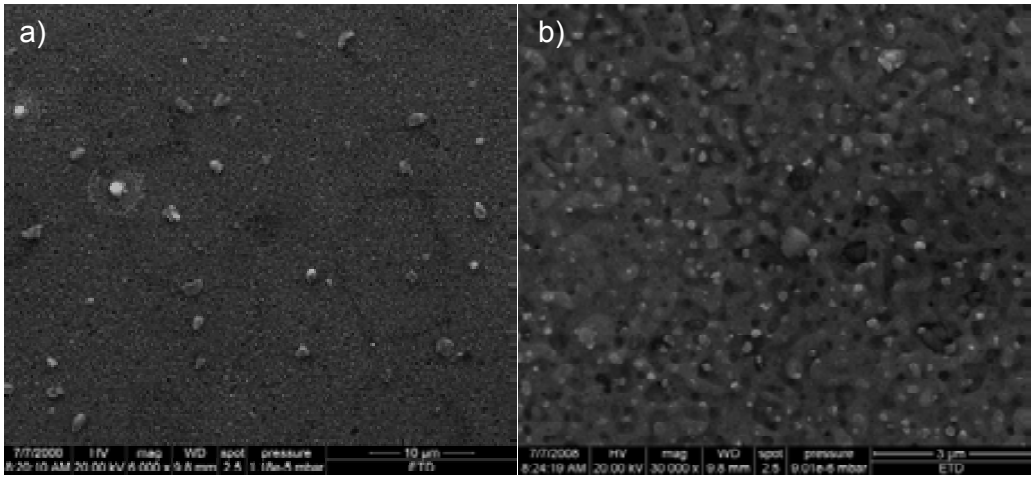

Figure 4.2–3 SEM planar morphology of ^{TFA}YBCO/^{MOD}CZO/YSZ of different magnifications: a) 6000 x; b) 30000 x. No a/b grains are observed on the surface of YBCO.

Superconducting properties of YBCO films were characterized by measuring J_c and T_c. A transport J_c of 5,2 MA/cm^2 was obtained for a 275 nm thick YBCO film on YSZ buffered ^{MOD}CZO at 77 K and zero-external field (Figure 4.2–4 a)). Figure 4.2–4 b) shows the magnetic field dependence of J_c at 77K for a YBCO/^{MOD}CZO/YSZ film, compared with a standard one (YBCO/LAO). It was demonstrated that in MOD films, J_c(H) at 77k is controlled by the interplay between the isotropic and anisotropic pinning contributions. At

low fields H < 1T, isotropic contribution dominates. At high fields, it is the anisotropic contribution which controls the pinning and a peak when H//c in the J_c vs. θ dependence is observed [12].

To parametrize the field dependence of J_c for H//c, the following equation was used [13]:

$$J_c(B) = J_c(0)\left[1+\frac{B}{B_0}\right]^{-\alpha}\left[1-\frac{B}{B_{irr}}\right]^2 \qquad \textbf{Eq. 4.2-1}$$

In this equation, the field B_0 sets the scale for transition from the low-field "J_c-plateau" to the power-law regime where $J_c \sim B^{-\alpha}$. For a physical interpretation, B_0 might be regarded as the field above which intervortex interactions compete with vortex pinning to suppress the critical current, while fields below B_0 characterize the individual vortex pinning regime with J_c relatively field independent [13].

With this in mind, we see in our results that, at 77K, the critical current density dependence with the magnetic field J_c (H//c) of both samples is strongly mediated by the anisotropic defect pinning contribution. As it can be seen in the graph, there are three different regions: one between 0T and 0,02T where a plateau is seen from which the values for J_c at self field can be extracted (4,5 MA/cm^2 for the standard vs. 5,2 MA/cm^2 for YBCO/^{MOD}CZO/YSZ); another one between 0,02T and 1T, when the magnetic field B_0 of the buffered sample increases, being double as compared to the standard film. This increase is probably due to an enhanced concentration of defects in the YBCO/CZO buffered film and, on this way, the single vortex pinning region increases. From the two plots we observed that, at low fields B < 1T, the J_c is strongly dominated by the isotropic pinning contribution. In the last region, beyond 2T, the J_c starts to decay fast, due to the proximity of H_{irr}. So, this confirms one more time, the hypothesis already known [12,14] of the strong influence of the isotropic defect pinning centers in controlling the high J_c at self field (5,2 MA/cm^2) in MOD-TFA CZO buffered YBCO thin films.

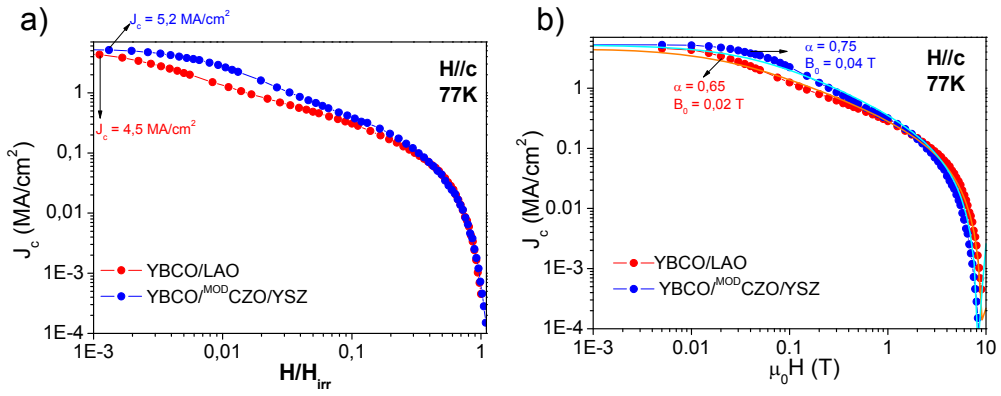

Figure 4.2–4 a)The J_c dependence of H/H_{irr} for a standard sample, YBCO/LAO, and a YBCO on ^{MOD}CZO/YSZ film; b) J_c magnetic field dependence for a standard and a CZO buffered sample from where values of the exponent α after fitting with the Eq. 4.2-1 is done.

For comparison, Figure 4.2–5 shows the T_c transition curve of YBCO films grown directly on LAO compared with the one for the ^{MOD}CZO buffered film. The measurements were performed both with the SQUID (Figure 4.2–5 a)) and PPMS (Figure 4.2–5 b)). The value of the $T_{c\ onset}$ is the same, 91,2 K, for the two samples. The standard film has a narrow transition width (ΔT_c = 5,45 K) more than double of the transition for the YBCO/^{MOD}CZO/YSZ (ΔT_c = 2,22 K) as shown in Figure 4.2–5 c). This could be because of the inhomogenities of the standard film.

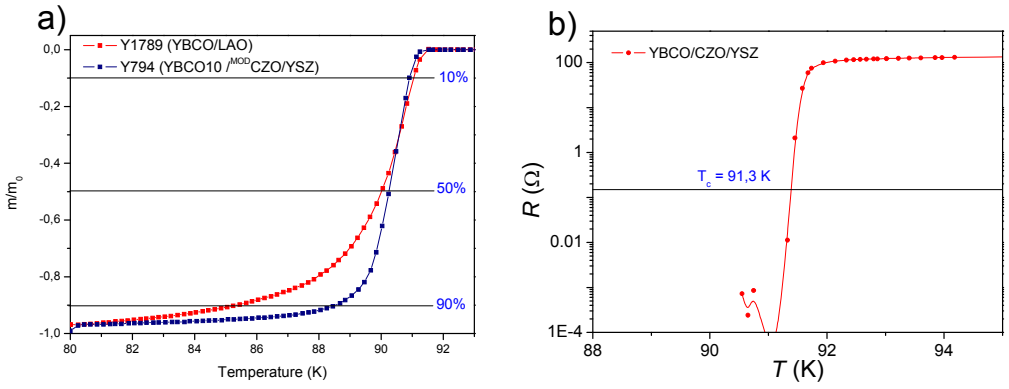

c)

Sample	T_c 10%	T_c 50%	T_c 90%	$T_{c\ onset}$	ΔT_c
^{TFA}YBCO/^{MOD}CZO/YSZ	90.9	90.3	88.68	91.2	2.22
YBCO/LAO	90.9	90.05	85.45	91.2	5.45

Figure 4.2–5 a)Temperature dependence of magnetic susceptibility measured at H = 2 Oe with SQUID for a standard sample (YBCO/LAO) and a YBCO film on ^{MOD}CZO/YSZ; b) Resistive measurement of T_c for the buffered film where a 0,01 mA current was used for the measurement; c) values of the temperature dependence of magnetic susceptibilities and transition width for the two samples.

4.2.2. ^{TFA}YBCO/Ag-^{MOD}CZO/YSZ

An YBCO layer deposited by MOD onto the Ag-CZO/YSZ buffer layers described in Chapter 3 (Section 3.4.5) with smooth and flat surface (95%) has also been characterized. The Ag content was 4,58% wt. The morphological characterization presented in Figure 4.2–6 shows that there is no important difference when a small quantity of silver is added in the CZO. Both YBCO films have a c-axis oriented growth with no a/b grains.

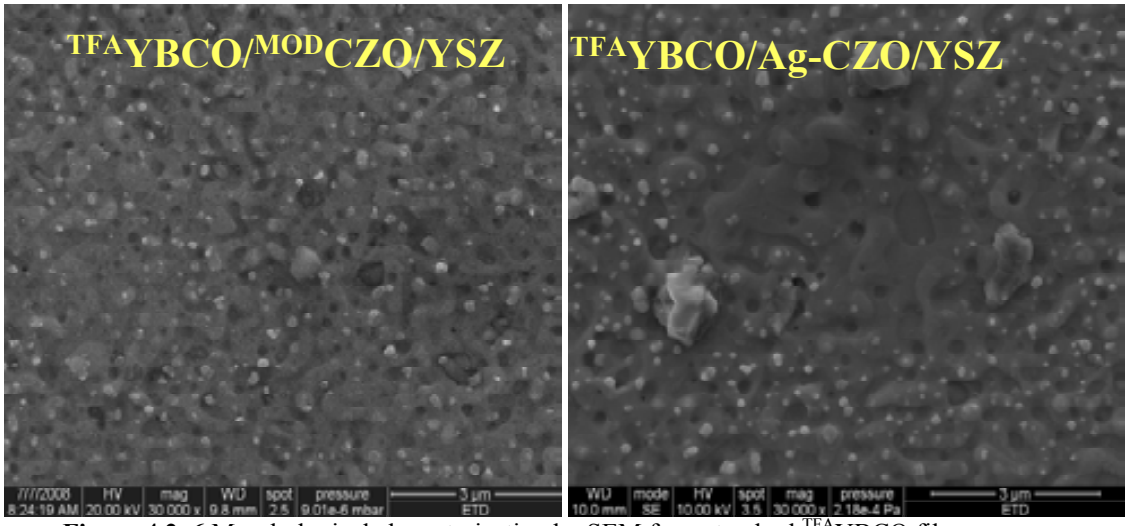

Figure 4.2–6 Morphological characterization by SEM for a standard ^{TFA}YBCO film grown on ^{MOD}CZO/YSZ (left) and also on the Ag doped CZO (right).

The XRD pattern of the YBCO sample on Ag-CZO shows that an epitaxial growth of the superconducting layer (250 nm) has been achieved (Figure 4.2–7 b)). No secondary phases associated to silver are observed. However, if we pay attention to this plot, we can see that a small amount of BYF (101) is present, which means that the YBCO is not totally converted. This fact could explain that a lower J_c is obtained.

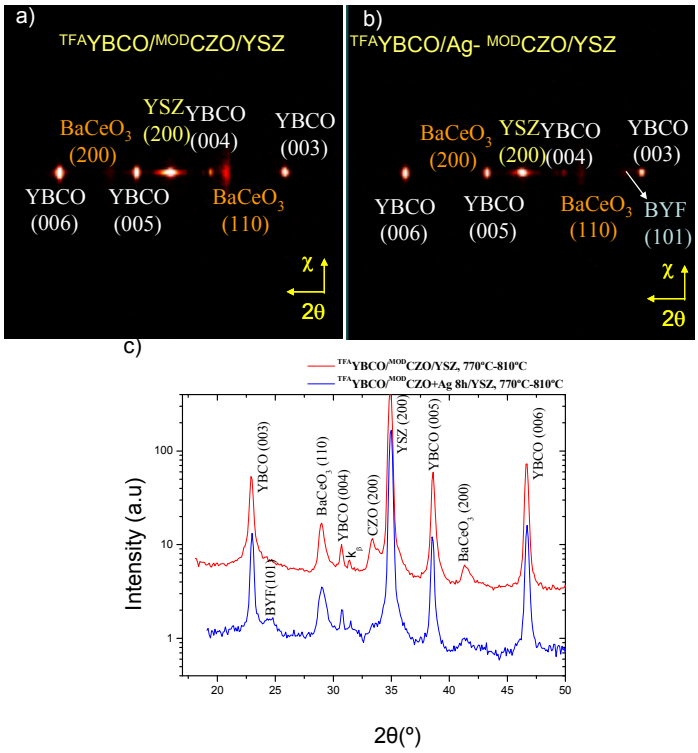

Figure 4.2–7 Comparison between XRDs for a) ^{TFA}YBCO/^{MOD}CZO/YSZ and b) ^{TFA}YBCO/Ag- ^{MOD}CZO/YSZ; c) integration in chi of the two previous frames.

Figure 4.2–8 a) shows a J_c comparison between the two films. When H//c, it can be noted that the J_c of the ^{TFA}YBCO/Ag- ^{MOD}CZO/YSZ is lower than the one of the film without silver (1,3 MA/cm^2 vs. 4,1 MA/cm^2). The planarity of the buffer cannot be the reason for this decrease because it had high values (88% Ag-YBCO and 90% YBCO) for both of the films. From this plot it can be roughly estimated also the values for the T_cs of the two films; a drop of T_c from 91,2K (^{TFA}YBCO/^{MOD}CZO/YSZ) to 86K (^{TFA}YBCO/Ag- ^{MOD}CZO/YSZ) has been registered (Figure 4.2–8 b)).

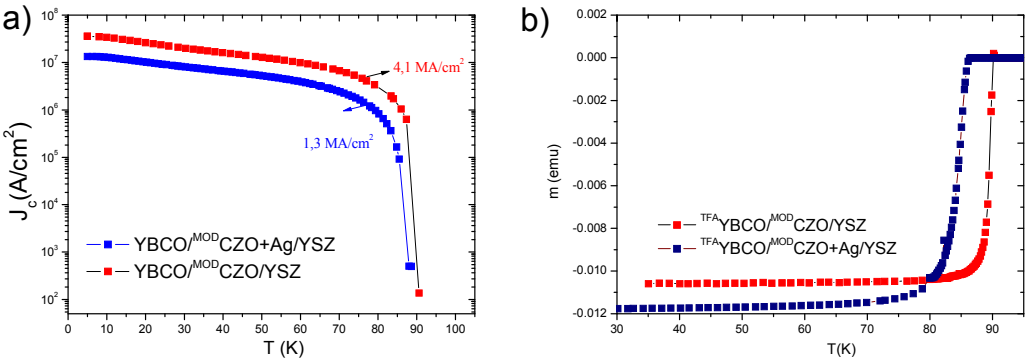

Figure 4.2–8 a) J_cs of two films: ^{TFA}YBCO/ ^{MOD}CZO+Ag/YSZ (blue) versus ^{TFA}YBCO/^{MOD}CZO/YSZ (red); b) temperature dependence of magnetic susceptibilities of the two films.

4.2.3. Ag-YBCO/^{MOD}CZO/YSZ

Large-scale power applications of HTSs need kilometres of polycrystalline conductors. Grain boundaries (GBs) are a problem for the progress of this issue because it is well known that these are associated with the strongly suppression of the transport critical current. Cheng et al. [15] studied the effect of different dopant elements in YBCO (Ca, Fe, Ag, etc.) in melt-textured polycrystalline samples showing that like Ca, which segregates in the GBs of YBCO, Ag also segregates in GBs, although it is usually believed that Ag doesn't occupy the lattice in YBCO single crystal. The explanation proposed is that a part of Cu could be replaced by Ag to reduce geometric distortion of Cu-O bonds, which results in a thinner effective GB and a higher $J_{c,GB}$ [16]. Pan et al. [17] and Li et al. [18] also showed the enhancement of J_c at low field of YBCO-Ag films prepared by PLD. Contrary to this, in thin films the mechanism when adding Ag is different because the c-axis nucleation of YBCO is enhanced in this case due to the decrease of the Ag-YBCO system peritectic temperature and also the growth can be done at lower temperatures [19]. Taking into account these results and also the ones obtained in the group by F. Martinez [20] in which more compact, less porous and with higher J_c were prepared using small addition of silver in the YBCO solution, various samples of 5%Ag-YBCO/^{MOD}CZO/YSZ have been grown by MOD at high (810ºC) and low temperatures (740ºC).

If we take a look to the surface of the silver doped samples, we note the particularity of this one. A very compact surface is seen when the growth is done at high temperature (770ºC-810ºC) with very low porosity and large terraces of about 1 μm (Figure 4.2–9 b)). Bigger grains forming terraces can be the result of decreasing the GBs number and size and the better alignment of the YBCO crystals due to the presence of silver. This phenomenon was observed also by Selvam et al. [16] using PLD. The Ag-YBCO film grown at low temperature (740ºC, Figure 4.2–9 c)) has similar look as the standard one (Figure 4.2–9 a)) with higher porosity and some big precipitates on the surface.

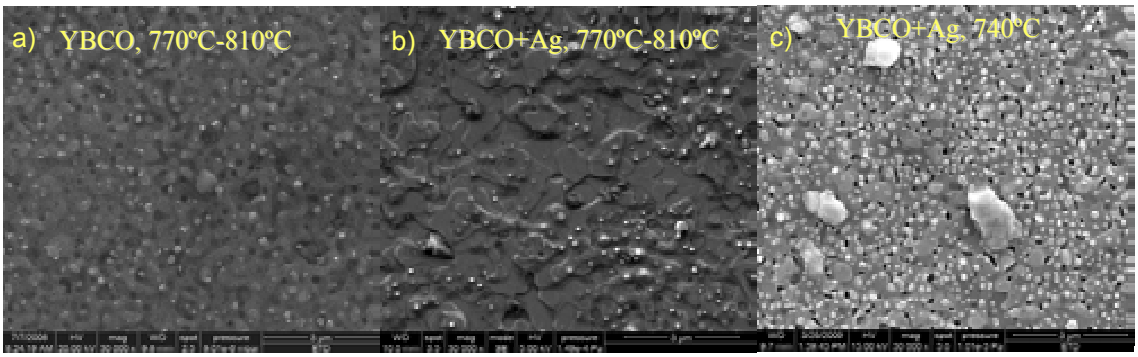

Figure 4.2–9 SEM micrografies of a standard ^{TFA}YBCO/^{MOD}CZO/YSZ (a) and two Ag-doped YBCO grown at high (b) and low temperature (c). All the samples have as buffer ^{MOD}CZO.

All the XRD results revealed that the out-of-plane orientation of the Y123 films in all samples is strong, with only the (00l) reflections being present. Typical XRD patterns of the Ag-YBCO films grown at high (770ºC-810ºC) and low temperature (740ºC) are shown in Figure 4.2–10. Therefore, it seems that there is no difference in the orientation of the samples. After checking the full width at half maximum (FWHM) for the (005) reflection peak for different samples, it was found that the values of the FWHM are the same (0,9º) for high and low temperatures, contrary to what was discover in the group previously (bigger value for 740ºC) [20]. Also, no secondary phases containing silver are observed because silver does not enter in the crystalline structure of YBCO; it is just an oxygen transporter.

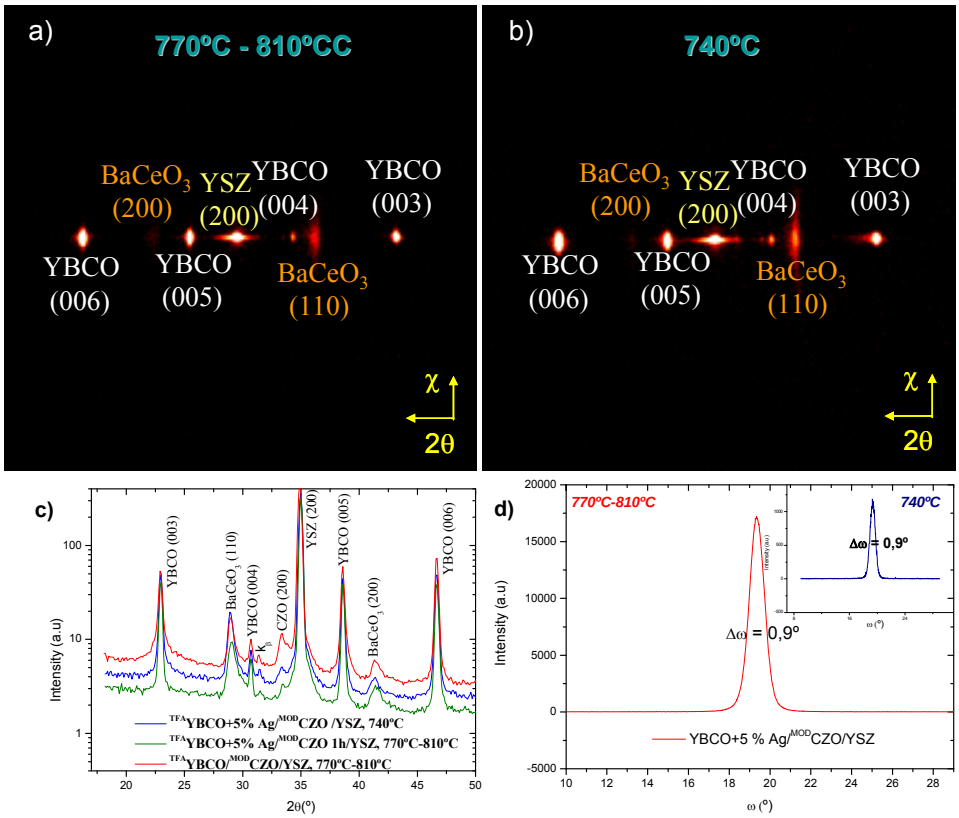

Figure 4.2–10 2D XRD pattern of 5%Ag-^{TFA}YBCO/^{MOD}CZO/YSZ grown at 740ºC (b) compared with one grown at 770ºC-810ºC; c) integration of the previous frames compared with a YBCO standard sample on ^{MOD}CZO/YSZ; d) misorientations out-of-plane of the two Ag doped YBCO films annealed at high temperature and at low temperature (inset); c-axis orientation is registered in all cases.

For testing the superconducting capabilities of the samples, magnetic hysteresis loops measured at different temperatures were performed with the SQUID. A relevant characteristic of the J_cs for the Ag-YBCO films was that at 77K and self field, the values are almost the same, independent of the growth temperature (around 2 MA/cm^2). However, these J_cs are lower than the J_c obtained for a standard ^{TFA}YBCO/^{MOD}CZO/YSZ (4,1 MA/cm^2).

Figure 4.2–11 a) shows this dependence. As a conclusion, we can say that we can grow samples with silver addition at low temperature and this does not decrease the J_c if we compare with the Ag-YBCO films grown at 770ºC-810ºC. Still a decrease is observed if they are compared with a ^{TFA}YBCO/^{MOD}CZO/YSZ sample, contrary to what was noted in the group on standard samples (YBCO/LAO) [20]. If we compared the samples grown on the CZO cap layer presented in Chapter 3 (Section 3.4.4) when different grain size was observed depending of the growth time (1h and 8 h), we does not note an important difference in the superconducting properties, both of them having the same J_c (around 1,9 MA/cm^2). The T_c onset defined at the onset of the diamagnetism is varied from 90,2K in the case of the

standard YBCO sample and 89,5K for the Ag doped YBCO grown at low temperature (Figure 4.2–11 b)). This fact supports that no Ag incorporation in the YBCO matrix appears, as it has been suggested previously through EDX measurements, suggesting that Ag is sublimated [20].

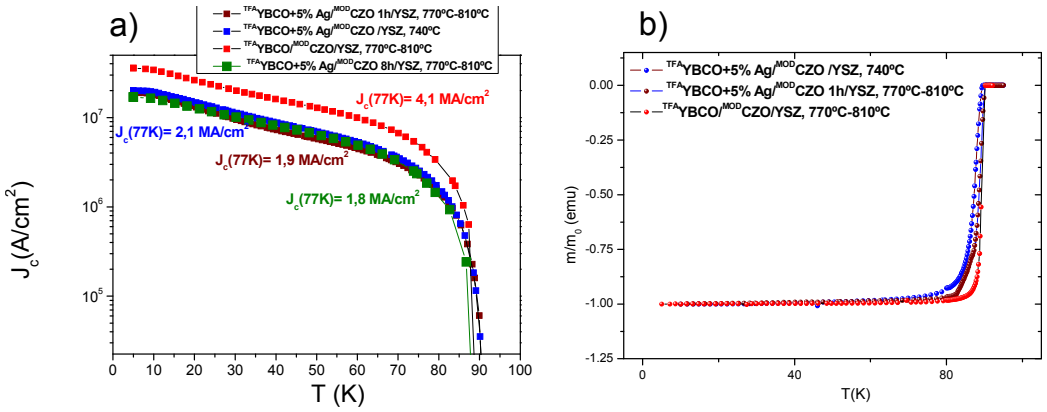

c)

Sample	T_c 10% (K)	T_c 50% (K)	T_c 90% (K)	$T_{c\,onset}$ (K)	ΔT_c (K)
Y1679=^{TFA}YBCO+5% Ag/^{MOD}CZO 1h/YSZ **770ºC - 810ºC**	**89.6**	**88.4**	**84**	**90.2**	**5.6**
Y1324=^{TFA}YBCO+5% Ag/^{MOD}CZO/YSZ **740ºC**	**88.7**	**87.6**	**82.7**	**89.5**	**6**
Y794=^{TFA}YBCO/^{MOD}CZO/YSZ **770ºC - 810ºC**	**90**	**89.2**	**87.9**	**90.2**	**2.1**

Figure 4.2–11 a) J_c dependence of the temperature for three different samples: ^{TFA}YBCO/^{MOD}CZO/YSZ, 770ºC-810ºC (red); ^{TFA}YBCO+5% Ag/^{MOD}CZO 1h/YSZ, 770ºC-810ºC (wine); ^{TFA}YBCO+5% Ag/^{MOD}CZO /YSZ, 740ºC (blue); b) temperature dependence of magnetic susceptibility for the Ag doped YBCO samples compared with the one for a standard sample (H = 2Oe); c) values of the T_c and transition widths.

As it can be seen in Figure 4.2–12, the J_c magnetic field dependence at 77K is different in every case. At low magnetic fields, there seems to be a slightly enhancement of the J_c in the case of the Ag doped YBCO samples if we compare with the standard film. On the other hand, the Ag-YBCO sample grown at high temperature presents a stronger dependence of J_c with the magnetic field than that grown at low temperature. The crossover point between the doped samples and the standard are different (lower magnetic field in the case of the doped sample grown at 740ºC). We can think that the irreversibility line decreases but the values of T_cs are quite similar as we saw before. This behaviour should be related to a modified defect structure in the sample grown at low temperature, but in order to correlate this with the pinning behaviour, a detailed TEM analysis would be required.

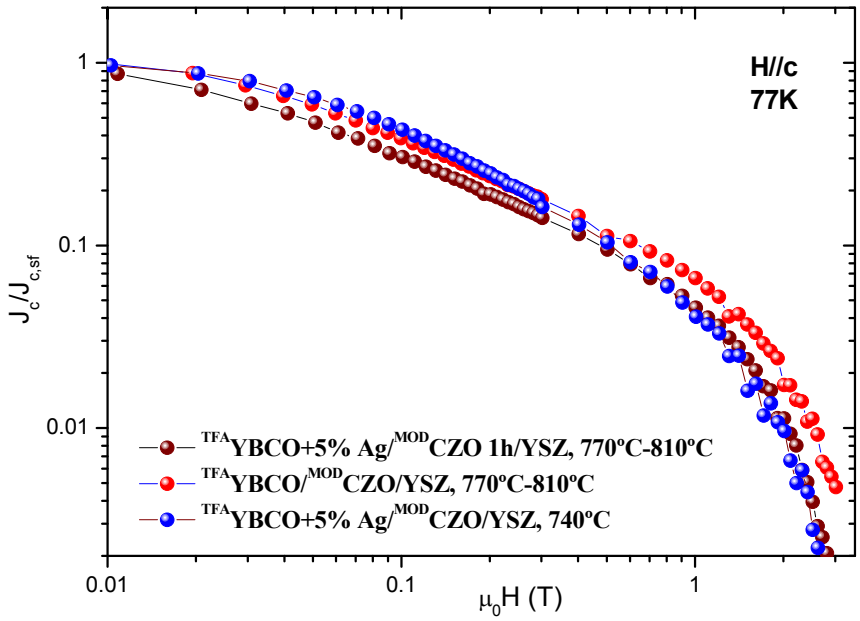

Figure 4.2–12 $J_c(H)$ curve for a standard YBCO sample on ^{MOD}CZO/YSZ compared with the ones for the Ag-YBCO grown at different temperatures.

4.2.4. ^{TFA}YBCO/^{MOD}CZO/^{PLD}LZO/LAO

For studying the capability of $La_2Zr_2O_7$ (LZO) buffer layers as a part of a RABiT coated conductor architecture, we have undertaken a study of YBCO film growth from TFA precursors on top of LZO buffer layers grown by PLD on single crystalline substrates. The growth of these buffer layers was carried out at IFW Dresden. After a growth at 780ºC, a severe reaction between YBCO and LZO was observed forming BZO at the interface (Figure 4.2–13 a)) and no J_c could be measured with a SQUID magnetometer. The polycrystalline fraction of YBCO represented by the reflexion (103) is weak. Figure 4.2–13 b) shows the SEM image where many inhomogenities can be observed at the surface. Although the growth process was changed (a double step was implemented), still no finite critical currents could be measured.

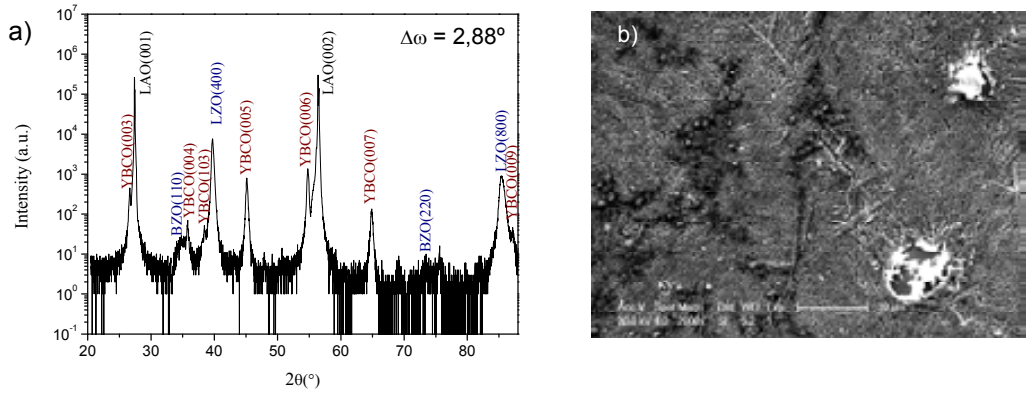

Figure 4.2–13 a) θ-2θ diffraction pattern where the reactivity between LZO and YBCO is seen; b) SEM top view of the inhomogenities found on the superconducting film surface.

From our observations, YBCO cannot be grown based on TFA precursors directly on the surface of LZO without forming $BaZrO_3$ which poisons tremendously the superconducting properties of the samples. In this case, an additional $Ce_{0,9}Zr_{0,1}O_{2-x}$ (CZO) buffer layer, known for its high chemical and structural compatibility with YBCO, is required to avoid the severe chemical reaction between LZO and YBCO [21]. The characterization of the CZO buffer was presented in Chapter 3 and the results showed a small roughness (1,2 nm) and high planarity (81%)(Section 3.5.1).

YBCO superconducting films were grown on the previous CZO buffer layers and the best value of J_c measured by SQUID was 2,3 MA/cm^2 at 77K. Because the growth was done at high temperature (810ºC) a mixture of $BaCeO_3$ and $BaZrO_3$ is observed in the XRD pattern, while the ΔΦ of the (103) YBCO reflection was found to be 1,5º (Figure 4.2–14 c)). No decrease of the reaction at the interface was observed when changing the nucleation temperature Figure 4.2–14 b). The diagonal on cube texture of YBCO and CZO is shown in the pole figure (Figure 4.2–14 d)). In order to reduce the reactivity we have tried to vary the nucleation temperature, from 770ºC to 740ºC. In this case, it was noted that the J_c at 77K decreases from 2,3 MA/cm^2 to 0,92 MA/cm^2 (Figure 4.2–14 e)).

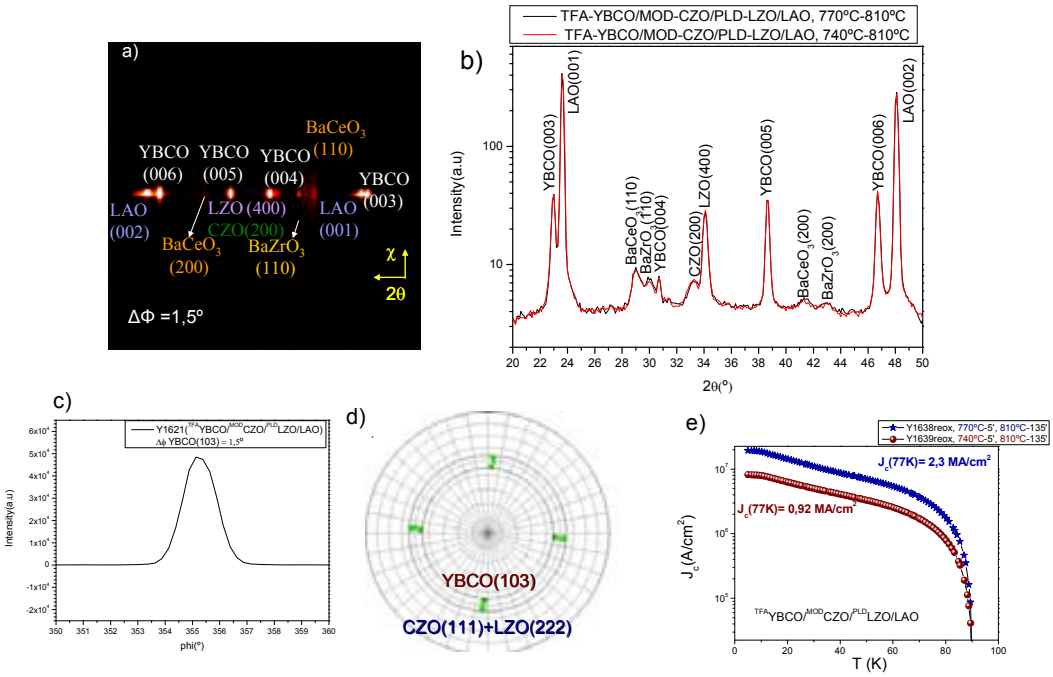

Figure 4.2–14 a) θ-2θ for TFA-YBCO/MOD-CZO/PLD-LZO/LAO; b) integration in chi of the two samples with different nucleation temperature (740ºC and 770ºC); c) rocking curve of YBCO(103); d) pole figure of epitaxial YBCO grown on top of MOD-CZO/PLD-LZO/LAO; e) J_c comparison between 2 YBCO films nucleated at different temperatures: 740ºC and 770ºC.

The typical surface topography measured by SEM is shown in Figure 4.2–15 when vary the nucleation temperature from 770ºC (a) to 740ºC (b). No difference in morphology is observed for the two samples: both films are compact with less porosity than the standard film grown on ^{MOD}CZO, but many precipitates are seen at the surface which have different composition from the YBCO matrix (Figure 4.2–15 c) and d)).

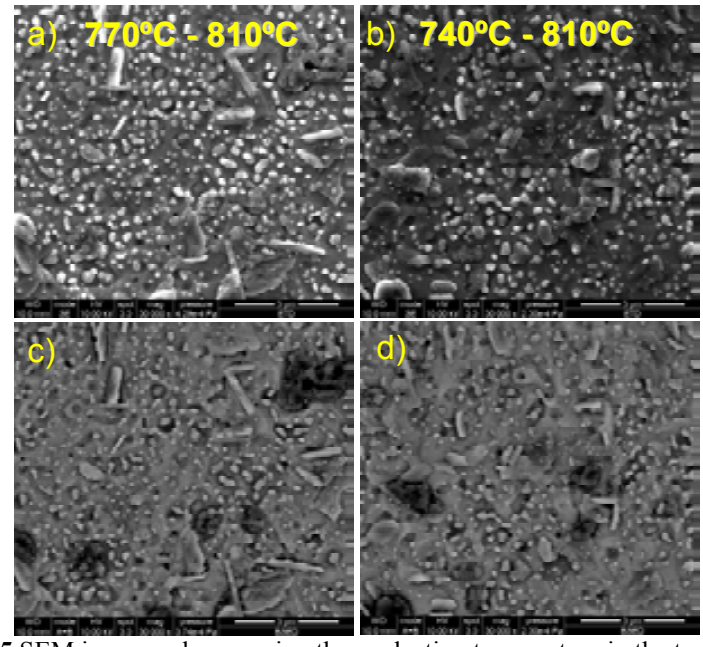

Figure 4.2–15 SEM images when varying the nucleation temperature in the two steps growth process: a) 770ºC-810ºC; b) 740ºC-810ºC. The images c) and d) are the composition images resulted from the first two.

X-ray diffraction technique allows also the determination of the microstrain through Williamson-Hall approach. This method will be described in detail in Chapter 6 (Section 6.2.6). In Figure 4.2–16, the Williamson-Hall plots for YBCO on ^{MOD}CZO/^{PLD}LZO/LAO are compared with those for a standard YBCO film grown on ^{MOD}CZO/YSZ. The drop of the J_c when decreasing the nucleation temperature to 740ºC can be explained in this graph also by the increment of the strain from 0,170% to 0,204% although the CZO surfaces of the two samples were similar (770ºC-810ºC: rms = 1,2 nm, 81% planarity vs. 740ºC-810ºC: rms = 1,6 nm, 73,2% planarity). This is consistent with what Zalamova et al. [22] observed before (ε is enhanced at lower growth temperatures). It was suggested that the saturation of the rms microstrain ε at long times indicates that grain growth occurs through a boundary diffusion process, as it is typically observed in low temperature oxide ex-situ film growth [23]. In conclusion, there is a strong dependence of self-field J_c with the microstrain of ex-situ grown YBCO films which can be noted here also. The relaxation of ε enhances J_c, thus suggesting that the mesoscale strain generated during the grain zipping process introduce a weak link behaviour in the boundaries, contrary to nanoscale rms strain which enhances vortex pinning [22]. If we compare the microstrain of YBCO/^{MOD}CZO/^{PLD}LZO/LAO with the one for YBCO/^{MOD}CZO/YSZ we note an increase from 0,134% to 0,170%. It seems that the use of two buffers introduces more strain in the structure of the sample than just one. This decrease of J_c could be correlated also with the decrease of planarity (from 90% for YBCO/^{MOD}CZO/YSZ to 81% for YBCO/^{MOD}CZO/^{PLD}LZO/LAO).

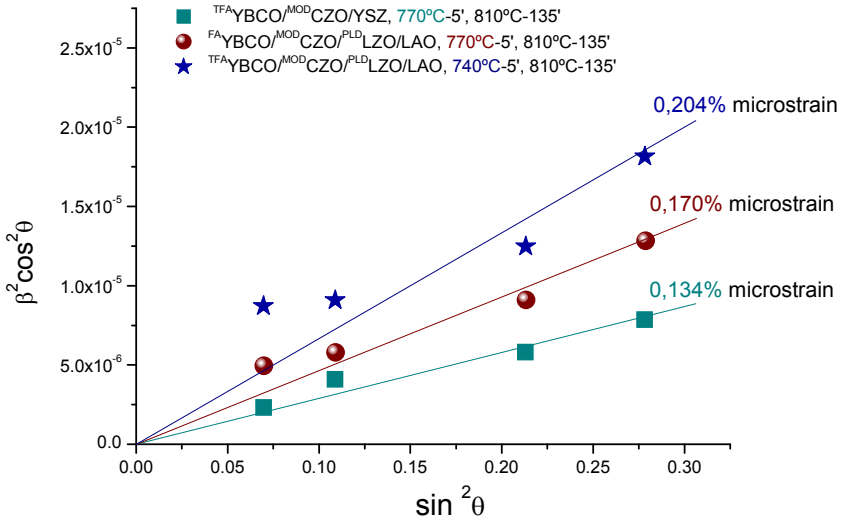

Figure 4.2–16 Williamson-Hall plots for two YBCO/^{MOD}CZO/^{PLD}LZO/LAO samples grown at different nucleation temperatures, 740ºC and 770ºC, compared with a YBCO/ ^{MOD}CZO/YSZ sample. The strain increases when the nucleation temperature decreases.

4.2.5. ^{TFA}YBCO/^{MOD}CZO/^{SPUT}YSZ/Al_2O_3

Applications such as resistive fault current limiters and microwave devices are some of the key technologies in applied superconductivity that benefit from the utilization of superconducting YBCO thin films on sapphire. For these applications, high-quality YBCO films are required in order to achieve high nominal power of fault current limiters or low microwave surface resistance (Rs) [24]. Witanachchi et al.[25] have studied the effect of different buffer layers on low temperature (i.e. in-situ) growth of superconducting YBCO thin films on sapphire (Al_2O_3) using plasma-assisted laser deposition. Their results are shown in Table 4.2-1.

Substrate	Deposition temperature	Buffer layer material (thickness)	T_c	J_c
Al_2O_3	450°C	Plain (no buffer layer)	75 K	4×10^3 (at 40 K)
Al_2O_3	450°C	MgO (500Å)	78 K	9×10^3 (at 40 K)
Al_2O_3	450°C	$BaTiO_3$ (500Å)	83 K	4.5×10^{-4} (at 40 K)
Al_2O_3	450°C	Ag (thickness not known)	75 K	–

Table 4.2-1 The results of YBCO using different buffer layers on sapphire substrates.

It can be easily seen that directly grown YBCO films on sapphire give a low J_c (4 x 10^3 A/cm^2) because of the high reactivity. Successful deposition of superconducting YBCO thin films has been possible through the use of buffer layer materials like CeO_2 to provide adequate lattice matching and prevent chemical reactions between Al_2O_3 and YBCO. Develos et al. [26] had investigated the nature and composition of the surface outgrowths found in YBCO films grown by pulsed laser deposition on CeO_2-buffered Al_2O_3 substrates and had obtained a high J_c value (>2.0×10^6 A/cm^2). Yamaguchi et al. [27] studied the optimum conditions (P_{O2}, V_{gas}) for the growth of Y123 films on CeO_2-buffered sapphire by MOD using a low-cost vacuum technique and obtained high J_c = 3,4 MA/cm^2. Until today, the maximal reported critical current (per unit width) for YBCO on sapphire was 100 A/cm [28]. Deutscher et al. have achieved twice this value in YBCO films of less than 1μm on sputtered YSZ buffers grown on sapphire [29].

In this thesis, we have used various ^{SPUT}YSZ/Al_2O_3 films grown at Tel Aviv University, Israel, to grow a cap layer of CZO, to decrease the lattice mismatch between YSZ and YBCO. The characterization of these cap layers was reported in Chapter 3 (Section 3.5.2). In the following step, YBCO thin films were grown on these buffered Al_2O_3 substrates. A double step growth process was used similar to that previously described. The double step process growth consists in two different temperatures: low temperature (770ºC) for the

nucleation and high temperature (810ºC) for the growth itself. Typical optical images of YBCO layers after pyrolisis are presented in Figure 4.2–17.

Figure 4.2–17 Typical optical microscopy images after pyrolysis for three different samples; the films are homogeneous but different defects caused by the dust are also observed on the surface.

In order to see the influence of the growth temperature in the superconducting properties, an increment of the temperature from 810ºC to 830ºC was done. In Figure 4.2–18 we can find the corresponding SEM images of two of the previous samples when the growth temperature was increased from 810ºC to 830ºC. We found that there are some notable differences between the two surface morphologies of YBCO, depending of the growth temperature. The sample grown at 810ºC is compact with many precipitates on the surface (Figure 4.2–18 a)), meanwhile the other one is more porous and less precipitates can be noticed (Figure 4.2–18 b)).

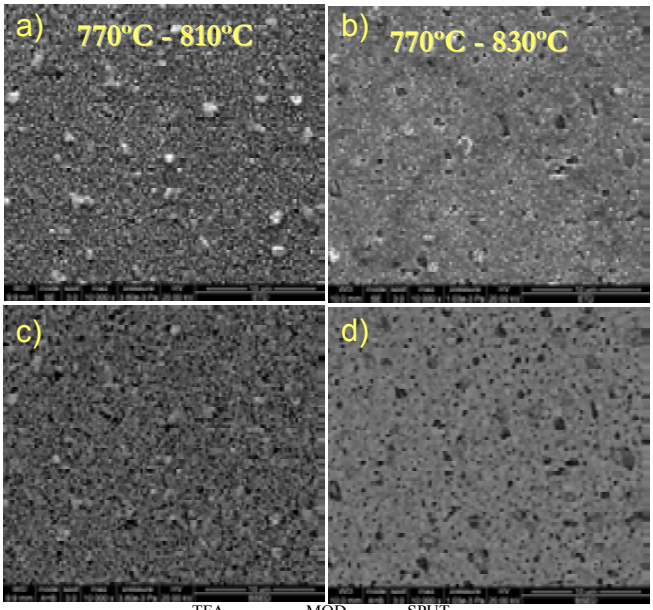

Figure 4.2–18 SEM images of two ^{TFA}YBCO/^{MOD}CZO/^{SPUT}YSZ/Al_2O_3 films grown at 810ºC (a) and 830ºC (b). Backscattered electron scans are also presented for the previous images (c and d). Differences in morphologies are notable with changing the growth temperature.

Figure 4.2–19 a) shows the diffraction patterns obtained for three ^{TFA}YBCO/^{MOD}CZO/^{SPUT}YSZ/Al_2O_3 samples. YBCO grows c-axis oriented indifferent of the growth temperature (810ºC or 830ºC). The FWHM of YBCO (005) peaks were found to be

around 0,7º and this means that the crystalline quality of these films cannot be increased with increasing the temperature, since the value of Δω is the same (Figure 4.2–19 b)).

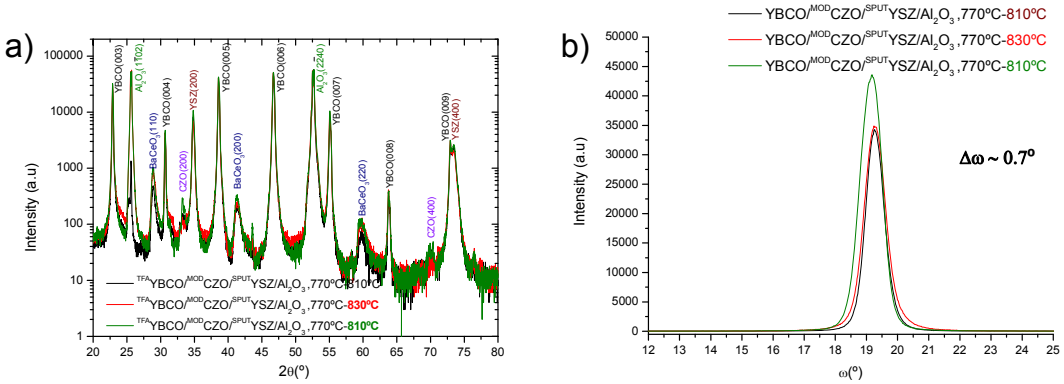

Figure 4.2–19 a) Diffraction patterns obtained by θ-2θ scanning of ^{TFA}YBCO grown on ^{MOD}CZO/^{SPUT}YSZ buffered sapphire substrates; no phase differences are observed for the samples grown at different temperatures 810ºC and 830ºC; b) misorientation out-of-plane for the three previous samples.

Microstrains were calculated from the Williamson Hall plot and the values are presented in Figure 4.2–20. It seems that by increasing the growth temperature, also the microstrain increases and the J_c decreases. The difference between the two samples in the graph presented with blue and green is given by the quality of the CZO cap layer which had different roughness (1.9 nm green, 3.4 nm blue).

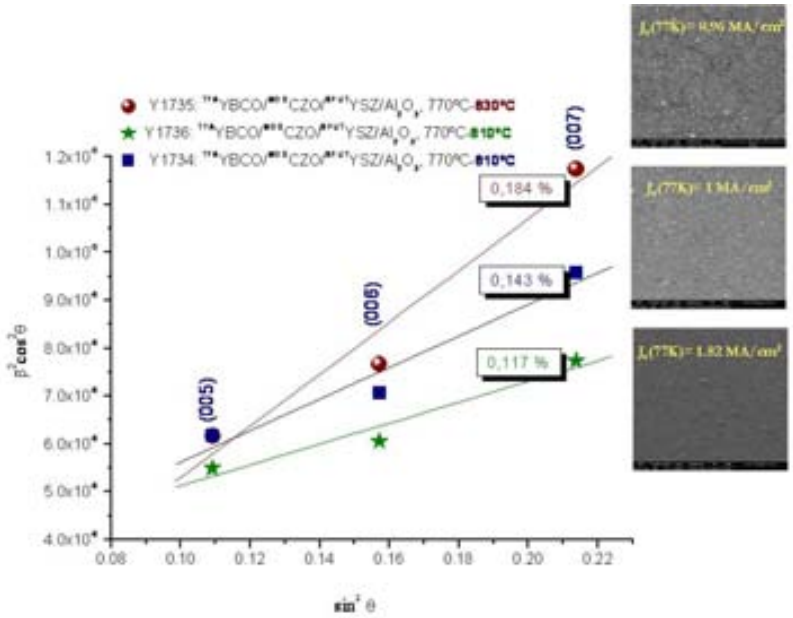

Figure 4.2–20 Williamson-Hall plots for three different ^{TFA}YBCO/^{MOD}CZO/^{SPUT}YSZ/Al_2O_3 samples where the values of the microstrain and a correlation with the SEM images and J_cs are seen. The microstrain increases with the temperature.

The superconducting properties of the samples were measured inductively and the best value 1,8 MA/cm^2 was obtained for the 770ºC-810ºC growth (Figure 4.2–21 a)). The magnetic field dependence of J_c presented in Figure 4.2–21 b) shows that, at low fields lower

than 1T, the pinning is dominated by the isotropic contribution and the number of defects when increasing the temperature to 830ºC is smaller (red curve).

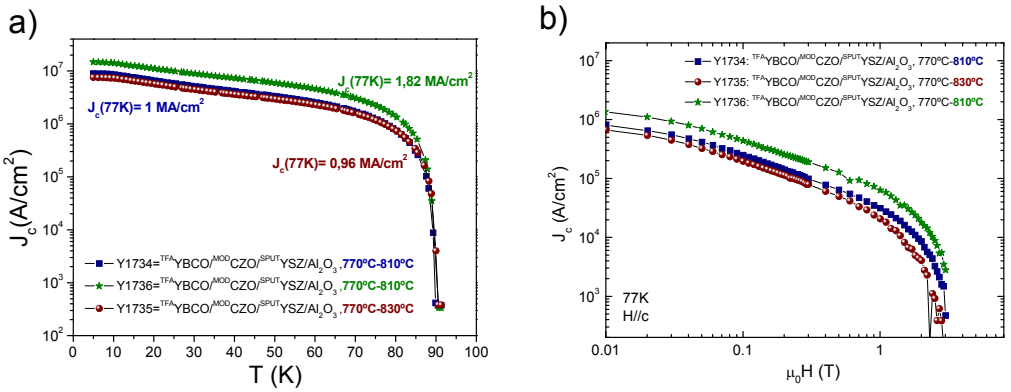

Figure 4.2–21 a) Critical current density J_c as a function of temperature for three different $^{TFA}YBCO/^{MOD}CZO/^{SPUT}YSZ/Al_2O_3$ samples; b) the magnetic field J_c dependence for the previous samples.

The normalized magnetization function temperature can be seen in Figure 4.2–22. The $T_{c\ onset}$ is observed for the three samples around 89K, slightly lower than the films prepared on $^{MOD}CZO/YSZ$ substrate (91,2K). The transition width is larger in the case of the sample grown at 830ºC (Figure 4.2–22 b)) and this is in concordance with the reduced J_c values presented above. We conclude, therefore, that the optimal growth temperature is 810ºC.

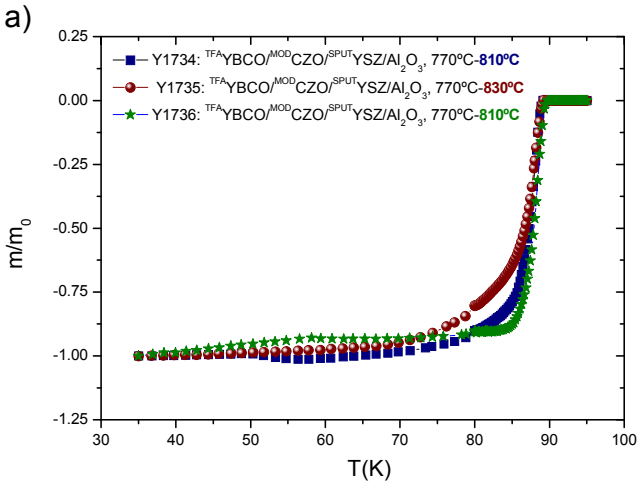

b)

Sample	T_c 10% (K)	T_c 50% (K)	T_c 90% (K)	$T_{c\ onset}$ (K)	ΔT_c (K)
Y1734=$^{TFA}YBCO/^{MOD}CZO/^{SPUT}YSZ/Al_2O_3$ 770ºC - 810ºC	**80**	**87.3**	**88.4**	**88.9**	**8.4**
Y1735=$^{TFA}YBCO/^{MOD}CZO/^{SPUT}YSZ/Al_2O_3$ 770ºC - 830ºC	**74.4**	**86.6**	**88.5**	**89**	**14.1**
Y1736=$^{TFA}YBCO/^{MOD}CZO/^{SPUT}YSZ/Al_2O_3$ 770ºC - 810ºC	**83**	**87.8**	**89**	**89.4**	**6**

Figure 4.2–22 a) Magnetic susceptibility measured at H = 2Oe showing that $T_{c\ onset}$ is reduced as compared to the film grown on $^{MOD}CZO/YSZ$; b) values of the T_cs and the transition width. When temperature increases the transition width also increases.

4.3. Conclusions

In this Chapter, we have investigated, starting from a ^{TFA}YBCO precursor solution, the influence of growth conditions on the superconducting performances of YBCO films grown on the cap layer ^{MOD}CZO when it is grown on different buffered substrates (YSZ, ^{PLD}LZO/LAO, ^{SPUT}YSZ/Al_2O_3). The steps of the YBCO synthesis solution and pyrolisis were the standard ones while growth conditions are different. A clear correlation with the quality of the cap layer was seen: the J_c increases with the planarity of the CZO.

Superconducting properties of YBCO films on YSZ were characterized by measuring J_c and T_c. A transport J_c of 5,2 MA/cm^2 was obtained for a 275 nm thick YBCO film on ^{MOD}CZO buffered YSZ at 77 K and zero-external field. An important point to note here is that, at 77K, critical current density dependence with the magnetic field (H//c) of both of a standard sample and a buffered one is strongly mediated by the anisotropic defect pinning contribution.

For studying the capability of LZO buffer layers as a part of a RABiT coated conductor, YBCO films grown from TFA precursors were deposited on top of ^{MOD}CZO/^{PLD}LZO/LAO. By varying the nucleation temperature, from 770ºC to 740ºC, it was noted that the J_c at 77K decreases from 2,3 MA/cm^2 to 0,9 MA/cm^2. Our work show that the typical decrease of J_c observed in RABiTS CC with this architecture cannot be associated to the LZO, but probably to an excess of roughness. This drop of the J_c when decreasing the nucleation temperature to 740ºC can be explained also by the increment of the strain from 0,170% to 0,204%, i.e the mesostrain has not been healed out.

Superconducting properties as high as 1,8 MA/cm^2 were also obtained for the 770ºC-810ºC growth on ^{TFA}YBCO/^{MOD}CZO/^{SPUT}YSZ/Al_2O_3. In this case, the crystallinity doesn't change when the temperature is increased. A small drop of T_c (89K) is registered comparing with 91,2K in the case of the standard film. This suggests that some impurification of the YBCO occurs.

The incorporation of silver salts in the YBCO precursor solution goes to an enhancement of the J_c with the magnetic field indifferent of the growth temperature. This fact suggest that, at least at low magnetic fields, defects are created in the doped films which play an important role as pinning centers. At self field, instead, the results are contrary to those obtained previous in the group on LAO, when an enhancement of J_c was noted. This result makes us think that the growth mechanism when adding Ag is different on YSZ buffered ^{MOD}CZO. More studies are needed in order to discover why this happens (to thin CZO,

roughness, reactivity?). No secondary reflections related with silver are observed. A flatter terraced surface is obtained and the porosity is decreased.

4.4. References

[1] X. Obradors, T. Puig, A. Pomar et al., "Chemical solution deposition: a path towards low cost coated conductors," Superconductor Science & Technology **17** (8), 1055-1064 (2004).

[2] X. Obradors, T. Puig, K .H. Buschow et al., "Encyclopedia of Materials: Science and Technology,," Pergamon Press, 4792 (2001).

[3] H. R. Kim, C. R. Park, S. W. Yim et al., "Recovery Characteristics of Coated Conductors," Ieee Transactions on Applied Superconductivity **20** (3), 2194-2198 (2010).

[4] Borhan A. Albiss and Ihab M. Obaidat, "Applications of YBCO-coated conductors: a focus on the chemical solution deposition method " J. Mater. Chem. **20**, 1836-1845 (2010).

[5] N. Roma and et al., "Acid anhydrides: a simple route to highly pure organometallic solutions for superconducting films," Superconductor Science and Technology **19** (6), 521 (2006).

[6] R . Wördenweber, "Growth of high-T_c thin films," Superconductor Science & Technology **12**, R86-R102 (1999).

[7] X. Yongli and S. Donglu, "A review of Coated Conductors Development."

[8] M. S. Bhuiyan, M. Paranthaman, and K. Salama, "Solution-derived textured oxide thin films - a review," Superconductor Science & Technology **19** (2), R1-R21 (2006).

[9] A. Llordes, K. Zalamova, S. Ricart et al., "Evolution of Metal-Trifluoroacetate Precursors in the Thermal Decomposition toward High-Performance $YBa_2Cu_3O_7$ Superconducting Films," Chemistry of Materials **22** (5), 1686-1694.

[10] A. Llordes, "Superconducting nanocomposite films grown by chemical solution deposition: synthesis, microstructure and properties," (2010, PhD thesis).

[11] H. Chen, K. Zalamova, A. Pomar et al., "Nucleation and growth rate influence on microstructure and critical currents of TFA-$YBa_2Cu_3O_7$ under low-pressure conditions," Journal of Materials Research **25** (12), 2371-2379.

[12] J. G. Royo, "Vortex pinning and critical currents in $YBa_2Cu_3O_{7-x}$ MOD-TFA thin films and Coated Conductors," PhD Thesis, UAB, Bellaterra (2008).

[13] Y. L. Zuev, D. K. Christen, S. H. Wee et al., "Near-isotropic performance of intrinsically anisotropic high-temperature superconducting tapes due to self-assembled nanostructures," Applied Physics Letters **93** (17), 172512-172513 (2008).

[14] T. Puig, J. Gutierrez, A. Pomar et al., "Vortex pinning in chemical solution nanostructured YBCO films," Superconductor Science & Technology **21** (3) (2008).

[15] C. H. Cheng and Y. Zhao, "Repair of grain boundary by preferential-doping in $YBa_2Cu_3O_{7-y}$," Physica C **463**, 174-177 (2007).

[16] P. Selvam, E. W. Seibt, D. Kumar et al., "Enhanced J(c) and improved grain-boundary properties in Ag-doped $YBa_2Cu_3O_{7-delta}$ films," Applied Physics Letters **71** (1), 137-139 (1997).

[17] A. V. Pan, S. V. Pysarenko, D. Wexler et al., "Multilayering and Ag-doping for properties and performance enhancement in $YBa_2Cu_3O_7$ films," Ieee Transactions on Applied Superconductivity **17** (2), 3585-3588 (2007).

[18] A. H. Li, X. L. Wang, H. K. Liu et al., "Effect of substrate surface modification using Ag nano-dots on the improvement of J(c) and microstructures in $YBa_2Cu_3O_7$ thin films grown on $LaAlO_3$ (100) by pulsed laser deposition," Journal of Electroceramics **16** (4), 605-609 (2006).

[19] A. Pomar F. Martínez-Julián, S. Ricart, A. Palau, T. Puig, X. Obradors, "Silver-assisted enhancement of c-axis nucleation in TFAYBCO thin films," to be published.

[20] F. Martinez, "Uso de sales inorgánicas y nanopartículas en el crecimiento de capas delgadas superconductoras crecidas por CSD," PhD Thesis, UAB, Bellaterra (2011).

[21] K. Knoth, R. Huhne, S. Oswald et al., "Growth of thick chemical solution derived pyrochlore $La_2Zr_2O_7$ buffer layers for $YBa_2Cu_3O_{7-x}$ coated conductors," Thin Solid Films **516** (8), 2099-2108 (2008).

[22] K. Zalamova, A.Pomar, A. Palau et al., "Mesoscale strain as a limiting factor of percolating currents in $YBa_2Cu_3O_7$ ex-situ grown superconducting thin films " To be published.

[23] V. F. Solovyov, K. Develos-Bagarinao, Q. Li et al., "Nature of $Y_1Ba_2Cu_3O_7$ nucleation centers on ceria buffers," Superconductor Science & Technology **23** (1).

[24] K. Develos-Bagarinao and H. Yamasaki, "$YBa_2Cu_3O_{7-delta}$ thin films with enhanced film properties grown on sapphire using Y_2O_3/CeO_2 bi-layer buffer," Thin Solid Films **517** (24), 6539-6545 (2009).

[25] S. Witanachchi, S. Patel, D. T. Shaw et al., "Low-temperature growth of mirror-like superconducting thin films on sapphire," Materials Letters **8** (1-2), 53-56 (1989).

[26] K. D. Develos, H. Yamasaki, A. Sawa et al., "On the origin of surface outgrowths in pulsed-laser-deposited $YBCO/CeO_2/Al_2O_3$ thin films," Physica C: Superconductivity **361** (2), 121-129 (2001).

[27] I. Yamaguchi, M. Sohma, K. Tsukada et al., "Preparation of large-size Y123 films on CeO_2-buffered sapphire substrates by MOD using a low-cost vacuum technique," Physica C **463**, 549-553 (2007).

[28] K. Develos-Bagarinao, H. Yamasaki, J. C. Nie et al., "Thickness dependence of J(c) for YBCO thin films prepared by large-area pulsed laser deposition on CeO_2-buffered sapphire substrates," Superconductor Science & Technology **18** (5), 667-674 (2005).

[29] B. Almog, "Superconducting wires and films for application," Barcelona, private communication (2010).

CHAPTER 5 COATED CONDUCTORS ON METALLIC SUBSTRATES

This chapter contains the results obtained on Stainless Steel metallic substrates with YSZ buffer layers deposited using one of the most promising method for obtaining Coated Conductors, Alternating Beam Assisted Deposition (ABAD). Characterization of the crystallographic texture was done mainly by X-Ray diffraction, with a number of other techniques used to study the surface morphology and superconducting parameters.

5.1. State of the art of the Coated Conductors

Second generation (2G) high temperature superconductor (HTS) wires are based on a coated conductor technology. They follow on from a first generation (1G) HTS wire consisting of a composite multifilamentary wire architecture. During the last couple of years, rapid progress has been made in the development of 2G HTS wire, which is now displacing 1G HTS wire for most if not all applications. The engineering critical current density of these wires matches or exceeds that of 1G wire, and the mechanical properties are also superior. Scale-up of manufacturing is proceeding rapidly, with several companies already supplying the order of 10 km annually for test and demonstration [1].

The production of these coated conductors has moved out of the laboratory and is now being produced in the quantity and with the performance required for large-scale commercial cable and coil demonstrations. Two major advantages of the 2G technology over the first generation (1G) HTS wire are the potential for lower cost and the ability to tailor wire dimensions and for specific applications [2].

Any manufacturing method for YBCO conductors relies on the epitaxial deposition of YBCO onto a textured template of one or more oxide buffer layers and a normal metal substrate. Three of the most used methods nowdays are presented in Figure 5.1–1. This template is usually created through introduction of texture either into the buffer layers by ion beam-assisted deposition (IBAD), or into the metal substrate by deformation texturing using the rolling-assisted biaxially textured substrate (RABiTS) approach. The IBAD method enables the use of strong, non-magnetic Ni-superalloy substrates on which an aligned YSZ is deposited by IBAD and protects the substrate. This process can achieve a high degree of texture with a layer of YSZ that is ~0.5 mm thick. But such a process is widely considered to be too slow to be commercial. IBAD of MgO produces good texture within the first 1-2 nm and thus may be rapid enough to be commercial, but the degree of texture in present IBAD-

MgO-coated conductors is as good as in IBAD-YSZ variants. Ion-texturing processes for buffer-layer deposition are receiving renewed attention owing to their simplicity, but their success depends on producing sufficient texture so to compete with the slower and more expensive IBAD process. All of these methods of producing a textured buffer layer involve physical vapour-deposition processes, which some believe are inherently too expensive for copper and iron replacement. An advantage of the RABiTS approach is that all buffer-layer and YBCO-coating steps can be performed with non-vacuum processes. A strong [100] cube texture is introduced into the substrate by conventional rolling and recrystallization. Although the RABiTS approach has been developed mainly with pure Ni, alloyed substrate materials are being developed to increase the strength and reduce the magnetism of the Ni [3].

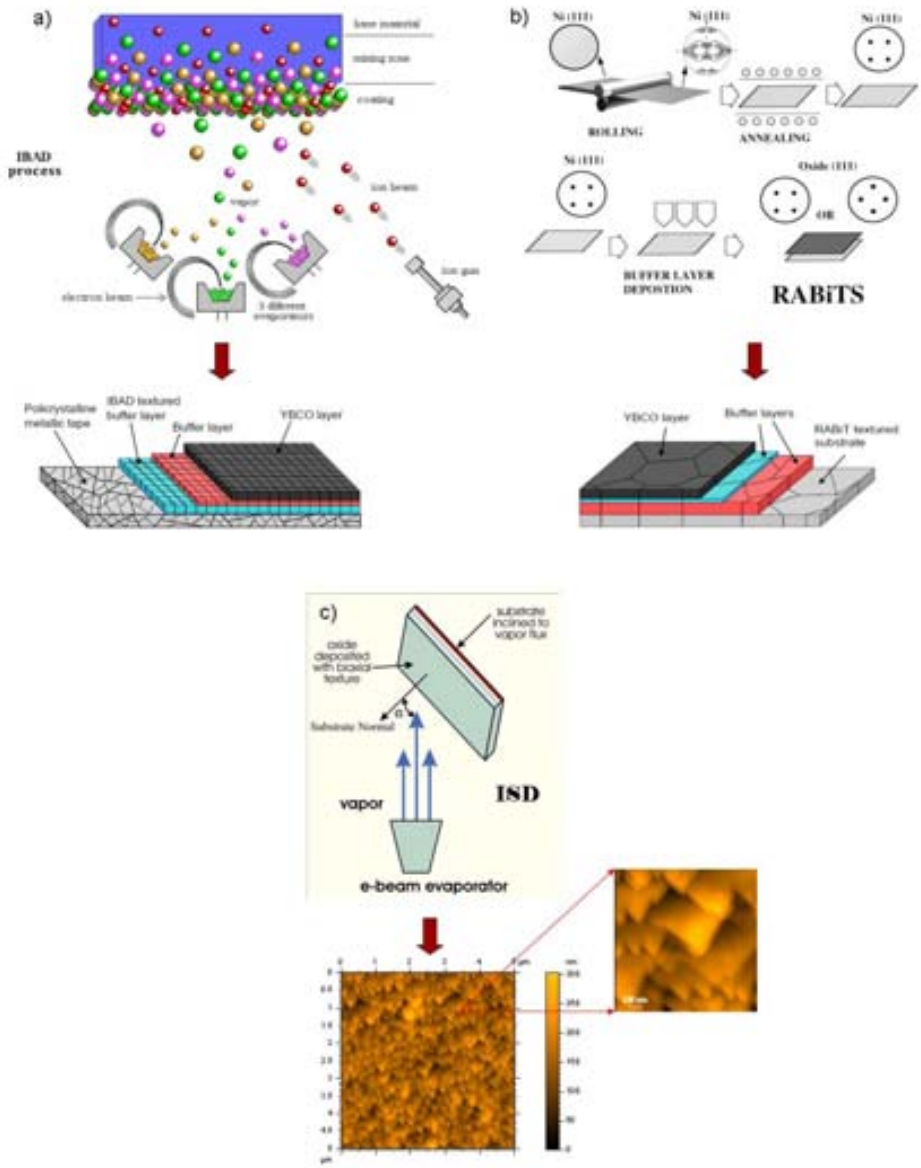

Figure 5.1–1 Three of the most used methods for obtaining coated conductors: a) Ion Beam Assisted Deposition (IBAD), realized in a vacuum chamber, which is a combination of two distinct physical operations: an ordinary Physical Vapor Deposition (PVD) on a substrate and a simultaneous bombardment of the surface with a low energy ion beam; b) Rolling-assisted biaxially-textured substrates (RABiTS) process which starts with a randomly oriented Ni bar/plate, followed by cold-rolling to produce a distinct copper-type rolling texture. This is followed by recrystallization to a cube texture and epitaxial metal and/or oxide buffer layer(s) are then deposited on the textured Ni [4]; c) Inclined Substrate Deposition (ISD) in which a flexible metallic substrate, such as Hastelloy, is held at an angle to the direction of the plume of an e-beam evaporation system, and a biaxially textured oxide layer, such as magnesium oxide (MgO), is obtained. An image of ^{ISD}MgO/Hasstelloy obtained by AFM is shown.

HTS–CCs are attracting much attention for practical applications of superconducting electrical and magnetic devices that can operate in liquid nitrogen temperature. Drastic improvements in the length and the current carrying capability of HTS– CC have been accomplished for last several years [5]. Companies all over the world are dealing with the challenge given by the long length CC production – cost. Following, a brief presentation of

the world leaders in CC will be done. The architectures with which these companies are working are presented in

Figure **5.1–2**.

American Superconductor Corporation (AMSC) has established a 2G HTS manufacturing process focused on four critical technical areas: low ac loss RABiTS substrates, high I_c in solution-based YBCO films, materials cost reduction [6]. The RABiTS™/MOD-YBCO (rolling assisted biaxially textured substrate/metal–organic deposition of $YBa_2Cu_3O_{7-\delta}$) route has been established as a low-cost manufacturing process for producing high performance second generation (2G) wire. American Superconductor Corporation (AMSC) has used this approach to establish a production scale manufacturing line based on a wide-web manufacturing process. This initial production line is currently capable of producing 2G wire in lengths to 500 m with critical currents exceeding 250 A cm^{-1} width at 77 K, in the self-field [2].

SuperPower Inc., another american company which uses IBAD (ion beam assisted deposition) and MOCVD (metal organic chemical vapour deposition) processes successfully demonstrated the scale-up of 2G HTS wire technology to manufacturing [6]. Their objectives achieved last year were:

- ✓ demonstrate high-yield manufacturing of kilometer-lengths of 2G HTS wires with critical currents exceeding 250 A/cm;
- ✓ develop scalable approaches to manufacture 2G wires with improved critical current retention in magnetic field without sacrificing throughput;
- ✓ reduce cost and improve efficiency of wire fabrication using simpler processes and fewer layers in our wire architecture;
- ✓ develop novel, scalable processes for multifilamentary 2G wires for low ac loss applications.

Los Alamos National Laboratory (LANL) obtained last year excellent results on YBCO films that were deposited by Reactive Co-evaporation (RCE) directly and epitaxially on the textured MgO layer [6]. They are also currently utilizing the solution deposition planarization (SDP) process for substrate preparation as a way to reduce the cost of the substrate and simplify the architecture even further. Specific results and accomplishments include:

- ✓ achieved over 4 MA/cm^2 (LN_2, self field) in a 1μm RCE-deposited YBCO on an MgO template with the simplified architecture using SDP;

- ✓ examination stacks of YBCO layers using alternating SDP/IBAD/RCE layer structures as a promising way to achieve high critical currents;
- ✓ STI are optimizing their HTS layer performance using second phase dopants and rare-earth element substitution in RCE.

Oak Ridge National Laboratory (ORNL) has conducted experiments on YBCO film deposition on faceted fibers made using the SSIFFS process and continued to investigate methods to achieve biaxial texture in substrates which are mechanically strong and have reduced magnetism. In the area of buffer layer development, the emphasis areas included – development of buffers which improve the texture compared to the substrate, development of multifunctional buffer layers, reduction in the number of buffer layers and development of more robust buffers.

In Japan, the ***Superconductivity Research Laboratory (SRL)***, ***Showa Electric Cables (SWCC)***, ***Chubu Electric Power Co., and Sumitomo Electric Industry (SEI)*** are the main players in this group. Trifluoroacetate (TFA) metal organic deposition (MOD) is a potentially low cost process since it does not require high vacuum apparatus and the materials spent was about 100% used to form superconducting layers. High performance GdBCO tape (368 m–304.8 A), setting the new world record, has been fabricated on PLD-CeO_2/IBAD-GZO buffered substrates by Fujikura Ltd. I_c under high magnetic fields was further improved to be 42 A at 77 K, 3 T in a short sample by the introduction of ZrO_2 which forms BZO nanorods working as artificial pinning centers. A long GdBCO tape with ZrO_2 doping over 60 m with a high I_c value of 220 A was obtained, which showed I_c higher than 30 A at 3 T. The extremely high I_c value of 735 A/cm-w was obtained in TFA-MOD films on CeO_2/IBAD-GZO/Hastelloy substrate due to the effect of Ba poor nominal composition [7]. Five hundred meter-long tapes with higher I_c values than 300 A/cm-width were realized by the pulsed laser deposition (PLD) and the metal organic deposition using trifluoroacetates (TFA-MOD) processings for the superconducting layer on the IBAD-GZO buffered substrates. In order to realize the low cost by the increasing the production rate of the ion beam assisted deposition (IBAD) layer, the process of IBAD-MgO was developed and a 1000 m-long IBAD buffer tape was fabricated at an extremely high production rate of 1 km/h [8].

In Europe, ***Bruker HTS*** is one of the leading manufacturers of HTS materials and devices, based on its broad conductor technology platform. Using a novel method, Alternating Beam Assisted Deposition (ABAD) for the YSZ buffer deposition and High Rate Pulsed Laser Deposition (HR-PLD) for the superconducting film, CC performance with

high critical currents up to 500 A/cm-w at 77K, SF and 5000 A/cm-w at 4.2K, 18T, when H||c was demonstrated [9].

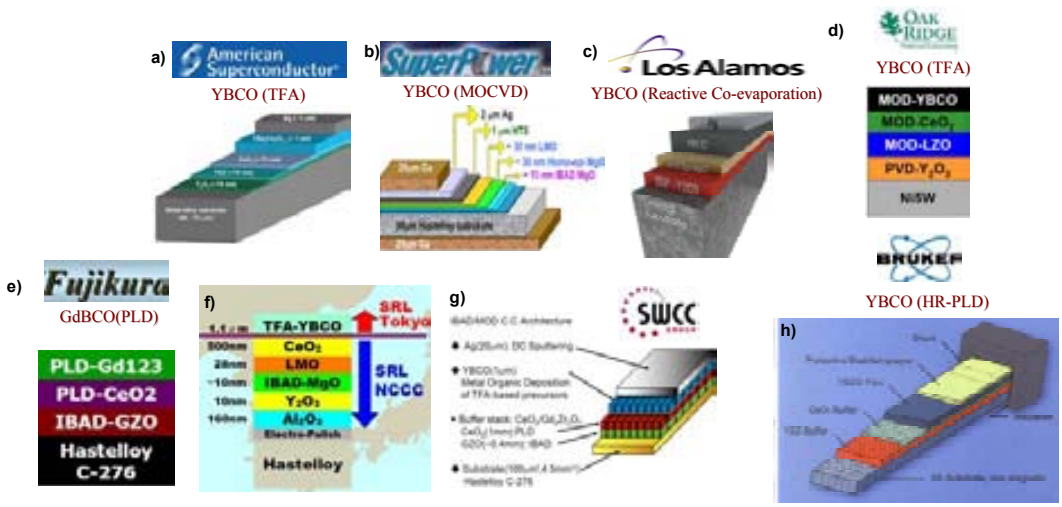

Figure 5.1–2 Overview of the Coated Conductors architectures used by companies all over the world.

5.2. Alternating Beam Assisted Deposition (ABAD) on Stainless Steel (SS) tapes

5.2.1. Characterization of the as received tapes

At present ion-beam assisted deposition (IBAD) is widely used in the processing of different templates. Alternating ion beam assisted deposition (ABAD) is an improved method developed by A. Usoskin et al. [10] at Bruker HTS, where the molecular beam and the ion beam are alternated, and was recently suggested in order to improve the quality of the texture [11]. In this method, the template film is periodically exposed to alternating deposition and etching pulses. A schematic view of a set-up developed for realization of this process with flexible substrate tape employed as a substrate 1 is shown in Figure 5.2–1. The tape is guided through the rollers 2a and 2b as a closed loop. Sequentially, each particular area of the tape is pulled through deposition zone D and after this passes through zone E for selective ion etching. All the process is realized in a high vacuum (10^{-6}-10^{-7} mbar) chamber that allows high speed (6000 l/sec) pumping in order to enable the operation of ion sources operated under considerable gas flows. The growing layer undergoes a series of alternating pulses of deposition and ion etching. The deposition of the buffer materials is realized in zone D and etching in zone E, about 30% of the material is removed by ion beam in an "alternation" movement. An angle of 55º is used for yttria-stabilized zirconia template processing and at the end, after a deposition / etching cycle 2-5 nm remains as thickness

[10]. Compared with the IBAD process, the ABAD facilitates a better quality in plane and also shorter time deposition is needed.

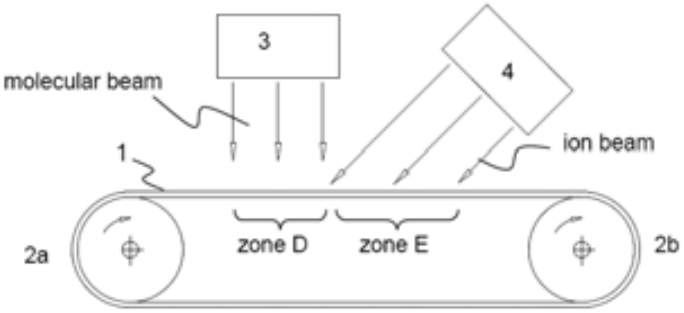

Figure 5.2–1 Schematic view of alternating beam assisted deposition (ABAD) employed for processing of in-plane textured template of buffer layer. 1 – metallic substrate, 2 – guide rollers, 3 – molecular beam source, 4 – ion beam source (assisted beam). Zones D and E correspond respectively to deposition and selective etching areas [10].

Several non-magnetic 0,1 mm thick CrNi Stainless Steel (SS) substrates with ^{ABAD}YSZ deposited on them were received from Bruker HTS, Germany. Before the deposition of the buffer layer, the substrates were polished until reaching a roughness of about 2-3 nm [11]. Surface quality of cap layers grown by metal organic decomposition is the key parameter to a good epitaxial growth of thin films as it was previously demonstrated for model samples grown on buffered single crystals [12]. In the case of films growing onto metallic substrates this is even more critical due to the inherent presence of substrate grain boundaries and roughness increase. In Figure 5.2–2 a) we present a topographic AFM image of the surface of the ABAD tape as received. Although the rms roughness value is relatively low (1,8 nm) it is interesting to note that flat area fraction is only 49% as seen in Figure 5.2–2 b). This image is obtained after defining flatness as a deviation of less than 1.8 nm (i.e. slightly higher than the YBCO unit cell length) of the mean surface value. With this threshold an image mask is applied to the original AFM measurement (i.e. Figure 5.2–2 a) and the resulting image is plotted in two colours: grey (blue online) meaning flat areas and black representing rough areas (Figure 5.2–2 b)). On the surface we can note through a line profile, some oriented channels of 4-6 nm height which appear due to the deposition process.

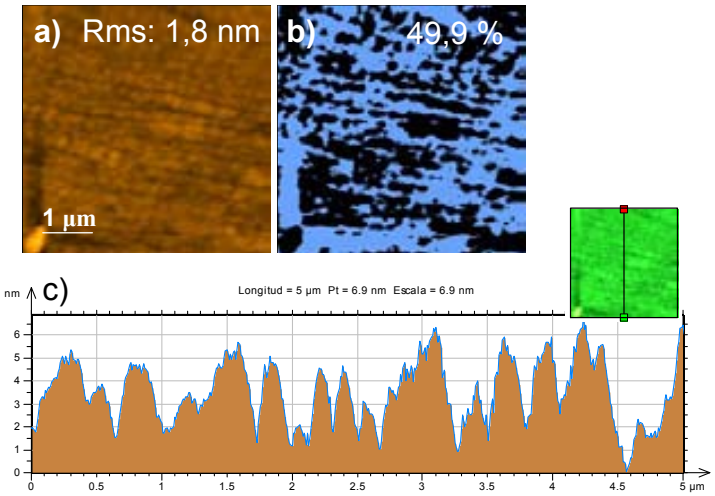

Figure 5.2–2 a) AFM topographic image of a ^{ABAD}YSZ/SS tape as received; b) binarization of the topographic previous image in which blue correspond to flat grains (a threshold value of 1,8 nm was taken into account for the calculation of the planarity).

Figure 5.2–3 a) shows a typical 2D θ-2θ XRD pattern for a ^{ABAD}YSZ grown on a Stainless Steel tape. The YSZ oxide shows diffraction peaks corresponding to (00*l*) planes. The substrate is polycrystalline represented by a cone in the diffraction pattern. This demonstrates the predominant *c*-axis orientation of the layers in the sample with in-plane misorientation of 10,2º and out-of-plane of 5,5º. Very good homogeneity of YSZ texture over nearly a 43 m-tapes in Bruker HTS, i.e. Δφ=10.3°±1.1° is obtained (Figure 5.2–3 b)).

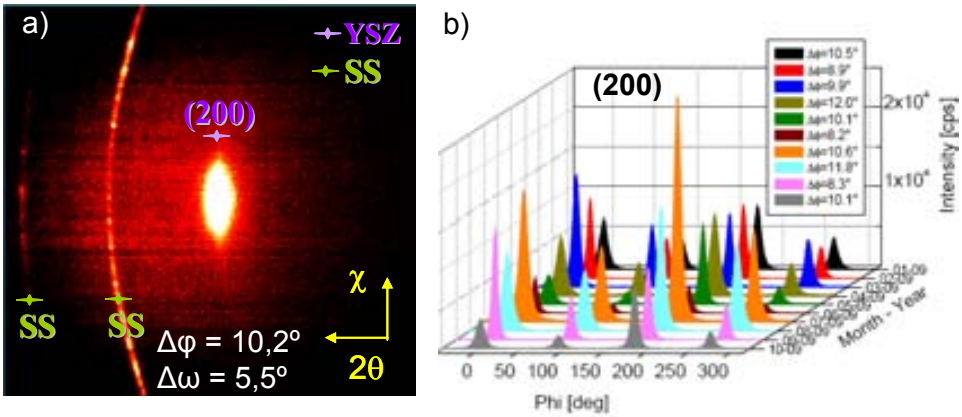

Figure 5.2–3 a) 2D XRD diffraction pattern with the values of the in-plane and out-of-plane misorientation; b) Quality control performed by Bruker HTS at the manufacturing plant in which the in-plane angular width ΔΦs of the textured ^{ABAD}YSZ films is measured on tapes of stainless steel 43m-long all around the year [13].

5.2.2. Crystallization of CZO and study of the planarity

The deposition of the YBCO superconducting film directly on the ^{ABAD}YSZ/SS was not fruitful because cracks appeared due to the high lattice mismatch between YSZ and YBCO (-5,71%). Because of this, the deposition of a cap layer, in this case $Ce_{0.9}Zr_{0.1}O_2$, is necessary (misfit YBCO-CeO_2 = -0,52%). Thin CZO films of about 20-30 nm were deposited by spin coating on the as-received ^{ABAD}YSZ/SS using a high temperature treatment (900ºC). The morphology of the ^{MOD}CZO was studied by Atomic Force Microscopy, which gives further information about the topography of the surface. If the same procedure for planarity is now applied to the surface image of the cap layer we can see that in spite of a rms roughness in excess of 3 nm (Figure 5.2–4 a)), the flat area fraction has been significantly increased, being now 68,5% with wider terraces (Figure 5.2–4 b)). This is possible due to the characteristic behaviour of CZO that tends to develop a terraced surface morphology as previously demonstrated [12,14].

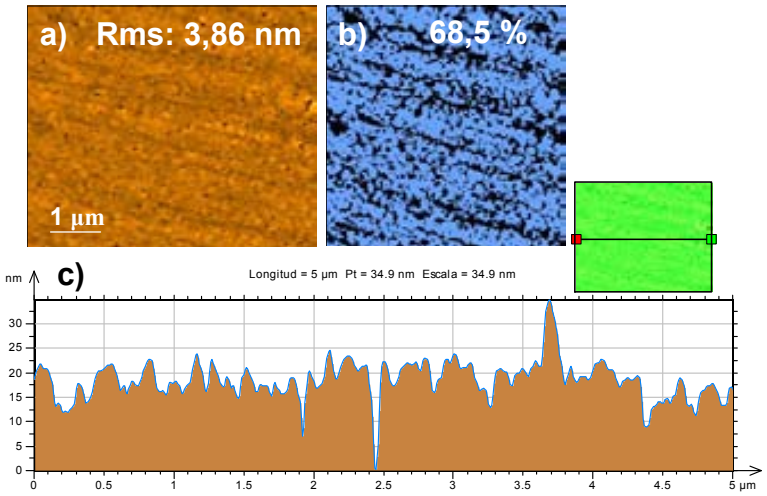

Figure 5.2–4 a) AFM image of a ^{MOD}CZO cap layer grown on the as-received ^{ABAD}YSZ/SS; b) binarization image of a) in which the planarity is improved to 68,5% compared with the planarity of as-received ^{ABAD}YSZ (49,9%); c) line profile of the topographic image.

The θ-2θ plot of Figure 5.2–5 a) and the integration in chi of this frame b) indicate that the ^{MOD}CZO grows epitaxial on the ^{ABAD}YSZ/SS. What is surprising to note is that, after the treatment at high temperature for growing CZO, (111) and (220) polycrystalline reflections of YSZ appear. The ratio between the epitaxial part of YSZ, the (200) reflection and the polycrystalline one, (111)+(220) was found to be 4,7 after integrating the GADDS frame of the respective reflections ($I_{YSZ(200)}$ = 803118; $I_{YSZ(111)}$ = 85548; $I_{YSZ(220)}$ = 84327). However, the higher reflection is still the desired one - (00l). Wang et al. [15] observed the same phenomenon when depositing CeO_2 on IBAD-YSZ/Hastelloy. The explanation can be

associated to a recrystallization of the ^{ABAD}YSZ layer at the high temperature necessary for the ^{MOD}CZO growth.

The rocking curve was measured to detect the degree of *c*-axis misorientation of the ^{MOD}CZO and to quantify the out-of-plane texture. The information obtained measuring rocking curves is equivalent to that obtained from the pole figures in c direction (direction of tilt). An out-of-plane misorientation $\Delta\omega = 6{,}6^{\circ}$ is obtained for (002) CZO (Figure 5.2–5 c)).

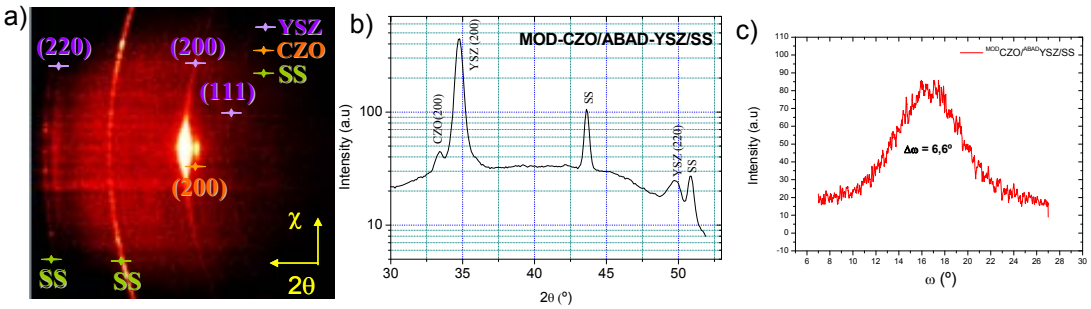

Figure 5.2–5 a) Epitaxial growth of ^{MOD}CZO on ^{ABAD}YSZ can be seen in the 2D XRD pattern; b) integration in chi of the previous frame; c) rocking curve of CZO (200).

For comparison with the ^{MOD}CZO grown in ICMAB on ^{ABAD}YSZ/SS, several tapes with ^{PLD}CeO$_2$/^{ABAD}YSZ/SS received from the same company-Bruker HTS-were investigated. The 40 nm CeO$_2$ was deposited by High Rate Pulsed Laser Deposition (HR-PLD) which permits to deposit long lengths in short time [16]. The morphological characterization was done and the AFM images of different series of tapes have shown roughnesses between 2-4 nm with some spikes of about 20-25 nm from place to place (Figure 5.2–6 a, b, c). A curiosity to note is that, from the XRD patterns, the CeO$_2$ appears like a shadow suggesting that the grains are much smaller than the ones obtained by MOD where big and flat terraces were obtained (Figure 5.2–6 d, e, f). Even after 2 hours annealing of the as-received cerium oxide at 800ºC, no improvement in the intensity of the reflection was observed.

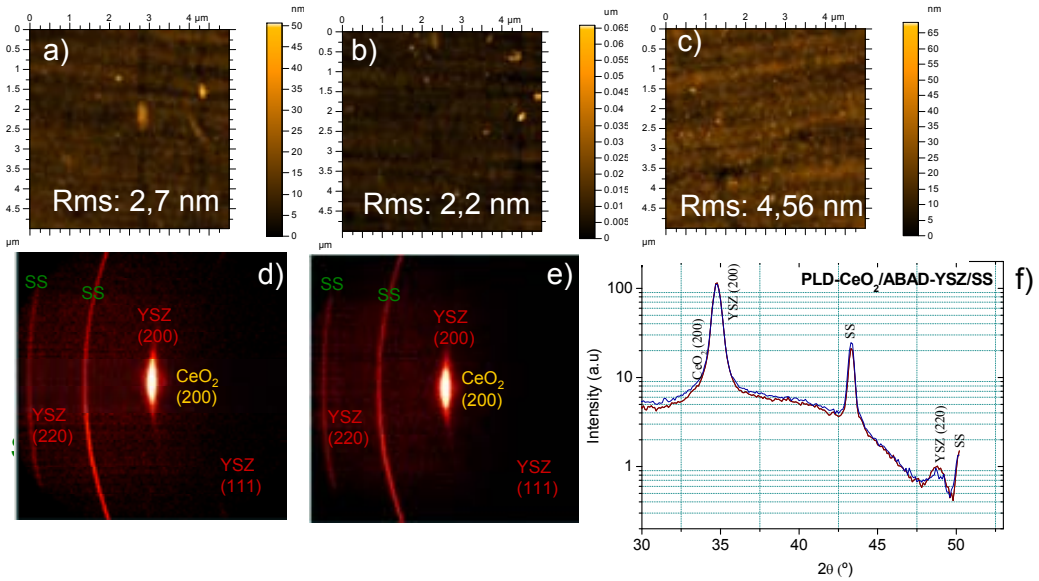

Figure 5.2–6 a), b), c) Morphologies by AFM of different series of $^{PLD}CeO_2/^{ABAD}YSZ/SS$; d), e) 2D XRD patterns of the first two series; f) integration in chi for the previous two XRD frames.

5.2.3. Effect of the Ag addition in the CZO precursor solution

After studying the effect of Ag additive in the CZO precursor solution on single crystals (Chapter 3) we applied the process to the metallic substrates. The addition to the solution was realized in the same way (by adding a small volume of a silver salt in methanol solution in the solution of CZO; 4,58% wt. Ag was used). Differences in morphology of the buffer after 1 hour and after 8 hours growth are seen (Figure 5.2–7 a) and d)). Comparing with the CZO without silver, a decrease of the roughness from 3,8 nm to 2,7 nm is observed when the growth time is 8 hours, while the roughness decreases to shorter times (1h). The origin of this phenomenon becomes clear when the surface planarity is analyzed (68% vs 78%-1h and 76%-8h) (Figure 5.2–7 c), f)). The structural characterization by XRD doesn't show any secondary silver phases and the CZO keep the (h00) texture (Figure 5.2–7 g) and h)).

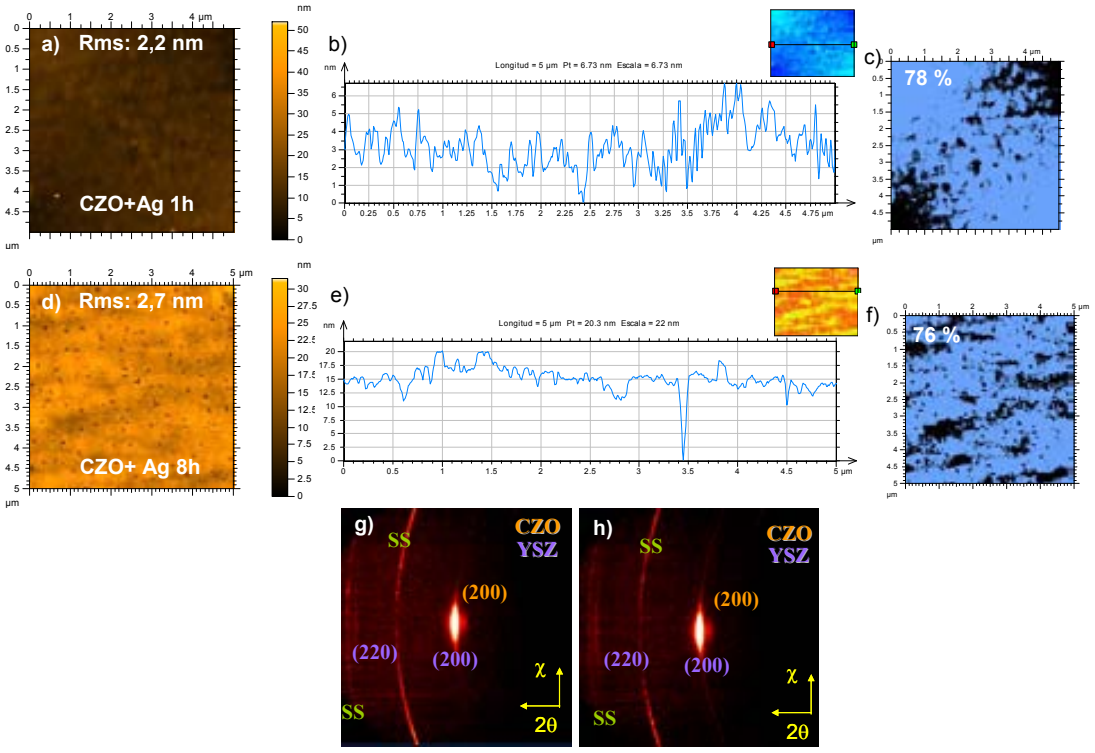

Figure 5.2–7 AFM images of the Ag-CZO grown 1h (a) and 8h (d); line profiles for the previous samples (b) 1h and (e) 8h; planarities of the samples (c) 1h and (f) 8h; XRD patterns of the previous buffer layers after 1h growth (g) and 8h (h).

5.2.4. Deposition and growth of YBCO on metallic substrates

5.2.4.1. ^{MOD}CZO/^{ABAD}YSZ/SS substrate

YBCO films were prepared by the trifluoroacetates route as described in detail previously (Chapter 4, Section 4.1.1) by using anhydrous precursor solutions with 1.5 M concentration. After spinning, the films were calcinated in a fast pyrolysis process at 310ºC in oxygen atmosphere. Subsequently films were grown in a wet atmosphere with 200 ppm of oxygen. Films were kept at growth temperature (770 ºC – 810 ºC) for 150 minutes before cooling down. Oxygenation was performed at 450ºC. The thickness of the grown films was 275 nm as determined by profilometer measurements. All the YBCO films were grown onto metal organic deposited (MOD) $Ce_{0.9}Zr_{0.1}O_2$ (CZO) cap layers [17].

A typical x-ray diffraction pattern is shown in the Figure 5.2–8 a). The pattern was obtained with an area detector so note that a standard θ-2θ measurement corresponds to a line scan in the center of the image in Figure 5.2–8 a). YBCO films are epitaxial with no sign of polycrystallinity. After YBCO growth it is not possible to identify any CZO reflections but, on the contrary, a clear indication of the formation of $Ba(Ce,Zr)O_3$ is seen. Epitaxial relationship between YBCO film and the underlying ^{ABAD}YSZ layer is shown in the pole figure of Figure 5.2–8 b). The quality of this epitaxy is observed in Figure 5.2–8 c) where we

have plotted a detail around one of the ϕ-scan peaks of the (103) YBCO reflection. The measured FWHM of the YBCO is 5º, while the average value for ^{ABAD}YSZ was 9.5º.

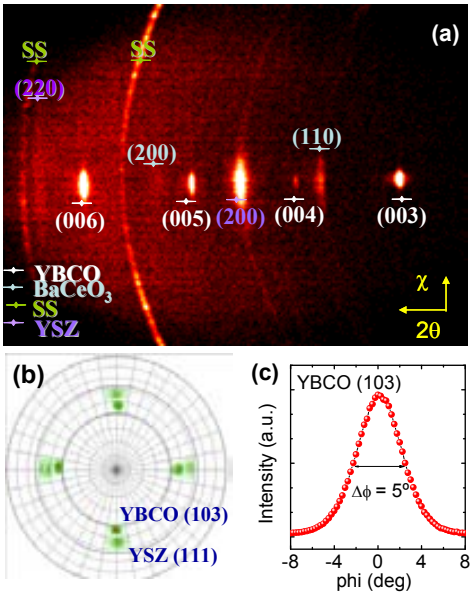

Figure 5.2–8 (a) X-ray diffraction pattern obtained with an area detector of a ^{TFA}YBCO film grown on ^{MOD}CZO buffered ^{ABAD}YSZ/SS metallic substrate. Epitaxial dots for the YBCO and YSZ layers are clearly distinguished of the polycrystalline rings coming from the stainless steel substrate. (b) Pole figure of the ^{TFA}YBCO film and of the ^{ABAD}YSZ layer showing the epitaxial relationship between them. (c) Detail of the Φ-scan of the (103) YBCO reflection. Arrows show the value of the full width at half maximum.

YBCO films were homogeneous and no sign of ab-oriented grains was found in scanning electron microscopy (SEM) images in agreement with the above x-ray diffraction results. An example of the surface of an YBCO coated conductor is shown in the SEM image of Figure 5.2–9. Note also that thin film is quite dense and only a few pores can be found. This morphology is quite similar to that obtained in TFA-YBCO films prepared on single crystalline substrates with the same growth conditions.

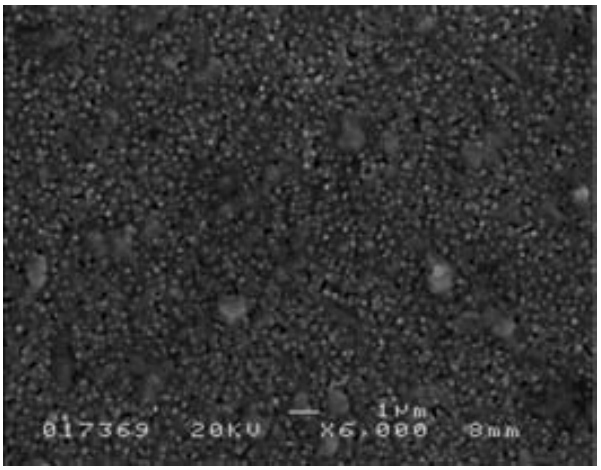

Figure 5.2–9 SEM image of the surface of a ^{TFA}YBCO/^{MOD}CZO/^{ABAD}YSZ/SS coated conductor.

Let us now examine the superconducting properties of the YBCO coated conductors. Figure 5.2–10 a) shows the field dependence at 77K of J_c of ^{TFA}YBCO coated conductor grown in this work (blue circles), compared to the typical results obtained for YBCO films grown onto ^{MOD}CZO-buffered YSZ single crystals (green circles). We first note that the critical current at self-field for ^{TFA}YBCO grown on ^{MOD}CZO/YSZ achieves a value of J_c = 5.2 MA/cm^2, the highest reported as far for a MOD multilayer, demonstrating the capabilities of CZO as cap layer. This value is almost a 25% higher than previously reported [12] and this enhancement is mostly due to the optimization of ^{TFA}YBCO growth and oxygenation conditions. For the coated conductor we have obtained J_c(77K) = 1.8 MA/cm^2 at self-field. This deviation between the behavior of both samples at low fields is a well-known effect usually attributed to that, in this field-region, J_c(H) of the coated conductor is dominated by pinning of Abrikosov-Josephson vortices at the grain boundaries [18,19]. However, above 2 T, it is the pinning of Abrikosov vortices inside the grains that controls the J_c(H) of the coated conductors and then, for high fields and up to the irreversibility line, we obtain the same curve as in single crystals [18]. This behavior has important implications for a practical point of view. Indeed, for applications intended to work at high fields the critical current will be dominated by the grain behavior thus making the requirements for epitaxial quality of the metallic substrate less restrictive and, as a consequence, more economic.

The results of Figure 5.2–10 a) suggest that the critical current density of the YBCO grains in the coated conductor, i.e, the intra-grain critical current was equal to the values obtained in single crystals and that the reduction of J_c at self-field is due to granularity. This can be confirmed by using the inductive methodology proposed by Palau et al. and [18] described in Chapter 6, Section 6.3.2. This methodology consists of analyzing the magnetic hysteresis loops of the YBCO coated conductor as the one shown in Figure 5.2–10 b). The most remarkable feature of this hysteresis loop is that the peak of magnetization in the returning branch of the loop occurs at a positive applied magnetic field (detail shown in the inset in Figure 5.2–10 b). This is due to the fact that the magnetization achieves a maximum when the local field in the grain boundaries is zero and this does not occur at zero applied field because the return field of the flux trapped into the grains must be taken into account. We have performed the above analysis to the coated conductor of Figure 5.2–10 b) and we have obtained J_c^{grain}(5K)= 40±10 MA/cm^2, $J_c^{intergrain}$(5K)= 13 MA/cm^2 and <2a> = 2 ± 1 μm which is consistent with the substrate grain size. Notice the high value of J_c^{grain}(5K) which, in addition, is in agreement with that obtained at 5K in single crystalline CZO buffered

films, hence confirming that the effects shown in Figure 5.2–10 a) are due to the granular behaviour of the coated conductor.

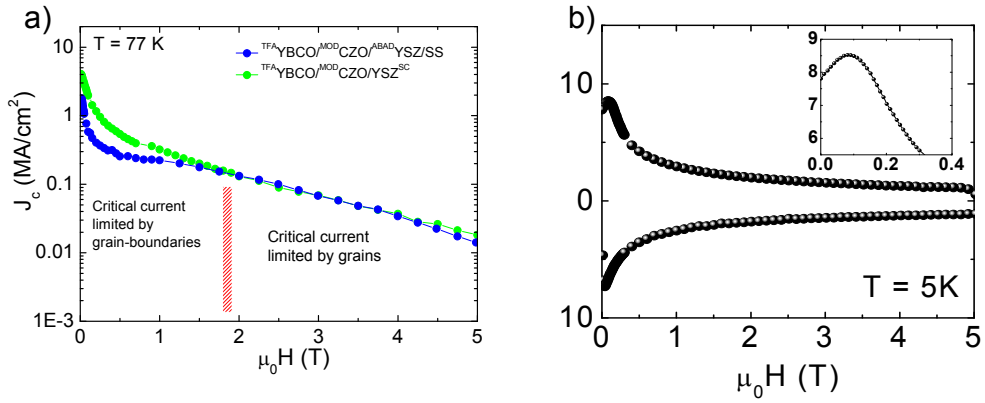

Figure 5.2–10 a) Critical current density at 77 K as a function of applied magnetic field parallel to the c-axis for ^{TFA}YBCO films grown on ^{MOD}CZO buffered YSZ single crystal (green circles) and ^{ABAD}YSZ/SS metallic substrate (blue circles). Note that granularity effects are only important below a crossover $H^* = 2T$. Above this field critical current of the coated conductors equals that of the single crystal suggesting that this regime is dominated by vortex pinning within the grains; b) Hysteresis loop of a YBCO coated conductor measured at 5K. The maximum of the magnetization appearing at positive applied field (see detail in the inset) is a sign of the granular behavior of the film. From the analysis of minor hysteresis loops an estimation of the intra-grain critical current density is obtained (see main text).

The angular dependence of the critical current density determined from transport measurements of the studied coated conductor was also analyzed. Figure 5.2–11 shows the $J_c(\theta)$ dependence at 7T and 77K for a ^{TFA}YBCO coated conductor (blue circles) and a ^{TFA}YBCO film grown on a ^{MOD}CZO cap layer on YSZ single crystal (red triangles). We see that the overall behavior for both samples is quite similar. Similar values of J_c for applied field parallel to the c-axis are obtained, as expected from results in Figure 5.2–10 a), though the critical current density for magnetic fields parallel to the ab-planes of the coated conductor is somehow reduced and consequently it has a smoother angular dependence. This could be a consequence of the intrinsic anisotropy of the YBCO material that brings the crossover field from grain to grain-boundary regime to much lower fields for H//ab [17].

Another feature that it is worth to mentioning is the clear peak for H//c. This peak is usually attributed to an anisotropic pinning contribution due to the presence of defects along the c-axis [20],[21]. This peak it was rarely observed in YBCO films grown by chemical methods because it is believed that their laminar growth mode does not promote such kind of defects. However, recently it was shown a similar peak for TFA-YBCO films grown on $^{MOD}La_{0.7}Sr_{0.3}MnO_3$ buffer layers [22] and on interfacial nanostructured substrates [23]. Although more microstructural information is needed to assess the origin of these effects, they are clearly suggesting that c-axis aligned defects in ^{TFA}YBCO films can be created and

their occurrence is probably linked to the morphology characteristics of the underlying surface that is controlling the YBCO nucleation [24].

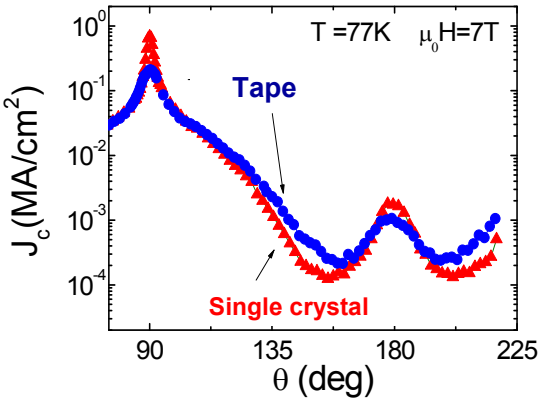

Figure 5.2–11 Angular dependence of the critical current density at 77K and 7T of ^{TFA}YBCO films grown on ^{MOD}CZO buffered YSZ single crystal (red triangles) and ^{ABAD}YSZ/SS metallic tape (blue circles) Field parallel to the ab-planes corresponds to 90º. At high fields and temperatures there is a peak when the field is parallel to the c-axis even in this chemical solution deposited YBCO films.

5.2.4.2. $^{PLD}CeO_2/^{ABAD}$YSZ/SS substrate

YBCO films were grown on the $^{PLD}CeO_2$ described in Section 5.2.2. The morphology of ^{TFA}YBCO deposited on $^{PLD}CeO_2/^{ABAD}$YSZ/SS buffer architecture at 770 °C-810ºC is shown in Figure 5.2–12. Figure 5.2–12 a) shows the optical microscopy surface view of YBCO after pyrolysis. Some defects due to pores and dust can be observed. The SEM micrograph (Figure 5.2–12 b)) indicates that there are no a/b grains on the surface. The porosity is still pretty high and could be improved.

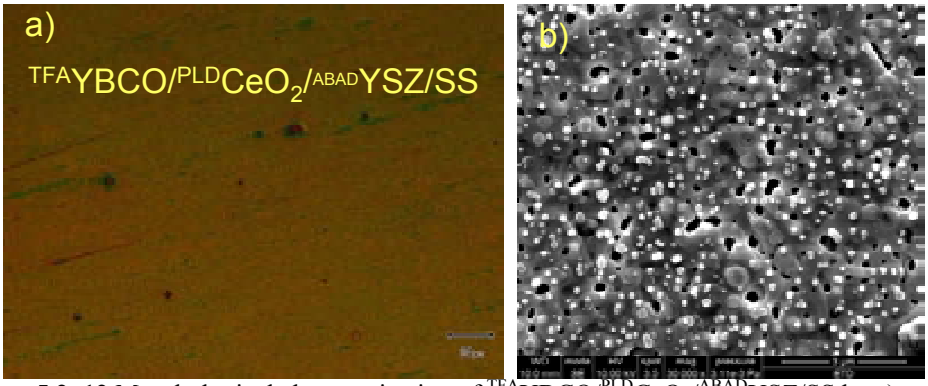

Figure 5.2–12 Morphological characterization of ^{TFA}YBCO/$^{PLD}CeO_2/^{ABAD}$YSZ/SS by a) optical microscopy; b) SEM.

Figure 5.2–13 shows the structural characterization by mean of XRD of a ^{TFA}YBCO film on $^{PLD}CeO_2/^{ABAD}$YSZ/SS with the thicknesses of about 200 nm, determined by TEM. As shown in Figure 5.2–13 c) and d), the misorientation in-plane was found to be around 5º (the same value was obtained on the tape with ^{MOD}CZO) and the one out-of-plane 4,4º. The good texture with the c-axis growth of YBCO can be noted in the pole figure (Figure 5.2–13 b)).

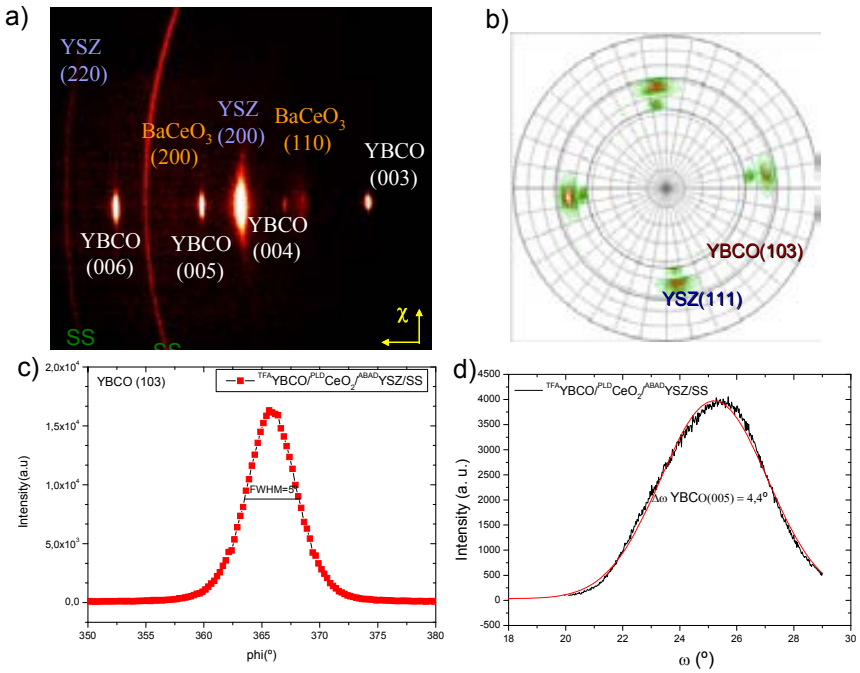

Figure 5.2–13 a) the 2D XRD pattern of ^{TFA}YBCO/^{PLD}CeO$_2$/^{ABAD}YSZ/SS; b) texture revealed by the pole figure; the misorientation in-plane (c) and out-of-plane (d). No secondary phases are seen.

With regard to the superconducting properties, we can note in Figure 5.2–14 a decrease of the self-field J_c for the YBCO on ^{PLD}CeO$_2$/^{ABAD}YSZ/SS compared with the YBCO on ^{MOD}CZO/^{ABAD}YSZ/SS (0,8 MA/cm^2 vs. 1,6 MA/cm^2 at 77K). This decrease can be explained by a reduced flat area of the cap layer from 68,5 % (^{MOD}CZO) to 58 % (^{PLD}CeO$_2$) which enhances granularity of the YBCO layer.

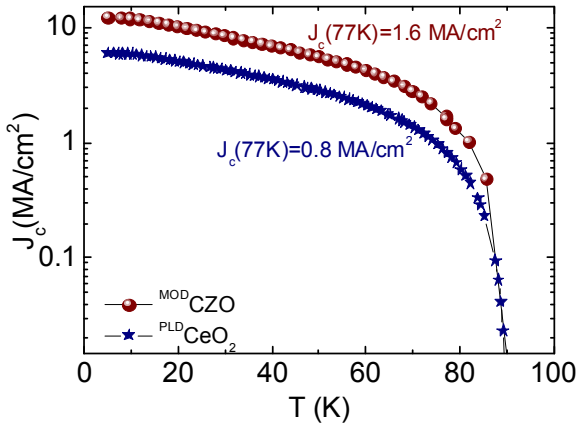

Figure 5.2–14 Comparison between the J_c temperature dependence in ^{TFA}YBCO/^{PLD}CeO$_2$/^{ABAD}YSZ/SS and ^{TFA}YBCO/^{MOD}CZO/^{ABAD}YSZ/SS.

The $T_{c,\ onset}$ was found to be 91,2 K (Figure 5.2–14 a)), the same that in the case of the single crystal. For the samples grown on metallic substrates we observe a broaden transition width when inductive measurements are performed. However a sharp transition is observed when T_c is measured by transport. This broadening can be attributed to low percolation in some regions of the sample due to the presence of inhomogeneous grain boundaries.

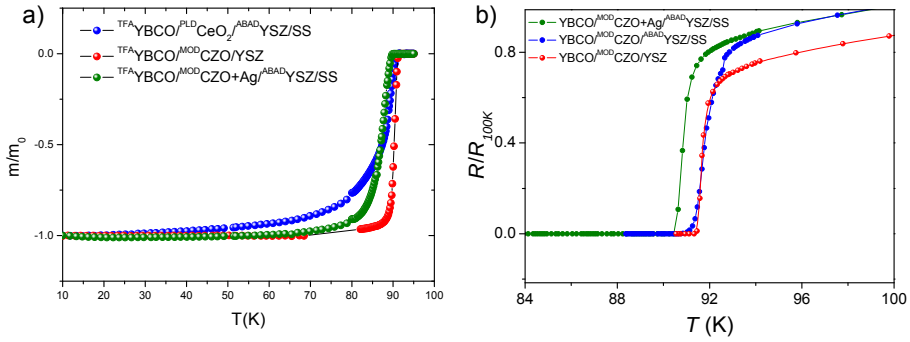

c)

Sample	T_c 10% (K)	T_c 50% (K)	T_c 90% (K)	$T_{c\ onset}$ (K)	ΔT_c (K)
^{TFA}YBCO/^{MOD}CZO/YSZ 770ºC - 810ºC	90	89.2	87.9	91.2	2.1
^{TFA}YBCO/^{PLD}CeO$_2$/^{ABAD}YSZ/SS 770ºC - 810ºC	90	87.3	68.5	91.2	21.5
^{TFA}YBCO/^{MOD}CZO+Ag/^{ABAD}YSZ/SS 770ºC - 810ºC	88.7	87.1	81.5	89.8	7.2

Figure 5.2–15 a) Temperature dependence of magnetic susceptibility measured at H = 2 Oe with SQUID for two CC on tape (blue and green) compared with CZO buffered YSZ; b) Resistive measurements values for the T_c of a film grown on single crystal and also on SS tape (^{PLD}CeO$_2$ and ^{MOD}CZO); c) values of T_cs and also of the transition widths of single crystal and tapes.

We mentioned before that the J_c decreases in the case of YBCO on ^{PLD}CeO$_2$ because of the decreasing of the flatness of the cap layer from 68,5 % (^{MOD}CZO) to 58 % (^{PLD}CeO$_2$). The flat area fraction is an extremely crucial parameter to take into consideration for the epitaxial growing of high quality multilayers as it was demonstrated before in the group and in the Chapter 4. For that purpose we will concentrate in the example of YBCO superconducting multilayers grown on top of cap layers with different surface morphologies. We have taken as a key parameter strongly influenced by the epitaxial quality, the self-field critical current density J_c of YBCO layers on different single crystals and on metallic substrates [25]. Figure 5.2–16 shows the self-field J_c at 77K of YBCO thin films as a function of flat area fraction of the underlying doped and undoped CeO_2 cap layer for single crystals (blue circles) and for metallic substrates (red stars). A clear shift towards reduced J_c values is detected in the case of the metallic substrates which matches with the granularity effect previously demonstrated in these CCs. The origin of this reduced intergranular J_c is

unknown at present. An increasing of the flat area in the case of the tapes is necessary for increasing the superconducting properties of the films (Figure 5.2–16 a)). There is still room for improvement as it can be seen from the J_c dependence of the in-plane misorientation (Figure 5.2–16 b)). We could speculate on the phenomenon mentioned in the previous chapter of mesoscopic strain limiting J_c^{GB}. It might happen than that this effect has not been completely eliminated in the CCs. Unfortunately, however, up to now we have been unable to determine experimentally the microstrain in YBCO films grown on metallic substrates.

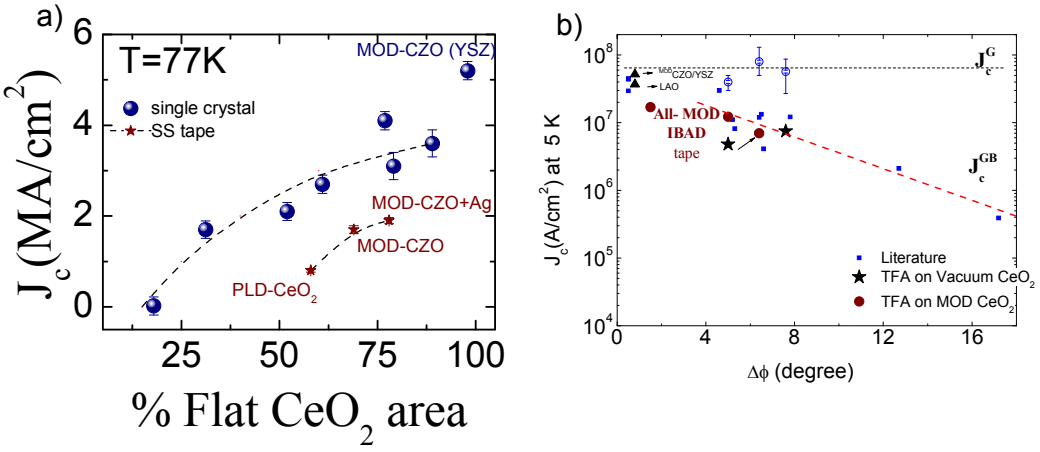

Figure 5.2–16 a) Correlation between J_c and flat area in the case of single crystals and CC; b) J_c dependence of the in-plane misorientation for different single crystals and tapes.

For studying the microstructure, a ^{TFA}YBCO/^{PLD}CeO$_2$/^{ABAD}YSZ/SS sample was prepared for High-resolution Transmission Electron Microscopy (HRTEM) using a site-selective focused ion-beam (FIB) milling technique, typically employing an in-situ lift-off procedure. The step by step preparation process in the in-situ FIB milling is presented in Figure 5.2–17. After the alignment of the interest zone horizontally and finding the Z position in the center of image, a protective 15,4μm x 0,6μm x 2,15μm platinum strip is deposited (Figure 5.2–17 a)). After this, milling of the "cleanup-trenches" at the front and back of the strip is performed (Figure 5.2–17 b)-e)) until 2 μm Pt strip remains. After rotation for making the specimen visible, using a low current beam current, the specimen is undercut and cut free from the left side (Figure 5.2–17 f)). A small portion is kept attached to the bulk sample in the upper right corner for maintaining the orientation. In the next stage, the Pt needle is slowly brought in, followed by the nanomanipulator which contacts the specimen in the upper left corner (Figure 5.2–17 g), h)). The contact is made by 2 μm of platinum and after that, a 300 pA beam current cuts the specimen free from the bulk sample (Figure 5.2–17 i)). The specimen is then attached to a copper grid (Figure 5.2–17 l)) and a picometric beam current is used to cut the probe free from the specimen (Figure 5.2–17 m)). For doing

HRTEM, this probe is not thin enough and for that a low beam current is used to reach the desired thickness, in this case 45,8 nm (Figure 5.2–17 n)-p)) [26].

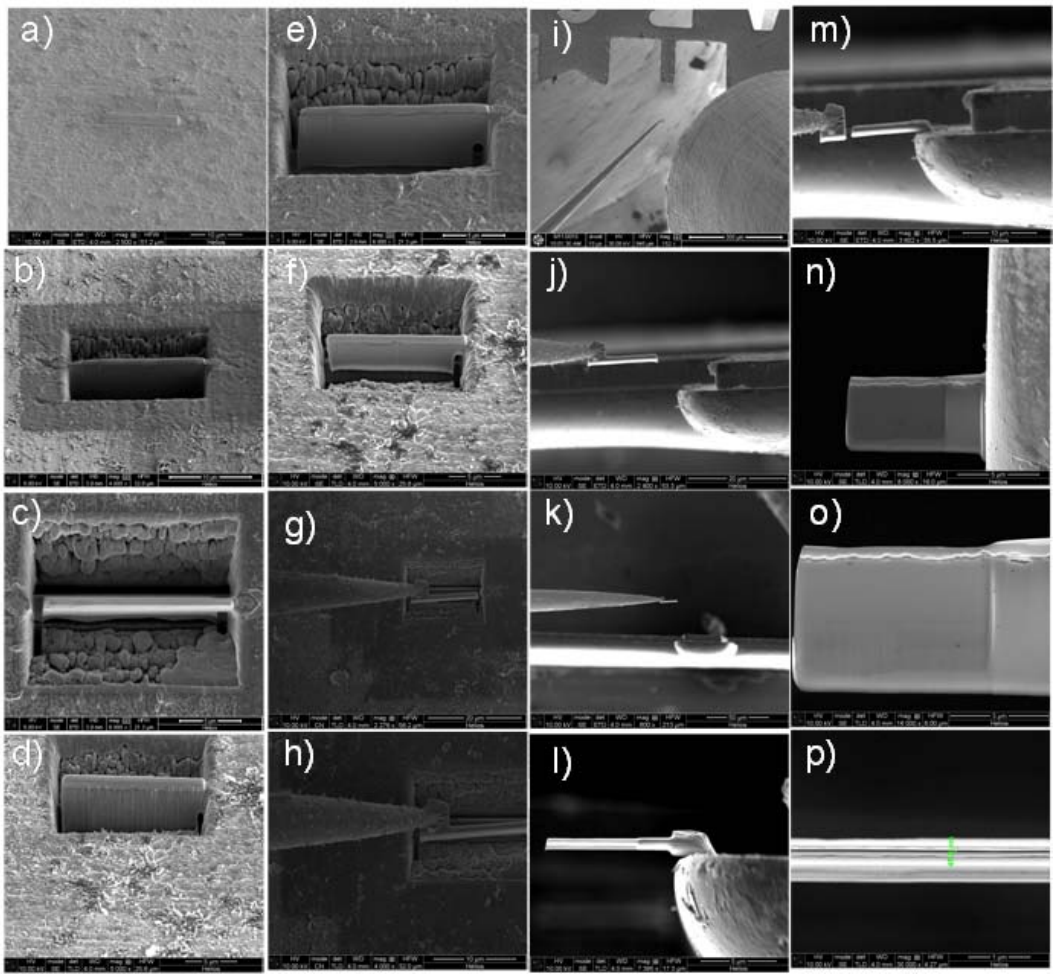

Figure 5.2–17 Step-by-step procedure for the HRTEM specimen preparation by an in-situ FIB milling process. a) deposition of a protective platinum strip; b)-f) the milling processes; g)-k) the in-situ specimen lift-off procedure; l)-m) cutting free the probe from the specimen; n)-o) milling for obtaining a thinner probe; p) the final thin specimen.

Due to some problems in the sample preparation the final lamellae was too thick for HRTEM observation. Because of that, only EELS and STEM (Z-contrast) analysis was made. The following composition of different HAADF (High-Angle Annular Dark-Field Scanning Transmisson) micrographs reveals how the geometry of the tape is, along almost 6 μm of sample (Figure 5.2–18 a)). The white thick layer on top corresponds to the Au protection layer deposited before FIB preparation. Different steps above YBCO can be distinguished due to the different height of the grains. Also there are some regions with darker contrast probably related to secondary phases (white arrows). Further HRTEM studies are needed for giving us more detailed information.

Figure 5.2–18 b) and c) correspond to an enlarged area of the sample. In the bright field (BF) image, due to diffraction contrast, the different grains of YBCO displayed on top of

YSZ are clearly shown. With ADF imaging (in STEM mode) it is possible to view a chemical distribution and how the architecture of the tape is. Every layer on the sample is labeled on the right side of the figure. An EELS profile was made across the green line showed in Figure 5.2–18 d) and the relative composition profile is displayed in Figure 5.2–18 e). The expected CeO_2 and YSZ layers are present. The tape features a ~30 nm thick layer of CeO_2 on top of YSZ. It is worth to notice that the barium content seems to be on both YBCO and inside the composition of the CeO_2 and even on the top of YSZ. Also there is slightly more Cu signal in the precipitate (green arrow) and a decreasing in the Ba signal suggesting that could be a Cu-rich secondary phase; again, the HRTEM analysis will reveal it.

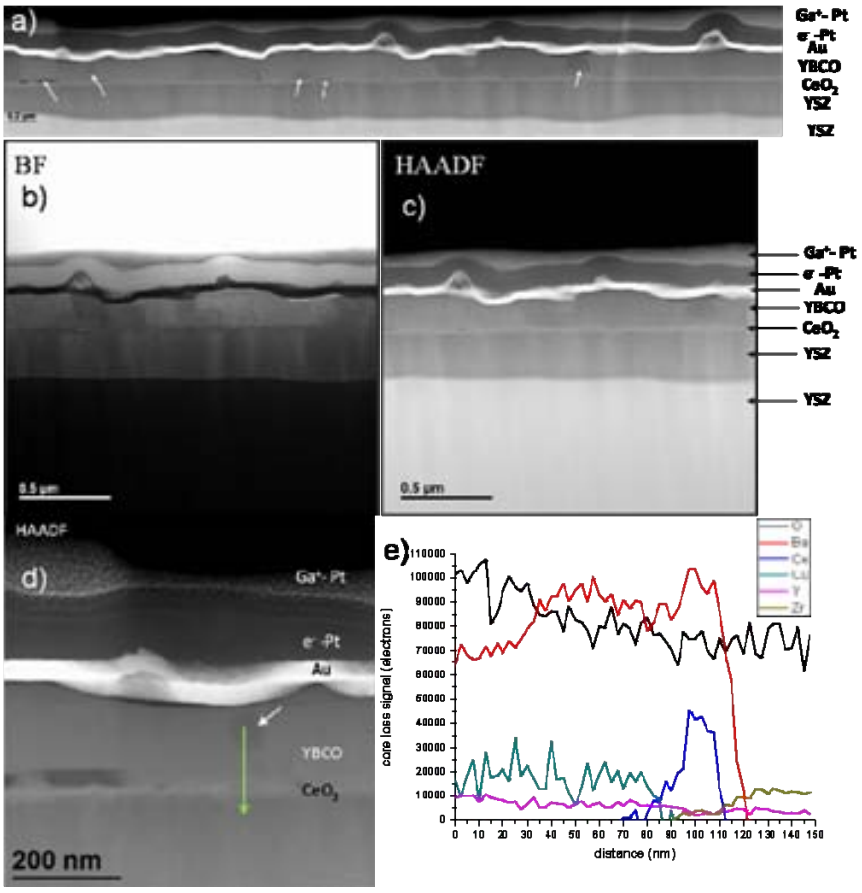

Figure 5.2–18 a) TEM image of the 6 µm of ^{TFA}YBCO/^{PLD}CeO_2/^{ABAD}YSZ/SS; b) Bright field (BF) image of an enlarged area; c) High-Angle Annular Dark-Field Scanning Transmisson (HAADF) micrograph; d) EELS profile along the green line; e) correspondent analysis of the previous EELS profile.

5.2.5. YBCO on Ag-CZO

As noted previously, one of the main attractions of second-generation wire based on YBCO is the promise that it will be useful at liquid nitrogen temperature in applications such as magnets, motors, and generators where high magnetic fields will be present [27]. To study this issue in detail, transport measurements were performed in magnetic fields in the case of the two CC, on the undoped ^{MOD}CZO and on Ag doped ^{MOD}CZO. Figure 5.2–19 a) shows the magnetic-field dependence, J_c (H//c and H//ab) at 77K for both of the samples. A slightly increase of the J_c at self field is registered from 1,75 MA/cm^2 (^{TFA}YBCO/^{MOD}CZO/^{ABAD}YSZ/SS) to 1,94 MA/cm^2 (^{TFA}YBCO/4,58% Ag-^{MOD}CZO 1h/^{ABAD}YSZ/SS). From the pinning point of view, at low magnetic fields between 0,004 T and 1 T, it seems that the number of defects along c axis increases in the sample containing Ag-CZO, and so, a pinning enhancement is registered compared with a standard CC sample (^{TFA}YBCO/^{MOD}CZO/^{ABAD}YSZ/SS, open red circles in the graph). The irreversibility field is around 6 T for both of the CC. The most important thing here is that, by decreasing the processing time of the CZO from 8 hours to 1 hour when doping with silver, the superconducting properties are not affected. This is a quite good achievement especially for the industry.

The PPMS allowed us also to characterize the two coated conductor tapes in fields up to 9 T. The measurements are shown in Figure 5.2–19 b) where the measurements have been done at six magnetic field levels from 0.1 T to 9 T. At each level, J_c, has been measured as a function of field orientation angle. The distinctive features are the intrinsic pinning peak at 90º (field parallel to the film plane), and the peaks at 180º, which correspond to flux pinning by c-axis correlated defects. When increasing the magnetic field, a higher angular dependence of J_c is observed for the ^{TFA}YBCO/4,58% Ag-^{MOD}CZO 1h/^{ABAD}YSZ/SS (circles) compared with ^{TFA}YBCO/^{MOD}CZO/^{ABAD}YSZ/SS (continuous line).

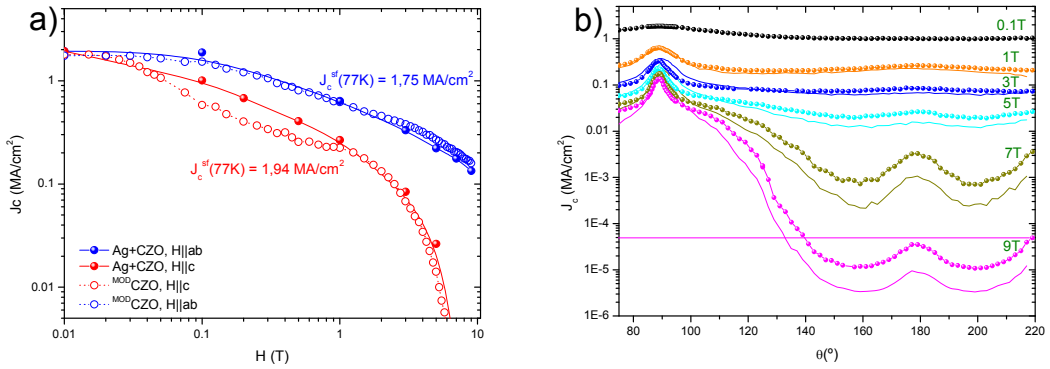

Figure 5.2–19 a) The magnetic field dependence of J_c when H//ab and H//c for ^{TFA}YBCO/^{MOD}CZO/^{ABAD}YSZ/SS and ^{TFA}YBCO/Ag-^{MOD}CZO/^{ABAD}YSZ/SS;b) comparison between magnetic field dependence of two CC: ^{TFA}YBCO/^{MOD}CZO/^{ABAD}YSZ/SS (continuous line) and ^{TFA}YBCO/Ag -^{MOD}CZO/^{ABAD}YSZ/SS (dots), at 77K over a full range of orientations.

5.2.6. Effect of doping YBCO with Ag on the ^{MOD}CZO/^{ABAD}YSZ/SS

We have shown in Chapter 4, Section 4.2.3, that the addition of small quantities of silver salts in the YBCO precursor solution leads to a flatter surface of the superconductor on YSZ single crystals and also that a lower temperature can be implemented for the growth process. In Coated Conductors, it is reported that the silver reduces the GBs and this way an enhancement of the J_c is noted. After all this, we studied the effect of the silver on the ^{TFA}YBCO-5%Ag/ ^{MOD}CZO/^{ABAD}YSZ/SS grown at low temperature and at high temperature. The characterization was done by using XRD and also SEM. Figure 5.2–20 a) shows the two θ-2θ plots for a Ag- doped CC grown at 740ºC and at 770ºC-810ºC where we can see that no silver phases appears and also that YBCO is c-axis oriented. The morphology obtained by SEM keeps the terraced surface obtained on YSZ and no a/b grains are observed (Figure 5.2–20 b)). The porosity is still too high and a method to try to decrease this is by increasing the temperature (i.e. 780ºC).

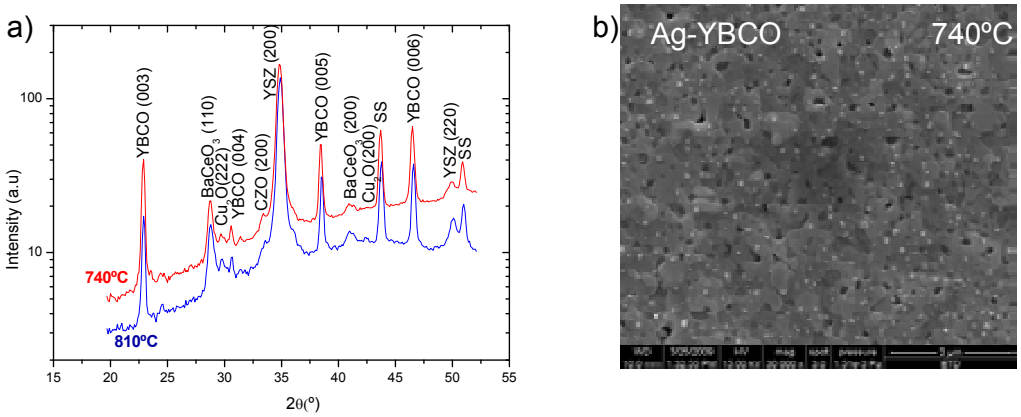

Figure 5.2–20 a) XRD integrated GADDS frames in the case of ^{TFA}YBCO-5%Ag/ ^{MOD}CZO/^{ABAD}YSZ/SS grown at 740ºC and 810ºC; b) SEM image of the sample grown at low temperature where large grains are formed.

The magnetic field dependence of J_c at 77K for several different Ag doped CCs are shown in Figure 5.2–21 a) (0,8 MA/cm^2-740ºC vs. 0,4 MA/cm^2-810ºC). No enhancement of J_c at self field is noted compared with a ^{TFA}YBCO/ ^{MOD}CZO/^{ABAD}YSZ/SS (1,7 MA/cm^2). From the J_c values obtained at low temperature (740ºC) and high temperature (810ºC), a higher J_c seems to be obtained with the growth at low temperature. The T_c value of the Ag doped CC (810ºC) registered a drop being 88.7K if we compared with the value obtained on single crystal (90.2K). The transition width is very high (20K) when doping with Ag, which can explain the low J_c due to inhomogenities or strain (Figure 5.2–21 b)). As we showed before (Section 5.2.4.2), this broadening can be attributed to low percolation in some regions of the sample due to the presence of inhomogeneous grain boundaries. A more detailed study of the influence of Ag addition on the growth needs to be performed in order to obtain optimal conditions for high J_c superconductors.

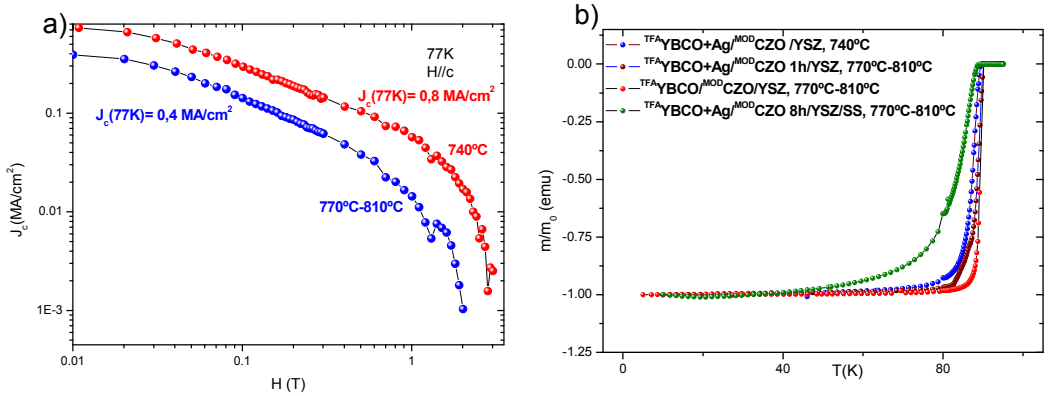

c)

Sample	T_c 10% (K)	T_c 50% (K)	T_c 90% (K)	$T_{c\ onset}$ (K)	ΔT_c (K)
^{TFA}YBCO+5% Ag/^{MOD}CZO 1h/YSZ **770ºC - 810ºC**	**89.6**	**88.4**	**84**	**90.2**	**5.6**
^{TFA}YBCO+5% Ag/^{MOD}CZO/YSZ **740ºC**	**88.7**	**87.6**	**82.7**	**89.5**	**6**
^{TFA}YBCO/^{MOD}CZO/YSZ **770ºC - 810ºC**	**90**	**89.2**	**87.9**	**90.2**	**2.1**
^{TFA}YBCO+5% Ag/^{MOD}CZO 8h/^{ABAD}YSZ/SS **770ºC - 810ºC**	**87.5**	**83.2**	**67**	**88.7**	**20.5**

Figure 5.2–21 a) J_c magnetic field dependence for two temperature growth for ^{TFA}YBCO-Ag/ ^{MOD}CZO/^{ABAD}YSZ/SS; b) Temperature dependence of magnetic susceptibility measured at H = 2 Oe, ZFC, with SQUID for Ag doped YBCO on single crystal (blue and wine) and tape (olive) compared with a standard undoped YBCO/^{MOD}CZO/YSZ (red); c) values of T_cs and transition widths.

5.3. Conclusions

In this chapter, Coated Conductors on metallic substrates using sol-gel method were carefully obtained and investigated. The first part is dedicated to a new method for CC production, similar to IBAD (Ion Beam Assisted Deposition), which it is called Alternating

Ion Beam Assisted Deposition (ABAD) and utilizes the alternation of the molecular beam and the ion beam. Several non-magnetic 0,1 mm thick CrNi Stainless Steel (SS) tapes with ^{ABAD}YSZ deposited on them were received from Bruker HTS, Germany. Although the rms roughness value is relatively low (1,8 nm) it is interesting to note that flat area fraction is only 49%. XRD demonstrates the predominant *c*-axis orientation of the layers in the sample with in-plane misorientation of 10,2º and out-of-plane of 5,5º. The deposition of the YBCO superconducting film directly on the ^{ABAD}YSZ/SS was not fruitful because cracks appeared due to the high lattice mismatch between YSZ and YBCO (-5,71%). Because of this, the deposition of a second buffer, in this case $Ce_{0.9}Zr_{0.1}O_2$, is necessary (misfit YBCO-CeO_2 = -0,52%). Thin CZO films of about 20-30 nm were deposited by spin coating on the as-received ^{ABAD}YSZ/SS using a high temperature treatment (900ºC). In spite of a rms roughness value of 3 nm, the flat area fraction has been significantly increased, being now 68,5%, due to the characteristic behaviour of CZO that tends to develop a terraced surface morphology. J_cs of 1,75 MA/cm^2 were obtained. For comparison with the ^{MOD}CZO grown in ICMAB on ^{ABAD}YSZ/SS, several tapes with $^{PLD}CeO_2$/^{ABAD}YSZ/SS received from the same company-Bruker HTS-were investigated. These films showed low roughness between 2-4 nm with some spikes of about 20-25 nm from place to place. Following the route initiated for the single crystals when small quantities of silver salt were added in the CZO precursor solution, a slightly increase of the J_c at self field is registered from 1,75 MA/cm^2 (^{TFA}YBCO/^{MOD}CZO/^{ABAD}YSZ/SS) to 1,94 MA/cm^2 (^{TFA}YBCO/4,58% Ag-^{MOD}CZO 1h/^{ABAD}YSZ/SS).

YBCO doped Ag films were obtained at low and high temperatures. Contrary to what we observed on single crystals, in the case of the SS tapes, the sample grown at 740ºC presents a higher J_c (0,8 MA/cm^2) but still lower than a standard tape (1,75 MA/cm^2).

5.4. References

[1] A. P. Malozemoff and et al., "Progress in high temperature superconductor coated conductors and their applications," Superconductor Science and Technology **21** (3), 034005 (2008).

[2] M. W. Rupich, X. P. Li, C. Thieme et al., "Advances in second generation high temperature superconducting wire manufacturing and R&D at American Superconductor Corporation," Superconductor Science & Technology **23** (1), 9 (2010).

[3] David Larbalestier, Alex Gurevich, D. Matthew Feldmann et al., "High-Tc superconducting materials for electric power applications," Nature **414** (6861), 368-377 (2001).

[4] A. Goyal, D. P. Norton, D. K. Christen et al., "Epitaxial superconductors on rolling-assisted biaxially-textured substrates (RABiTS): a route towards high critical current density wire," Applied Superconductivity **4** (10-11), 403-427 (1996).

[5] K. J. Song, S. Kang, S. H. Kim et al., "The comparative study of magnetic properties for YBCO coated conductors based on RABiTS and IBAD templates," Physica C: Superconductivity **470** (20), 1419-1421.

[6] "2010 Advanced Cables and Conductors Peer Review," Alexandria, Virginia (2010).

[7] Y. Shiohara and et al., "Present status and future prospect of coated conductor development and its application in Japan," Superconductor Science and Technology **21** (3), 034002 (2008).

[8] T. Izumi; Y. Shiohara, "R&D of coated conductors for applications in Japan," Physica C (2010).

[9] A. Usoskin, K. Schlenga, and M. Waschulewski, "Low Cost Processing," CCA 2010, Japan (2010).

[10] A. Usoskin and L. Kirchhoff, "In-Plane Texturing of Buffer Layers by Alternating Beam Assisted Deposition: Large Area and Small Area Applications," Mater. Res. Soc. Symp. Proc. **1150**, 117-122 (2009).

[11] A. Usoskin, L. Kirchhoff, J. Knoke et al., "Processing of long-length YBCO coated conductors based on stainless steel tapes," Ieee Transactions on Applied Superconductivity **17** (2), 3235-3238 (2007).

[12] M. Coll, J. Gazquez, R. Huhne et al., "All chemical $YBa_2Cu_3O_7$ superconducting multilayers: Critical role of CeO_2 cap layer flatness," Journal of Materials Research **24** (4), 1446-1455 (2009).

[13] A. Hallbauer, L. Kirchhoff, A. Rutt et al., "Alternating beam assisted deposition (ABAD) and it's up-scaling towards large area manufacturing of HTS coated conductors," CCA 2009, Barcelona (2009).

[14] M. Coll, J. Gazquez, F. Sandiumenge et al., "Nanostructural control in solution-derived epitaxial Ce1-xGdxO2-y films," Nanotechnology **19** (39) (2008).

[15] S S Wang, Z Han, W Schmidt et al., "Chemical solution growth of CeO_2 buffer and YBCO layers on IBAD-YSZ/Hastelloy templates " Supercond. Sci. Technol. **18**, 1468 (2005).

[16] A. Usoskin and H. C. Freyhardt, "YBCO-Coated Conductors Manufactured by High-Rate Pulsed Laser

Deposition," MRS BULLETIN, **29** (No. 8), 583-589 (August 2004).

[17] V. R. Vlad, K. Zalamova, M. Coll et al., "Growth of Chemical Solution Deposited $^{TFA}YBCO/^{MOD}(Ce, Zr)O_2/^{ABAD}YSZ/SS$ Coated Conductors," Ieee Transactions on Applied Superconductivity **19** (3), 3212 (2009).

[18] A. Palau, T. Puig, J. Gutierrez et al., "Pinning regimes of grain boundary vortices in $YBa_2Cu_3O_{7-x}$ coated conductors," Physical review B **73** (13) (2006).

[19] L. Fernandez, B. Holzapfel, F. Schindler et al., "Influence of the grain boundary network on the critical current of $YBa_2Cu_3O_7$ films grown on biaxially textured metallic substrates," Physical review B **67** (5), 052503 (2003).

[20] L. Civale, B. Maiorov, A. Serquis et al., "Angular-dependent vortex pinning mechanisms in $YBa_2Cu_3O_7$ coated conductors and thin films," Applied Physics Letters **84** (12), 2121-2123 (2004).

[21] J. Gutierrez, T. Puig, and X. Obradors, "Anisotropy and strength of vortex pinning centers in $YBa_2Cu_3O_{7-x}$ coated conductors," Applied Physics Letters **90** (16) (2007).

[22] A. Hassini, A. Pomar, J. Gutierrez et al., "Atomically flat MOD $La_{0.7}Sr_{0.3}MnO_3$ buffer layers for high critical current $YBa_2Cu_3O_7$ TFA films," Superconductor Science & Technology **20** (9), S230-S238 (2007).

[23] J. Gutierrez, T. Puig, M. Gibert et al., "Anisotropic c-axis pinning in interfacial self-assembled nanostructured trifluoracetate-$YBa_2Cu_3O_{7-x}$ films," Applied Physics Letters **94** (17) (2009).

[24] A. Pomar, M. Coll, A. Cavallaro et al., "Interface control in all metalorganic deposited coated conductors: Influence on critical currents," Journal of Materials Research **21** (9), 2176-2184 (2006).

[25] M. Coll, A. Pomar, T. Puig et al., "Atomically Flat Surface: The Key Issue for Solution-Derived Epitaxial Multilayers," Applied Physics Express **1** (12) (2008).

[26] Zia Rahman, Satyajit Shukla, Hyoung Cho et al., "Tutorial: In-Situ Site-Selective FIB for High Resolution TEM Sample Preparation," Microscopy and Analysis **20** (3), 9-11, UK (2006).

[27] S. R. Foltyn, P. N. Arendt, P. C. Dowden et al., "High-T_c coated conductors-performance of meter-long YBCO/IBAD flexible tapes," Applied Superconductivity, IEEE Transactions on **9** (2), 1519-1522 (1999).

CHAPTER 6 NANOCOMPOSITES FILMS – A ROUTE FOR VORTEX PINNING ENHANCEMENT

Enhancing the in-field critical current density (J_c) is a key research topic in the production and development of second generation (2G) superconductors. This is a requirement of large-scale applications in electric power industry which need large supercurrents in high applied magnetic fields. A potential route for achieving this goal is by introducing artificial defects in the superconductor matrix in order to produce modifications in its microstructure [1].

This chapter is dedicated to the development of $BaZrO_3$-$YBa_2Cu_3O_{7-x}$ and $BaCeO_3$-$YBa_2Cu_3O_{7-x}$ nanocomposites thin films by MOD using the in-situ approach. Barium zirconate is the most attractive material to induce artificial pinning centers both in YBCO thin films, in order to increase the critical current density. Detailed characterization by SEM, XRD and TEM of $BaZrO_3$ (BZO) nanocomposite grown by MOD will be presented. Determination of epitaxial/random fraction of nanoparticles will be done and also the micro strain along c axis will be studied. The transfer of this successful approach to SS metallic tapes will be discussed. The effect of another oxide, $BaCeO_3$, with perovskite structure was investigated as a new way to enhance the pinning and the results are reported here.

6.1. State of the Art

Power applications of superconductors require conductors with high pinning forces at high temperatures. For such applications, the most promising materials are the second-generation $YBa_2Cu_3O_{7-x}$ (YBCO) tapes. The epitaxial thin-film structure of these materials allows generation of the highest critical-current densities observed so far in high-temperature superconductors (HTS), although the vortex-pinning mechanism remains controversial. Achieving high pinning forces requires an effective immobilization of vortices in a dense structure of defects with nanometric dimensions [2]. There are a number of defect types that can act as pinning centers (Figure 6.1–1): precipitates, twin boundaries, in-plane misorientation, threading dislocations, surface roughness, antiphase boundaries, voids, out-of-plane misorientation, misfit dislocations, planar defects, point defects [3].

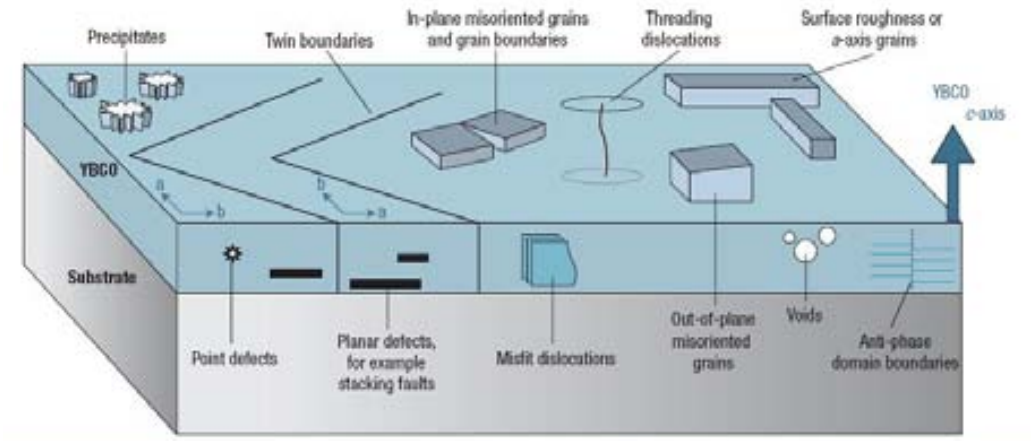

Figure 6.1–1 Many thin-film defects have been proposed as flux pinning sites in YBCO; anything that locally disturbs the crystalline perfection over a scale of 1–10 μm is a candidate. Strain fields associated with defects may also pin vortices. The challenges in engineering defect structures for the best performance are to determine which ones are beneficial, and to tailor their density to produce the desired effect without obstructing current.

Research carried out by several authors has shown that flux pinning in PLD-YBCO and MOD-YBCO films can be improved by controlling nanostructure via BZO doping. There are 3 reasons for which BZO is used as artificial pinning centers in YBCO matrix:

(a) the melting temperature of BZO compared with YBCO is high and this way, the growth kinetics is slow and the resultant particles are small;

(b) in the YBCO, zirconium does not substitute, so there is no reactivity between BZO and YBCO;

(c) although BZO can grow epitaxial with YBCO, it has a large lattice mismatch (approximatively 9%), so strain between the phases could introduce defects for enhanced pinning [4].

Nowadays, there are studies from groups all over the world about these artificial pinning centers (APC) in the superconducting matrix [5],[6]. A point to improve in this field is the superconducting performance under magnetic fields. By physical methods, in the development of the PLD process for superconducting layers, the BZO nano-rods dispersed in the GdBCO phase improved the J_c value under magnetic fields (H//c) obtaining 60 m-long GdBCO tape with BZO nano-rods with the I_c of 30,5 A [7]. In the case of the TFA-MOD process it is considered that it is more difficult to introduce the artificial pinning centers into the YBCO films, but it was successfully realized by ISTEC achieving I_c values of 115A (1T) and 35 A (3T) for BZO-$Y_{0.77}Gd_{0.23}Ba_2Cu_3O_{7-y}$(YGdBCO). At Los Alamos Laboratory, further potential of the films was evaluated in ultra-high magnetic fields and it was confirmed that high irreversibility fields over 50T for YGdBCO films with BZO

nanoparticles can be achieved [8]. Kobayashi H. et al. [9] fabricated YBCO multilayer films by Pulse Laser Deposition (PLD) on $^{PLD}CeO_2/^{IBAD}GZO$/Hastelloy in which a pinning effective "bamboo structure", formed by a columnar microstructure of YBCO/BZO nanorods can be seen.

The control of the combination of two effective pinning centers (randomly distributed nanoparticles and self-assembled columnar defects) is possible and effective. By simply changing the temperature or growth rate during pulsed-laser deposition of $BaZrO_3$-doped $YBa_2Cu_3O_7$ films, it was possible to vary the ratio of these defects, tuning the field and angular critical-current (I_c) performance to maximize I_c. The defects microstructure is governed by the growth kinetics and the best results are obtained with a mixture of splayed columnar defects and random nanoparticles (Figure 6.1–2) [10].

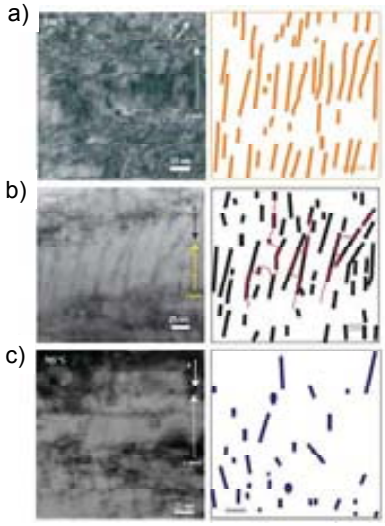

Figure 6.1–2 Variation of microstructure with growth temperature. a–c; cross-sectional TEM using the bright-field condition (left column) of film with T_{dep} = 840ºC (a), T_{dep} = 785ºC (b) and T_{dep} = 765ºC (c) and corresponding vectored positions of defects (right column). Red lines in the right panel of b represent possible configurations of vortices pinned by several defects [10].

Strickland N. M. [11] et al. obtained thick MOD-based YBCO films doped with BZO nanoparticles on Ni-5%W buffered Y_2O_3/YSZ/CeO_2 metallic substrates. Their results have shown that J_c is enhanced when H//c and remain unchanged for field applied parallel for up to 10%BZO addition. The I_c at 300-400 mT perpendicular field is 66% enhanced with a maximum pinning force of 5 GN/m^3. Gutierrez J., Llordes A. et al. [2] demonstrated that in chemically derived BZO/YBCO, two types of nanodots coexist:

a) epitaxial, nucleating heterogeneously at the interface with the substrate;
b) randomly oriented in the YBCO matrix, which are mainly responsible for the enhancement of the pinning.

A maximum pinning force of 78 GNm^{-3} was achieved at 65K for $SrTiO_3$ (STO) single crystals; this value is 500% higher than that of low-temperature NbTi superconductors at 4.2 K thus rising the possibility of many high-field applications [2]. The influence of the amount of $BaZrO_3$ (BZO) on the structure and properties of $YBa_2Cu_3O_{7-x}$ (YBCO)/LAO films was systematically investigated. The YBCO films having 7 mol % BZO have a maximum critical current density (J_c) value (77 K, 0 T) of 6.0 MA/cm^2. The enhanced J_c derives from a high density of BZO nanoparticles existing in the YBCO matrix. It is believed that with increasing BZO amount, J_c of the YBCO films begins to decrease due to larger particles [12].

In literature, there are two principal techniques for the preparation of the nanocomposites: *in situ* and *ex situ* approach. The experimental preparation of ^{TFA}YBCO nanocomposites by *in situ* technique is based on the modification of the YBCO precursor solution by adding small quantities of salts in the solution [13]. In the *ex situ* approach, the most important feature is that the embedded nanostructures do not perforce showing a specific crystallographic orientation with the surrounding YBCO matrix and the nucleation is homogeneous within the amorphous precursor matrix [14].

In this thesis, all the nanocomposite samples were prepared using the in-situ technique.

6.2. $BaZrO_3$-YBCO growth and characterization on ^{MOD}CZO/YSZ

6.2.1. Preparation of the BZO doped YBCO precursor solution

The standard process for the preparation of YBCO solution optimized in ICMAB was modified and used also for the preparation of the nanocomposite precursor solution [15]. The mechanism of the preparation is very simple and can be seen in the Figure 6.2–1 (the example presented is the typical one for a ^{TFA}YBCO solution with 7% BZO dopant). Initial YBCO solution was compensated in order to achieve the 1:2:3 concentration adding small quantities of $Y(TFA)_3$) and $Ba(TFA)_2$ salts. For 7% BZO dopant phase are needed n mols of $Ba(TFA)_2$ and n mols $Zr(acac)_4$ in 2 ml of YBCO solution. If the Zr salt was brought from Aldrich, the Ba salt used was synthesized in the lab at T_{amb} resulting from the reaction between $BaCO_3$ and trifluoroacetic acid (the final white salt was obtained after performing an evaporation of the solvents under vacuum at T~85°C). Until reaching the final masses, we took into account that, in the $BaZrO_3$ structure, Y substitutes partially Zr and for this reason, small quantity of $Y(TFA)_3$ (aprox. 20% of Zr) were added at the final solution [13]. After

stirring and filtering, the resultant BZO-YBCO solution was sealed in a glass vial under N_2 atmosphere, and this way, it was found to be stable aprox. 2 weeks.

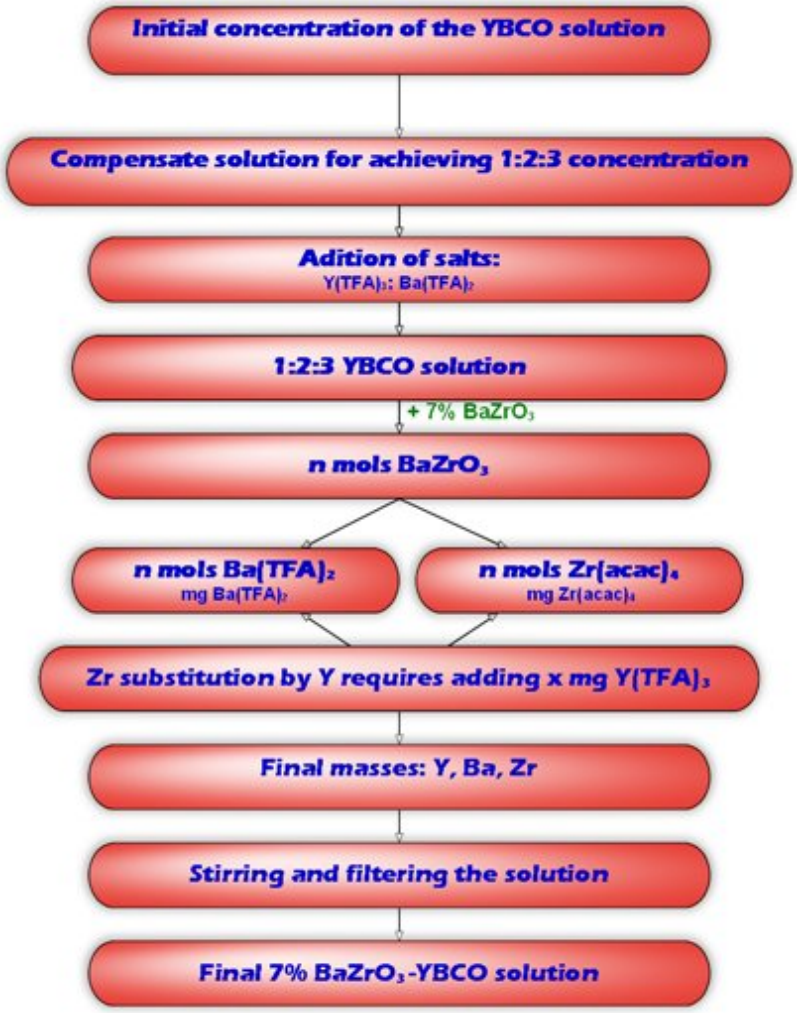

Figure 6.2–1 Typical BZO-YBCO solution preparation process (an example of 7% BZO/YBCO nanocomposite). The initial three steps intend to compensate the YBCO solution and differ in each case.

6.2.2. Morphological and structural characterization

In order to study the effect that the BZO nanoparticles have inside the YBCO matrix, not just the J_c is an important parameter. A complete characterization-morphological, structural and microstructural-is needed for understanding this effect. Samples with different amount of BZO (7%wt. and 13%wt) were prepared on ^{MOD}CZO/YSZ substrates starting from a precursor solution prepared as shown in Section 6.2.1. The previous CZO buffer layer presents small roughness (less than rms = 2,5 nm) and high percentage of flat area (higher than 85%). Gel films were prepared by depositing this solution on 5x5 mm^2 CZO buffered

YSZ substrates by spin coating using a spinning rate of 6000 rpm kept during 2 min. These films were treated with two heating stages in order to fabricate the superconducting film: pyrolisis at low temperature (310ºC) and the standard growth process on CZO (nucleation-770ºC and growth-810ºC). The YBCO films obtained with the above parameters had a thickness of 275 nm (7% BZO) and 250 nm (13% BZO) respectively.

In order to obtain information of the structure and morphology of specific individual defects and to understand the flux pinning centers mechanism, the samples were examined by X-ray diffraction using a 2D diffractometer (General Area Detector Diffraction System). The quality of out-of-plane alignment is estimated by performing a rocking curve around the (005) reflection of YBCO. Scanning Electron Microscopy (SEM) was used to investigate the surface morphology.

The compound $BaZrO_3$ has an ideal cubic perovskite structure with a space group Pm-3m (211) and a lattice parameter a of 4,19 Å. The misfit with the YBCO of about +8,91 % [16] makes of the barium zirconate an attractive material for increasing the critical current density. In its structure, the oxygen atoms sit at the corners of a simple cubic unit cell, the zirconium atoms sit on the faces and the barium atom sits at the center (Figure 6.2–2).

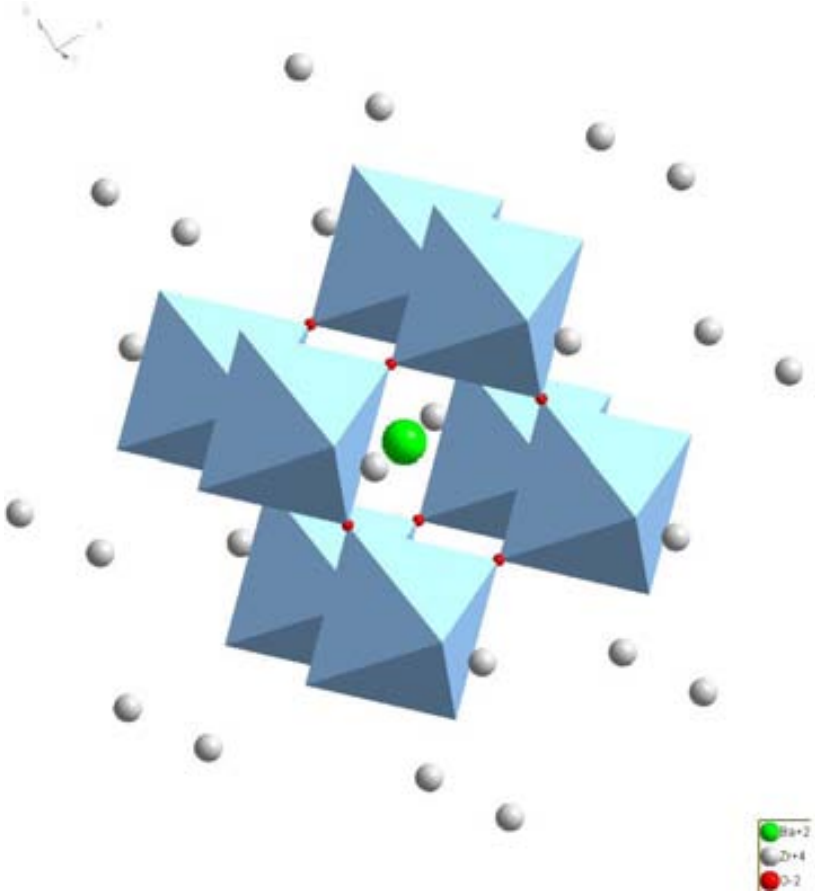

Figure 6.2–2 The reprezentation of the BZO perovskite structure realized with the program Diamond 3.2 (Ba^{+2} atoms are in green, Zr^{+4} in grey and O^{-2} atoms in red).

As it was mentioned before, usually in our standard ^{TFA}YBCO growth conditions, BZO particles can be formed. For films grown on $LaAlO_3$ substrates, it was previously demonstrated that two populations of BZO nanoparticles coexist: i) epitaxial particles nucleating at the interface with the substrate and ii) non-coherent BZO particles randomly distributed in the YBCO matrix and mainly responsible of the enhanced pinning behavior observed in those nanocomposites. Thus, the identification of these random BZO particles is a crucial issue in the study of such nanocomposites [17]. In our case, two typical x-ray diffraction patterns recorded using a general area detector system of two ^{TFA}YBCO-BZO nanocomposites with different amounts of dopant (7% and 13%) grown on ^{MOD}CZO/YSZ are shown in Figure 6.2–3 a). Epitaxial spots corresponding to the (00l) YBCO reflections can be easily identified. The absence of other reflections or rings in the YBCO phase excludes any non epitaxial fraction of the YBCO film. The reactivity between YBCO and CZO, and the subsequent formation of $Ba(Ce,Zr)O_3$, makes more difficult such identification by means of x-ray diffraction due to the similarity between their respective lattice parameters (a_{BZO} = 4,19 Å and a_{BCO} = 4,43 Å). In order to increase the signal-to-noise ratio we have performed a chi-integration of the pattern. The result of this integration is plotted as a θ-2θ graph (Figure 6.2–3 b)). Now, in this figure we can observe that the discrimination between $BaZrO_3$ nanoparticles and $Ba(Ce,Zr)O_3$ is possible. This integration shows that both (110) polycrystalline reflection and (200) epitaxial reflection of BZO are present thus confirming the existence of both populations of BZO nanoparticles [17]. In Figure 6.2–3 d), the rocking curves of chemically doped YBCO films around (005) diffraction peak are shown, in order to estimate the quality of out-of-plane alignment. The full width at half maximum (FWHM) of the (005) for 7% BZO sample is 0,6º, indicating a well oriented BZO doped YBCO films. For the second sample with more nanoparticles inside, the peak is broadened and the out-of-plane misorientation higher (FWHM~1º). The out-of-plane texture of YBCO is deteriorated with higher BZO contents following the same tendency registered in the BZO-YBCO films on LAO or STO substrates.

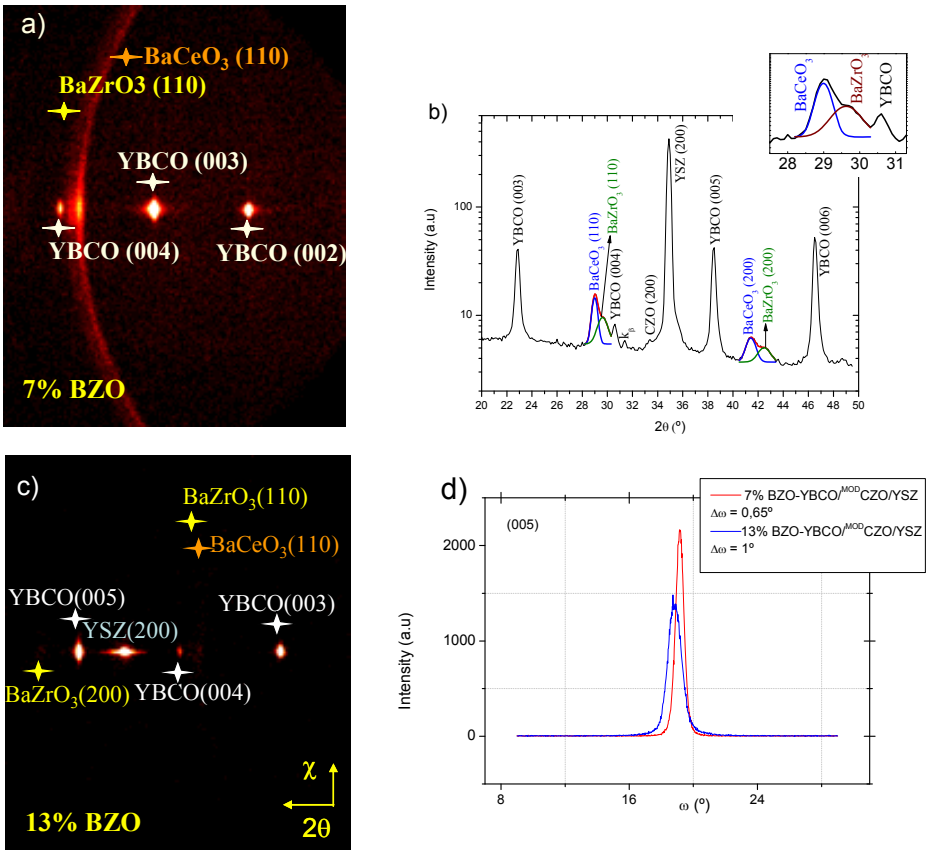

Figure 6.2–3 2D θ-2θ scan of a 2 BZO doped ^{TFA}YBCO/^{MOD}CZO/YSZ samples with different amount of dopant 7% BZO (a) and 13% BZO (c); b) integration of the θ-2θ frame for 7% BZO, in which, after applying a fit, the 2 different phases – BZO and $Ba(Ce,Zr)O_3$ - can be differentiated. The intensities in the two cases are different because of the θ-2θ scanning time (1h for 7% and 30 minutes for 13%); d) out-of-plane orientation of the grains deduced from the (005) YBCO reflection in the two nanocomposites.

Figure 6.2–4 shows the SEM surface morphologies for the two samples. In the case of 7% BZO doping, the surface presents some nanosized particles which don't appear in the case of 13% BZO. The connectivity between grains is still low due to a high porosity and hence there is still room for improvement. In the second case, the surface seems to have 2 zones (one lighter and the other darker) which can appear because of the different composition of the solution in those zones. In both cases, no a/b grains are observed.

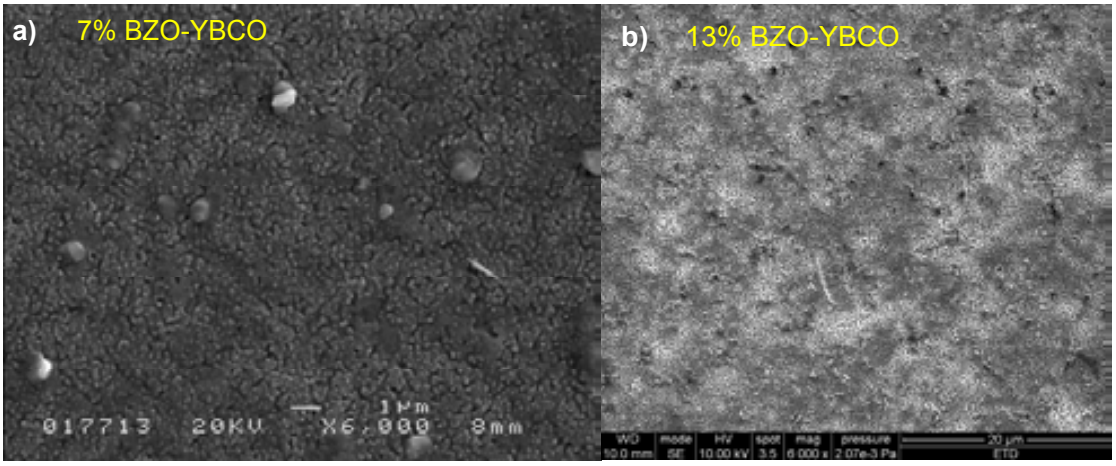

Figure 6.2–4 SEM of a) 7% BZO-YBCO and b) 13% BZO-YBCO films where the c-axis orientation is visible with no a/b planes.

6.2.3. Microstructure by TEM

Microstructure is one key parameter to be taken into account in understanding the mechanism of pinning enhancement into BZO nanocomposites and correlate what is happening inside the YBCO matrix when nanoparticles are introduced with the superconducting properties. In this section, the microstructure of a sample with 7% BZO-YBCO on ^{MOD}CZO/YSZ based on the deposition of chemical solutions, has been investigated using cross-section transmission electron microscopy. Before analysing the microstructure of this nanocomposite, let us summarize the results investigated in the group by A. Llordes [13] by mean of HRXRD and TEM for a nanocomposite on single crystal, without an intermediate buffer. HRXRD technique revealed several peaks and rings where three main orientations of BZO are observed:

1. <001> orientation // [001] YBCO
    - <100>BZO//[00l]YBCO ($\chi = 0^{o}$)
    - <110>BZO//[00l]YBCO and <100>BZO//<110>YBCO ($\chi = 45^{o}$)
    - <001>BZO//[001]YBCO and <100>BZO//[100]YBCO ($\chi = 90^{o}$)

2. <110> orientation // [001] YBCO
    - $\chi = 0^{o}$: $<110>_{BZO}//[001]_{YBCO}$ or $<111>_{BZO}//[100]_{YBCO}$
    - $<100>_{BZO}//[001]_{YBCO}$ and $<100>_{BZO}//[100]_{YBCO}$ ($\chi = 45^{o}$)
    - $<100>_{BZO}//[001]_{YBCO}$ and $<100>_{BZO}//[110]_{YBCO}$ (weak peaks)
    - <110>BZO//[001]YBCO ($\chi = 90^{o}$)
    - [11-2]BZO//[001]YBCO and <111>BZO//[100]YBCO ($\chi = 55^{o}$)

3. <111> orientation // [001] YBCO
    - $<111>_{BZO}//[001]_{YBCO}$ ($\chi = 0º$)
    - $<100>_{BZO}//[001]_{YBCO}$ ($\chi = 55º$)
    - $<110>_{BZO}//[001]_{YBCO}$ ($\chi = 35º$)
    - $<111>_{BZO}//[110]_{YBCO}$ ($\chi = 90º$)

Additionally to these three orientations, another three new ones were confirmed by TEM:

4. $<111>_{BZO}//[100]_{YBCO}$ and $<110>_{BZO}//[001]_{YBCO}$
5. $<11\text{-}2>_{BZO}//[001]_{YBCO}$ and $<111>_{BZO}//[100]_{YBCO}$
6. $<11\text{-}2>_{BZO}//[001]_{YBCO}$ and $<111>_{BZO}//[110]_{YBCO}$

Figure 6.2–5 is a low magnification image showing a cross-section TEM micrograph of the 7% BZO-YBCO/^{MOD}CZO/YSZ film. Misfit relaxation is noted at the CZO/YSZ interface due to the misfit dislocations. During the preparation with the PIPS system, the YBCO matrix was milled by the Ar^+, although the BZO + CZO phases remained.

An interfacial phase of 1 – 2 unit cells thick, which can be $BaZrO_3$ or (Zr)-$BaCeO_3$

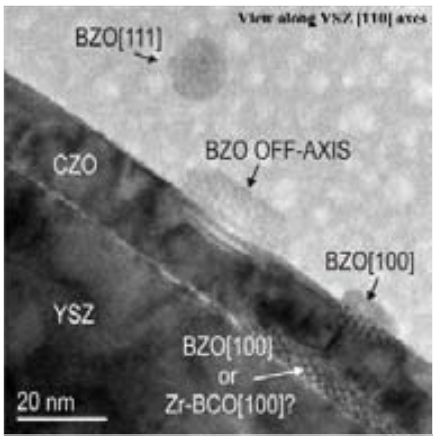

Figure 6.2–5 Low magnification image showing the CZO grown on top of the YSZ substrate. Some BZO nanoparticles are observed in the YBCO matrix, which remains amorphous due to sample preparation process.

(BCO) is also observed, either as a continuous layer or as inclusions (Figure 6.2–6). The formation of BZO or (Zr)-$BaCeO_3$ at the CZO/YSZ interface requires the diffusion of Ba through the CZO buffer during the growth of the YBCO film which may be favoured at grain boundaries or discontinuities of the CZO buffer layer. The epitaxial relation of this reactive phase could be:

- (001)[100]BZO or BCO//(001)[110]F (where F refers to both fluorite structures, YSZ and CZO).
- (110)[111] BZO or (Zr)-BCO//(001)[110]F.

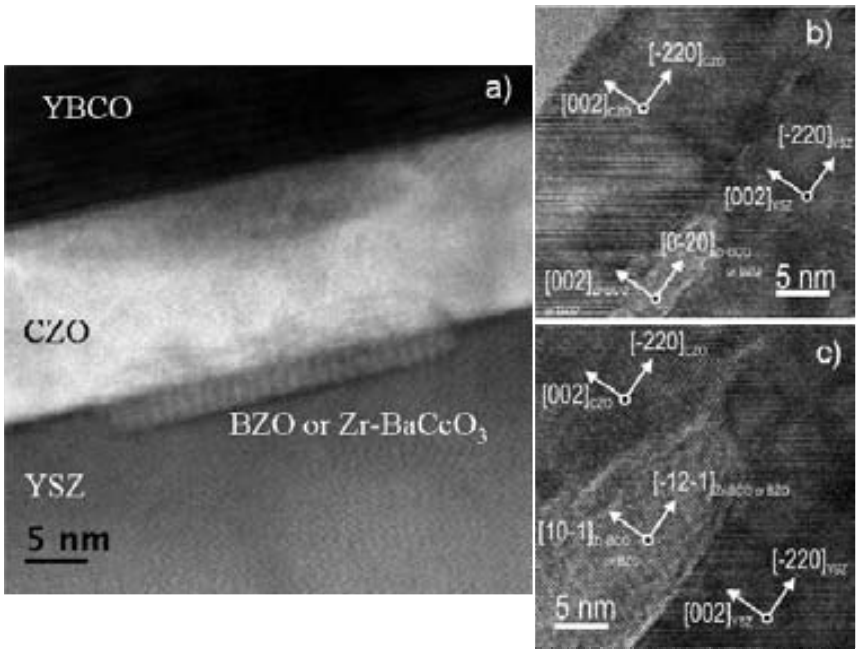

Figure 6.2–6 a) STEM image taken with a Cs-corrected (spherical aberration corrected) JEOL JEM-2100F TEM microscope where brightness increases monoatomically with atomic number Z and TEM sample thickness. Thus, because brighter atomic column means higher Z value (Z_{Ce} = 58, Z_{Zr} = 40, Z_{Ba} = 56) we could say that the strange phase at the interface CZO/YSZ is either BZO or BCO; b), c) HRTEM micrographs of different orientation and their indexing using FFT of the phase located at the substrate buffer interface who penetrates into the YSZ.

Figure 6.2–7 is a high resolution TEM image looking through the [110] zone axis of the substrate in which we can see that the buffer, with a cubic phase, grows cube on cube on the substrate. The epitaxial relationship between CZO and YSZ is:

(001)CZO//(001)YSZ

[100]CZO//[100]YSZ

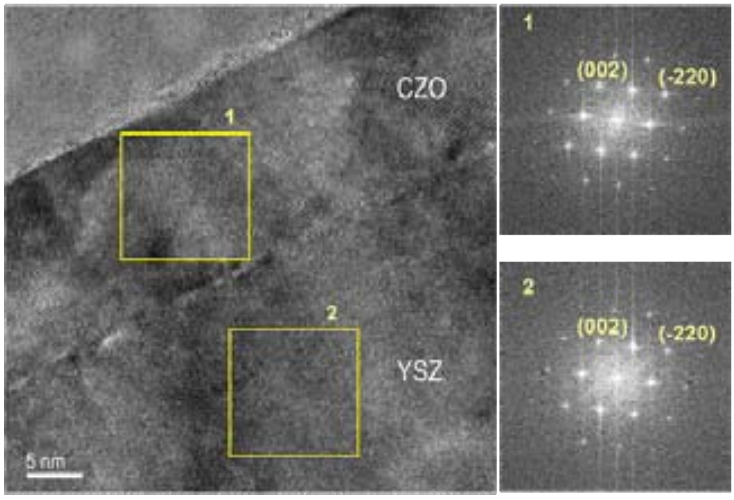

Figure 6.2–7 Fast Fourier Transforms (FFT) of the squared areas labelled with 1 (CZO) and 2 (YSZ) in the HRTEM image showing the all arquitecture.

Now, talking about the nucleation of the nanocomposite inside the superconducting matrix, we noted that there are 3 types of BZO nanodots:

1) one which have a heterogeneous nucleation in the YBCO matrix and grows epitaxially cube on cube with YBCO (Figure 6.2–8 a)):

(001)BZO//(001)YBCO

[100]BZO//[100]YBCO

2) another one when <110> BZO directions are rotated with respect to the [010] directions of YBCO, suggesting a random orientation on the a(b)-c plane of YBCO. In this case, they would correspond to a $[111]_{BZO}//a(b)_{YBCO}$ fibber texture. (Figure 6.2–8 b)):

3) and also a new orientation was found within 1º (Figure 6.2–8 c)): (001)[110]BZO//(001)[100]YBCO.

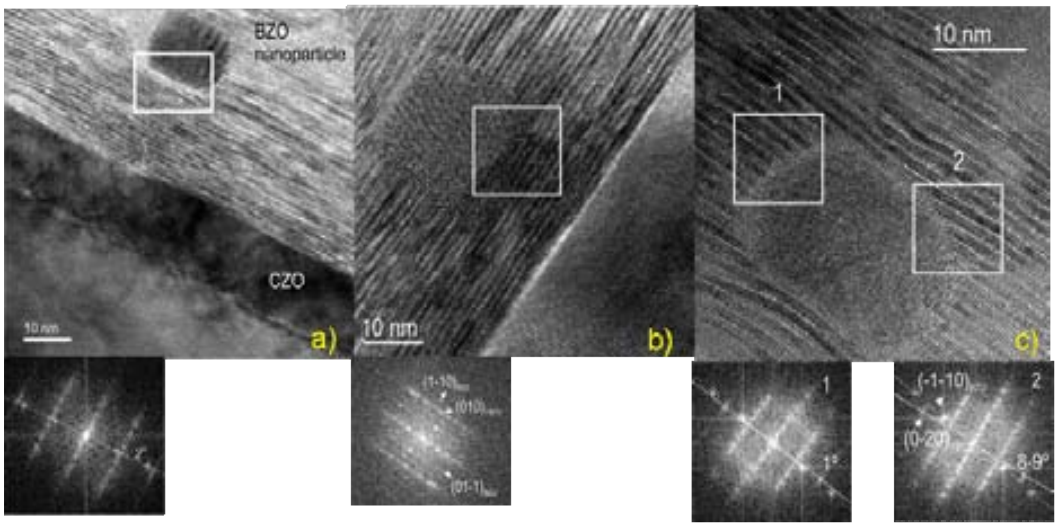

Figure 6.2–8 a) A BZO nanoparticle, [100] BZO//[100]YBCO, nucleated slightly misoriented to the ⊥ direction in the YBCO matrix; b) another BZO particle as viewed along the [111] zone axis. In this case, the (1-10) planes of the BZO are disoriented by around 8.5º respect to the orthogonal in-plane YBCO direction; i.e. respect to the (010) YBCO planes; c) new orientation found within 1º when (001)BZO//(001)YBCO and [110]BZO//[100]YBCO.

Other phases have been found to nucleate on the CZO buffer layer. Figure 6.2–9 a) is a low magnification HRTEM showing three different particles on top of the CZO surface: two BZO nanoparticles and a (001) Y_2O_3 nanodot, probably associated to the (010) BZO particle. In agreement with other references [18,19], [19] (-101) Y_2O_3 has been found to nucleate on top of the CZO buffer layer (Figure 6.2–9 b)).

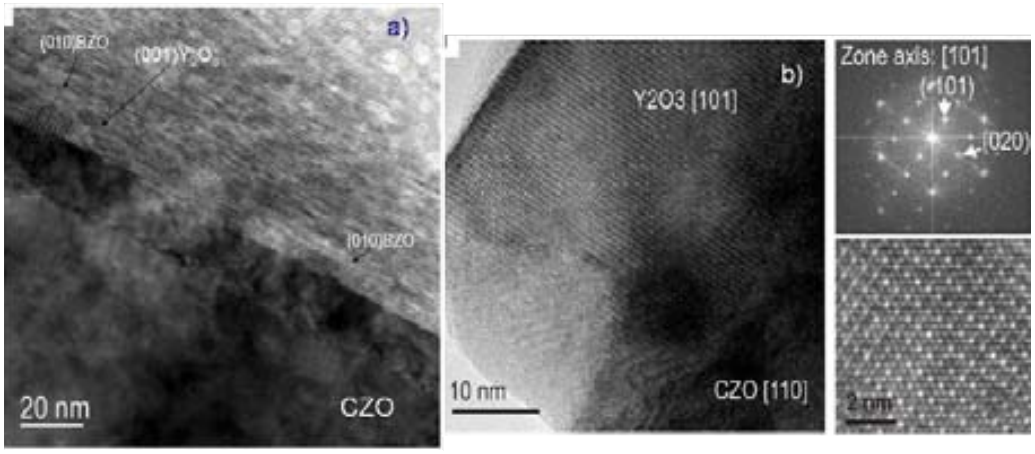

Figure 6.2–9 a) low magnification HRTEM image showing different nanoparticles: BZO and Y_2O_3; b) (-101) Y_2O_3 nucleates on top of the CZO buffer layer.

Another important aspect here is the degree of relaxation of the buffer layer taking into account the dislocations present in the phase maps from Figure 6.2–10. First image 1) shows the three phases: YSZ substrate, CZO buffer layer and a BZO nanodot grown on the CZO film. The second image 2) is a phase map for -220 reflections of YSZ and CZO and for 020 of BZO. Every change of 2π in the phase (change from black to white) is a dislocation in the CZO side. Thus, the mean distance between dislocations as measured experimentally is: $<S_{exp}>$ = 4,019 nm, where the theorethical value for CeO_2 is $<S_{CeO2}>$ = 4,07 nm. In the case of dopping with Zr, the unit cell would be slighly smaller; therefore the in-plane compressive mismatch would be smaller and, consequently: $S_{CZO}>S_{CeO2}$. This means that, in any case, there are enough dislocations for the buffer layer to be fully relaxed. The third image 3) is the phase map for the 002 reflections of YSZ, CZO and BZO. The distance between 2π phase changes is slightly different but very close to the case of the in-plane (previous map) parameter and out-of-plane parameter for BZO: 1.299 nm and 1.135 nm respectively. i.e. the dot must be almost fully relaxed. In the case of the CZO buffer layer, the distance for the phase shift to occur for the out-of-plane direction is every 6.033 nm, which is larger than the 4.019 nm measured for the in-plane parameter. However, this phase map presents more dispersion and thus higher error.

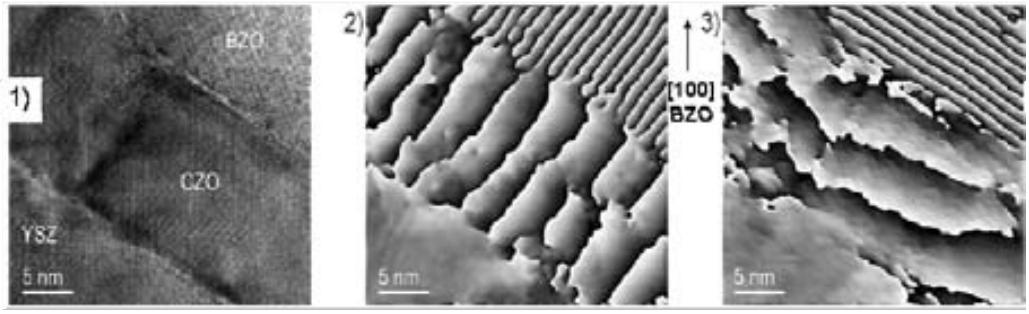

Figure 6.2–10 1) HRTEM image showing the three phases: YSZ, CZO and BZO; 2) phase map for -220 reflections of YSZ and CZO and 020 of BZO where the buffer is fully relaxed; 3) phase map for the 002 reflections of YSZ, CZO and BZO.

Starting from the phase maps for $g_{-220,YSZ\ and\ CZO}$ and $g_{020,BZO}$, values and $g_{-111,YSZ\ and\ CZO}$ and $g_{-101,BZO}$, values, the in-plane and out-of-plane strain maps are shown in Figure 6.2–11. The YSZ substrate was taking as the reference. The matching distances calculated from these strain values are: $d_{in\text{-}plane,CZO} = 1.907$ Å (while $d_{(-220),CZO} = 1.902$ Å) and $d_{in\text{-}plane,BZO} = 2.134$ Å (while $d_{(020),BZO} = 2.095$ Å). The out-of-plane matching distances: $d_{out\text{-}of\text{-}-plane,CZO} = 2.696$ Å (while $d_{(002),CZO} = 2.69$ Å) and $d_{out\text{-}of\text{-}plane,BZO} = 2.168$ Å (while $d_{(020),BZO} = 2.095$ Å). The bulk values taken into account in calculation for the three phases were: $a_{YSZ} = 5{,}13$ Å, $a_{CZO} = 5{,}38$ Å, $a_{BZO} = 4{,}19$ Å and the strain was calculated with Eq. 6.2-1 :

$$\varepsilon = \frac{d_{YSZ} - d_{CZO\ or\ BZO}}{d_{YSZ}} \qquad \textbf{Eq. 6.2-1}$$

As a conclusion, from these strain maps, it is evident that the CZO buffer layer is fully relaxed on the YSZ substrate and the BZO nanoparticle is also relaxed as compared to YSZ.

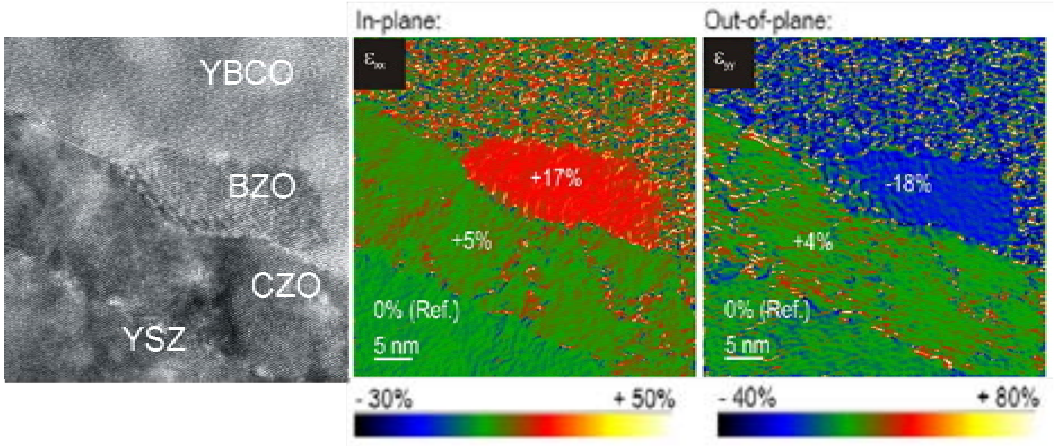

Figure 6.2–11 General overview HRTEM image, in-plane and out-of-plane strain maps of YSZ, CZO and YBCO. The BZO nanoparticle penetrates into the buffer. The substrate was taking as reference for calculating strains. The spacial resolution of the measurement is 0,6 nm. ε_{xx} (error) = 2%, ε_{yy} (error) = 3%.

6.2.4. Quantification of the random/epitaxial fraction nanoparticles

As we saw in the Section 6.2.2, by mean of XRD the distinction between the two types of BZO nanoparticles – epitaxial and random oriented - can be done. What about the quantitative percentage determination of these two nanoparticles orientations? A new methodology for calculating this, and which propose a quantitative phase analysis considering the two orientations (single - crystal and random) of the same phase as two distinct phases, was developed by A. Llordes in the group [13]. The measurements were done using a 2D detector diffractometer and the first step was a θ-2θ scan, after which an incident angle ω where the maximum of the BZO is encountered is fixed (ω=15°) for 1 hour. The others parameters taken into account for (110) of BZO were χ=45° and φ=0°. The volume fractions for both random and epitaxial phases were estimated from the Eq. 6.2-1:

$$I = I_0 K \lambda^3 V^{-2} m_{hkl} P L v F_{hkl}^2 \qquad \textbf{Eq. 6.2-2}$$

where K is a constant that depends on the instrument characteristics, V is the volume of the unit cell, m_{hkl} is the multiplicity of the hkl reflection, P is the polarization factor, L the so - called Lorentz factor $L=(\cos\theta \sin^2\theta)^{-1}$, F_{hkl} is the structure factor and v is the effective diffracting volume of the sample, including the effects of absorption. P has the form $(1 + C \cos^2\theta) / (1 + C)$, where $C = 1$ for an unpolarized beam and $C = \cos^2\theta_m$ if an incident - beam monochromator is used, θ_m being the Bragg angle of the monochromator [13].

Ideally,

$$\frac{I_{random}}{I_{epitaxial}} = \frac{v_{random}}{v_{epitaxial}} \qquad \textbf{Eq. 6.2-3}$$

$$\text{and } \frac{I_{random}}{I_{epitaxial}} = \frac{I_{ring}^{exp}(360/\Delta\chi)4\pi}{8I_{pole}^{exp}} \qquad \textbf{Eq. 6.2-4}$$

From Eq. 6.2-2, Eq. 6.2-3 and having into account that $v_{random} + v_{epitaxial} = 100$, it was calculated that 80-90% from the 10% BZO nanocomposite are randomly oriented in the YBCO matrix.

However, the intent to translate this approach to one of our BZO composites (13% BZO-YBCO) grown on ^{MOD}CZO/YSZ failed because of the formation of another phase, $BaCeO_3$ (a = 4,40 Å) with similar lattice parameter as BZO (a = 4,19 Å). This new phase, resulted from the reaction of YBCO with CZO in the growth process at high temperature (810ºC) making impossible to differentiate the two reflections (Figure 6.2–12). We would like to remaind, however, that we have observed at least three types of biaxially textured BZO

nanoparticles: 1) [100]BZO//[100]YBCO; 2) [110]BZO//[100]YBCO; 3) [110]BZO//[001]YBCO.

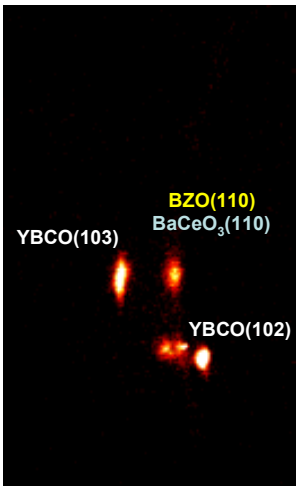

Figure 6.2–12 2D XRD pattern of the 13 % BZO on ^{MOD}CZO/YSZ substrate.

6.2.5. Superconducting properties

A fundamental property that makes superconductors attractive for power applications is the ability to carry high currents without losses. Between material defects and J_c there is a complex relationship. Parameters like size, shape, composition and interactions with the matrix of the defects, are important parameters when talking about pinning force. The pinning itself can be divided in two categories: strong –isotropic and anisotropic- and weak. In ICMAB was done a classification of defect contribution to flux pinning by separating isotropic defects from the overall measuring magnitudes ($J_c(\theta)$ and $T_{irr}(\theta)$) thus obtaining the anisotropic defects. Isotropic defects are those whose vortex pinned length does not depend on the orientation of the magnetic field, and consequently, their contribution to J_c follows the Blatter scaling approach, i.e. J_c and T_{irr} follow the intrinsic mass anisotropy of YBCO. The most typical example is point defects. Instead, anisotropic defects are those defects whose vortex pinned length depends on the orientation of the magnetic field [20],[21].

In our case, the dependence at 77K of J_c with the magnetic field of a pure YBCO film and a 7% BZO doped one shown in Figure 6.2–13 reveals that the BZO addition reduces the J_c value at self field (3,1 MA/cm^2 against 5,2 MA/cm^2 for a pure YBCO on buffered ^{MOD}CZO/YSZ substrate) but, in field, the performances of the nanocomposite film are increased, being already a factor two higher at 0.5T. From the angular dependence at 77K and 7T, it is seen that the BZO introduction induces the formation of correlated defects. Apart from the intrinsic peak at 90º when the magnetic field is parallel to ab plane, a broad

peak at 180º (H//c) is exhibited by the BZO doped YBCO. This peak is smaller than in the case of ^{TFA}YBCO/^{MOD}CZO/YSZ and the reduction of the anisotropy of J_c in the nanocomposite is associated to the enhancement of the pinning due to BZO nanoparticles [17].

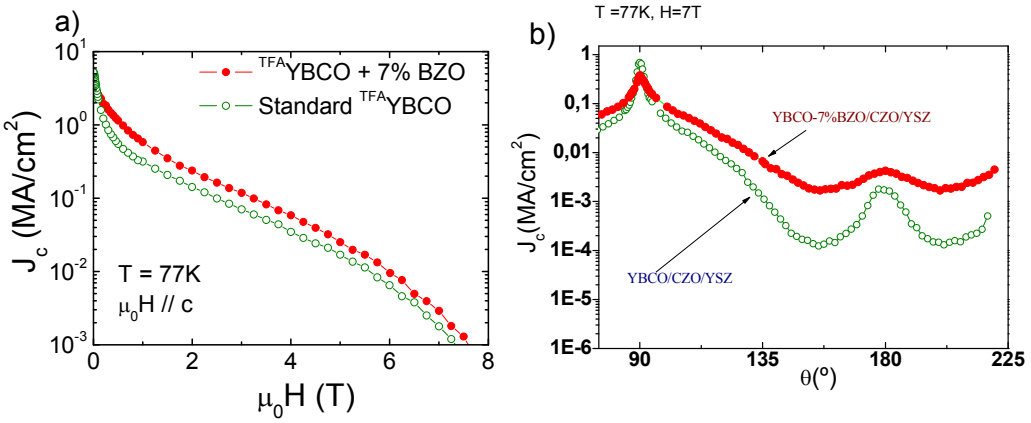

Figure 6.2–13 a) Field dependence of the critical current density at 77K of a ^{TFA}YBCO-BZO nanocomposite (red solid circles) compared to the standard ^{TFA}YBCO film (open circles). Both films were grown on the same conditions on ^{MOD}CZO buffer layers on YSZ single crystals. Vortex pinning enhancement in the YBCO-BZO nanocomposite is evident; b) Angular dependence at 77K and μ_0H=7T of the critical current density of a ^{TFA}YBCO-BZO nanocomposite (red solid circles) and of a ^{TFA}YBCO standard sample with CZO as buffer layer. Both samples were grown on ^{MOD}CZO/YSZ. The reduced anisotropy of J_c in the nanocomposite is associated to the enhanced pinning due to the BZO nanoparticles.

Also, another important point is that J_c decreases with increasing the content of nanoparticles (Np) from 3,1 MA/cm^2 for 7% BZO to 2,2 MA/cm^2 for 13% BZO (Figure 6.2–14). Nanoparticles increase reduces the percolating current and so, the quality of YBCO decreases above ~10% mol. of nanoparticles.

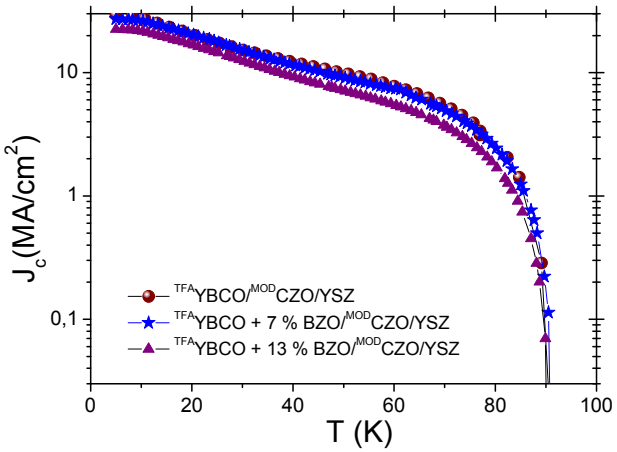

Figure 6.2–14 J_c versus T for a pure YBCO film compared with a 7% BZO-YBCO and a 13% BZO-YBCO films. All samples were grown on ^{MOD}CZO/YSZ.

Figure 6.2–15 shows J_c normalized to J_c^{sf} as a function of H/ H_{irr} for samples grown on LAO and CZO buffered YSZ substrates. We can observe that in both cases for the BZO-YBCO nanocomposites the $J_c(H)$ dependence present a much smother behaviour than for the standard samples, associated to an enhancement of isotropic defects generated in the nanocomposites. Moreover, for the standard samples we observe that the film grown on top of CZO buffered substrate present an enhancement of J_c with respect to the one grown on LAO, associated to a large amount of anisotropic defects induced by the buffer layer. This enhancement is also noted in the nanocomposites.

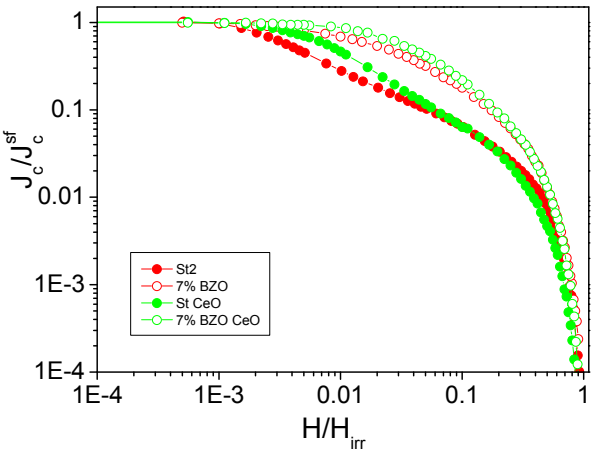

Figure 6.2–15 Comparison of J_c normalized to J_c^{sf} as a function of H/ H_{irr} at 77K for samples grown on LAO and CZO buffered YSZ substrates for different samples. A clear enhancement of the pinning is noted in all the cases of the BZO nanocomposites.

From the angular dependence of J_c at 77K and 1T (Figure 6.2–16 a)) we can see that all the nanocomposites have lower J_c dependence with magnetic field orientation than the standard samples. This trend is observed for LAO, ^{MOD}CZO buffered YSZ substrates and also on tapes. The ratios between J_c(H//ab) and J_c(H//c) are seen in Figure 6.2–16 b).

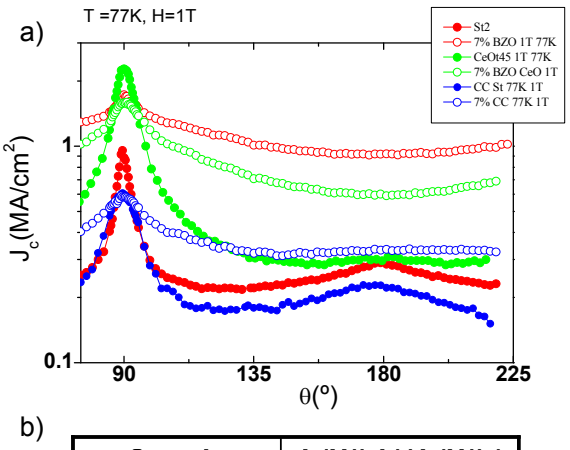

b)

Sample	J_c(H//ab)/J_c(H//c)
Std.	4.3
BZO Std.	1.9
Std. CZO	7.5
BZO Std. CZO	2.7
CC	2.6
BZO-CC	1.8

Figure 6.2–16 a) Angular dependence of J_c at 77K and 1T for nanocomposites on LAO, ^{MOD}CZO/YSZ and also on tapes (open circles) compared with the undoped YBCO films (full circles); b) the ratios J_c(H//ab)/J_c(H//c) for the samples presented in a).

6.2.6. Williamson-Hall plot – a method for calculating the microstrain in the BZO-YBCO compound

Crystals are 3 dimensional periodic formations of single atoms or atom groups [22]. A perfect crystal would extend in all directions to infinity, so we can say that no crystal is perfect due to its finite size (Figure 6.2–17). This deviation from perfect crystallinity leads to a broadening of the diffraction peaks. However, above a certain size (100-500 nm) this type of broadening is negligible. Extended defects such as stacking faults, dislocations in layered materials, antiphase boundaries, disrupt the atomic arrangement of a crystal, typically along a 2D plane. These defects effectively terminate a crystallographically ordered domain of the crystal. Thus as far as x-rays are concerned, one crystal ends and a new crystal begins at the extended defect [23].

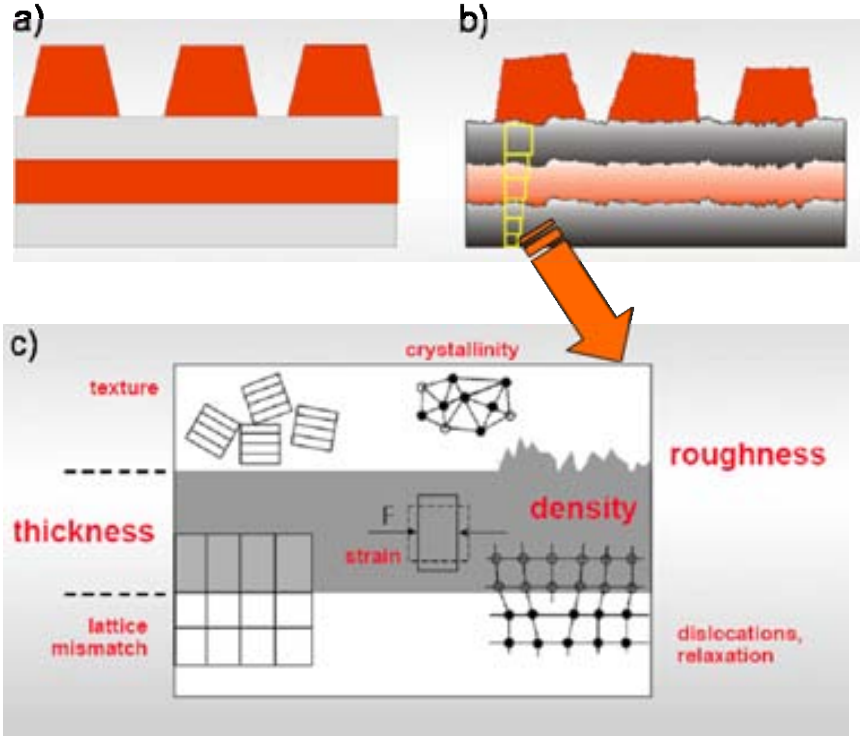

Figure 6.2–17 a) a perfect sample; b) sample's imperfections such as: roughness, strain/lattice mismatch, gratings shape, lattice defects, dislocations, lattice tilts, etc.; c) thin film real structure [22]

There are several sources from which peak broadening comes (instrumental effects; finite crystallite (not particle) size (< 100-500 nm); strain; extended defects) and also methods of extracting size & strain information:

- Scherrer formula (average size, neglects strain);
- Integral breadth methods (provide average values of size and strain);
- Peak shape methods (provide size and strain distributions).

The strain is defined as the deformation of an object divided by its ideal length, $\Delta d/d$. In crystals, two types of strain can be observed (Figure 6.2–18):

- ***Uniform strain*** which causes the unit cell to /contract in an isotropic way and this simply leads to a change in the unit cell parameters and shift of the peaks; there is no broadening associated with this type of strain.
- ***Non-uniform strain (microstrain; mesostrain = strain associated to GB)*** which leads to systematic shifts of atoms from their ideal positions and to peak broadening. This type of strain arises from the following sources [23]:
  - Point defects (vacancies, site-disorder)
  - Plastic deformation (cold worked metals, thin films)
  - Poor crystallinity.

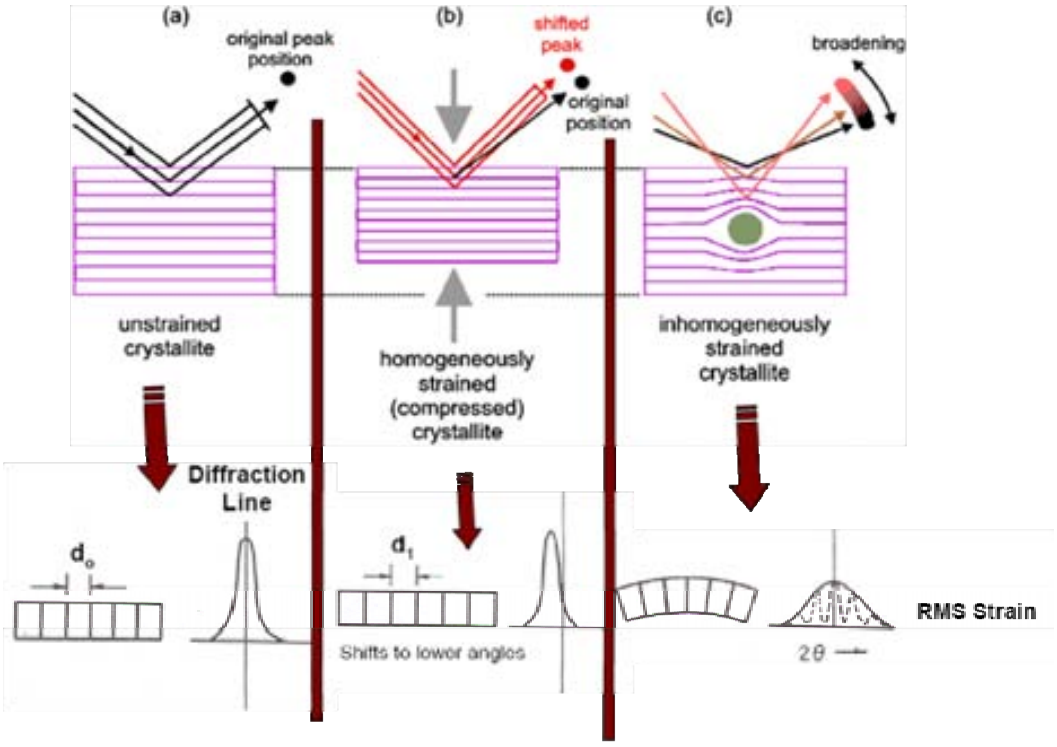

Figure 6.2–18 Effect of lattice strain on diffraction peak position and width: a) no strain; b) uniform or homogeneous strain where peak moves and no shape changes $(d_1-d_0)/d_0$; c) non-uniform or inhomogeneous strain when peak broadens and $d_1 \neq$ constant.

One method for calculating the isotropic strain along c axis is the Williamson - Hall plot attributed to G. K. Williamson and his student, W. H. Hall [24]. A. Llordes from ICMAB's group used also the same method in her thesis for calculating the microstrain of the BZO-YBCO nanocomposites [13]. It relies on the principle that the approximate formulae for size broadening, β_L, and strain broadening, β_e, vary quite differently with respect to Bragg angle, θ:

$$\beta_L = \frac{K\lambda}{L\cos\theta} \qquad \textbf{Eq. 6.2-5}$$

$$\beta_e = C\varepsilon\tan\theta \qquad \textbf{Eq. 6.2-6}$$

where C is a constant equal to 4-5 and ε is the microstrain.

One contribution varies as 1/cosθ and the other as tanθ. If both contributions are present then their combined effect should be determined by convolution. The simplification of Williamson and Hall is to assume the convolution is either a simple sum $\beta_{total} = \beta_{instrumental} + \beta_{sample}$ (Lorentzian) or sum of squares $\beta_{total}^2 = \beta_{instrumental}^2 + \beta_{sample}^2$ (Gaussian). Using the former of these then we get:

$$\beta_{tot} = \beta_e + \beta_L = C\varepsilon \tan\theta + \frac{K\lambda}{L\cos\theta} \qquad \textbf{Eq. 6.2-7}$$

If we multiply this equation by cosθ we get:

$$\beta_{tot}\cos\theta = C\varepsilon \sin\theta + \frac{K\lambda}{L} \qquad \textbf{Eq. 6.2-8}$$

and comparing this to the standard equation for a straight line (*m* = slope; *c* = intercept):

$$y = mx + c \qquad \textbf{Eq. 6.2-9}$$

we see that by plotting $\beta_{tot}\cos\theta$ versus $\sin\theta$ we obtain the strain component from the slope (**C**ε) and the size component from the intercept (Kλ/*L*). Such a plot is known as a Williamson-Hall plot and is illustrated schematically in Figure 6.2–19 a). β is called integral breadth and has the value close to FWHM (Figure 6.2–19 b)) [25].

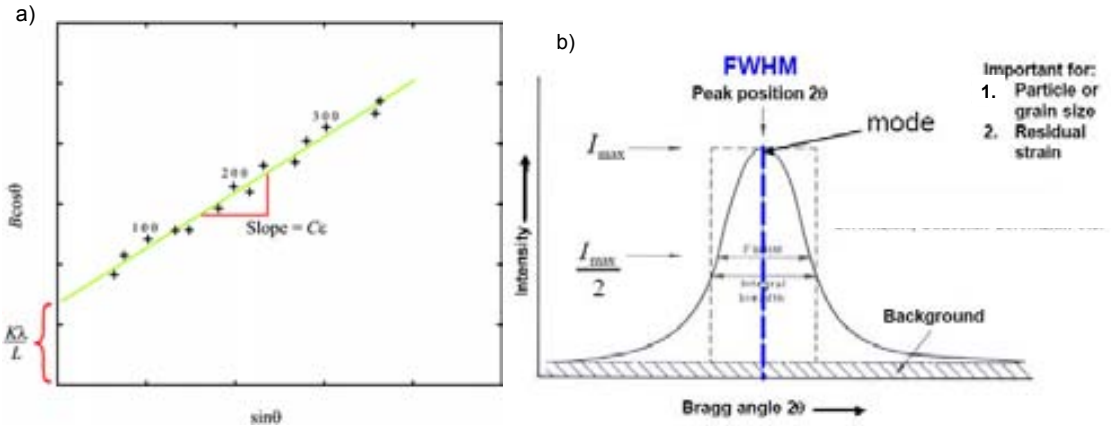

Figure 6.2–19 a) Plot of the microstrain using Williamson Hall method [25]; b) the most important parameters of a diffraction peak-between them the integral breadth, β [26].

Let's talk now about our samples. The *(00l)* - YBCO lines taking into account here were measured with a Siemens diffractometer and are the following: (004), (005), (007), (008). Special experimental conditions were used (steptime: 5,5 s and stepsize 0,02º). A standard SiO_2 sample was used as reference for calculating the $\beta_{instrumental}$ of each peak. The integral breadth, β, and the 2θ position of the measured Bragg peaks, after doing a profile fitting using the FullProf Suite program are shown in Table 6.2-1.

SAMPLE	(00l)	2θ (°)	β_{obs} (°)	$\sin^2\theta$	$\beta^2\cos^2\theta$
^{TFA}YBCO/^{MOD}CZO/YSZ	(004)	30,61	0,1248	0,06967	2,32812E-6
	(005)	38,51	0,1519	0,10875	4,10752E-6
	(007)	54,96	0,1881	0,21293	5,8195E-6
	(008)	63,67	0,2192	0,27823	7,86986E-6
7% BZO - ^{TFA}YBCO/^{MOD}CZO/YSZ	(004)	30,62	0,1721	0,06972	6,30764E-6
	(005)	38,53	0,2527	0,10886	1,51781E-5
	(007)	55,01	0,3552	0,21328	2,75734E-5
	(008)	63,71	0,4138	0,27854	3,4938E-5
13% BZO - ^{TFA}YBCO/^{MOD}CZO/YSZ	(004)	30,62	0,2639	0,06972	1,76499E-5
	(005)	38,53	0,2926	0,10886	2,10843E-5
	(007)	55,02	0,5208	0,21336	6,23325E-5
	(008)	63,69	0,7569	0,27839	1,23239E-4

Table 6.2-1 Three different arquitectures and their parameters for calculating the Williamson Hall (W-H) strain.

Figure 6.2–20 shows the dependence of $\beta^2\cos2\theta$ versus $\sin^2\theta$ for 7% BZO-YBCO/^{MOD}CZO/YSZ and 13% BZO-YBCO/^{MOD}CZO/YSZ compared with a reference sample of ^{TFA}YBCO/^{MOD}CZO/YSZ in which the microstrain can be calculated from the slope and the crystallite size from the intercept. We will focus now on the microstrain deduced from the broadening of the peaks. For the pure YBCO on ^{MOD}CZO buffered YSZ we obtain ε = 0,124 % meanwhile for the 7% BZO nanocomposite ε = 0,287 %, i.e an increment of 102 %. In the case of the sample with 13% BZO the microstrain increases even more reaching ε = 0,453 %. Compared with the pure YBCO sample this value is 241 % bigger, thus showing that the BZO nanoparticles are very effective in increasing the distorsions of the YBCO lattice.

In order to deeper investigate the anisotropy of the diffraction - line broadening in the nanocomposites and in pure YBCO films, in the group was performed Rietveld refinement by using the MAUD program in which both isotropic and anisotropic models of strain - size are implemented. The Delft Model was used, which is an Integral Breadth - based method, to model the isotropic peak broadening. Then, anisotropic size and strain parameters are modelled with the so - called Popa rules, which are based on convergent series of symmetrised spherical harmonics [13].

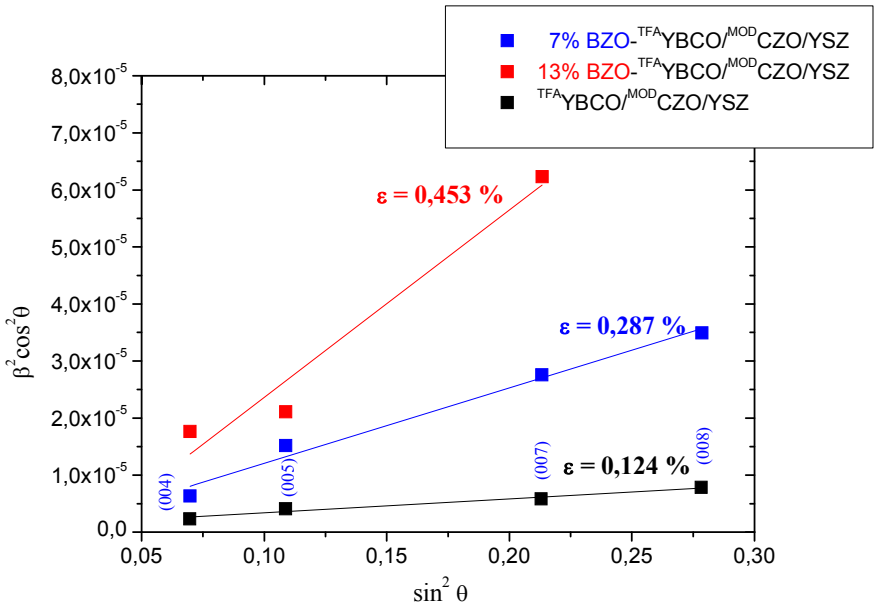

Figure 6.2–20 Microstrains calculated from Williamson Hall plot using (00l) lines of YBCO for 13% mol. BZO-YBCO, 7% mol. BZO-YBCO and pure YBCO on ^{MOD}CZO buffered YSZ.

The YBCO distorsion is evidenced also by the plot of the microstrain ε versus the c-axis misorientation measured by the out-of-plane Δω of YBCO showed in Figure 6.2–21, in the 3 cases: pure YBCO, 7% BZO-YBCO and 13% BZO-YBCO. Increasing the Δω by introducing more nanoparticles leads to an increase of the microstrain. Around a BZO nanoparticles, the CuO_2 planes suffers some kind of "bending" which generates an increase of Δε and strain (see Figure 6.2–8).

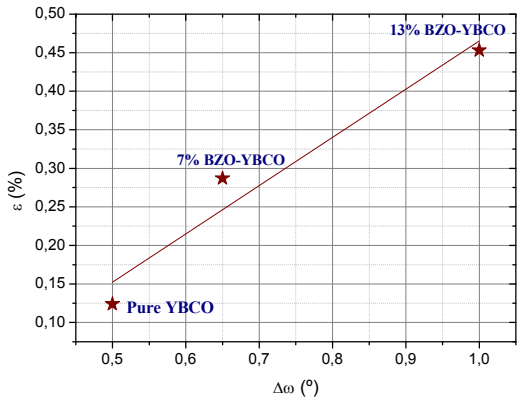

Figure 6.2–21 Microstrain versus misorientation out-of-plane for: pure YBCO, 7% BZO and 13% BZO. All the samples were prepared on ^{MOD}CZO/YSZ.

6.3. Transfer of the nanocomposite approach to SS tapes: BZO-YBCO/^{MOD}CZO/^{ABAD}YSZ/SS

6.3.1. Characterization

This paragraph will be related to the transfer to metallic tapes of introducing BZO nanoparticles into the YBCO matrix to enhance vortex pinning. On CZO buffered single crystals, as we saw before, we obtained J_cs of 3,1 MA/cm^2 (Section 6.2.5). We applied the previous successful approach to Stainless Steel substrates. A small and broad peak is observed in the XRD pattern. This peak corresponds to the polycrystalline part of BZO and indicates that the particles of the nanocomposite are small. The misorientation of the grains in plane is $\Delta\varphi$ = 5,6º (Figure 6.3–1 a)). The SEM micrograph from the Figure 6.3–1 b) shows no ab grains on the surface and also that there is still room for improvement because the porosity is still high. The morphology is similar with the one encountered in the nanocomposite on single crystal with 7% BZO addition.

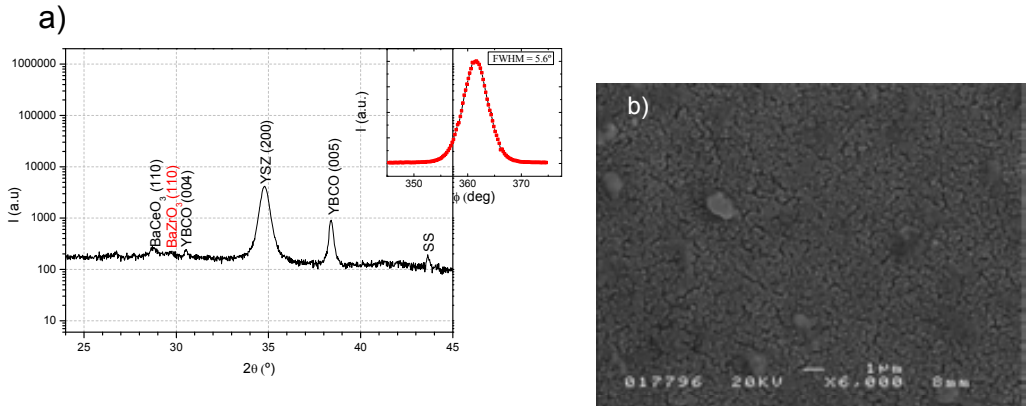

Figure 6.3–1 a) θ-2θ scan of 7% BZO-^{TFA}YBCO/^{MOD}CZO/^{ABAD}YSZ/SS with a misorientation of the grains in plane of 5,6º (inset); b) SEM micrograph of the previous BZO nanocomposite on metallic substrate.

6.3.2. Granularity in BZO nanocomposites on SS tapes compared with pure YBCO CC

In engineering applications and in fundamental science, grain boundaries in oxide superconductors are of central importance. Although they have been closely studied for more than a decade, there is still by no means a consensus on the properties of individual boundaries, or their collective behaviour when current percolates in a granular material. A quantitative description of current and flux percolation is essential for the practical specification of conductors and for charting routes to conductor optimization. The problem has three parts: (i) the properties of individual grains and grain boundaries, (ii)

microstructure, texture and grain morphology, and (iii) the macroscopic geometrical constraints such as conductor size and shape. J. Evetts showed that, based on the angular variation in an applied magnetic field of the grain boundary critical current, the grain morphology as well as texture are two very important parameters for the critical current of a coated conductor [27].

It is well known that, the critical current density J_c in polycrystalline or granular superconducting material is hysteretic with applied field H due to the focusing of the field within the boundary between adjacent grains. This is of concern in the so-called coated conductors, wherein a superconducting film is grown on a granular, but textured, surface of a metal substrate. Using transport current via an applied potential in strip geometry it was noted that the effect observed by inductive method is not as pronounced using transport current, probably due to a large difference in criterion voltage between the two types of measurements [28]. D. Larbalestier [29] did also a nice review talking about grain boundaries in cuprates and pnictides showing that in cuprates, experience with YBCO and Bi-2223 shows that misorientations of only a few degrees decrease the critical current density significantly; the critical angle at which depression of the intragrain current density starts in [001] tilt grain boundaries being as small as 2-3°. In a broad sense the better properties of YBCO compared to Bi-2223, which corresponds to the 1st to 2nd generation HTS conductor technology change, can be plausibly explained just in terms of the much worse uniaxial texture (FWHM ~12°) of Bi-2223, as compared to the biaxial texture of ~5° possible in YBCO. Intergranular current does exist. The GBs do obstruct the current (10º misorientation in GB decrease very much the J_c) and for RABiTs, a misorientation of 7º leads to a J_c = 0,7 MA/cm^2 which increases tremendously to 3,1 MA/cm^2 when the GB misorientation decreases just 0,5º.

Talking now about our case, we saw in Chapter 5 (Section 5.1.4.1) by comparing the J_c (H) for a single crystal with the one of the CC, that, above 2T, the J_c merge in the two cases being the same. This suggests that the reduction of J_c at self-field it is just due to granularity and it will be demonstrated here. This can be confirmed by using an inductive methodology developed previously by A. Palau et al. [30]. This methodology consists in analyzing the magnetic hysteresis loops of the YBCO coated conductor as the one shown in Figure 6.3–2. The most remarkable feature of this hysteresis loop is that the peak of magnetization in the returning branch of the loop occurs at positive applied magnetic field. This is due to the fact that the magnetization achieves a maximum when the local field in the grain boundaries is zero and this do not occurs at zero applied field because the return field of the flux trapped

into the grains must be taken into account. This return field can be estimated by performing minor hysteresis loops with increasing maximum field and determining the saturation of peak position. In summary we have two experimental values, saturated peak position H_{peak} and saturation field H_{max} that allow us to estimate the grain critical current density from the following equations:

$$\frac{H_{peak}}{H_{\max}} = g\left((a/L)\right) \qquad \textbf{Eq. 6.3-1}$$

and

$$J_c^G = \frac{H_{peak}}{Lx(a/L)} \qquad \textbf{Eq. 6.3-2}$$

where *g* and *x* are dimensionless factors which depends on a/L, L being the sample thickness [30]. We have performed the above analysis to a ^{TFA}YBCO/^{MOD}CZO/^{ABAD}YSZ/SS sample and we have obtained J_c^{grain}(5K)= 40±10 MA/cm^2. This is the same value obtained at 5K in single crystalline samples hence confirming that the effects shown in Chapter 5 (Figure 5.2-10 a)) are due to the granular behaviour of the coated conductor [31],[17]. The case of 7% BZO- ^{TFA}YBCO/^{MOD}CZO/^{ABAD}YSZ/SS was also studied and the value obtained was J_c^{grain} (5K)= 70±20 MA/cm^2 (<a> = 2,06 μm), almost double than for a pure YBCO CC. The values of J_c^{GB} at 5K are much lower (13 MA/cm^2 for pure YBCO CC and 6 MA/cm^2 for 7% BZO-YBCO CC) because, at low magnetic fields, the regime where the grain boundary pinning dominates is enlarged.

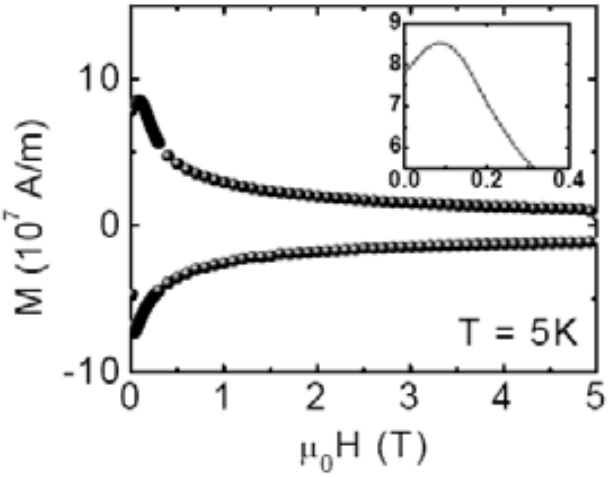

Figure 6.3–2 Hysteresis loop of a YBCO coated conductor measured at 5K. The maximum of the magnetization appearing at positive applied field is a sign of the granular behavior of the film. From the analysis of minor hysteresis loops an estimation of the intra-grain critical current density is obtained [17].

6.3.3. Effect of the $J_c(H)$ dependence comparing with single crystals

In general, when the density of pinning sites is increased, at the beginning, the macroscopic self-field J_c is also increased, but beyond some optimum density the performance will deteriorate because of the strain produced by these nanoparticles. Beyond ~ 10% mol. nanoparticles the J_c decreases. The applied magnetic field (H) has also a very important contribution here. At low H, vortices are far apart, minimizing their mutual interactions and in this "single vortex pinning" regime, J_c is independent of H. When H starts to increase, the interaction vortex-vortex is increased and the J_c decreases [3].

In the Figure 6.3–3 a), we compare the field dependence of J_c of BZO nanocomposite grown on SS and single crystal. Notice that above a certain magnetic field, $\mu_0 H_m$ = 4T, both J_c curves merge. This field, H_m, separates the region dominated by the current limiting effect at the grain boundaries ($H<H_m$) from that dominated by pinning at the grains ($H>H_m$). This magnetic field is $\mu_0 H_m$ =4T for the nanocomposite grown on a single crystal and tape. For these cases, H_m is much higher than that observed for a standard ^{TFA}YBCO film grown on a single crystal and tape ($\mu_0 H$ =2 T). This is probably due to the smoother field dependence of J_c in ^{TFA}YBCO-BZO that enlarges the regime where grain limitation dominates. These results should be taken into account when designing vortex pinning for certain field applications of coated conductors [17]. Figure 6.3–3 b) shows the angular dependence of a BZO doped YBCO compared with a SS standard sample at 1T and 77K. The anisotropy in J_c is strongly reduced in the nanocomposite and the overall $J_c(\theta)$ behaves clearly different and the peak in J_c when H//c (θ =180º) observed in the standard tape has been hidden in the

nanocomposite. This peak is usually attributed to the presence of defects along the c-axis direction and its apparently absence in the nanocomposite implies that pinning is dominated by the isotropic contribution induced by the BZO inclusions [2],[17].

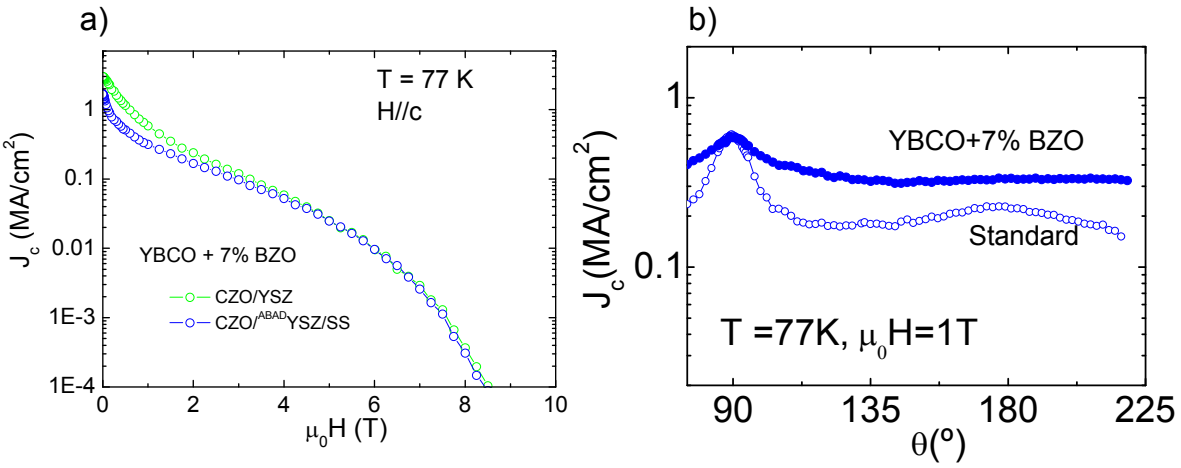

Figure 6.3–3 a) Comparison between the field dependence of critical current density of a BZO nanocomposite on ^{MOD}CZO/YSZ and on ^{MOD}CZO/^{ABAD}YSZ/SS; b) angular dependence of the J_c for a BZO-^{TFA}YBCO nanocomposite compared with the dependence of a standard film.

The volume pinning force density was calculated using the definition $F_p = J_c \, x \, H$ and the results are shown in Figure 6.3–4. With increasing H, J_c decreases. In this graph, $F_{p\,max}$ of 7% BZO on ^{MOD}CZO/YSZ (5,9 GN/m^3) and on ^{MOD}CZO/^{ABAD}YSZ/SS CC (3,5 GN/m^3) is larger than that of the pure YBCO on ^{MOD}CZO (3,2 GN/m^3 for single crystal and 2,7 GN/m^3 for tape). This fact suggests that pinning centers become more effective in 7% BZO doped YBCO films than that of the others.

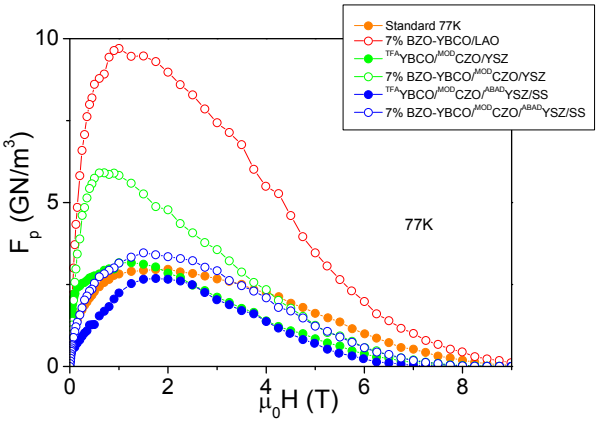

Figure 6.3–4 Pinning force density as a function of external H at 77 K of a 7% BZO doped YBCO films on different substrates (single crystal, buffered single crystal and metallic tape) compared with the one for standard pure YBCO on different substrates.

6.4. $BaCeO_3$-YBCO nanocomposites

6.4.1. State of the Art

In the last few years, doping the YBCO films with non-superconducting perovskites $BaMO_3$ (M = rare-earth metal) or some other nanoparticles has been widely studied.

We'll report here the effect of another oxide, $BaCeO_3$, with perovskite structure which was investigated. In melt-textured and bulk YBCO samples, $BaCeO_3$ has been found to improve the microstructure and superconducting properties. These results and also the similarity between $BaZrO_3$ (a = 4,19 Å) and $BaCeO_3$ (a = 4,40 Å) provided the motivation to study the effect and structure of $BaCeO_3$ doped TFA-YBCO thin films. Although there were no references of nanocomposites with $BaCeO_3$ using in-situ MOD approach, we found in the literature some groups which used BCO as a secondary phase utilizing physical deposition methods. T. Holesinger et al. [32] from Los Alamos National Laboratory have recently shown that the progression of I_c capacity for films of moderate thickness (≤ 2μm), containing different inclusions for pinning, improve had steadily increased over the last years. They achieved I_cs between 500-1000 A/cm^2 for BZO, $BaCeO_3$, $BaSnO_3$ and other phases (Figure 6.4–1).

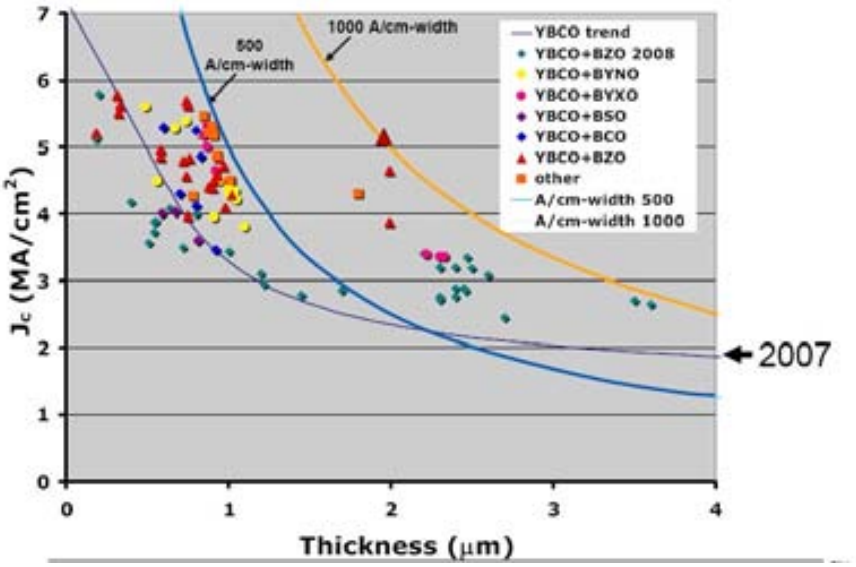

Figure 6.4–1 The dependence of J_c with the thickness for different nanocomposites.

Several bottom-up processes to incorporate pinning centers into YBCO films were studied by different routes. The switching target method by Haugan et al.[33], the mixture target method by Driscoll et al [34], and the surface decoration method by Matsumoto et al.[35],[6] were developed independently using PLD.

The influence of the amount of $BaZrO_3$ (BZO) on the structure and properties of $^{MOD}YBa_2Cu_3O_{7-x}$ (YBCO) films was systematically investigated by Ding et al.[36]. The YBCO films having 7 mol % BZO have a maximum critical current density (J_c) value (77 K, 0 T) of 6.0 MA/cm^2. The enhanced J_c derives from a high density of BZO nanoparticles existing in the YBCO matrix. With increasing BZO amount, J_c of the YBCO films begins to decrease due to larger particles.

Nanocomposite HTS materials have, indeed, open a new path towards the achievement of enhanced vortex pinning in HTS however, up to now, the strategy has been always to generate controlled nanosized spared volumes of non-superconducting secondary crystalline phases. In-situ grown nanocomposite films (PLD, MOCVD) are attached to use epitaxial nanodots and hence very detailed knowledge about self-organization principles and elastic properties is required to reach optimized materials [37].

The effect of $BaCeO_3$ nanoinclusions in the YBCO by MOCVD and PLD which generate macrostrain was also reported [38]. XRD study of composite films with $BaCeO_3$ revealed complex behaviour of these systems and critical differences between Zr and Ce substitution. It is argued that Ce substitution leads to possibly larger particle size of the secondary perovskite phase, than in case of Zr doping. On the other hand, critical temperature is not reduced in YBCO+BCO composites, while T_c gradually decreases with increase of Zr doping. The results obtained on BZO inclusions are consistent with observations of other authors [1], while detailed study of BCO admixture phase is reported here for the first time.

Following the physical route, an optimization of the $BaCeO_3$ concentration in YBCO films prepared by pulsed laser deposition was also performed by M. Irjala [39]. $BaCeO_3$'s effect on the growth process is complex above the 4 wt% and causes a variation of the twin structure of YBCO from uniaxial to triaxial around 6 wt%. Comparing with BZO, there is less strain for 10 wt% $BaCeO_3$ and the twin structure is clearly seen. Highest J_cs were obtained for low $BaCeO_3$ concentration (2 wt% and 4 wt%)(Figure 6.4–2).

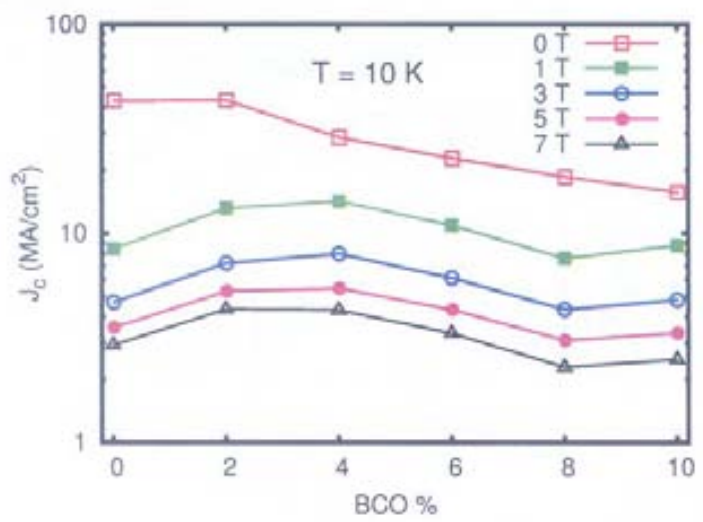

Figure 6.4–2 J_c function content of $BaCeO_3$ at 10K in selected fields [39].

6.4.2. Nucleation, growth and characterization on LAO and ^{MOD}CZO/YSZ

$BaCeO_3$ is a perovskite with a lattice parameter of a = 0,4396 Å from the cubic space group Pm -3m (Figure 6.4–3).

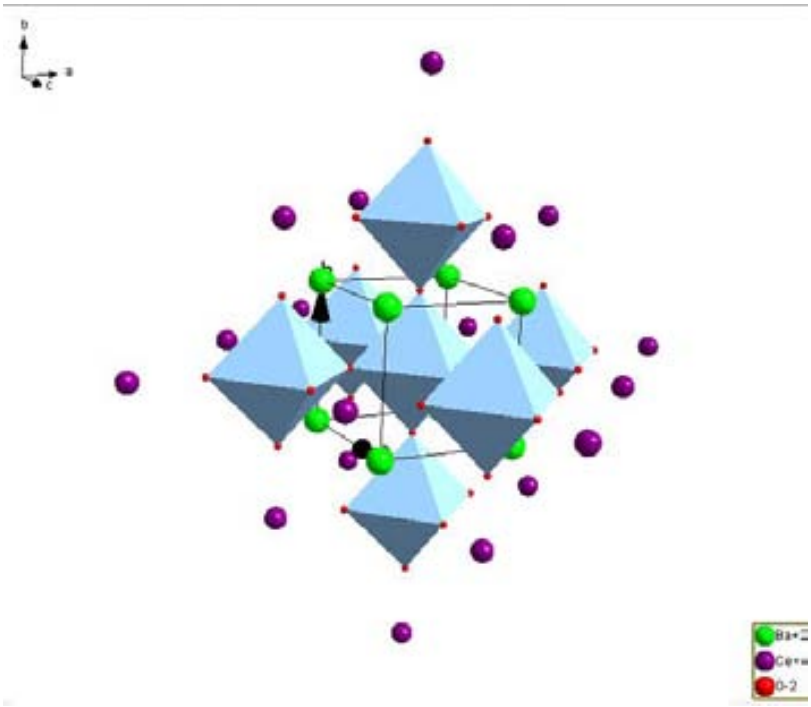

Figure 6.4–3 Crystallographic representation of cubic $BaCeO_3$ structure.

Composite films with different amount of $BaCeO_3$ (7%,10%,20% mol.) on LAO substrates were studied. The inclusions were introduced in the YBCO matrix by the addition of Ce(III) acetyl acetonate salt to the initial precursor solution. In spite of the large mismatch

with YBCO (Table 6.4-1), the inclusions grow epitaxial within the superconducting matrix using MOCVD [38].

	in plane [a]	out-of-plane [b]
$BaZrO_3$	+8,3	+7,1
$BaCeO_3$	+14,0	+12,8
[a]determined as $(a_{BMO}-a_{YBCO})/a_{YBCO} * 100\%$. [b]determined as $(3a_{BMO}-c_{YBCO})/c_{YBCO} * 100\%$.		

Table 6.4-1 Lattice mismatch (%) of YBCO with $BaZrO_3$ and $BaCeO_3$.

The behaviour of this new MOD-grown nanocomposite is similar with the one of BZO: the BCO nanoparticles nucleate prior to YBCO growth. This could be seen in the Figure 6.4–4 which represents a quench of 0 minutes at high temperature (810ºC). Besides YBCO (00l) reflections, a combination of CuO, $BaCeO_3$, OF and Y225 is seen. From the simultaneous observation of the precursors of YBCO with BCO and only very weak intensities of (00l) YBCO allow us to conclude that BCO nucleate (homogeneously and heterogeneously) before the heterogeneous nucleation of YBCO.

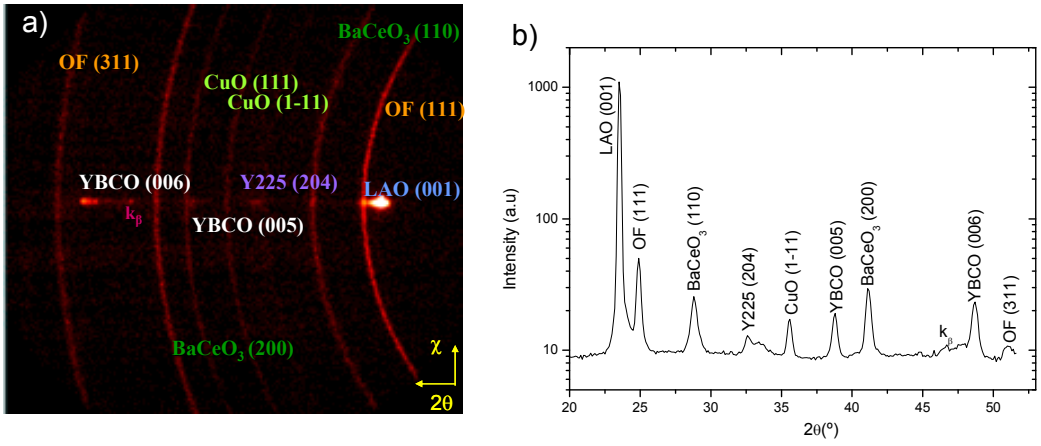

Figure 6.4–4 a) XRD phase distribution after a 0 minutes quench at 810ºC for 20 %$BaCeO_3$-YBCO/LAO; b) integration in χ of the previous frame.

Structural characterization was done using 2D General Area Detector Diffractometer System (GADDS). The frames obtain for different content of $BaCeO_3$ are presented in Figure 6.4–5. In the case of 20% $BaCeO_3$, the (110) and (200) reflections of $BaCeO_3$ are visible after a scan of 1 hour.

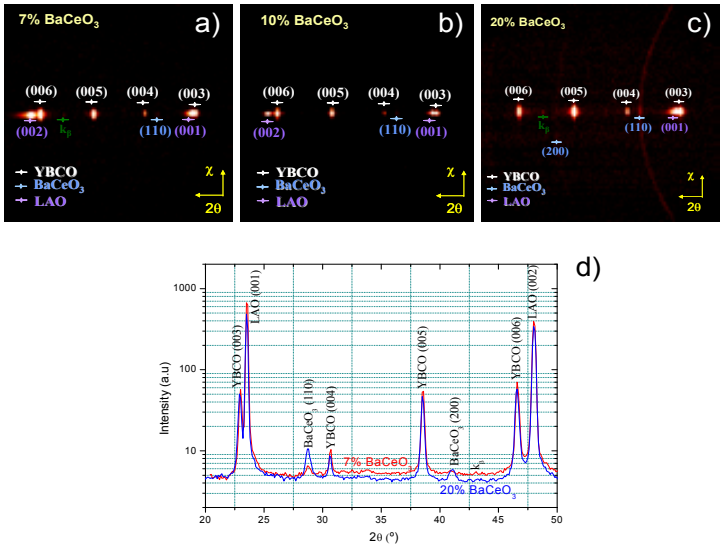

Figure 6.4–5 2D XRD patterns for different amount of $BaCeO_3$ doping in the YBCO matrix: a) 7%, b) 10% and c) 20%; d) integration in χ of the frames a) and c).

Figure 6.4–6 shows the micrographs obtain by SEM for three different nanocomposites with 7%, 10% and 20% $BaCeO_3$ addition. The morphology changes with increasing the content of dopant. Meanwhile for 7% content the YBCO grains are c-axis oriented but still the surface is high porous, for 10% $BaCeO_3$ we have two populations of precipitates: some less than 100 nm and others of about 500 nm reaching 1 μm in some places. For 20% less porosity is observed but still there are lots of small precipitates on the surface.

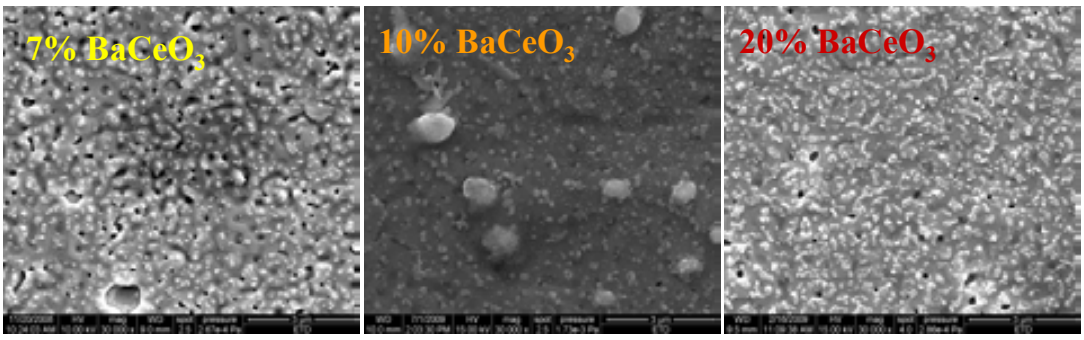

Figure 6.4–6 SEM micrographs of nanocomposites with 7%, 10%, 20% $BaCeO_3$ additions in YBCO.

In the Figure 6.4–7 there is the typical 2D XRD pattern for a 7% $BaCeO_3$-YBCO prepared on a ^{MOD}CZO buffered YSZ. Figure 6.4–7 b) represents the integration in chi of the previous θ-2θ scan (a). The quantity of $BaCeO_3$ is bigger than in the case of the samples prepared on LAO, because this phase is formed also from the reaction between YBCO and CZO at high temperature. Similar with BZO, two different types of nanoparticles are observed: epitaxial ones given by (200) reflection and random ones-(110) $BaCeO_3$.

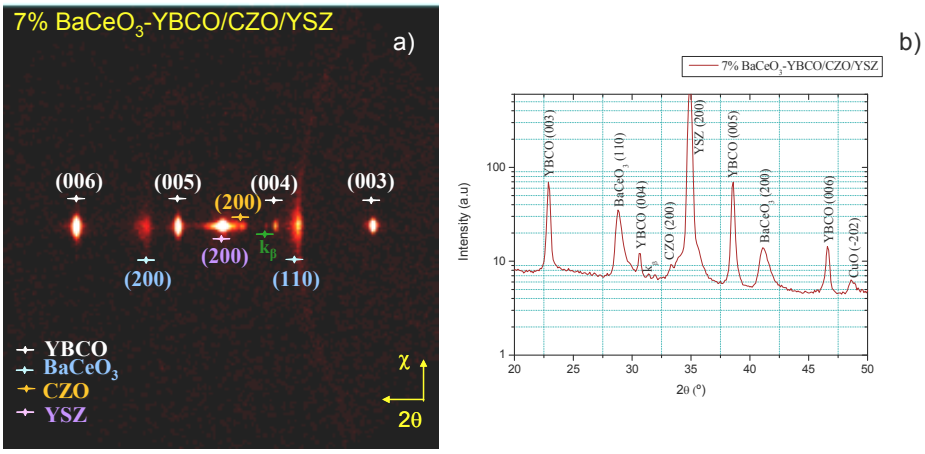

Figure 6.4–7 a) θ-2θ pattern obtained with a bidimensional detector diffractometer of a 7% $BaCeO_3$-YBCO composite prepared on ^{MOD}CZO/YSZ; b) integration of the previous frame in chi.

If we look to the surface, the morphology is a little bit different when CZO is present than in the standard case. For 10% $BaCeO_3$ additive, a high porosity can be seen in Figure 6.4–8 a). This porosity could be the reason for the lower J_c at self-field and, in conclusion, this have to be decreased.

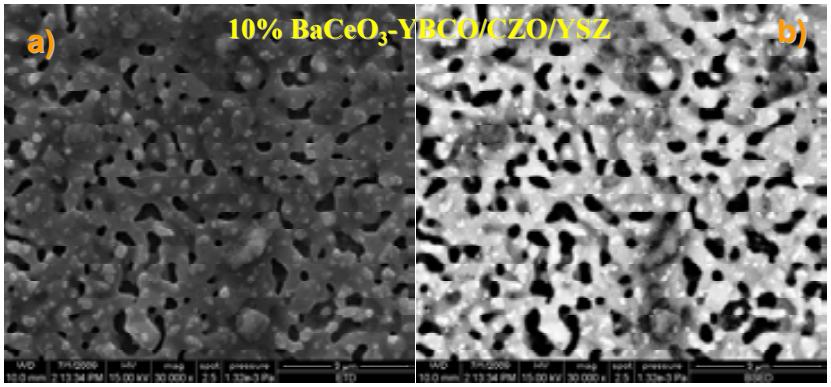

Figure 6.4–8 a) SEM images for 10% $BaCeO_3$; b) back scattered electrons mode image of a). The sample was prepared on ^{MOD}CZO buffered YSZ substrates.

6.4.3. Dimension of the nanoparticles

In 1918, P. Scherrer showed that, when parallel monochromatic radiation falls on a random oriented mass of crystals, the diffracted beam is broadened when the particle size is small [40]. This formula relates the mean (volume average) crystallite size, *L*, of a powder to the broadening, β, of its powder diffraction peaks (ignoring other effects such as strain):

$$\beta_L = \frac{K\lambda}{L\cos\theta} \qquad \textbf{Eq. 6.4-1}$$

where θ is the usual Bragg angle, λ is the radiation wavelength, and K is a constant which depends on the assumptions made in the theory (e.g. the peak shape and crystallite habit, spherical crystallites being the easiest case to interpret) but is anyway close to unity and often taken as 0.9. Thus we see that β and *L* are reciprocally related: the greater the broadening the smaller the crystallite size and vice-versa. It is worth having a quick "intuitive glance" at why this should be so: because the interference from *n* = 2, 3, 4..... up to *n* = 1,000 and more, scattering centres produces fringes which ultimately become "diffraction" in three dimensions. These fringes start off being very broad at low *n* and become indefinitely sharp as $n \rightarrow \infty$. Another way of looking at this is to note that interference cannot occur if *n* = 1 and even the most primitive interference requires at least two centres (*n* = 2); then as *n* increases further the interference becomes more and more precise according to the number of contributing scatterers. In practice the sharpness eventually stops increasing when some other limit is reached, such as the inherent instrumental broadening, $\beta_{instrument}$, or a theoretical limit known as the Darwin limit. For real powder samples and diffractometers this limit is reached when the crystallite size, *L*, is around 1-10 μm (or larger). So the use of peak broadening to determine crystallite size is normally limited to cases where the average crystallite size is ≤ 1 μm [25].

The mean particles size was calculated using the Scherrer formula and values of 49,2 nm (200) x 28,4 nm (110) showed a particular shape, a lamellar one, for the $BaCeO_3$ nanoparticles, different of the 15 nm round shape of the BZO determined by TEM. In any case, the BCO particle size is found to be much larger than in the case of BZO.

6.4.4. Quantification of the random/epitaxial fraction

After the methodology developed in the group by A. Llordés, we calculated the epitaxial and random volume fractions. Due to the low volume fraction of the nanoparticles it was necessary to measure during 1h at the fixed ω value. Although ω was optimized to accomplish the Bragg condition for the (110) BCO planes, the tails of nearby YBCO poles are also detected due to the bi‑dimensionality of the detector [13]. The steps followed for doing this measurement with GADDS were some simple ones. First a φ scan of the zone where (110) BCO should be textured is done (φ = 0º). Then, in this zone, another φ scan of 0,2º is done for searching the maximum of the epitaxial peak. Once the maximum is found (in this case it is approximated because the epitaxial part is weak), the conditions of the measurement are: 2θ = 28.8, ω = 14.4º, χ = 70, φ = 359, time of measurement 3600 s in step.

From the measurements, it was clearly seen that there are two textured parts of the $BaCeO_3$ (Figure 6.4–9 a)):

1. (110) $BaCeO_3$ $\chi = 0^o$ ***** [110] $BaCeO_3$ // [001] LAO;
2. (110) $BaCeO_3$ $\chi = 45^o$ ***** [001] $BaCeO_3$ // [001] LAO.

From the calculation it results that the polycrystalline fraction dominates. The results of the random/epitaxial part obtained for three different content of $BaCeO_3$ nanoparticles are presented in Figure 6.4–9 b).

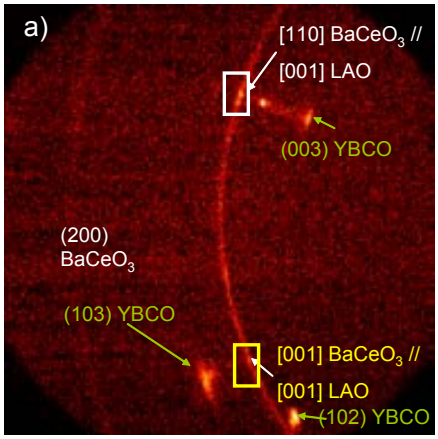

b)

% mol $BaCeO_3$	V_{ep} %	V_{poli} %
7 %	53.39	46.61
10 %	28.59	71.40
20 %	9.91	90.09

Figure 6.4–9 a) 2D XRD pattern of the nanocomposites measured at fixed ω; b) values of the random/epitaxial volumes of the $BaCeO_3$ different amount YBCO samples.

If we compare this nanocomposite with BZO and Y_2O_3, it can be clearly seen that meanwhile $BaCeO_3$ and $BaZrO_3$ remain mostly random oriented, Y_2O_3 is mainly epitaxial (Figure 6.4–10).

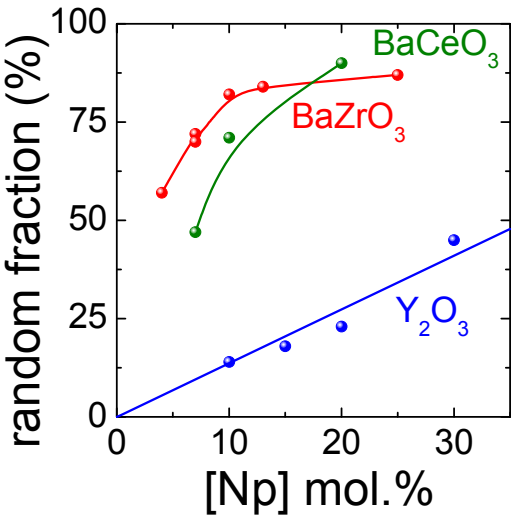

Figure 6.4–10 Representation of the random fraction function the content of nanoparticles for three different additives: Y_2O_3, $BaZrO_3$, $BaCeO_3$.

6.4.5. Microstrain

Small grains and lattice distortions caused by lattice defects are reflected in a broadening of the X-ray diffraction peaks. Some typical lattice defects are: i) dislocations, ii) unrelaxed misfits between coherent phases, iii) severely distorted grain boundaries in nanocrystalline materials, iv) strains between coherent sheets, especially in strained layer structures, v) point defects, vi) second phase particles or inclusions, vii) concentration gradients in nonequilibrium multiphase materials or viii) stacking faults, etc. Krivoglaz [41] has classified lattice defects according to the character of their strain fields: first or second class defects (the notation: 'I' or 'II' class is also used) have strain fields of long- or short-range character, respectively. As a thumb rule their strain fields decay as the reciprocal or the square of the reciprocal of the distance from the defect. The defects i) to iv) are of first class, and v) to vii) are of second class. Stacking faults are a peculiar kind of lattice defect. The planar parts of them act as boundaries in certain crystallographic directions, thus creating smaller 'particle size' in these directions. This part of these defects, if separable at all, causes 'size broadening' without 'strain broadening'. The bounding partial dislocations, especially if they are in the interior of the crystallite, however, correspond to the I class defects causing 'strain broadening'. An important conclusion of Krivoglaz's classification is that, if the crystal is large enough (i.e. there is no 'size broadening') true diffraction peak broadening (in this case only 'strain broadening') is caused only by the I class defects [42].

Line width analysis of the XRD patterns by means of Williamson Hall plot for the $BaCeO_3$ nanocomposites was performed (Figure 6.4–11). As reported in our group [13], the microstrain for a standard pure YBCO film on LAO is 0,09 %. We note that the microstrain of the nanocomposite with 7% $BaCeO_3$ is increased (0,159 %) compared with a standard film but still not reaching the value 0,287 % of the nanocomposite with 7% BZO. This value becomes bigger if we put 20% $BaCeO_3$ inside the YBCO (0,285 %).

The size in the case of the two nanocomposites is different (BCO is bigger than BZO). This can be related with the nucleation of the nanoparticles. There is a critical radius r* when the nucleation takes place. For values lower than r*, the formed nuclei are instable and just for values higher than r*, stable grains could be obtained during the growth process. The critical radius of a nucleus can be calculated with the following equation:

$$r^* = -2\frac{\gamma}{\Delta G_v} \qquad \textbf{Eq. 6.4-2}$$

where r* is the critical radius, γ = surface free energy per unit area , and ΔG_v is the volumetric free Gibbs energy.

In conclusion, for forming nanoparticles starting from a solution through homogeneous nucleation, it is necessary to exist a saturation of the species to grow. In this case, a higher change of the Gibbs energy will be registered. More saturation we have, higher number of nuclei will be formed and lower size this will have [14].

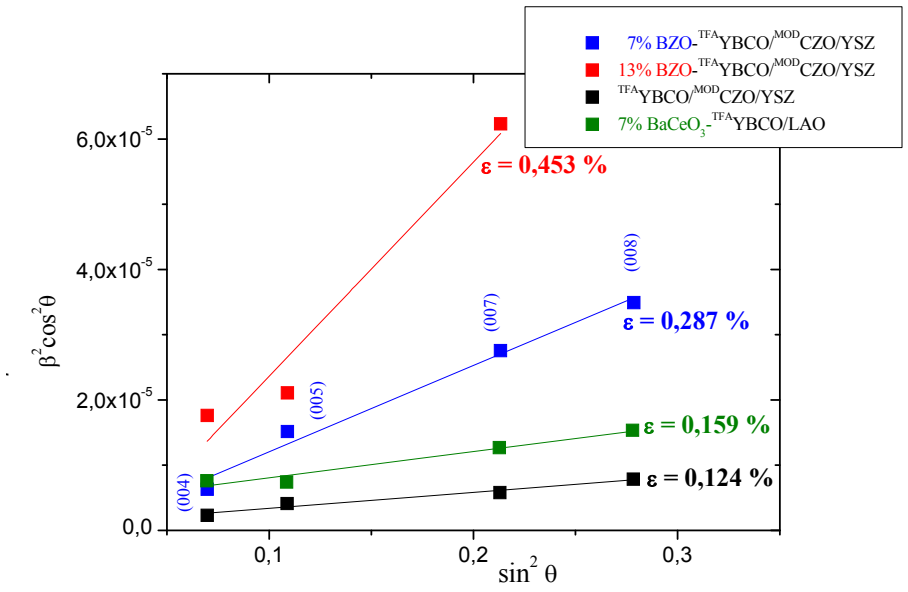

Figure 6.4–11 Williamson-Hall plot for calculating the microstrain in the case of $BaCeO_3$ and $BaZrO_3$.

The fact that the BCO nanoparticles have a higher diameter shows that there is a lower "incoherent specific interface", and in this way, less type I defects are generated. The microstrain dependence versus the incoherent specific interface is shown in Figure 6.4–12. A single linear behavior of the nanostrain occurs with the incoherent specific interface of nanodots. This latter parameter takes into account the percentage of random nanodots and the corresponding nanodot size. Hence, this result is a clear demonstration that the non coherent interface between the nanodots and the YBCO matrix is the controlling parameter for the inhomogeneous nanostrain generation in the CSD nanocomposites [37].

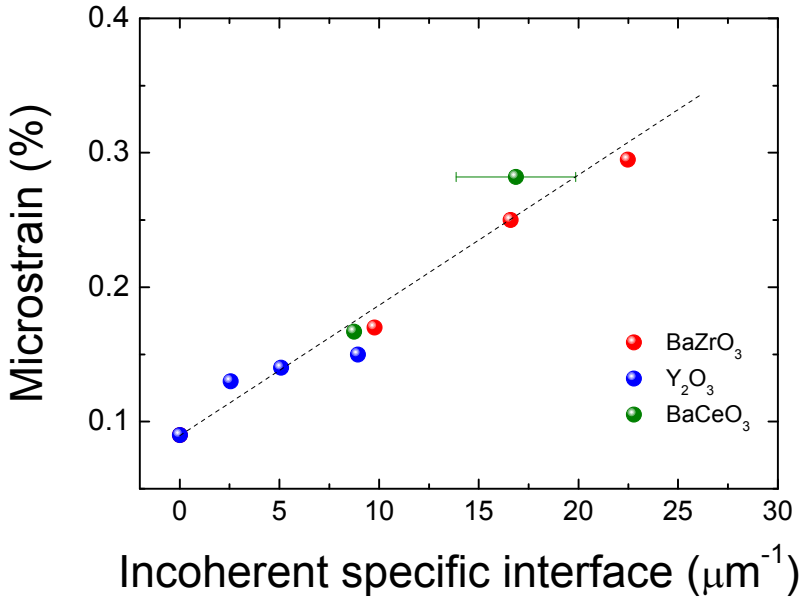

Figure 6.4–12 Microstrain versus incoherent specific interface for three different nanocomposites: BCO, BZO, Y_2O_3.

6.4.6. Effect of the $BaCeO_3$ doping in the YBCO superconducting properties

From our previous studies and also from other groups which use PLD [43] it was shown that addition of an admixture phase BZO (or any other dielectric phase, e.g., $BaSnO_3$ (BSO) or Y_2O_3) to "pure" YBCO thin films creates an additional defect nanostructure within the films. This defect nanostructure is formed by nano-sized particles of admixture phase, which play the role of strong point-like pinning centers for Abrikosov vortices, as well as columnar defects, which in turn result from the self-organization of the nanoparticles into linear structures (directed primarily along the *c* axis) and additional dislocations in the film material, generated by these nanoparticles.

The BMO (M = Zr, Ce) nanoparticles in our MOD films are dispersed throughout the film thickness, providing an enhancement in the flux pinning properties compared to undoped YBCO film. The major influence of this phenomenon is due to defects indused by

theses nanoparticles (microstrain) and not by the nanoparticle itself. The superconducting properties at 77K of such nanocomposites are decreasing with the increasing of the $BaCeO_3$ content (J_c(7% $BaCeO_3$) = 2,7 MA/cm^2, J_c(10% $BaCeO_3$) = 1,57 MA/cm^2, J_c(20% $BaCeO_3$) = 0,54 MA/cm^2)(Figure 6.4–13 a)). This could be because with more nanocomposite is introduced in the YBCO, the strain for accommodating these particles is higher. Investigations into the behaviour of the critical current density in magnetic fields at 50 K reveal an enhancement of J_c in the YBCO film with 20% $BaCeO_3$ doping compared with a standard sample (Figure 6.4–13 b)). This enhancement is lower than in the case of doping with BZO.

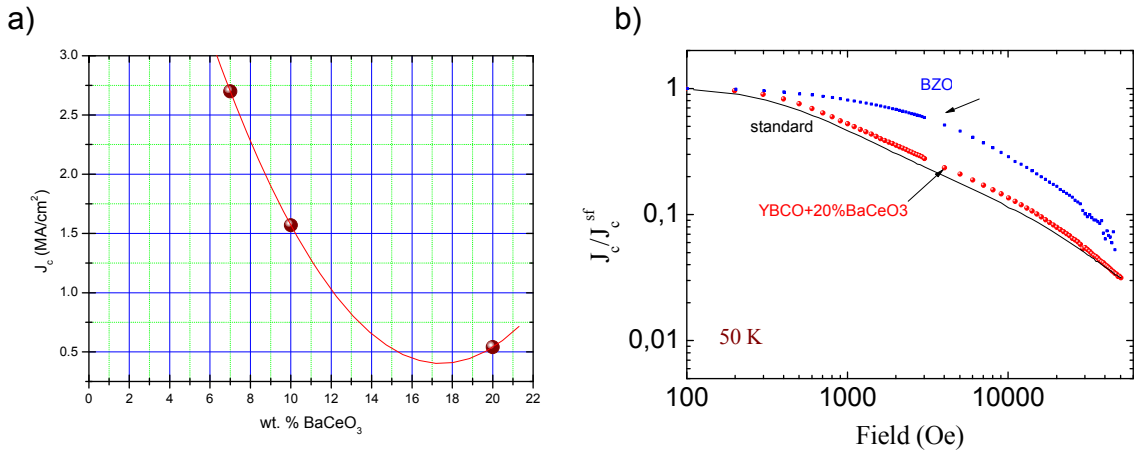

Figure 6.4–13 a) The self-field J_c function $BaCeO_3$ content dependence; b) J_c function magnetic field for a 20%$BaCeO_3$ doped YBCO sample compared with a BZO nanocomposite.

In Figure 6.4–14 a), the normalized magnetization versus temperature curves are shown for different architectures containing pure YBCO on LAO and on ^{MOD}CZO buffered YSZ and also with different dopants ($BaCeO_3$ and $BaZrO_3$). The values of T_c and the transition width are presented in Figure 6.4–14 b). As reported in other references [44], nanocomposites films present a reduction of the T_c as compared with standard pure YBCO. In this case, the decrease in T_c could be attributed to the macrostrain as other experiments have shown [45]. When the strain produced by the insertion of the nanoparticles in the superconductor increases, the transition width increases. Also, in most samples the transition width is determined by sample inhomogeneities resulting in different values of T_c within the sample. Such effects are often caused by imperfect oxygen doping in oxide superconductors or by surface degradation.

a)

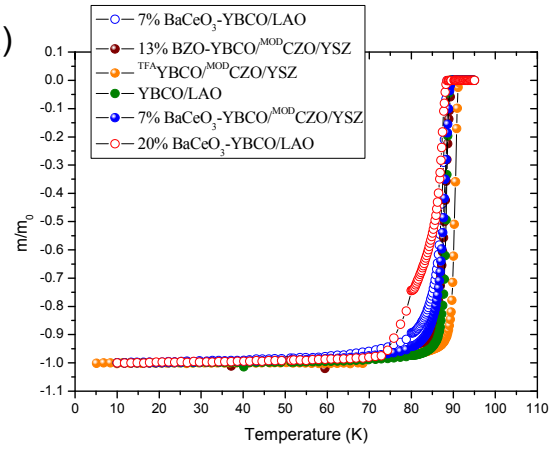

b)

Sample	T_c 10%	T_c 50%	T_c 90%	ΔT_c	$T_{c,onset}$
YBCO/^{MOD}CZO/YSZ	90.9	90.24	88.68	2.22	91.2
YBCO/LAO	88	88.5	86.5	1.5	89.7
7% $BaCeO_3$-YBCO/^{MOD}CZO/YSZ	88.84	87.65	83.45	5.39	89.3
13% BZO-YBCO/^{MOD}CZO/YSZ	89.20	87.68	83.67	5.53	89
7% $BaCeO_3$-YBCO/LAO	88.84	87.85	80	8.84	88.2
20% $BaCeO_3$-YBCO/LAO	87.72	85.64	75.83	11.89	88.2

Figure 6.4–14 Critical temperatures for different architectures, both pure YBCO and BZO and $BaCeO_3$ YBCO nanocomposites.

If we plot the dependence of the T_c(50%) function the percentage of nanoparticles, we can see a tendency of decreasing with more nanoparticles (Np) are inside the superconducting matrix (Figure 6.4–15). However, the $T_{c,onset}$ remains constant.

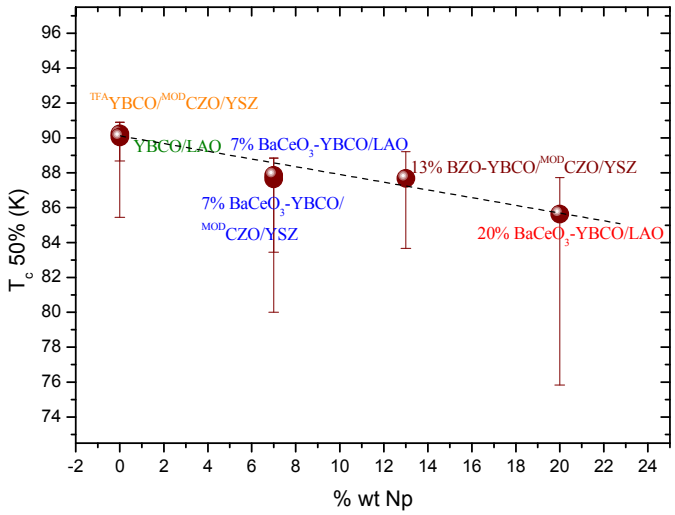

Figure 6.4–15 The dependence of the T_c on the content of nanoparticles for the BZO and BCO series.

6.5. Conclusions

Successful nanocomposites films with $BaREO_3$ (RE = Zr, Ce) inclusions were grown on both ^{MOD}CZO buffered YSZ single crystalline substrates and ^{MOD}CZO/^{ABAD}YSZ/SS metallic tapes using the in-situ approach for vortex pinning enhancement. The crystallinity and microstructure of epitaxial $BaREO_3$-YBCO/^{MOD}CZO/ YSZ (00l) films were investigated by a two-dimensional x-ray diffraction and TEM. Two different types of nanoparticles are observed: epitaxial ones given by (200) reflection and random oriented ones-(110) $BaREO_3$. Also, increasing the $\Delta\omega$ by introducing more nanoparticles leads to an increase of the microstrain. If we compare these two nanocomposites, $BaCeO_3$ and BZO, with Y_2O_3, it can be clearly seen that meanwhile $BaCeO_3$ and $BaZrO_3$ remain mostly random oriented, Y_2O_3 is mainly epitaxial. By mean of TEM, CZO buffer layers exhibit a good overall epitaxial quality. Defects such as low angle grain boundaries or buffer layer discontinuities are observed and could act as diffusion paths for Ba which leads to nucleation of BZO or (Zr)-$BaCeO_3$ at the CZO/YSZ interface. Unexpectedly, (Zr)-$BaCeO_3$ was not found at the YBCO/CZO interface. The preferential nucleation at the CZO/YSZ interface can be tentatively associated to lattice mismatch effects.

High J_c have been achieved with MOD-(Ce,Zr)O_2 as cap layer for all nanostructurated CC architectures reaching values of J_c(77K)= 3,1 MA/cm^2 (7% BZO-YBCO/^{MOD}CZO/YSZ), J_c(77K)= 2,7 MA/cm^2 (7% $BaCeO_3$ on single crystal) and J_c(77K)= 1,7 MA/cm^2 (tapes). These nanostructured CC exhibit enhanced vortex pinning properties (reduced anisotropy, smooth magnetic field dependence).

6.6. References

[1] S. Kang, A. Goyal, J. Li et al., "Flux-pinning characteristics as a function of density of columnar defects comprised of self-assembled nanodots and nanorods in epitaxial $YBa_2Cu_3O_{7\text{-delta}}$ films for coated conductor applications," Physica C **457**, 41 (2007).

[2] J. Gutierrez, A. Llordes, J. Gazquez et al., "Strong isotropic flux pinning in solution-derived $YBa_2Cu_3O_{7-x}$ nanocomposite superconductor films," Nature Materials **6** (5), 367 (2007).

[3] S. R. Foltyn, L. Civale, J. L. MacManus-Driscoll et al., "Materials science challenges for high-temperature superconducting wire," Nat Mater **6** (9), 631 (2007).

[4] L. Ciontea, G. Celentano, A. Augieri et al., "Chemically Processed $BaZrO_3$ Nanopowders as Artificial Pinning Centres," 8th European Conference on Applied Superconductivity (Eucas'07) **97** (2008).

[5] X. Obradors, T. Puig, A.Palau et al., "Nanostructured superconductors with efficient vortex pinning," Comprehensive Nanoscience and Technology **5** (in press).

[6] K. Matsumoto and P. Mele, "Artificial pinning center technology to enhance vortex pinning in YBCO coated conductors," Superconductor Science & Technology **23** (1) (2010).

[7] Y. Yamada, A. Ibi, S. Miyata et al., "IBAD-PLD method coated conductor with high critical current in a magnetic field," Journal of the Japan Institute of Metals **71** (11), 1011 (2007).

[8] T. Izumi; Y. Shiohara, "R&D of coated conductors for applications in Japan," Physica C (2010).

[9] Y. Yamada H. Kobayashi, A. Ibi, S. Miyata, Y. Shiohara, T. Kato, T. Hirayama, "Investigation of in-field properties of YBCO multi-layer film on PLD/IBAD metal substrate," **463-465**, 661 (2007).

[10] B. Maiorov, S. A. Baily, H. Zhou et al., "Synergetic combination of different types of defect to optimize pinning landscape using $BaZrO_3$-doped $YBa_2Cu_3O_7$," Nature Materials **8** (5), 398 (2009).

[11] N. M. Strickland, N. J. Long, E. F. Talantsev et al., "Enhanced flux pinning by $BaZrO_3$ nanoparticles in metal-organic deposited YBCO second-generation HTS wire," Physica C **468**, 183 (2008).

[12] F. Ding; H. Gu; T. Zhang, "Influence of $BaZrO_3$ Amount on Microstructure and Properties in $YBa_2Cu_3O_{7-x}$ Films Prepared by TFA-MOD Process," J Supercond Nov Magn (2010).

[13] A. Llordes, "Superconducting nanocomposite films grown by chemical solution deposition: synthesis, microstructure and properties," (2010, PhD thesis).

[14] F. Martinez, "Uso de sales inorgánicas y nanopartículas en el crecimiento de capas delgadas superconductoras crecidas por CSD," PhD Thesis, UAB, Bellaterra (2011).

[15] N. Roma and et al., "Acid anhydrides: a simple route to highly pure organometallic solutions for superconducting films," Superconductor Science and Technology **19** (6), 521 (2006).

[16] X. Yongli and S. Donglu, "A review of Coated Conductors Development."

[17] A. Pomar, V. R. Vlad, A. Llordes et al., "Enhanced Vortex Pinning in YBCO Coated Conductors With BZO Nanoparticles From Chemical Solution Deposition," Ieee Transactions on Applied Superconductivity **19**, 3258 (2009).

[18] J. Gazquez, "TEM investigation of growth mechanisms and microstructure of model YBCO coated conductor architectures deposited by metalorganic decomposition," PhD Thesis (2006).

[19] K. Verbist, A. L. Vasiliev, and G. Van Tendeloo, "Y_2O_3 inclusions in $YBa_2Cu_3O_{7-\delta}$ thin films," Appl. Phys. Lett. **66**, 1424 (1995).

[20] T. Puig, J. Gutierrez, A. Pomar et al., "Vortex pinning in chemical solution nanostructured YBCO films," Superconductor Science & Technology **21** (3) (2008).
[21] J. Gutierrez, T. Puig, and X. Obradors, "Anisotropy and strength of vortex pinning centers in $YBa_2Cu_3O_{7-x}$ coated conductors," Applied Physics Letters **90** (16) (2007).
[22] A. Ulyanenkov, "Introduction to High Resolution X-Ray Diffraction/X-ray Characterization of Thin Layers," http://x-ray.kjist.ac.kr/Publication/reference/intro-HRXRD.pdf (21.-23. May 2003 Uckley).
[23] http://www.chemistry.ohio-state.edu/~woodward/ch754/powder_diffraction.pdf.
[24] G. K. Williamson and W.H.Hall, "X-Ray line broadening from field aluminium and wolfram " Acta Metallurgica **1**, 22-31 (Jan. 1953).
[25] P. Barnes, S. Jacques, and M. Vickers, "Determination of size and strain," http://pd.chem.ucl.ac.uk/pdnn/peaks/sizedet.htm (Birkbeck College, University of London).
[26] "X-Ray Diffraction," http://web.pdx.edu/~pmoeck/phy381/Topic5a-XRD.pdf.
[27] Jan E Evetts, "Transport properties of low-angle grain boundaries and granular coated conductors," Superconductor Science and Technology **17** (5) (2004).
[28] A A Gapud, D K Christen, R Feenstra et al., "On narrowing coated conductor film: the emergence of granularity-induced field hysteresis of transport critical current," Superconductor Science and Technology **21,**, 075016 (2008).
[29] D. C. Larbalestier, in *"Grain Boundaries in Cuprates and Pnictides - Are There Reasonable Hopes for Better Properties?", MRS Spring 2010* (5-9 April, San Francisco, USA, 2010).
[30] A. Palau, T. Puig, X. Obradors et al., "Simultaneous determination of grain and grain-boundary critical currents in $YBa_2Cu_3O_7$-coated conductors by magnetic measurements," Phys. Review B, **75**, 054517 (2007).
[31] V. R. Vlad, K. Zalamova, M. Coll et al., "Growth of Chemical Solution Deposited $^{TFA}YBCO/^{MOD}(Ce, Zr)O_2/^{ABAD}YSZ/SS$ Coated Conductors," Ieee Transactions on Applied Superconductivity **19** (3), 3212 (2009).
[32] T. Holesinger, M. Feldmann, B. Maiorov et al., "Nano-Engineering of Phase Separable Inclusions for High Performance YBCO Thick Films," CCA 2009, Barcelona (22-24 November 2009).
[33] Haugan T, Barnes PN, and et al. Wheeler R, " Addition of nanoparticle dispersions to enhance flux pinning of the $YBa_2Cu_3O_{7-x}$ superconductor " Nature **430** (7002), 867 (2004).
[34] J. L. MacManus-Driscoll, S. R. Foltyn, Q. X. Jia et al., "Strongly enhanced current densities in superconducting coated conductors of $YBa_2Cu_3O_{7-x}$ + $BaZrO_3$," Nat Mater **3** (7), 439 (2004).
[35] P. Mele and et al., "Enhanced high-field performance in PLD films fabricated by ablation of YSZ-added $YBa_2Cu_3O_{7-x}$ target," Superconductor Science and Technology **20** (3), 244 (2007).
[36] Fazhu Ding, Hongwei Gu, and Teng Zhang, "Influence of $BaZrO_3$ Amount on Microstructure and Properties in $YBa_2Cu_3O_{7-x}$ Films Prepared by TFA-MOD Process," J Supercond Nov Magn (2010).
[37] A. Llordés, A. Palau, R. Vlad et al., "Nanoscale strain-induced pair suppression as a source of vortex pinning in high-temperature superconductors," To be published.
[38] A. V. Boytsova, A. R. Kaul, S. V. Samoilenkov et al., "Thin film nanocomposites based on YBCO with defects comprised of self-assembled inclusions," Journal of Physics **234** (Conference Series), 012008 (2010).
[39] M. Irjala, H. Huhtinen, R. Jha et al., "Optimization of BCO concentration in YBCO Films Prepared by Pulsed Laser Deposition," Applied Superconductivity, IEEE Transactions on **21** (3), 2762 (2011).

[40] A. L. Patterson, "The Scherrer formula for X-Ray particle size determination," Phisical Review **56**, 978 (1939).
[41] M. A. Krivoglaz, "Theory of X-ray and Thermal Neutron Scattering by Real Crystals," Plenum (New York) (1969).
[42] T. Ungar, "Strain Broadening Caused by Dislocations," JCPDS-International Centre for Diffraction Data (1997).
[43] A.A. Kalenyuk, A. L. Rebikov, V.O. Moskalyuk et al., "Microwave properties of high-temperature superconducting YBCO(BZO) thin films with admixture nano-particles," IEEE Trans. Appl. Supercond. (2010).
[44] A. Augieri et al., "Critical current density of $YBa_2Cu_3O_{7-x}$ films with $BaZrO_3$ inclusions on $SrTiO_3$ and Al_2O_3 substrates " J. Phys.: Conf. Ser. **97** (012209) (2008).
[45] W.D Markiewicz, "Strain Dependence of the Critical Temperature T_c of Polycrystalline Nb_3Sn Superconductors," IEEE Trans. Appl. Supercond. **17**, 2631 (2007).

CHAPTER 7 GENERAL CONCLUSIONS

In this dissertation, we have obtained and characterized nanostructured YBCO based second generation (2G) coated conductors obtained by chemical solution routes in order to establish the limits of performance that are reachable and addressed materials challenges to improve properties and decrease the manufacturing cost without compromising their performance levels.

Starting with a brief history of the superconductivity and the description of the YBCO properties, followed by a summary of the experimental techniques used, the next focus was on the synthesis and characterization of doped CeO_2 used in different architectures as cap layer. Starting from acetylacetonates salts, a high stability doped CeO_2 precursor solution with time and good wettability was obtained and deposited onto different substrates (YSZ, ^{PLD}LZO/LAO, ^{SPUT}YSZ/Al_2O_3). Time, p_{O2}, content of Ag additives and growth temperature conditions could also influence the mobility in 10% Zr-doped CeO_2 films. An open issue is still the influence of the oxygen partial pressure on the GB mobility. GBs in Wolmer Weber films needs to be "zipped" and stress or defects there need to be healed. It is suggested that when the percentage of oxygen vacancies is too high (Ar/H_2), the mobility is reduced. The optimal combination of temperature-time and p_{O2} allowing to achieve a high percentage of surface planarity was determined, while a shortening of the required annealing time could be used when Ag additives are used.

By investigating the influence of increasing the precursor solution concentration from 0,25 M to 0,4 M, we have found by XRD and RHEED analysis that the films contain also a certain amount of randomly oriented nanocrystals. In this case, the addition of a small concentration of a Ag additive seems to be helpful for enhancing the epitaxial structure.

The morphology of the doped CeO_2 cap layer revealed by AFM was found to be different, depending of the growth atmosphere, as it was previously shown at ICMAB. Under reducing atmosphere, the doped CeO_2 film is inherently granular with poor planarity (52,6 %), as a result of grain growth inhibition induced by grain-boundary contamination with C impurities. The surface of the sample annealed in O_2 presents large flat terraced grains, very different from the rounded ones found in a reducing atmosphere. The mobility of the GB increases with dopants, Gd^{3+} and Zr^{4+}, although the mechanism is different in the two cases. Large surface flatness (90% planarity) and small roughness (rms = 0,8 nm) were obtained for the CZO cap layers when they were annealed in O_2 atmosphere.

The second step in this complex process of obtaining coated conductors was the analysis of the deposition and growth of YBCO on different substrates (YSZ, ^{PLD}LZO/LAO, ^{SPUT}YSZ/Al_2O_3) with ^{MOD}CZO cap layers.

Superconducting properties of YBCO films on YSZ were characterized and transport J_c values of 5,2 MA/cm^2 were obtained for a 275 nm thick YBCO film on ^{MOD}CZO buffered YSZ single crystals at 77 K and zero-external field. At 77K, critical current density dependence with the magnetic field (H//c) of both a standard sample and a buffered one is strongly mediated by the anisotropic defect pinning contribution.

For studying the capability of LZO buffer layers as a part of a RABiTS coated conductor, YBCO films grown from TFA precursors were deposited on top of a ^{MOD}CZO/^{PLD}LZO/LAO architecture. By varying the nucleation temperature, from 770ºC to 740ºC, it was noted that the J_c at 77K decreases from 2,3 MA/cm^2 to 0,9 MA/cm^2. Our work show that the typical decrease of J_c observed in RABiTS CC with this architecture cannot be associated to the LZO, but probably to an excess of roughness in the metallic substrates. This drop of the J_c when decreasing the nucleation temperature to 740ºC can be correlated to the enhanced microstrain which leads to conclude that the mesostrain associated to the grain boundaries has not been healed out.

Critical current densities at 77K as high as 1,8 MA/cm^2 were also obtained for the 770ºC-810ºC growth of the ^{TFA}YBCO/^{MOD}CZO/^{SPUT}YSZ/Al_2O_3 architecture, although a small drop of T_c (89K vs. 91,2K in the standard film) suggests that some impurification of YBCO occurs. Also, in this case, the reactivity between CZO and YBCO has been found higher than in the case of a YBCO/^{MOD}CZO/YSZ film. This fact is shown by the different intensities of the (110) $BaCeO_3$ peak in the two cases.

The incorporation of silver salts in the YBCO precursor solution goes to an enhancement of the J_c with the magnetic field indifferent of the growth temperature but, at self field, the J_c is lower, which is contradictory with the previous results obtained in the group. A flatter terraced surface is obtained and the porosity is decreased. More investigations are necessary in this case.

Besides the analysis of single crystal substrates, the transfer of the knowledge to metallic substrates was done. Coated Conductors on ^{ABAD}YSZ/SS metallic substrates using chemical solution deposition methods were obtained and carefully investigated. Several non-magnetic, 0,1 mm thick, CrNi Stainless Steel (SS) substrates with biaxially textured ^{ABAD}YSZ layers deposited on them, received from Bruker HTS, Germany have been used. These substrates display low rms roughness value (~1,8 nm) and a flat area fraction of about 49%. The

deposition of the YBCO superconducting film directly on the ^{ABAD}YSZ/SS did not lead to high quality coated conductors because macrocracks appeared due to the high lattice mismatch between YSZ and YBCO (-5,71%). Because of this, the deposition of a cap layer, in this case $Ce_{0.9}Zr_{0.1}O_2$, is necessary (misfit YBCO-CeO_2 = -0,52%). Thin CZO films of about 20-30 nm were deposited by spin coating on the as-received ^{ABAD}YSZ/SS using a high temperature treatment compatible with the substrate architecture. In spite of a relatively high rms roughness (~ 3 nm), the flat area fraction has been significantly increased, being now ~69%, due to the characteristic behaviour of CZO which tends to develop a terraced surface morphology. J_cs of 1,75 MA/cm^2 at 77K were obtained on such metallic substrates. For comparison purposes with the ^{MOD}CZO process developed in ICMAB on ^{ABAD}YSZ/SS, several substrates with the ^{PLD}CeO_2/^{ABAD}YSZ/SS architecture, received from the same company-Bruker HTS, were also investigated. Our results are slightly better on ^{MOD}CZO cap layers and we associate this to an enhanced surface planarity of the cap layer. Following the route initiated at ICMAB for the YBCO growth on single crystal substrates, when small quantities of silver salt were added in the CZO precursor solution, a slight increase of the planarity and hence of the J_c at self field, is registered, from 1,75 MA/cm^2 (^{TFA}YBCO/^{MOD}CZO/^{ABAD}YSZ/SS) to 1,94 MA/cm^2 (^{TFA}YBCO/Ag-^{MOD}CZO/^{ABAD}YSZ/SS), although, in the latter case, the cap layer could be annealed during a shorter time.

A clear correlation between the J_c of YBCO thin films, the flat area fraction of the underlying doped and undoped CeO_2 cap layer and the YBCO film mesostrain has been demonstrated. An increase of the flat area in the case of the metallic substrates is necessary to achieve high values of the critical current density of the YBCO films.

YBCO films with Ag additives were obtained in a certain range of growth temperatures, in single crystals and metallic substrates. On single crystals, usually at 740ºC, the J_c decreases more without Ag [1]. In the case of the SS tapes, the sample grown at 740ºC presents a higher J_c (0,8 MA/cm^2) than the Ag-YBCO with standard double step process (770ºC-810ºC) but this is still lower than a YBCO tape (1,75 MA/cm^2) with a double step process (770ºC-810ºC). Although, there is no improvement in J_c, films can be grown at lower temperatures when adding Ag.

The in-situ approach for vortex pinning enhancement by obtaining nanocomposite films, with $BaMO_3$ (M = Zr, Ce) nanodots, on both ^{MOD}CZO buffered YSZ single crystalline substrates and ^{MOD}CZO/^{ABAD}YSZ/SS metallic substrates was investigated. Two different types of nanoparticles are observed: epitaxial ones given by the (200) reflection and randomly oriented ones-(110) $BaMO_3$. The out-of-plane misorientation of the YBCO films

increases with the concentration of the nanoparticles in parallel to a lattice with an enhanced nanostrain. From the 2D XRD measurements, it seems that in the two nanocomposites, $BaCeO_3$ and BZO, the nanodots remain mostly random oriented. By means of TEM analysis, we have found that CZO cap layers exhibit a good overall epitaxial quality. Defects such as low angle grain boundaries or cap layer discontinuities are observed which could act as diffusion paths for Ba which then leads to nucleation of BZO or (Zr)-$BaCeO_3$ at the CZO/YSZ interface. Unexpectedly, (Zr)-$BaCeO_3$ was not found at the YBCO/CZO interface. The preferential nucleation at the CZO/YSZ interface can be tentatively associated to lattice mismatch effects. Also TEM analysis reveal that the BZO nanodots display some highly mismatched epitaxial orientations such us: [100]BZO//[100]YBCO, [111]BZO//[010]YBCO and [110]BZO//[100]YBCO.

High J_c values have been achieved with MOD-$(Ce,Zr)O_2$ cap layers for all nanostructured CC architectures, reaching values of J_c(77K)= 3,1 MA/cm^2 (7% BZO-YBCO/^{MOD}CZO/YSZ), J_c(77K)= 2,7 MA/cm^2 (7% $BaCeO_3$-YBCO/LAO) and J_c(77K)= 1,7 MA/cm^2 (7% BZO-^{TFA}YBCO/^{MOD}CZO/^{ABAD}YSZ/SS). These nanostructured CC exhibit enhanced vortex pinning properties (reduced J_c anisotropy, smoother magnetic field dependence) and so, they are very promising as high performance coated conductors for high fields and high temperatures applications.

Future directions:

So far, we have devoted a lot of effort to fabricate and characterize coated conductors on ABAD metallic substrates at the laboratory scale. Understanding better the correlation cap layer roughness and planarity with the microstrain developed in the YBCO film and his influence on the superconducting properties has been proved to be important to improve the quality of the CC. The next challenge to face is to keep or improve the quality of YBCO in-plane texture ($\Delta\Phi$=5º), while the J_c limited by grain boundaries is reduced and approaches the intragrain J_c values. On the other hand, while the beneficial effect of preparing nanocomposites has been clearly demonstrated, the self-field critical current densities need to be further improved. The combination of both achievements should lead to very competitive coated conductors prepared by cost-effective methodologies such as chemical solution deposition.

7.1. References

[1] F. Martinez, "Uso de sales inorgánicas y nanopartículas en el crecimiento de capas delgadas superconductoras crecidas por CSD," PhD Thesis, UAB, Bellaterra (2011).

CONFERENCES AND CONGRESSES

Oral:

- 2nd Annual NESPA Network Meeting, Rust (Austria), 1 - 3 October 2008, "YBCO nanostructured thin films on doped CeO_2 buffered substrates";

- HIPERCHEM Meeting, Barcelona (Spain), 5-7 March 2008, "All solution doped CeO_2 based Coated Conductors";

- Energy Challenges. Material challenges for future applications in energy and environment, XaRMAE, December 2007, Barcelona (Spain), "All solution CeO_2 based coated conductors";

- MRS Spring Meeting 2010, 5-9 April San Francisco (USA), "Single $Ce_{0.9}Zr_{0.1}O_{2-\delta}$ Buffer Architecture Coated Conductors Based on MOD Method";

- NESPA final meeting, 13-14 September, Cambridge (UK), "Nanostructuration of simple architectures with CZO as cap layer for Coated Conductors".

Posters:

- European Conference on Applied Superconductivity, EUCAS 2007, 16-20 September, Belgium, "Multilayers growth of all chemical YBCO/CeO_2/$La_2Zr_2O_7$/Ni RABiT Coated Conductors";

- Applied Superconductivity Conference - ASC 2008, 17 – 22 August 2008, Chicago (USA), "Nucleation and growth of chemical solution deposited TFA-YBCO/MOD-$(Ce,Zr)O_2$/ABAD-YSZ/SS coated conductors";

- NESPA Midterm meeting, 19-20 March 2009, Barcelona, "Simple architectures based on the MOD $(Ce,Zr)O_2$ for Coated Conductors ";

- NANOSELECT, 9-10 July 2009, Sant Benet, Barcelona, "Coated Conductors with epitaxial MOD $(Ce,Zr)O_2$ as cap layer";

- European Conference on Applied Superconductivity, EUCAS 2009, 13-17 September Dresden, Germany, "Coated Conductors with epitaxial MOD $(Ce,Zr)O_2$ as cap layer";

- International Workshop on Coated Conductors for Applications (CCA09), 22-24 November 2009, Barcelona, Spain, "MOD Deposition of $Ce_{0.9}Zr_{0.1}O_{2-\delta}$ Single Buffer Layer for $YBa_2Cu_3O_{7-x}$ Coated Conductors";

- NANOSELECT, 14-16 July 2010, Sant Feliu de Guixols, Girona, Spain ":"MOD Deposition of $Ce_{0.9}Zr_{0.1}O_{2-\delta}$ Single Buffer Layer for $YBa_2Cu_3O_{7-x}$ Coated Conductors";

- Applied Superconductivity Conference - ASC 2010, 1 – 6 August 2010, Washington (USA), "Development of ^{TFA}YBCO Coated Conductors on ^{ABAD}YSZ substrates".